U.PORTO

Impact of AGN and nebular emission on the estimation of stellar properties of galaxies

Leandro Saúl Machado Cardoso
Departamento de Física e Astronomia, Faculdade de Ciências, Universidade do Porto
Instituto de Astrofísica e Ciências do Espaço

Advisors
Jean Michel Gomes & Polychronis Papaderos
Instituto de Astrofísica e Ciências do Espaço

Dissertation submitted to the University of Porto
for the degree of Doctor of Philosophy in Astronomy

Porto, July 2017

Acknowledgements

I thank Jean Michel Gomes and Polychronis Papaderos for their guidance. I also thank my colleagues at the Instituto de Astrofísica e Ciências do Espaço and Centro de Astrofísica da Universidade do Porto for creating an amicable and creative workplace.

I acknowledge funding by Fundação para a Ciência e a Tecnologia through the grants: CAUP-07/2013-BI in the context of the project FCOMP-01-0124-FEDER-029170 & PTDC/FIS-AST/3214/2012; CAUP-03/2015-BI in the context of the project FCOMP-01-0124-FEDER-029170 & PTDC/FIS-AST/3214/2012, and CIAAUP-01/2016-BI in the context of the project UID/FIS/04434/2013 & POCI-01-0145-FEDER-007672.

Acima de tudo, agradeço à minha família pelo apoio incondicional. Afinal, sempre me tornei num cientista louco, Mãe!

Porto, 20 July 2017

Summary

The study of galaxy formation and evolution with data from large-scale surveys relies to a large extent on an automated and robust application of spectral synthesis to derive physical properties of galaxies. However, most of the state-of-the-art codes used to decompose the galaxy optical spectrum into its elementary spectral components adopt mainly stellar ingredients. Therefore, this work aims to quantify the impact of emission produced by an active galactic nucleus (AGN) and excited gas on the estimation of fundamental stellar properties of galaxies with currently available spectral synthesis. The thesis is organised as follows.

Chapter 1 briefly reviews the physical framework of spectral synthesis in an historical context. The discussion proceeds with an overview of the state of the art regarding the spectral contribution of AGN and nebular emission and their impact on the derived physical properties. Moreover, it is presented a description of the structure and objectives of the thesis.

Chapter 2 describes the creation with the evolutionary spectral synthesis code Rebetiko of purely-stellar synthetic spectra of galaxies aiming to reproduce the star formation histories of different Hubble-type galaxies. Population spectral synthesis is then applied to these spectra to assess the robustness of current codes in recovering fundamental stellar properties (e.g. formation history, total mass, mean age, mean metallicity). Results show the dependence of systematic uncertainties on the adopted base library and the star formation history of the galaxy.

Chapter 3 focuses on the impact of an AGN continuum model in the synthetic spectra on the estimation of stellar properties assuming different strategies of modelling the AGN. Results are used to place an AGN detection threshold under which a population spectral synthesis code is unable to reliably distinguish between the stellar and AGN continua. Moreover, results show that a purely-stellar modelling approach can lead to severe systematic biases on the estimated stellar properties, uncertainties which can be greatly attenuated when adopting an adequate AGN modelling approach.

Chapter 4 introduces to the analysis the nebular emission produced by HII and AGN narrow-line regions. Population spectral synthesis is again applied in order to study the impact of nebular emission due to starlight and/or AGN on the estimated stellar properties. Results show that a purely-stellar modelling approach can lead to severe systematic biases on the stellar properties. A pilot study with the code Fado reveals the importance of simultaneous modelling the stellar and nebular emission in order to derive a robust estimate of the star formation history of star-forming galaxies.

Finally, chapter 5 summarises the main results of this work and their implication to the interpretation of galaxy formation and evolution with state-of-the-art spectral synthesis. The text concludes with a few remarks on promising avenues for the improvement of the physical framework of spectral synthesis.

`Keywords:` galaxy formation – galaxy evolution – stellar content of galaxies – active galaxies – star-forming galaxies

Sumário

O estudo da formação e evolução de galáxias com dados de grandes levantamentos depende em grande medida numa aplicação automatizada e robusta de síntese espectral para a obtenção de propriedades físicas de gálaxias. No entanto, a maioria dos actuais códigos utilizados para decompor o espectro óptico de uma galáxia nas suas componentes espectrais elementares adoptam principalmente ingredientes estelares. Portanto, este trabalho procura quantificar o impacto da emissão produzida por um núcleo galáctico activo (*active galactic nucleus*, AGN) e gás excitado na estimação de propriedades estelares essenciais de galáxias com síntese espectral actualmente disponível. A tese está organizada da seguinte forma.

O captulo 1 revê de forma sucinta o desenvolvimento físico da síntese espectral num contexto histórico. A discussão procede com uma visão geral do estado da arte em relação às contribuições espectrais da emissão de AGN e nebular para os espectros de galáxias e impacto destas nas propriedades físicas derivadas. Além disso, é apresentada uma descrição da estrutura e objectivos da tese.

O capítulo 2 descreve a criação de espectros sintéticos puramente estelares com o código de síntese espectral evolutiva Rebetiko de galáxias que procuram reproduzir as histórias de formação estelar de diferentes gálaxias de tipo Hubble. Síntese espectral populacional é de seguida aplicada a estes espectros para avaliar a robustez dos actuais códigos na recuperação de propriedades estelares fundamentais (e.g. história de formação, mass total, idade média, metalicidade média). Os resultados mostram a dependência de incertezas sistemáticas na biblioteca adoptada e na história de formação estelar da galáxia.

O capítulo 3 foca-se no impacto de um modelo do contínuo de AGN em espectros sínteticos na estimação de propriedades estelares assumindo diferentes estragégias de modelação do AGN. Os resultados são usados para colocar um limite de detecção de AGN sob o qual um código de síntese espectral populacional é incapaz de distinguir com fiabilidade entre os contínuos estelar e do AGN. Além disso, os resultados mostram que um método de modelação puramente estelar pode levar a severos vieses sistemáticos nas propriedades estelares estimadas, incertezas estas que podem ser significativamente atenuadas quando adoptando um adequado método de modelação do AGN.

O capítulo 4 introduz na análise a emissão nebular produzida por regiões HII e de linhas estreitas de AGN. Síntese espectral populacional é de novo aplicada para estudar o impacto de emissão nebular devida à luz estelar e/ou do AGN nas propriedades estelares estimadas. Os resultados mostram que método de modelação puramente estelar pode levar a vieses sistemáticos severos nas propriedades estelares. Um estudo piloto com o código Fado revela a importância de modelar simultaneamente a emissão estelar e nebular para derivar um estimativa robusta da história de formação estelar de galáxias formando estrelas.

Finalmente, o captulo 5 resume os principais resultados deste trabalho e a implicação destes na interpretação da formação e evolução de galáxias usando a actual síntese espectral. O texto conclui com algumas observaçãos sobre direcções promissoras para o melhoramento da concepção física de síntese espectral.

`Palavras-chave:` formação de galáxias – evolução de galáxias – contéudo estelar de galáxias – galáxias activas – galáxias com formação estelar

Contents

List of Figures

1 Introduction

Light of celestial bodies can reveal much about their nature. This idea crystallised over the 20$^{\text{th}}$ century during the dawn of Modern Astronomy with the introduction and development of photometry and spectroscopy. This lively branch of Natural Sciences has taken great strides towards a deeper understanding of the Universe. The solid foundation laid along the same century on galaxy formation and evolution marked an analogous crossover for Extragalactic Astronomy (e.g. Hubble 1926; Hubble 1929; Schmidt 1959; Faber & Jackson 1976; Tully & Fisher 1977; Tinsley 1980; Sandage 1986; Lilly *et al.* 1996; Madau *et al.* 1996; Kennicutt 1998). However, the analysis of galaxy observations under the preview of theoretical astrophysics remains largely an untraveled road. This realisation is both humbling and exciting.

If one were to read the lifebook of a galaxy one could learn on its first chapters the environmental conditions upon its birth from a cosmological point of view. It could be described on the first pages how the baryonic coalescence process induced by dark matter halos lead to the ignition of the first stars with the collapse and fragmentation of pristine and massive gas clouds. It could also be detailed how these and subsequent stellar populations formed, evolved and eventually died, changing in the process the chemical composition of the *interstellar medium* (ISM). Following chapters could trace the morphological scars of the galaxy in order to reconstruct the history of interactions with its closest neighbours, thus detailing galactic merger episodes or other interactions with its environment. It might also have been that the galaxy spent most of its life in isolation, thus serving as a prototype of secular evolution. On the one hand, the narrative might reveal the physical details of an *active galactic nucleus* (AGN) phase and its role on the matter cycle of the galaxy. On the other hand, it could also be detailed the contribution of *nebular emission* (NE) to the light output of the galaxy as characterised by the ISM chemical composition. Later chapters could reveal the inevitable end of the stellar activity of the galaxy with the description of how the last light came to be shed by its longer-lived low-mass stars. Apart from all the complexity inherent to the study of galaxies detailed in this idealised book, one can at least wonder about the information that can be recovered from the study of the light emitted by a galaxy.

The understanding of galaxy formation and evolution has seen major advances over the past decades, mostly due to the advent of large-scale spectroscopic surveys (e.g. York *et al.* 2000; Colless *et al.* 2001; Jones *et al.* 2004) and a constant improvement of theoretical models of spectrophotometric and chemical evolution (e.g. Tinsley 1980; Krüger, Fritze-v. Alvensleben & Loose 1995; Fioc & Rocca-Volmerange 1997; Bruzual & Charlot 2003; Vazdekis *et al.* 2010). Indeed, important results have been brought to light over the last decades in Extragalactic Astronomy, from which it can be highlighted: (**a**) star formation in high-mass galaxies seems to have predominantly occurred at high redshifts, while a fraction of their low-mass local counterparts still show a relatively high specific star formation rate, an observable known as *galaxy downsizing* (e.g. Cowie *et al.* 1996; Cimatti, Daddi & Renzini 2006); (**b**) evidence suggests that galaxies can be divided based on their stellar activity as *blue star-forming* and *red quiescent galaxies*, a result commonly referred to as the *galaxy colour-bimodality* (e.g. Gladders & Yee 2000; Strateva *et al.* 2001) (**c**) cosmic star formation seems to have peaked at $z \sim 1$, approximatively 6 Gyr ago (e.g. Heavens

et al. 2004), and (**d**) more massive galaxies tend to have more metals than their less massive counterparts, a result illustrated by a tight correlation between stellar mass and gas-phase metallicity (e.g. Tremonti *et al.* 2004).

Spectral synthesis (SS) has proved to be an essential tool to analyse galactic observables and interpret important physical properties of galaxies (e.g. stellar and nebular extinctions, stellar kinematics, stellar mass, age and metallicity) by exploiting the information encoded in spectra of galaxies. Indeed, SS can play an important role in piecing back together the book detailing the formation and evolution even of the most inconspicuous galaxy. This can be accomplished by creating synthetic spectra with empirically-founded assumptions on, for example, the stellar *initial mass function* (IMF), *star formation history* (SFH) and *chemical evolution history* (CEH), that can be compared to observations to recover galaxy properties. Conversely, observed spectra can be directly decomposed into the fossil records of star-formation episodes in order to estimate the SFH and CEH of a galaxy.

The main objective of this monograph is to provide an quantitative answer to the following question: *What is the relative impact of AGN and NE on the estimation of stellar properties of galaxies with state-of-the-art SS?* This question leads to important research topics in Modern Extragalactic Astronomy and Astrophysics, with a particular focus on spectral modelling of galaxies with emission emitted by stars, AGN and gas. This chapter recalls astrophysical concepts essential to this endeavour and briefly reviews the state of the art on this subject. Section 1.1 introduces SS from an historical point of view, with its two main approaches being presented in Subsections 1.1.1 and 1.1.2. Section 1.2 presents a summary of the state of the art of SS regarding particularly optical-based studies of AGN and NE in Subsections 1.2.1 and 1.2.2, respectively. Finally Section 1.3 outlines the main structure and objectives of this thesis.

1.1 Spectral synthesis

The SFH and CEH of galaxies can be estimated either through direct or indirect methods. In the former category falls, for instance, the spectral classification of stars by resolving stellar populations in *colour-magnitude diagrams* (CMDs). However, the capabilities of current observing facilities and instrumentation limit the applicability of this technique to the solar neighbourhood, a few Local Group galaxies and its close vicinity (e.g. Sánchez-Blázquez *et al.* 2006). On the latter category is SS, which allows the inference of different physical properties such as the SFH of a galaxy by decoding its spectrum into the relative spectral contributions of its different stellar populations. Particular focus is given to the second method in the following discussion.

The concept of viewing a galactic spectrum as a combination of stellar spectra came to be at the turn of the twentieth century. Scheiner (1899) observed for the first time the striking similarity between the optical spectrum of Great Andromeda Nebula and the solar spectrum. Öhman (1934) confirmed this observation and noted that the Fraunhofer sodium doublet D1λ5896 & D2λ5890 Å of the nebula were clearly stronger than those of the sun. This can now be interpreted as early evidence for the intrinsic spectrophotometrical difference between individual stars and composite stellar populations.

However, extragalactic spectral synthesis studies also came into focus when Whipple (1935) analysed photometric reductions of 38 galaxies in the Coma-Virgo cluster and formalised the idea of estimating the relative contribution of different stellar spectral types from integrated light of a galaxy by comparing it to standard stars located in the solar neighbourhood in a CMD. It would be Baade (1944a) who would put this concept into practice by performing the photometric reduction of red exposures of M 32, NGC 205 and the central region of the Andromeda nebula and resolving the corresponding stellar populations on an Hertzsprung-Russel diagram (Rosenberg 1910). Baade (1944b) then applied a similar methodology to observations of NGC 147 and NGC 185, at the time newly found members of the Local Group of galaxies.

Morgan (1956) continued this trial-and-error approach of modelling by hand the relative contributions of different stellar spectral types when analysing the integrated spectra of globular clusters. Moreover, Wood (1966) used narrow-band photometry between 3400 and 7300 Å to study the stellar content of 20 galaxies by comparing their colours to those of 93 field stars. Although good agreement was found for E to S0 galaxies, the computed *mass-to-light* (M/L) ratio values were found to be smaller than the dynamic M/L values used to calibrate the synthesis. Moreover, results showed that all galaxies had metal-to-hydrogen ratios similar to the Milky Way. These conclusions were later recognised to be due the limitation in stellar diversity of performing SS using solely stars in the solar neighbourhood.

SS became common practice when evolutionary spectral synthesis and galactic chemical evolution

were established by Tinsley (1968, 1972, 1980) and Tinsley & Gunn (1976). Major improvements over the following decades lead to the transition from modelling techniques relying on fluxes, colours, *equivalent widths* (EWs) of spectral absorption features and/or bandpasses (e.g. Faber 1972; Joly 1974; O'Connell 1976; Bica 1988) to a more optimal exploitation of spectral information with a full-spectrum modelling approach (e.g. Cid Fernandes *et al.* 2005; Tojeiro *et al.* 2007; Koleva *et al.* 2009). The transition from longslit and single-fiber to *integral field unit* (IFU) spectroscopy during the past decade proved also to be an important step in the spatial distribution analysis of esssential galaxy physical properties (e.g. Sarzi *et al.* 2006, 2010; Kehrig *et al.* 2012; Papaderos *et al.* 2013; Gomes *et al.* 2016a,b,c; Li *et al.* 2015; Belfiore *et al.* 2016; Ibarra-Medel *et al.* 2016). Notwithstanding, the true potential of SS was revealed with the dawn of large-scale surveys (e.g. SDSS, York *et al.* 2000; 2dFGRS, Colless *et al.* 2001; 6dFGRS, Jones *et al.* 2004) and the more recent IFU-based surveys (e.g. SAURON, Bacon *et al.* 2001; CALIFA, Sánchez *et al.* 2012; SAMI, Croom *et al.* 2012; MaNGA, Bundy *et al.* 2015), marking a perception shift of how SS can be applied in Extragalactic Astronomy with optimal efficiency to recover in a reliable manner the information encoded in the spectra of galaxies.

At the same time, it is important to consider that SS suffers from substantial limitations and poorly quantified uncertainties (e.g. Conroy, Gunn & White 2009). For instance, only a few works have focused on the particular task of accounting for the effects of dust (e.g. Charlot & Fall 2000), nebular (e.g. Krüger, Fritze-v. Alvensleben & Loose 1995; Leitherer *et al.* 1999; Zackrisson *et al.* 2001; Anders & Fritze-v. Alvensleben 2003; García-Vargas *et al.* 2013) or AGN emission to the optical spectra of galaxies (e.g. Schmitt, Storchi-Bergmann & Cid Fernandes 1999; Cid Fernandes *et al.* 2004, Moultaka 2005). Indeed, it is not yet fully clear the influence that these spectral components might have on the interpretation of the SFH and other physical properties of galaxies using purely-stellar SS. Reviews by Walcher *et al.* (2011), Conroy (2013) and Cerviño (2013) provide a detailed discussion of physical framework, historical context, achievements and limitations of SS.

Extragalactic Astronomy saw around the 1970s the emergence of two seemingly divergent yet complementary approaches for the estimation of the SFHs, CEHs and other physical properties of galaxies. Among many terms, these methods are known as Evolutionary Spectral Synthesis (Subsection 1.1.1) and Population Spectral Synthesis (Subsections 1.1.2). The following discussion addresses both approaches by briefly describing the fundamental mathematical formulation behind each and by reviewing their conception and development in an historical context.

1.1.1 Evolutionary spectral synthesis

Evolutionary spectral synthesis (ESS) allows for the inference of galaxy physical properties by comparing spectrophotometric observables to evolutionary synthesis models. Synthetic photometry or spectroscopy is created by considering empirically founded assumptions and/or *ad hoc* initial conditions on, for example, the stellar IMF, *star formation rate* (SFR), gas mass fraction and stellar metallicity variations with time (e.g. Tinsley 1968, 1972; Spinrad & Taylor 1972; Tinsley & Gunn 1976; Renzini 1981; Bruzual 1983; Krüger, Fritze-v. Alvensleben & Loose 1995; Arimoto & Yoshii 1986, 1987; Charlot & Bruzual 1991; Fioc & Rocca-Volmerange 1997; Vazdekis 1999; Leitherer *et al.* 1999; Bruzual & Charlot 2003; Le Borgne *et al.* 2004; Vázquez & Leitherer 2005 Coelho *et al.* 2007; Kotulla *et al.* 2009; Mollá, García-Vargas & Bressan 2009; Vazdekis *et al.* 2010; Coelho 2014; Röck *et al.* 2016). Evolutionary models can be compared to observables, for instance, by applying Bayesian inference or a minimisation procedure such as the minimum chi-squared χ^2 estimation,

$$\chi^2 = \sum_{\lambda} \left[(O_\lambda - M_\lambda)\ w_\lambda \right] , \tag{1.1}$$

where O_λ is the the spectral flux of the observed spectrum, M_λ is the spectral flux of the synthetic model that closest matches O_λ, w_λ is the inverse of the error of the observation and λ is the wavelength. The synthetic model flux M_λ is usually created by linearly combining smaller building blocks such as spectra of individually resolved stars or synthetic simple/single stellar populations, the later being an important ingredient in current SS of galaxies.

The term *simple stellar population* (SSP) introduced by Renzini (1981) refers to a coeval and chemically homogenous group of stars formed from an instantaneous burst. There are two main approaches to create SSPs, which mainly differ in their post-main sequence treatment: (**a**) isochrone synthesis (Chiosi, Bertelli

& Bressan 1988; Maeder & Meynet 1988; Charlot & Bruzual 1991) computes the stellar population flux by assuming an IMF and integrating the flux contributions of the individual stars along an isochrone within a given mass range, usually up to the end of the early asymptomatic giant branch, with later stages like the thermally-pulsing of the *asymptotic giant branch* (AGB) being described by individual recipes (e.g. Bruzual & Charlot 2003; Vazdekis *et al.* 2010), and (**b**) fuel consumption (Renzini & Buzzoni 1986; Buzzoni 1989; Maraston 1998) uses the so-called *fuel* variable, which is the amount of hydrogen and/or helium available for nuclear burning, to track the number of post-main sequence stars with similar ages and chemical compositions (e.g. Maraston 2005).

Assuming the isochrone synthesis as an illustrative case, the spectral evolution of a stellar population $F_{\lambda}^{\rm SSP}(t, Z)$ of age t and metallicity Z can be determined by assuming an IMF $\Phi(m)$ (e.g. Salpeter 1955; Kroupa 2001; Chabrier 2003) and integrating the stellar spectra along an isochrone of age t,

$$F_{\lambda}^{\rm SSP}(t, Z) = \int_{m_{low}}^{m_{up}} \Phi(m)\ F_{\lambda}^{\star}(m, t, Z)\ {\rm d}m, \tag{1.2}$$

where m_{low} and m_{up} are the mass lower and upper limits, respectively, and $F_{\star}^{\star}(m, t, Z)$ is the spectrum of a star with zero-age main sequence mass m. The flux of a *composite stellar population* (CSP) $F_{\lambda}^{\rm CSP}(t)$ representing the overall stellar content of a galaxy of age t can then be computed by linearly combining SSPs of different ages and metallicities weighted by the SFR $\Psi(t) = {\rm d}M_{\star}/{\rm d}t$,

$$F_{\lambda}^{\rm CSP}(t, Z) = \int_{0}^{t} \Psi(t - t')\ F_{\lambda}^{\rm SSP}(\lambda, t', Z)\ {\rm d}t', \tag{1.3}$$

where $F^{\rm SSP}(\lambda, t', Z)$ represents the SSP spectral library as a function of the wavelength λ, age t' and metallicity Z. Kotulla *et al.* (2009) provides a schematic yet detailed overview of the determination of SPS and CSP models. Additional terms can be added to Equation 1.3 to include additional galaxy spectral components (e.g. nebular and AGN emission).

The inception of ESS can be traced to works such as Tinsley (1968, 1972), Spinrad & Taylor (1972) and Tinsley & Gunn (1976). For instance, Tinsley (1968) constructed evolutionary histories of galaxies by regulating two main parameters: the initial rate of gas consumption during stellar formation and the birth rate of very low-mass stars. The resulting synthetic galaxies were compared to local galaxies with respect to colours, M/L ratios, relative mass of gas and stellar spectral types contributing to the light. It was found a reasonably good match between the evolutionary models and observations of different types of galaxies according to the morphological classification proposed by Hubble 1926 and expanded by de Vaucouleurs (1959). Subsequent works such as Renzini (1981) and Bruzual (1983) introduced more sophisticated methods to account for different stellar evolutionary stages using improved stellar theory and observations. Tinsley (1980) provides a comprehensive review of the essential formalism of ESS.

Different efforts have been carried out in order to present a clear and consistent picture of galaxy formation and evolution by analysing different galaxy constituents and properties. For example, Krüger, Fritze-v. Alvensleben & Loose (1995) compared optical and infrared photometric bands of evolutionary *spectral energy distribution* (SED) models including nebular continuum and emission-lines with local blue compact dwarfs. It was shown that NE plays an important role in describing the photometric observables of starburst galaxies such as the observed dwarf galaxies. Moreover, Fioc & Rocca-Volmerange (1997) presented spectrophotometric evolutionary models with NE covering the *ultraviolet* (UV) to the *near-infrared* (NIR) range from 220 Å up to 5 μm for both starburst and evolved galaxies. One of the innovations of this study was the extension of evolutionary models to the NIR and inclusion of stellar tracks extending to the thermally-pulsing AGB and post-AGB evolutionary phases, which are particular relevant to the production of ionising photons in old stellar populations. Moreover, Leitherer *et al.* (1999) presented an approach of including the most significant evolutionary stages of massive stars and produced synthetic SEDs covering the important 10^6–10^9 yr stellar evolutionary stages for five metallicities in the $Z = 0.001$–0.04 range. As to be expected, it was found that the stellar content of starburst galaxies are mainly composed of young and metal-poor stellar populations.

The progress made on stellar evolution and stellar observations led Bruzual & Charlot (2003) (hereafter BC2003) to become one of the most well-known ESS efforts in the last decades. BC2003 presented SSP evolutionary models with ages between 0.1 Myr and 20 Gyr for six metallicities ($Z = 0.0001$, 0.0004, 0.004, 0.008, 0.02 and 0.05, with $Z_{\odot} = 0.02$) covering the electromagnetic spectral range of 91–160000 Å with a $\sim$3 Å resolution at *full width half maximum* (FWHM) between 3200 and 9500 Å. The evolutionary models

are based on the theoretical BaSeL (Bessell *et al.* 1989, 1991; Fluks *et al.* 1994; Allard & Hauschildt 1995; Rauch 2002), observational STELIB (Le Borgne *et al.* 2003) and observational Pickles (Fanelli *et al.* 1992; Pickles 1998) stellar spectral libraries which cover the wavelength ranges 91–1600000 Å, 3200–9500 Å and 1205–25000 Å with median resolving powers of 300, 2000 and 500, respectively. Moreover, BC2003 adopted Salpeter (1955) and Chabrier (2003) IMFs with stellar masses in the range $m \in [0.01\text{–}100]\ M_{\odot}$ and stellar tracks models from the Padova (Alongi *et al.* 1993; Bressan *et al.* 1993; Fagotto *et al.* 1994a,b; Girardi *et al.* 1996, 2000) and the Geneva groups (Schaller *et al.* 1992; Charbonnel *et al.* 1996, 1999). The evolutionary tracks were complemented with models of both thermally-pulsing AGB and post-AGB stellar evolutionary phases to grant a wide metallicity coverage and good treatment of the most important post-main sequence evolutionary phases. BC2003 showed these models to be able to reproduce typical galaxy spectra in the Early Data Release of the SDSS (Stoughton *et al.* 2002). These and similar evolutionary models (e.g. Maraston 2005; Vazdekis *et al.* 2010) proved particularly impactful in studies of the mass-assembly history of large samples of galaxies in the optical (e.g. Kauffmann *et al.* 2003a,b,c; Heavens *et al.* 2004; Brinchmann *et al.* 2004; Tremonti *et al.* 2004) and in high-redshift studies by providing physical constraints to the first galaxies formed in the universe (e.g. Schaerer & Pelló 2005; Schaerer & de Barros 2009).

Some of the most cited ESS codes and groups are: PÉGASE (Fioc & Rocca-Volmerange 1997; Le Borgne *et al.* 2004); GALEV (Krüger, Fritze-v. Alvensleben & Loose 1995; Anders *et al.* 2004; Kotulla *et al.* 2009); Starburst99 (Leitherer *et al.* 1999, 2010; Vázquez & Leitherer 2005); YGDRASIL (Zackrisson *et al.* 2001); GALAXEV (BC2003); Maraston (Maraston 2005); MILES (Vazdekis *et al.* 2010; Röck *et al.* 2016); Coelho (Coelho *et al.* 2007; Coelho 2014), and PopStar (Mollá, García-Vargas & Bressan 2009).

1.1.2 Population spectral synthesis

Population spectral synthesis (PSS) aims to estimate the SFH, CEH and other properties of a galaxy by decomposing its spectrum into building blocks such as SSPs and other spectral constituents (e.g. Spinrad & Taylor 1971; Faber 1972; Joly 1974; O'Connell 1976; Bica 1988; Schmidt, Bica & Dottori 1989; O'Connell 1996; Pelat 1997, 1998; Heavens, Jimenez & Lahav 2000; Cid Fernandes *et al.* 2005; Ocvirk *et al.* 2006a,b; Tojeiro *et al.* 2007; MacArthur, González & Courteau 2009; Koleva *et al.* 2009). Equation 1.1 can be rewritten so that an observed continuum is decomposed into elemental spectral components such as SSPs by finding a best-fit synthetic model that minimises χ^2 in,

$$\chi^2(\vec{x}, M_{\lambda_0}, A_V, v_\star, \sigma_\star, \theta) = \sum_{\lambda} \left[(O_\lambda - M_\lambda) w_\lambda \right], \tag{1.4}$$

where $\vec{x}$ is the population vector representing either light or mass fractional contributions to the total synthetic flux at the normalisation wavelength λ_0 of each i$^{\rm th}$ SSP base element, with $i \in [1, ..., N_\star]$ and $N_\star$ being the number of elements in the base, M_{λ_0} is the synthetic flux at λ_0, A_V is the V-band extinction, $v_\star$ and $\sigma_\star$ are the stellar shift and broadening velocities, respectively, and θ represents potential non-stellar variables. In the case of a purely-stellar spectral decomposition, the reconstruction of the model M_λ can be interpreted as the age- and metallicity-dating of *fossil records* of star formation episodes encoded in the spectrum O_λ.

The synthetic spectrum M_λ can be explicitly written as a linear combination of $N_\star$ SSPs as,

$$M_\lambda(\vec{x}, M_{\lambda_0}, A_V, v_\star, \sigma_\star, \theta) = M_{\lambda_0} \left[\sum_{i=1}^{N_\star} x_i \ F_{\lambda,i} \ r_\lambda \right] \otimes G(v_\star, \sigma_\star) + \Theta_\lambda, \tag{1.5}$$

where x_i is the fractional contribution in either stellar light or mass of the i$^{\rm th}$ base element in $\vec{x} = \sum_{i=1}^{N_\star} x_i$, $F_{\lambda,i}$ is the flux of the i$^{\rm th}$ element normalised at the λ_0 monochromatic flux, $r_\lambda = 10^{-0.4(A_\lambda - A_{\lambda,0})}$ is the reddening term and A_λ the extinction at λ, $G(v_\star, \sigma_\star)$ is a Gaussian function representing a stellar velocity distribution centred at $v_\star$ and broadened by $\sigma_\star$, and Θ_λ is a generic term representing other potential spectral components (e.g. AGN, NE). Both Equations 1.4 and 1.5 illustrate the fact that the estimated SFH and CEH are a discretised version of their true functions, since star formation episodes are interpreted as single bursts of star formation of different ages and metallicities.

The inception of PSS can be traced to works such as Spinrad & Taylor (1971), Faber (1972), Joly (1974) and O'Connell (1976). For instance, Faber (1972) introduced a quadratic programming technique to decompose the integrated colours of M 31, M32 and M 81 galaxies into stellar population components

and estimated the mean absorption-line strengths, stellar population ages, luminosity function and M/L ratios. Moreover, Joly (1974) compared EW measurements from the central region of M 31 to a sample of solar neighbourhood stars classified according to their spectral type, luminosity class and metallicity. Among other results, it was shown that the central region of M 31 is composed of super metal-rich stars, a dwarf enriched main sequence and hot stars, thus implying a continuous star formation. Early PSS studies also showed that it is possible to decompose galaxy observables into spectrophotometric properties of resolved stars or stellar clusters (e.g. Bica 1988; Schmidt, Bica & Dottori 1989) in order to avoid assuming any particular scenario for the formation of the stellar populations (e.g. IMF, evolutionary tracks). However, this method was discontinued due to hard-to-quantify degeneracies related to the observed age and metallicity diversity of resolved stellar clusters.

PSS has proven particularly impactful in the analysis of large samples of galaxies (e.g. Kauffmann *et al.* 2003a,b,c; Heavens *et al.* 2004; Tremonti *et al.* 2004). For instance, Kauffmann *et al.* (2003a) analysed 10^5 galaxies from the SDSS *data release* (DR) 1 (Abazajian *et al.* 2003) and presented a method to estimate the SFH of galaxies based on two stellar absorption line features: the 4000 Å break strength D4000 and the Balmer absorption-line index $H\delta_A$. It was shown that the combined use of the two indices provides constraints on the mean age of the stellar population of a galaxy and on stellar mass fractions formed in recent bursts. Among other results, it was found that the integrated SFR sharply decreases with decreasing redshift (Madau *et al.* 1996). Kauffmann *et al.* (2003b) then showed that, on the one hand, low-mass galaxies have low values of D4000 and high values of $H\delta_A$, indicating young stellar populations are more numerous, and that, one the other hand, high-mass galaxies have high values of D4000 and low values of $H\delta_A$, suggesting that old stellar populations dominate in terms of light contribution. This result is also known as *galaxy downsizing* (Cowie *et al.* 1996). Heavens *et al.* (2004) used MOPED (Heavens, Jimenez & Lahav 2000) to also analyse spectra of SDSS DR 1 galaxies (Abazajian *et al.* 2003) and concluded that the SFH of the universe peaked at $z \sim 1$, also founding evidence indicating that massive galaxies have their star formation peak earlier than low massive galaxies, in agreement with the downsizing effect (Cowie *et al.* 1996; Cimatti, Daddi & Renzini 2006).

Despite its success, PSS was plagued in its first years by severe limitations such as the use of arbitrarily and unquantified assumptions and inherent degeneracies between the adopted models (e.g. O'Connell 1996; Pelat 1997, 1998). Pelat (1998) tackled the so-called *uniqueness of solution* algebraic problem (e.g. Wood 1966) arising when there were less EWs of absorption lines to synthesise than stars in the data base, meaning less observables than degrees of freedom. It was shown that the existence of a solution does not guarantee its uniqueness, although an approximation to it can in principle be made. Moreover, treatment of noise data and degeneracies between adopted evolutionary models (e.g. Faber 1972; Worthey 1994) are examples of important limitations of current PSS. Some of these issues were tackled and partially solved with the refinement of the mathematical approach to the synthesis problem (e.g. Pelat 1997, 1998; Worthey 1994), the advent of intermediate to high-resolution evolutionary models (e.g. BC2003; Vazdekis *et al.* 2010) and introduction of self-consistent and robust codes (e.g. Cid Fernandes *et al.* 2005; Tojeiro *et al.* 2007).

Some of the most cited PSS codes have slightly different goals: MOPED uses a lossless data compression method to increase computational speed (Heavens, Jimenez & Lahav 2000; Reichardt *et al.* 2001); STARLIGHT applies a full-spectrum modelling approach combined with a mixture of Metropolis algorithm and simulated annealing to explore the parameter space (Cid Fernandes *et al.* 2005, hereafter CF2005); STECMAP/STECKMAP applies least squares while keeping stable the inversion method and applying an optimal regularisation (Ocvirk *et al.* 2006a,b); VESPA aims at maximum robustness of derived parameters (Tojeiro *et al.* 2007, 2009); POPSYNTH simultaneous retrieves stellar population and kinematic profiles (MacArthur *et al.* 2009), and ULySS determines stellar atmospheric parameters and reconstructs the SFHs of galaxies (Koleva *et al.* 2009).

1.2 State of the art

The often interchangeably use of PSS and ESS may lead to the incorrect assumption that these SS approaches are conceptually similar. In part, this is due to the fact that PSS relies largely on advances made in ESS results such as SSPs to quantify its robustness in recovering physical properties from galaxy observables. For instance, there are studies that apply both SS approaches to quantify the degree of confidence with which stellar properties are determined with PSS (e.g. Goerdt & Kollatschny 1998; Cid

Fernandes *et al.* 2005). However, it is important to bare in mind that the most important distinction between ESS and PSS is their parametric and non-parametric nature, respectively. Indeed, in ESS is assumed a specific SFH analytical form, whereas this is not often the case in PSS.

Albeit significant improvements made in SS throughout the years, poorly explored uncertainties and overlooked spectral ingredients (e.g. AGN emission in active galaxies, NE in star-forming galaxies) can hinder the study of physical properties of galaxies. One of these shortcomings is known as the *age-metallicity degeneracy* that arises from the inability of distinguishing between metal-rich and young galactic spectra from metal-poor and old ones, and vice versa (e.g. Faber 1972; Worthey 1994). Moreover, the disentanglement of the interplay between the SFH, gas excitation mechanisms and stellar kinematics in PSS has not yet been carried out in a comprehensive manner (e.g. Pelat 1997, 1998). A strategy often adopted to overcome these degeneracies is to perform statistical analysis with large data sets and advanced computational methods, such as Monte Carlo simulations (e.g. Cid Fernandes *et al.* 2005) or Bayesian inference, in order to reduce possible systematic biases inherent to the current SS physical framework. One of the main objectives of this work is to quantify some of these limitations with the intension of providing a critical assessment of current SS.

For instance, an interesting and not fully explored application of SS is to galaxies with light contributions of non-stellar origin. Several studies have addressed the importance of modelling dust absorption and emission (e.g. Silva *et al.* 1998; Draine 2003), AGN emission (e.g. Bon, Popović & Bon 2014; Hayward & Smith 2015; Ciesla *et al.* 2015) and the NE that rises from reprocessing of stellar light by the gas in interstellar medium (e.g. Zackrisson, Bergvall & Leitet 2008; Schaerer & de Barros 2009; Martín-Manjón *et al.* 2010; García-Vargas, Mollá & Martín-Manjón 2013). The following discussion briefly describes how AGN (Subsection 1.2.1) and NE (Subsection 1.2.2) spectral contributions modify the observed spectrum of a galaxy and how they might impact the estimated stellar population properties.

1.2.1 AGN emission

The physical mechanism responsible for AGN activity in the majority of massive galaxies is thought to be a matter-accreting *super massive black hole* (SMBH) at the centre of its host galaxy (Kormendy & Richstone 1995; Richstone *et al.* 1998). The SMBH has a typical mass of $M_\bullet = 10^6$–$10^{10}\,M_\odot$ and a diameter comparable to that of the solar system (Lynden-Bell 1969). AGN are particular interesting astrophysical objects since they emit across the whole electromagnetic spectrum at high bolometric luminosities (10^{44}–10^{48} erg s^{-1}). The current favoured unification model proposes that the different AGN types are intrinsically the same and that differences between each are mainly due to the inclination angle between the line-of-sight of the observer and the plane of accretion onto the SMBH (Antonucci 1993; Urry & Padovani 1995). From the different types of AGN, Seyfert galaxies (Seyfert 1943) are the most common in the local universe and can be broadly classified as Type 1 or Type2, depending on whether they display, in addition to narrow-line emission, signs or not of broad-line emission, respectively. The study of AGN phenomenology is particular relevant given results mounting over the last decades that indicate a co-evolution between galaxies and their SMBHs, as reviewed by Heckman & Best (2014).

Evidence suggests that the AGN optical continuum might result from the combined effect of synchrotron radiation predominately detected in radio and the blackbody radiation peaking in the UV due to the accretion disk feeding the SMBH (O'Dell 1986). The UV-to-NIR *featureless continuum* (FC) rising from the accretion disk in a AGN, such as Seyfert galaxies, is usually parameterised by a *power-law* (PL) as $F_\nu \propto \nu^{-\alpha}$ (e.g. Koski 1978; Veilleux & Osterbrock 1987; Mathews & Ferland 1987; Heckman 1980; Kauffmann *et al.* 2003c; Cid Fernandes *et al.* 2004; Hao *et al.* 2013). The relative contribution of the AGN FC to the spectra of galaxies as been topic of debate for several decades (e.g. Koski 1978; Ho, Filippenko & Sargent 1995; Ho, Filippenko & Sargent 1997; Cid Fernandes, Storchi-Bergmann & Schmitt 1998; Storchi-Bergmann *et al.* 1998; Schmitt, Storchi-Bergmann & Cid Fernandes 1999; Eracleous & Halpern 2001; Ho, Filippenko & Sargent 2003; Cid Fernandes *et al.* 2004; Garcia-Rissmann *et al.* 2005; Ho 2008; Vega *et al.* 2009). However, only recently first attempts were made to examine the impact of AGN radiation to the estimation of other physical properties (e.g. Bon *et al.* 2014 Hayward & Smith 2015; Ciesla *et al.* 2015).

On the one hand, Bon, Popović & Bon (2014) created 7000 integrated synthetic spectra of Seyfert 2 galaxies and used ULySS (Koleva *et al.*, 2009) to estimate the contribution of the stellar and PL spectral components. This work showed that stellar populations are well estimated when the *signal-to-noise* (S/N) ratio is higher than 20 and the stellar contribution to the total flux is higher than 10%. On the other hand,

Hayward & Smith (2015) used hydrodynamical simulations and radiative transfer to test SED modelling in the recovery of physical parameters (e.g. V-band extinction, stellar mass, dust luminosity and mass, SFR). It was applied the SED modelling code MAGPHYS (da Cunha, Charlot & Elbaz 2008) to synthetic SEDs between the UV and millimetre and it was found that most physical parameters are overall well recovered. However, major merger simulations revealed that AGN contamination leads to a stellar mass overestimation no more than ∼0.03 dex shortly after starburst peaks induced by first pericentric passage and final coalescence.

Meanwhile, Ciesla *et al.* (2015) investigated properties of galaxies hosting an AGN by performing SED modelling between the UV and submillimetre with CIGALE (Noll *et al.* 2009) of synthetic SEDs of active galaxies based on the semi-analytic galaxy formation model GALFORM (Cole *et al.* 2000). Results showed that the exclusion of AGN models in the fit can lead to the overestimation of the stellar mass by up to ∼150% and the SFR by up to ∼300%, depending of AGN spectral type and SFH. Both overestimations increase with the AGN overall contribution to the total infrared luminosity $x_{\rm AGN}^{\rm IR}$. Moreover, the inclusion of AGN templates in the fit can still lead to the overestimation of the AGN light fraction up to ∼100%, depending on the AGN spectral shape and $x_{\rm AGN}^{\rm IR}$. On the one hand, the recovered AGN light fraction tends to its true value with increasing $x_{\rm AGN}^{\rm IR}$. On the other hand, the estimated mass and SFR show uncertainties up to ∼40% (∼0.15 dex) and ∼40–50 %, respectively, depending on the AGN spectral shape and $x_{\rm AGN}^{\rm IR}$.

These results highlight the importance of accounting for an AGN spectral contribution when applying SS to estimate, for instance, the SFH of active galaxies. However, it is important to bare in mind that the impact of the AGN continuum on the estimation of other physical properties (e.g. stellar mass, mean age and mean metallicity) with full-spectrum PSS is still poorly understood.

1.2.2 Nebular emission

NE is composed of recombination lines of hydrogen H and helium He, continuum emission due to free-free, free-bound and two photon emission, collisional-line emission and other emission-line mechanisms, such as, resonance-fluorescence and di-electronic recombination (e.g. Osterbrock 1989; Osterbrock & Ferland 2006). Some of the most prominent physical structures in galaxies associated with this type of emission are planetary nebulae or supernovae marking the life of low-mass ($0.8 < M_\star < 8\ M_\odot$) and high-mass stars ($M_\star > 8\ M_\odot$), respectively, *HII regions* (HIIRs) enveloping recently formed stellar populations and *narrow-* or *broad-line regions* (NLR and BLR, respectively) surrounding the innermost regions of an AGN. The treatment of NE in SS can be a quiet complex task. Simplified assumptions such as case B recombination theory (Osterbrock 1989; Osterbrock & Ferland 2006) are considered in several ESS codes (e.g. Krüger, Fritze-v. Alvensleben & Loose 1995; Fioc & Rocca-Volmerange 1997, 1999; Leitherer *et al.* 1999; Mollá *et al.* 2009). Moreover, several photoionisation codes allow a detailed description of the physical state of the gas (e.g. MAPPINGS III, Sutherland & Dopita 1993; CLOUDY, Ferland *et al.* 1998) that enable the creation of evolutionary models with a more realistic description of NE (e.g. Zackrisson *et al.* 2001, 2008; Martín-Manjón *et al.* 2010).

Studies of NE in galaxies were greatly aided when Baldwin, Phillips & Terlevich (1981) introduced the concept of using the emission-line flux ratios [NII]λ6583/H$\alpha\lambda$6563 and [OIII]λ5007/H$\beta\lambda$4861 (hereafter BPT1981 diagram) in order to characterise the nature of the radiative sources responsible for ionising ISM gas. This tool relies on the fact that the ionising spectrum of an AGN is orders of magnitude harder than that produced by stars. The emission-line ratios can then be compared to models, for instance, of interstellar gas excitation by AGN, young and massive stars (e.g. Ferland *et al.* 1998; Kewley *et al.* 2001) or shocks (e.g. Dopita & Sutherland 1995, 1996) in order to characterise its main excitation source. Veilleux & Osterbrock (1987) expanded this concept by introducing two more diagnostic tools based on the line ratios [SII]$\lambda\lambda$6717,6731/Hα and [OI]λ6300/Hα also coupled with [OIII]λ5007/Hβ (hereafter VO1987 diagrams). One of the key features of all of these diagnostics is that they are based on easily-measurable optical emission lines with small wavelength separations in order to minimise reddening effects. These tools have been extensively used to help distinguish between different excitation sources in a wide range of galaxy studies (e.g. Kauffmann *et al.* 2003c; Stasińska *et al.* 2006, 2008; Kehrig *et al.* 2012; Meléndez *et al.* 2014; McElroy *et al.* 2015).

Several studies throughout the years have shown the fundamental role of NE to optical continuum of star-forming and active galaxies. In particular, models have shown that nebular continuum and emission-lines can account up to ∼60 percent of the monochromatic luminosity at ∼5000 Å in AGN and

starburst galaxies (e.g. Papaderos *et al.* 1998; Zackrisson, Bergvall & Leitet 2008; Papaderos & Östlin 2012) and in optical broadband photometry, specially at low metallicities (Anders & Fritze-v. Alvensleben 2003. Krüger, Fritze-v. Alvensleben & Loose (1995) found that emission lines can contribute up to ∼45% to optical broadband photometry and that nebular continuum alone can account for up to ∼10 and 30% of the total optical and NIR emission, respectively. Moreover, Martín-Manjón *et al.* (2010) showed by comparing SEDs with and without NE that the the inferred mass of young star clusters can vary up to a factor ∼2.5. More recently, Pacifici *et al.* (2015) found that that SFRs can be be overestimated by up ∼0.12 dex if nebular emission is neglected in SED modelling.

Another important issue with current SS studies has to do with the impact that NE has on the estimation of the SFH and other physical properties of galaxies. Such exercise becomes particularly important considering that most PSS codes were conceived without taking into consideration NE as an physical ingredient (e.g. Heavens, Jimenez & Lahav 2000; Cid Fernandes *et al.* 2005; Tojeiro *et al.* 2007; MacArthur *et al.* 2009; Koleva *et al.* 2009), even though most of these are often applied to star-forming and/or active galaxies.

1.3 Thesis

This monograph presents a quantitative assessment of the impact of AGN and NE on the estimation of stellar properties of galaxies with state-of-the-art SS. This is accomplished by applying a combination of ESS and PSS ingredients to study potential biases and trends on the estimated stellar populations (e.g. SFH, total mass, mean age, mean metallicity) using synthetic optical spectra of galaxies. This work is organised as follows.

Chapter 2 describes the creation of a library of synthetic CSPs for different SFHs aiming to reproduce different Hubble-type galaxies. These synthetic spectra were subsequently fitted with a state-of-the-art PSS to the recover the main stellar properties by decomposing the spectrum into *fossil records* of star formation episodes. The analysis is focused on the impact that variations on the adopted base library and SFH have on the estimated physical properties. The found results provide valuable insight to the application of PSS to purely-stellar spectra that can be transposed when modelling, for instance, galaxies without evident non-stellar spectral signatures.

Chapter 3 investigates the impact of an AGN spectral component in recovering stellar information from synthetic active galaxies. This library of synthetic spectra was created by adding a simple AGN FC model to the CSPs presented in Chapter 2. PSS was then applied to these spectra considering different approaches for the handling of the AGN component. A quantitative AGN detection threshold is proposed by analysing how a PSS code discriminates between the blue and red continua of an AGN and an evolved CSP, respectively, in a galaxy leaking its Lyman-continuum radiation. A subsequent analysis of the PSS results of synthetic active galaxies with different SFHs provides powerful constraints to the viability of PSS to large samples of galaxies harbouring an AGN.

Chapter 4 explores the impact of NE originating from stellar and AGN photoionisation on the estimation of the main stellar population properties. HIIR and NLR simulations are computed with a state-of-the-art photoionisation code employing empirical- and theoretical-founded assumptions on the physical conditions of the two types of nebulae. PSS is first applied to the synthetic spectra of HIIRs to isolate the impact of NE due to photoionisation of solely starlight on the main stellar population properties. Afterwards, PSS is applied to models containing stellar, AGN and NE in order to analyse the combined effect and potential degeneracies between the different spectral components on the estimation of the the same physical quantities. Finally, a conceptional overview and demonstration of the capabilities of the PSS code FADO show the importance of a self-consistent computation of NE to a robust estimation of SFH and CEH of star-forming galaxies.

Finally, Chapter 5 summarises the main results of this study by drawing its main implications to the interpretation of stellar population properties of star-forming and/or active galaxies with SS. This is particular timely at the dawn of IFU spectroscopy, which enables a more detailed analysis of the physical structures and processes responsible for the formation and evolution of galaxies.

2

Purely-stellar galaxy models

Purely-stellar synthetic spectra of galaxies were created with the ESS code Rebetiko. These models aim to reproduce the spectral evolution of different Hubble-type galaxies on the basis of simply analytical functions of their SFR as a function of time. The synthetic spectra were used to evaluate the robustness and reliability of state-of-the-art PSS codes in determining fundamental stellar population properties (e.g. mass, mean age and mean metallicity) from synthetic galaxy spectra. The analysis was focused on the effect of the adopted SSP base library and the assumed SFH on the estimated physical properties.

This chapter is organised as follows. Section 2.1 presents the ESS code Rebetiko used to create a library of purely-stellar synthetic galaxy spectra covering a wide range of SFHs in Section 2.2. Section 2.3 describes the spectral modelling of the synthetic spectra with a state-of-the-art PSS code. On the one hand, Subsection 2.3.1 explores the impact that different SSP base libraries used in PSS have on the estimated stellar population properties. On the other hand, Subsection 2.3.2 focuses on the influence that the assumed SFH has on the synthesis results.

2.1 ESS code Rebetiko

The ESS code *Reckoning galaxy Emission By means of Evolutionary Tasks with Input Key Observables* (Rebetiko, Papaderos & Gomes in prep.) computes synthetic spectra of galaxies including both stellar and NE (continuum and lines) arising through the reprocessed ionising UV flux of stars. The spectral evolution of a galaxy can be expressed as,

$$F_\lambda(t,Z) = \int_0^t \Psi(t-t')\ F_\lambda^{\rm SSP}(t',Z)\ {\rm d}t' + \frac{\gamma_{\rm eff}(T_e)}{\alpha_{\rm B}(T_e)}\ \int_0^t \Psi(t-t')\ q^{\rm SSP}(t',Z)\ {\rm d}t'. \tag{2.1}$$

The first integral represents the sum of the SSP spectra $F_\lambda^{\rm SSP}$ of age t and metallicity Z weighted by the SFR $\Psi(t) = {\rm d}M_\star/{\rm d}t$. The second integral represents the nebular continuum determined by multiplying the number of stellar ionising photons ($\lambda \leq 911.76$ Å or $E \geq 13.6$ eV) represented by the term $\int_0^t q^{\rm SSP}(t',Z)\ {\rm d}t'$ by the SFR and the ratio between the effective continuous emission coefficient $\gamma_{\rm eff}$ and the case B recombination coefficient $\alpha_{\rm B}$. In particular, the nebular continuum is computed on the assumption of case B recombination under typical HIIRs physical conditions, such as, low electron density ($n_e \leq 100$ cm^{-3}) and an average electron temperature of $T_e = 10^4$ K (Osterbrock 1989; Osterbrock & Ferland 2006). Moreover, $\gamma_{\rm eff}$ is computed following the standard procedure of combining the contribution from hydrogen H and helium He atoms, which depends on the 2-photon (Nussbaumer & Schmutz 1984), free-free and free-bound (Brown & Mathews 1970) emission. It is worth noting that other species do not significantly contribute to the continuum emission and can be neglected (Brown & Mathews 1970 for a

full discussion). The $\gamma_{\rm eff}$ coefficient can be expressed as,

$$\gamma_{eff} = \gamma(\mathrm{HI}) + \gamma(2q) + \frac{n(\mathrm{He}^{+})}{n(\mathrm{H}^{+})}\ \gamma(\mathrm{HeI}) + \frac{n(\mathrm{He}^{++})}{n(\mathrm{H}^{+})}\ \gamma(\mathrm{HeII}), \tag{2.2}$$

where γ(HI), γ(HeI) and γ(HeII) are the total emission coefficients of HI, HeI and HeII taking into account free-free and free-bound emission processes, $\gamma(2q)$ is the 2-photon emission coefficient and $n(\mathrm{H}^{+})$, $n(\mathrm{He}^{+})$ and $n(\mathrm{He}^{++})$ are the densities of Hydrogen once ionised, Helium once ionised and Helium twice ionised, respectively. The total recombination coefficient $\alpha_{\rm B}(T_e = 10000\ \mathrm{K}) = 2.59 \times 10^{-13}\ \mathrm{cm}^3\ \mathrm{s}^{-1}$ follows Osterbrock & Ferland (2006). Finally, the H emission-lines fluxes are computed considering different electron temperatures and densities (Hummer & Storey 1987) and the UV ionising output from the stellar populations (Zanstra 1961) for radiation-bounded HIIRs. Line fluxes from heavier elements are computed assuming the semi-empirical calibration from Anders & Fritze-v. Alvensleben (2003) as a function of the nebular metallicity normalised to Hβ. A discretised version of Equation 2.1 suitable for numerical implementation can be written as,

$$F_\lambda(t, \langle Z \rangle) \approx \sum_i\ \Delta M(t - t_i) F_\lambda^{\rm SSP}\left[t_i, Z(t - t_i)\right]\ +\ \frac{\gamma_{\rm eff}(T_e)}{\alpha_{\rm B}(T_e)}\ \sum_i \Delta M(t - t_i)\ q^{\rm SSP}\left[t_i, Z(t - t_i)\right], \tag{2.3}$$

assuming small steps in time $\Delta t'$ and $\Psi(t) = dM(t')/dt \approx \Delta M(t_i)/\Delta t_i$.

The SFR function $\Psi(t)$ in Equation 2.1 describes how the gas mass is converted into stars throughout time and aims to approximate the SFH of different Hubble-type galaxies (Hubble 1926; de Vaucouleurs 1959). It is expected that environmental effects, such as galaxy harassment and mergers, combined with secular evolution processes of star formation might lead to highly stochastic SFHs of galaxies residing in high-density environments (e.g. galaxy clusters and their periphery). The stochastic nature of SFH is indeed suggested by semi-analytic (e.g. Quillen & Bland-Hawthorn 2008) and hydrodynamical simulations (e.g. Boquien, Buat & Perret 2014). Since the true SFHs of galaxies in these environments can be of considerable complexity to be modelled, it is common practice to assume simple analytical formulae for the evolution of their SFR with time (e.g. Fioc & Rocca-Volmerange 1997; Gavazzi *et al.* 2002; Kotulla *et al.* 2009).

Figure 2.1.1 illustrates the SFR functions adopted in this work that aim to represent in a simple parametric form the spectral evolution of galaxies of different Hubble types. The SFR allows REBETIKO to keep track at each evolutionary time step of the relative contribution of the SSPs composing a given CSP at the evolutionary stage t. The adopted functions normalised to total stellar mass $M_\star$=1 at t=15 Gyr can be broadly classified as:

- *Exponentially declining*: $\Psi(t) = \Psi_0 e^{-t/\tau}$, where Ψ_0 is the initial SFR value and τ is the e-folding timescale regulating the sharpness of the decline. This form is commonly used to describe the SFH of most Hubble types (e.g. Fioc & Rocca-Volmerange 1997; BC2003; Kotulla *et al.* 2009; Serra *et al.* 2011) and tends to a continuous star formation when $\tau \to \infty$ and to an instantaneous burst when $\tau \to 0$. These limits are thought to adequately represent the formation history of stellar populations in galactic disks and bulges, respectively. This analytical form is physically motivated by the Kennicutt-Schmidt law (Schmidt 1959; Kennicutt 1989), which assumes that the SFR per unit area is proportional to a power of the local H gas surface density. Functions with $\tau = 0.001$ (`TAU1`), 1 (`TAU2`) and 3 Gyr (`TAU3`) are represented in Figure 2.1.1 by the *magenta*, *red* and *orange lines*, respectively;
- *Continuous*: $\Psi(t) = \Psi_0$, where Ψ_0 is the initial and constant SFR value. A continuous SFR function is usually assumed in disk galaxy models (e.g. Kotulla *et al.* 2009). A continuous SFR (`CONT`) is represented in 2.1.1 by the *green line*;
- *Delayed*: $\Psi(t) = \Psi_0 \delta^4 e^{-t/\gamma}\left[1 - e^{-(t/\gamma)^3}\right]$, where $\gamma = 1/(\sqrt{2\pi} \times \delta)$, Ψ_0 is the initial SFR value and δ defines the cosmic time of the burst (Papaderos & Gomes in prep.). This analytical form is based on a function proposed by Papaderos *et al.* (1996) to fit the surface brightness profiles of BCD galaxies that show a flattening at the central core. This function has been proposed to explain, for instance, the delayed negative feedback from both star formation or an AGN (Quillen & Bland-Hawthorn 2008) on star formation with cosmic time. Functions with $\delta = 0.1$ (`DEL1`), 0.3 (`DEL2`), 0.5 (`DEL3`), 0.7 (`DEL4`) and 1 (`DEL5`), corresponding to SFR peaks at $z \sim 1.3$, 2.8, 3.9 5.9 and 9.8, are represented by

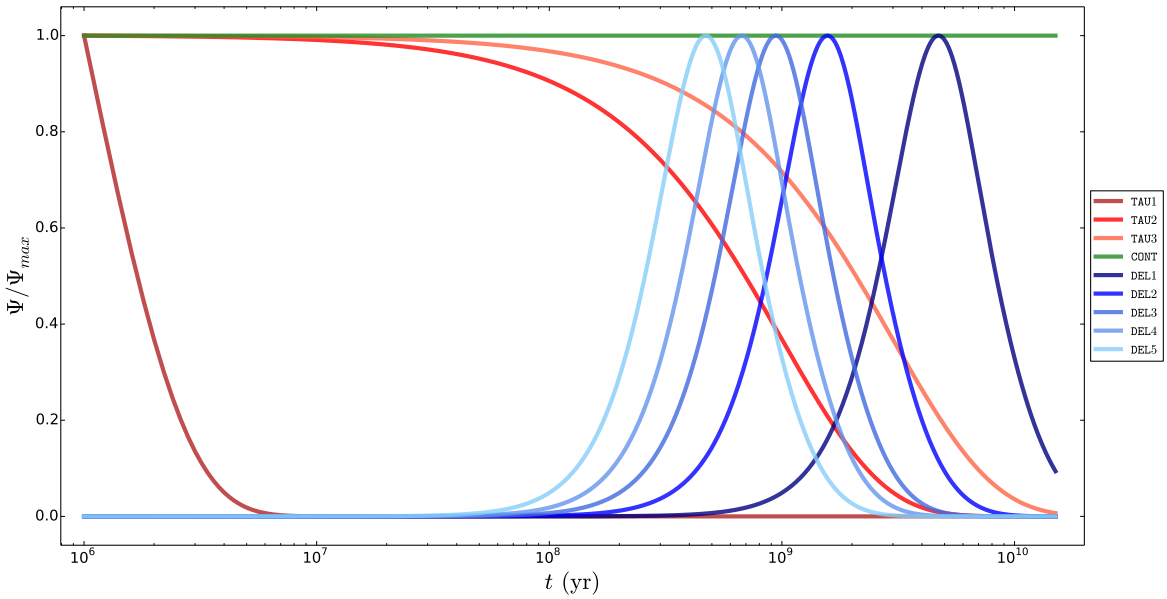

Figure 2.1.1: SFHs adopted with the ESS code REBETIKO to assemble a library of CSPs for different Hubble-type galaxies. Red, green and blues lines represent exponentially declining, continuous and delayed SFHs, respectively.

dark blue to *cyan lines*, respectively.

REBETIKO also computes for each SFH the time evolution of several quantities of interest, such as: (**a**) the SFR in units of $M_\odot$ yr^{-1} and the specific SFR defined as sSFR $\equiv$ SFR$/M_\star$ in units of yr^{-1}; (**b**) the recent SFR inferred from the Hα luminosity L(Hα) following the semi-empirical expression SFR $= 7.93 \times 10^{-42}$ L(Hα) erg s^{-1} for solar metallicity (Kennicutt 1998); (**c**) the currently available total stellar mass $M_\star$ in units of solar mass $M_\odot$, which is the stellar mass after correcting for the returned mass fraction to the ISM by stellar winds and supernovae; (**d**) the light- and mass-weighted mean stellar ages $\langle \log t_\star \rangle_{L,M}$ and metallicities $\log\langle Z_\star \rangle_{L,M}$; (**e**) the luminosities and EWs of H emission-lines, such as, the Hα and Hβ Balmer lines, assuming case B recombination and radiation-bounded HIIRs; (**f**) the D4000 defined as the ratio of the integrated flux within 4000–4100 Å and 3850–3950 Å narrowbands (Balogh *et al.* 1999); (**g**) a measure of the Balmer jump BJ $=$ I(3646^-) /I(3646^+), with I(3646^-) and I(3646^+) denoting the mean flux within a window of 100 Å bluewards and redwards of 3646 Å, respectively; (**h**) the absorption Lick/IDS indices that are commonly used as tracers of age and metallicity of stellar populations: Hδ_A, Hδ_F, CN1, CN2, Ca4227, G4300, Hγ_A, Hγ_F, Fe4383, Ca4455, Fe4531, C24668, $H\beta$, Fe5015, Mg1, Mg2, Mgb, Fe5270, Fe5335, Fe5406, Fe5709, Fe5782, NaD, TiO1 and TiO2 (Trager *et al.* 1998), and (**i**) colours referring to the standard Johnson (Johnson & Morgan 1953) and Cousins *UBVRI* filter systems (Cousins & Jones 1976) and SDSS *ugriz* photometry (Doi *et al.* 2010), for both the Vega standard system (Bohlin & Gilliland 2004) and AB magnitudes (Oke 1974).

Several improvements to REBETIKO are scheduled for the near future. Specially important from these is a chemical consistent version of the code that will allow to compute a realistic metallicity evolution of CSPs. This will be made possible by keeping track of the stellar matter expelled during stellar evolution to the ISM that leads to the chemical evolution of the subsequently formed SSPs. Similar to GALAXEV (BC2003), the code shall also be able to compute SSPs for a wide range of IMFs (e.g. Salpeter 1955; Kroupa 2001; Chabrier 2003), stellar libraries (e.g. MILES, Sánchez-Blázquez *et al.* 2006) and evolutionary tracks (e.g. Padova 1994, Alongi *et al.* 1993; Bressan *et al.* 1993; Fagotto *et al.* 1994a,b; Girardi *et al.* 1996; Girardi *et al.* 2000; Geneva 2000, Schaller *et al.* 1992; Charbonnel *et al.* 1996, 1999).

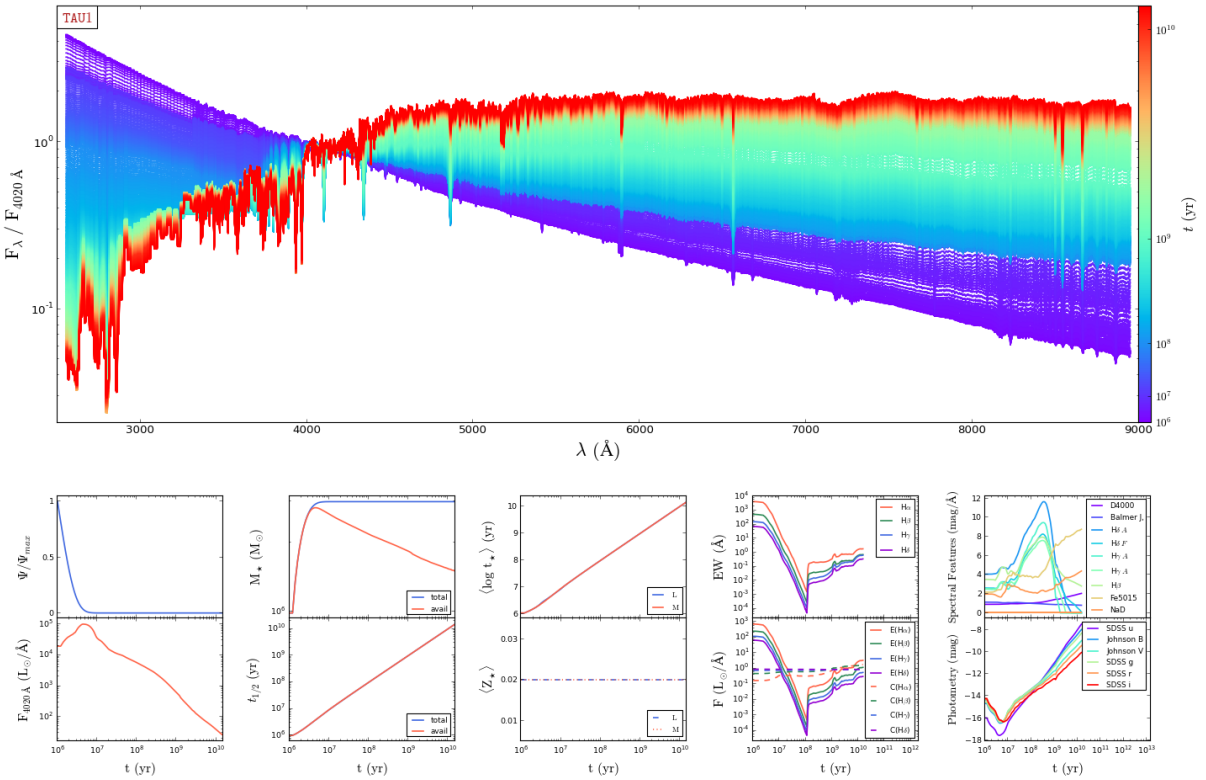

Figure 2.2.1: Synthetic CSP spectra normalised at $\lambda_0 = 4020$ Å and other spectrophotometric quantities computed with REBETIKO for an instantaneous burst SFH, labeled as `TAU1` in Figure 2.1.1. Colour coding on the main panel represents the CSP age t. Smaller panels from left- to right-hand side and top to bottom display as a function t, respectively: star formation rate $\Psi(t)$ (blue line); flux at normalisation wavelength F_{λ_0} (red line); total ever formed (blue line) and currently available (red line) stellar mass $M_\star$; total (blue line) and available (red line) half-age of all stellar populations $t_{1/2}$; mean stellar age $\langle \log t_\star \rangle$ weighted by light (blue line) and mass (red line); mean stellar metallicity $\langle Z_\star \rangle$ weight by light (blue line) and metallicity (red dashed line); predicted EWs of the Balmer emission lines Hα (red line), Hβ (blue line), Hγ (green line) and Hδ (violet line); predicted total luminosity (full lines) and the monochromatic luminosity continuum of the same emission lines at their respective wavelengths (dashed lines); selected Lick/IDS indices, and photometric magnitudes for passbands of selected photometric systems.

2.2 Synthetic spectra of CSPs

A library of purely-stellar CSP evolutionary models was computed with REBETIKO assuming the first integral of Equation 2.1. A set of 716 evolutionary models covering the full optical range between 2500 and 9000 Å was produced for each SFH with ages between 1 Myr and 15 Gyr, roughly uniformly distributed in logarithmic scale in order to ensure a good coverage of the most important galactic evolutionary stages. These purely-stellar models were assembled by convolving BC2003 SSPs with solar metallicity ($Z_\odot = 0.02$), Padova 1994 evolutionary tracks (Alongi *et al.* 1993; Bressan *et al.* 1993; Fagotto *et al.* 1994a,b; Girardi *et al.* 1996) and a Chabrier (2003) IMF with the SFHs described in Section 2.1 and assuming S/N = 1000 at $\lambda_0 = 4020$ Å. Dust absorption and reemission and line broadening by kinematics were neglected in these models in order to minimise the degrees of freedom during PSS modelling.

Figures 2.2.1 and 2.2.2 show CSP spectra normalised at $\lambda_0 = 4020$ Å for instantaneous burst and continuous SFHs (labeled as `TAU1` and `CONT` in Figure 2.1.1, respectively). Bottom panels show different physical primary and secondary properties of the evolutionary models as a function of CSP age t, from *left-* to *right-hand side* and *top* to *bottom*: (**a**) SFR; (**b**) monochromatic flux at the normalisation wavelength F_{λ_0}; (**c**) total stellar mass $M_\star$; (**d**) stellar half-age $t_{1/2}$; (**e**) light- and mass-weighted mean stellar age $\langle \log t_\star \rangle_{L,M}$ and (**f**) mean stellar metallicity $\log \langle Z_\star \rangle_{L,M}$; (**g**) predicted H absorption-line EWs and (**h**)

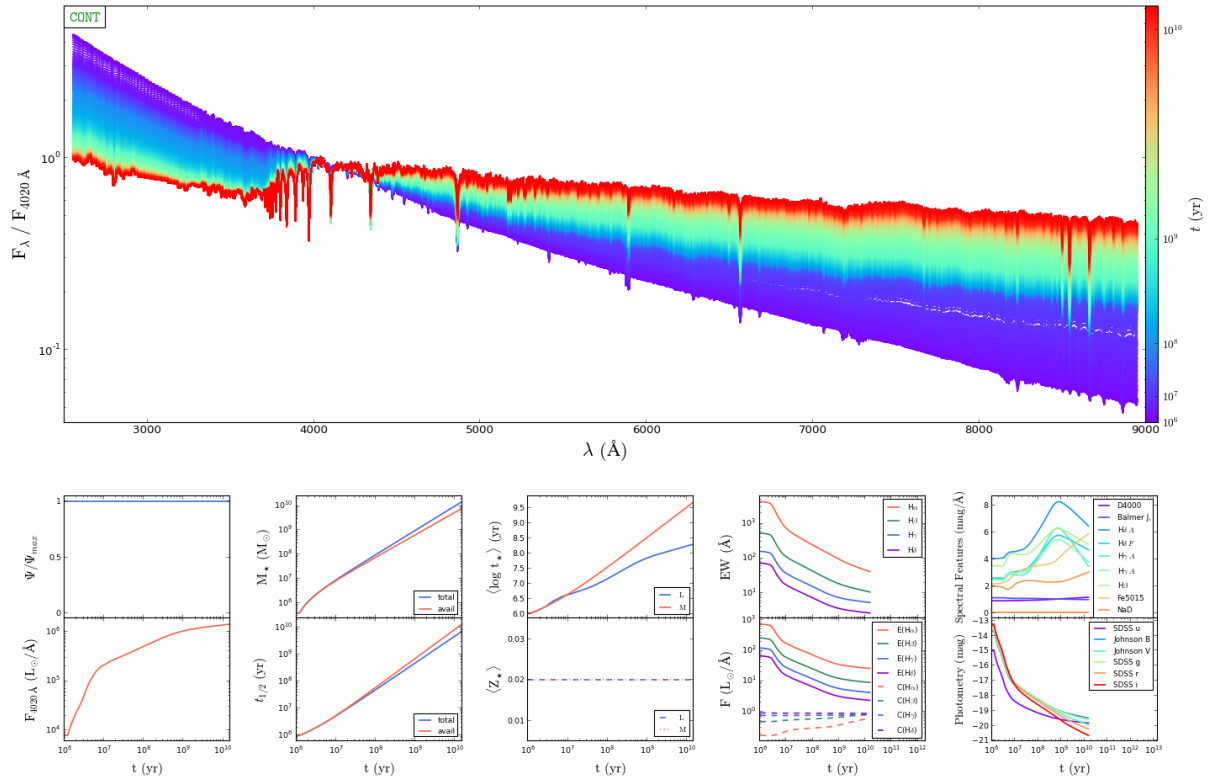

Figure 2.2.2: Synthetic CSP spectra normalised at $\lambda_0 = 4020$ Å and other spectrophotometric quantities computed with REBETIKO for a continuous SFH, labeled as `CONT` in Figure 2.1.1. Panel display configuration and legend details are identical to those in Figure 2.2.1.

continuum and predicted emission-line fluxes of the first four lines of Balmer series; (**i**) magnitudes of several spectral indices of the Lick/IDS system (e.g. Worthey & Ottaviani 1997; Worthey *et al.* 1994; Trager *et al.* 1998; Balogh *et al.* 1999), and (**j**) magnitudes of several passbands in the modified Johnson and SDSS photometric systems. Figures A.1.1–A.1.9 in Appendix A present similar figures for each of the SFHs presented Figure 2.1.1.

This library of synthetic spectra containing purely-stellar emission was constructed to analyse the impact that the addition of a non-stellar spectral component has on the estimated stellar population properties. On the one hand, Chapter 3 focuses on the effect of an AGN FC parameterised by a power-law $F_\nu \propto \nu^{-\alpha}$. On the other hand, Chapter 4 investigates the impact of NE on composite stellar and AGN spectra using the photoionisation code CLOUDY (Ferland *et al.* 1998). This analysis is fundamental to understand the impact that AGN and NE spectral components have on full-spectrum PSS modelling of galaxy spectra. The objective is to present a thorough and systematic analysis of the robustness and reliability of state-of-the-art PSS codes on the recovery of the SFH and CEH of star-forming and/or Seyfert galaxies. Therefore, the spectral synthesis results of the CSP models presented and discussed in this chapter serve as a reference in the light of which the modelling analysis of more complex spectra can be examined and better understood.

2.3 Analysis of stellar properties with PSS

Different PSS codes have been used to study galaxy formation and evolution (e.g. Heavens, Jimenez & Lahav 2000; Cid Fernandes *et al.* 2005; Ocvirk *et al.* 2006a,b; Tojeiro *et al.* 2007, 2009; MacArthur *et al.* 2009; Koleva *et al.* 2009). From these, STARLIGHT (CF2005) stands out for being a user-friendly software which is widely used and has been applied to a plethora of different galaxy formation and evolution studies

(e.g. Stasińska *et al.* 2006, 2008; Coziol *et al.* 2011; Vaona *et al.* 2012; Benítez *et al.* 2013; Papaderos *et al.* 2013; Torres-Papaqui *et al.* 2013; Cid Fernandes *et al.* 2014). CF2005 showed that STARLIGHT can recover from synthetic spectra with S/N = 10 the stellar mass within an uncertainty of ∼0.1 dex and both the mean stellar age and metallicity within ∼0.2 dex, which is a very good result among similar codes (e.g. Ocvirk *et al.* 2006a,b; Tojeiro *et al.* 2007, 2009; Koleva *et al.* 2009). Given these considerations, the latest public version of STARLIGHT (version v04) was assumed in this work to be a good representative of state-of-the-art PSS codes.

The objective is to evaluate the ability of a typical PSS code in retrieving stellar population properties by comparing the synthesis output of STARLIGHT with that of the input evolutionary model created with REBETIKO. The most common stellar building blocks used with a code such as STARLIGHT are SSPs evolutionary models (e.g. BC2003; Sánchez-Blázquez *et al.* 2006; Vazdekis *et al.* 2010; Mollá, García-Vargas & Bressan 2009). As with REBETIKO in Subsection 2.2, STARLIGHT was applied in this work using BC2003 SSPs to avoid introducing complex uncertainties that arising from the use of SSPs with different IMFs, stellar spectral libraries or evolutionary tracks. This means that the following PSS analysis in fact yields lower limits to the estimated stellar population properties uncertainties, since both REBETIKO and STARLIGHT applications consider the same basic evolutionary ingredients.

The adopted modelling procedure was as follows: (**a**) STARLIGHT fits were performed between 3400 and 8900 Å in order to take advantage of the resolution of the STELIB stellar library (Le Borgne *et al.* 2003) and following applications of the code to large spectroscopic data sets from SDSS (e.g. Asari *et al.* 2007; Ribeiro *et al.* 2016); (**b**) stellar kinematics and A_V were set to zero; (**c**) application to models discussed in Chapters 2 and 3 assume no clipping method, since these do not have emission-lines or significant noise, whereas for Chapter 4 models it was adopted a 3σ clipping method and a composite spectral mask to avoid spectral regions with prominent optical emission lines, and (**d**) each input model was fitted 10 times while changing the seed numbers regulating the initial guesses in the parameter space to better evaluate formal uncertainties. This modelling procedure reduces the number of degrees of freedom during the parameter exploration with PSS and aims to isolate potential uncertainties of physical properties on variations of SFH and adopted base library. This also allows in Chapters 3 and 4 to isolate the impact of AGN and NE to the estimation of the same physical properties.

A fundamental question pertaining to PSS concerns the adopted base of elements used to decompose the input spectrum into its spectral building blocks. At least two considerations are warranted when composing a base library (**a**) how well the selected SSPs cover the age and metallicity of the input CSP, and (**b**) computational time cost per fit. The distribution package of STARLIGHT comes with two SSP base libraries: Base $\mathcal{N}$ has 15 ages (t = 0.001, 0.00316, 0.00501, 0.01, 0.02512, 0.04, 0.10152, 0.28612, 0.64054, 0.90479, 1.434, 2.5, 5, 11 and 13 Gyr) and 3 metallicities (Z = 0.004, 0.02 and 0.05), and Base $\mathcal{S}$ comprises 25 ages (t = 0.001, 0.00316, 0.00501, 0.00661, 0.00871, 0.01, 0.01445, 0.02512, 0.04, 0.055, 0.10152, 0.1609, 0.28612, 0.5088, 0.90479, 1.27805, 1.434, 2.5, 4.25, 6.25, 7.5, 10, 13, 15 and 18 Gyr) and 6 metallicities (Z = 0.0001, 0.0004, 0.004, 0.008, 0.02 and 0.05). Both libraries have BC2003 SSPs with Padova 1994 evolutionary tracks (e.g. Alongi *et al.* 1993; Bressan *et al.* 1993; Fagotto *et al.* 1994a,b; Girardi *et al.* 1996) and a Chabrier (2003) IMF. On the one hand, the former is typically adopted for initial test-fits to obtain a first estimate of the SFH of the galaxy, as it takes just ∼40 seconds when modelling a REBETIKO CSP spectrum using a single core of a Intel® Core™ i7 CPU 870 @ 2.93GHz workstation desktop. On the other hand, the later library is adopted when seeking to reconstruct a more detailed SFH and it takes ∼240 seconds to perform a fit to the same type of spectrum. This implies a computational time cost of roughly 1 and 6 months to fit the 9 (SFHs) × 716 (evolutionary stages) × 10 (for statistical purposes) purely-stellar CPS with Base $\mathcal{N}$ and $\mathcal{S}$, respectively. Taking this into consideration, a new base library was tailored-made for this work given the required large number of PSS spectral fits.

Base $\mathcal{L}$ was built with 25 ages (t = 0.001, 0.00209, 0.00316, 0.00501, 0.00661, 0.00817, 0.01, 0.01445, 0.02512, 0.04, 0.055, 0.10152, 0.1609, 0.28612, 0.5088, 0.9047, 1.27805, 1.434, 2.5, 4.25, 6.25, 7.5, 10, 13 and 15 Gyr) for 4 metallicities (Z = 0.004, 0.008, 0.02 and 0.05) with Padova 1994 evolutionary tracks (e.g. Alongi *et al.* 1993; Bressan *et al.* 1993; Fagotto *et al.* 1994a,b; Girardi *et al.* 1996) and a Chabrier (2003) IMF. This base has an age coverage similar to that of Base $\mathcal{S}$, although without the lowest 2 metallicity values of the later (Z = 0.0001 and 0.0004). Moreover, the SSP with 18 Gyr in Base $\mathcal{S}$ was substituted by a SSP with 0.00209 Gyr in Base $\mathcal{L}$ to strengthen the sampling of very young stellar spectra and to have more realistic SSP models under the current accepted age of the Universe (∼14 Gyr, Planck Collaboration *et al.* 2016). Base $\mathcal{L}$ takes ∼110 seconds and ∼2.7 months to perform a fit to, respectively, 1 and 9 (SFHs)

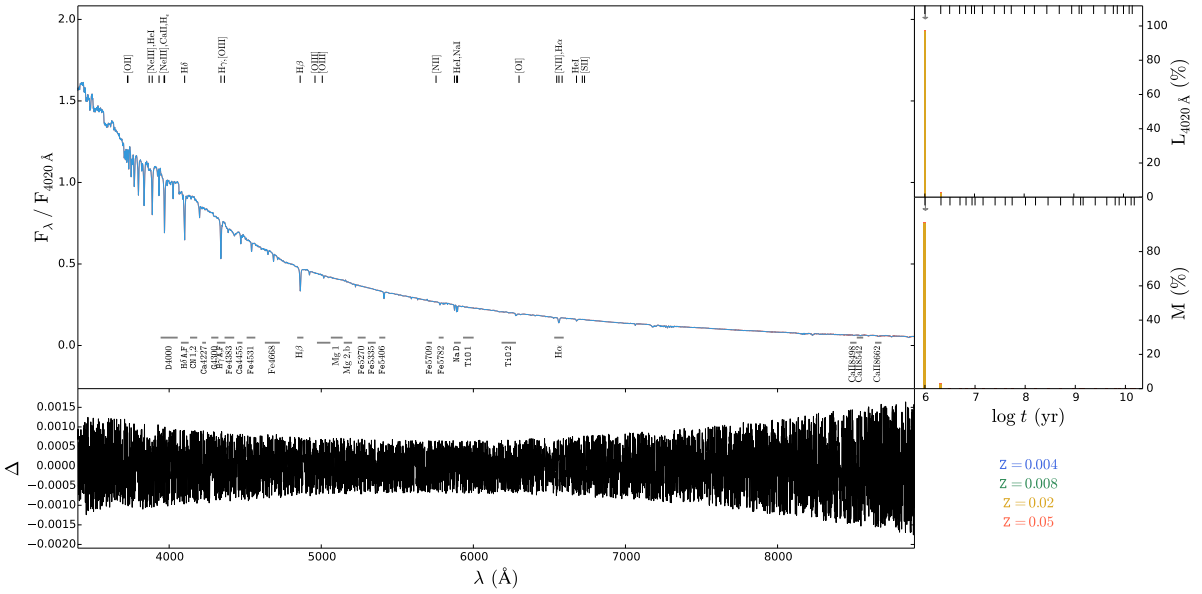

Figure 2.3.1: STARLIGHT spectral modelling results for a CSP with 1 Myr, solar metallicity and instantaneous burst SFH. Main panel: Red and blue lines represent the input and best-fit spectra, respectively. Top annotations indicate the wavelength of several emission lines and bottom annotations show the wavelength coverage of several indices in the extended Lick/IDS system and other relevant absorption features. Bottom panel: Black line represents the residuals spectrum resulting from subtracting the best-fit from the input spectrum. Top right-hand side panel: SFH in light fractions. Bottom right-hand side panel: SFH in mass fractions. Blue, green, yellow and red bars represent SSPs with $Z = 0.004$, 0.008, 0.02 and 0.05, for $Z_\odot = 0.02$. Small vertical lines on the top x-axis represent the age coverage of the SSPs in the adopted base library. Moreover, the grey arrows represent the light- and mass-weighted mean stellar age on the top and bottom panels, respectively.

× 716 (evolutionary stages) × 10 (for statistical purposes) CSPs using a single core of a state-of-the-art workstation. This is a significant reduction of the computational time cost at a satisfactory compromise in metallicity coverage.

As an example of an application of STARLIGHT to a REBETIKO CSP spectrum, Figure 2.3.1 shows the average results of 10 STARLIGHT spectral fits using Base $\mathcal{L}$ to a CSP with 1 Myr, solar metallicity and instantaneous burst SFH. The input and fitted spectra are represented by the *red* and *blue lines* in the *main panel*, respectively. Moreover, wavelengths of several emission lines and absorption-line indices are labeled above and below the spectra, respectively. The residuals spectrum resulting from subtracting the best-fit model found by STARLIGHT from the input spectrum is represented by the *black line* in the *bottom panel*. The estimated SFHs in light and mass fractions are displayed on the *top* and *bottom right-hand side panels*, respectively, with metallicities $Z = 0.004, 0.008, 0.02$ and 0.05 being represented by *blue, green, yellow* and *red bars*, respectively. Overall, the figure shows a very good fit with low residuals. The estimated total stellar mass $\log M_\star = 5.74\ M_\odot$, mean stellar age $\langle \log t_\star \rangle \simeq 6.01$ yr and mean stellar metallicity $\log\langle Z_\star \rangle \simeq -1.7$ are very close to input values of $\log M_\star = 5.73\ M_\odot$, $\langle \log t_\star \rangle = 6$ yr and $\log\langle Z_\star \rangle = -1.70$.

On the one hand, Subsection 2.3.1 compares synthesis results between Base $\mathcal{N}$, $\mathcal{S}$ and $\mathcal{L}$ for the most important stellar population properties (e.g. total mass, mean age and mean metallicity) and instantaneous burst and continuous SFHs. On the other hand, Subsection 2.3.2 compares synthesis results for every SFH after the selection in Subsection 2.3.1 of the base library that best minimises algebraic and physical degeneracies of the synthetic spectra.

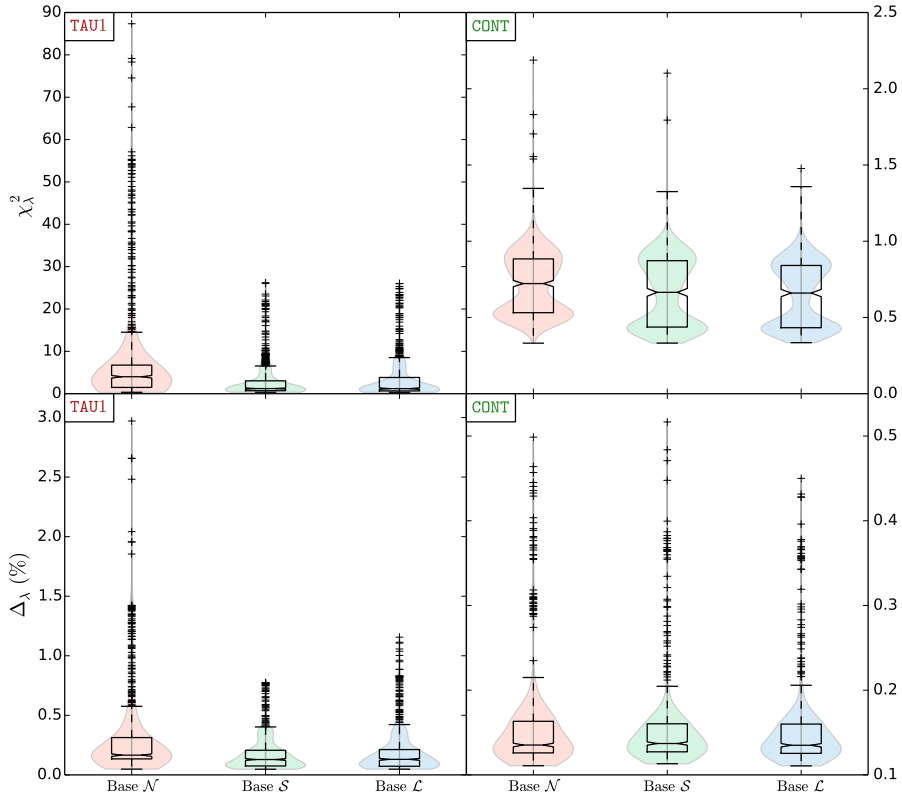

Figure 2.3.2: Violin plots of the reduced chi-squared χ^2_λ (top panels) and mean absolute percentage error between input and best-fit models Δ_λ (bottom panels) for instantaneous burst (left-hand side panels) and continuous SFHs (right-hand side panels). Red, green and blue colours represent results for Base $\mathcal{N}$, $\mathcal{S}$ and $\mathcal{L}$, respectively.

2.3.1 Dependence on the base libray

The difference between data O_λ and model M_λ in a minimisation procedure as represented in Equations 1.1 and 1.4 can be quantified for example by dividing the best-fit χ^2 value by the assumed number of degrees of freedom in the parameter space exploration. This estimate is often referred to as the *reduced chi-squared* χ^2_λ which, in the case of full-spectrum PSS, is the χ^2 value corresponding to the optimal linear combination of spectral elements that best reproduce the observed stellar spectrum divided by the considered number of wavelength or flux points λ,

$$\chi^2_\lambda = \frac{\chi^2}{\lambda}. \tag{2.4}$$

A good solution usually has $\chi^2_\lambda \lesssim 1$. The likelihood between data and model can also be quantified using the *mean absolute percentage error* Δ_λ between observation and model,

$$\Delta_\lambda = \frac{|O_\lambda - M_\lambda|}{O_\lambda} \times 100. \tag{2.5}$$

Figure 2.3.2 shows box-and-whiskers and violin plots of χ^2_λ (*top panels*) and Δ_λ (*bottom panels*) for instantaneous burst (*left-hand side panels*) and continuous SFHs (*right-hand side panels*) for Bases $\mathcal{N}$ (*red*), $\mathcal{S}$ (*green*) and $\mathcal{L}$ (*blue*). The violin plots assume a Guassian kernel density plot and outliers are presented by the symbol "+". A comparison between left- and right-hand side panels shows that the median values of χ^2_λ and Δ_λ for the instantaneous burst are, on average, respectively higher and lower that those for the continuous SFH. Differences between the interquartile ranges, Guassian distribution

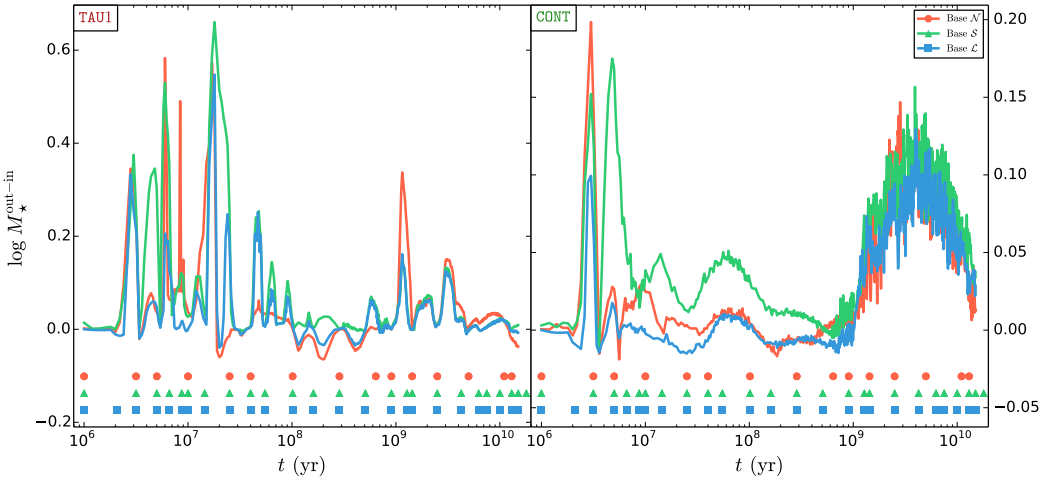

Figure 2.3.3: Difference in the total stellar mass $M_\star$ between STARLIGHT (out) and REBETIKO (in) values as a function of CSP age t for instantaneous burst (left panel) and continuous SFHs (right panel). Red, green and blue lines represent results with Bases $\mathcal{N}$, $\mathcal{S}$ and $\mathcal{L}$, respectively. Red dots, green triangles and blues squares represent the age coverage of the Bases $\mathcal{N}$, $\mathcal{S}$ and $\mathcal{L}$.

shapes and median values for each parameter also show that better fits are generally found using Base $\mathcal{S}$ for an instantaneous burst and Base $\mathcal{L}$ for a continuos SFH. This can be understood considering the following. On the one hand, the larger number of metallicities in Base $\mathcal{S}$ assures that lower differences between best-fit and input spectra are found in early evolutionary stages of an instantaneous burst SFH. On the other hand, Base $\mathcal{L}$ provides on average slightly better spectral fits to a continuous SFH due to its roughly uniform age coverage in logarithmic scale. Although statistical estimators such as χ^2_λ and Δ_λ help to quantify the likelihood between O_λ and M_λ, spectral synthesis results of stellar population physical properties show that this does automatically guarantee that the estimated physical properties are closest to their true value the lower are the inferred χ^2_λ and Δ_λ.

Figure 2.3.3 shows the difference in the currently available *total stellar mass* $M_\star$ between the STARLIGHT (*out*) and REBETIKO (*in*) values as a function of CSP age t for instantaneous burst (*left-hand side panel*) and continuous SFHs (*right-hand side panel*). Results with Bases $\mathcal{N}$, $\mathcal{S}$ and $\mathcal{L}$ are represented by the *red*, *green* and *blue lines*, respectively. Moreover, the age coverage of the SSPs in Bases $\mathcal{N}$, $\mathcal{S}$ and $\mathcal{L}$ between 1 Myr and 15 Gyr is depicted as *red dots*, *green triangles* and *blue squares* respectively. The results show mass overestimation peaks up to $\sim$0.6 and $\sim$0.2 dex for instantaneous burst and continuous SFHs. These uncertainties are similar for all adopted base libraries and most seem to be correlated to a poor age coverage by all base libraries, as they tend to be located within the ages of two successive SSPs. This can be understood particularly for instantaneous burst SFH results considering the following. The CSPs for the instantaneous burst SFH in Figure 2.2.1 show the largest spectral shape diversity when compared to other SFHs (Figures A.1.2–A.1.9 in Appendix A). Indeed, CSPs in Figure 2.2.1 can be interpreted as an approximation of the spectral evolution of the solar-metallicity BC2003 SSPs between 1 Myr and 15 Gyr for Padova 1994 evolutionary tracks and a Chabrier (2003) IMF. Thus, it would be necessary to adopt roughly all SSPs within this age interval in a given base library to allow STARLIGHT to properly sample the CSP spectral shape for this SFH before estimating the stellar mass and other physical properties. This point becomes clearer when interpreting the mean stellar age and mean stellar metallicity for the same set of models. Also interestingly, the mass shows an overestimation bump for the continuous SFH when $10^9 \lesssim t \lesssim 15 \times 10^{10}$ yr, which likely illustrates the degeneracies between SSPs due to the marginal change in spectral shape over this age interval. Moreover, mass differences are overall smaller when adopting Base $\mathcal{L}$.

The SFH and CEH of a galaxy can be represented to a first order by its mean stellar age and mean stellar metallicity. The mean stellar age and metallicity of stellar populations can be determined by considering the ages and fractional contributions weighted by light and mass of the SSPs that compose

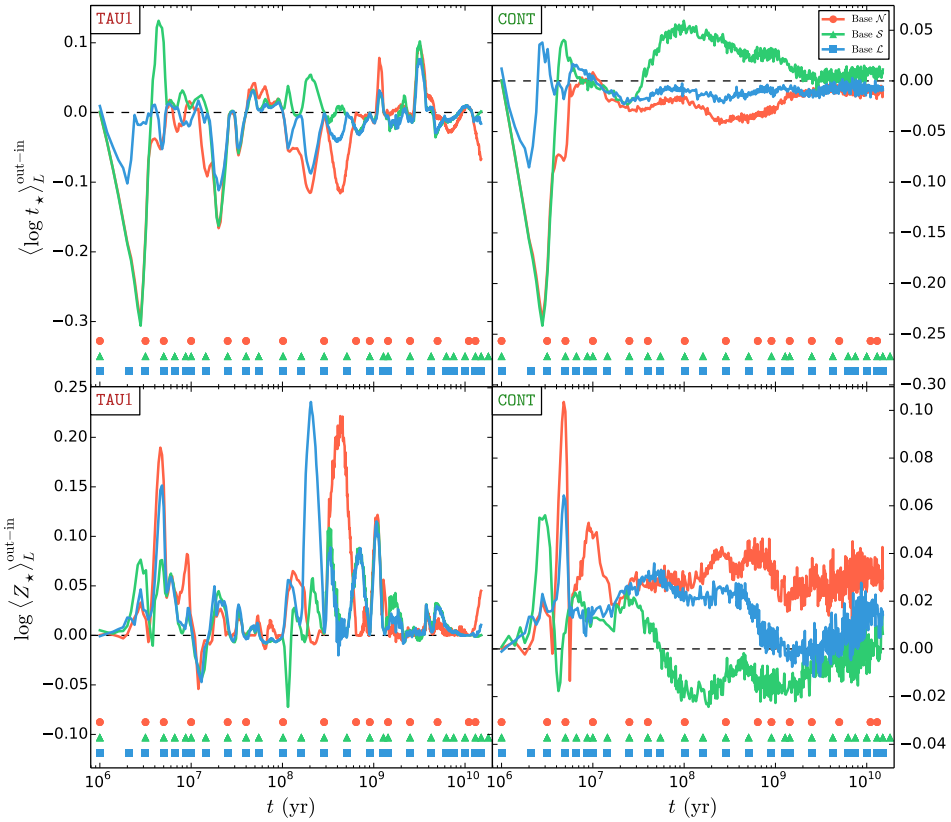

Figure 2.3.4: Difference in the light-weighted mean stellar age $\langle \log t_\star \rangle_L$ (top row panels) and mean stellar metallicity $\log \langle Z_\star \rangle_L$ (bottom row panels) between STARLIGHT (out) and REBETIKO (in) values as a function of CSP age t for instantaneous burst (left-hand side panel) and continuous SFHs (right-hand side panel). Legend details are identical those in Figure 2.3.3.

the model spectrum M_λ in Equation 1.4. The mean logarithmic stellar age weighted by light and mass can be written as, respectively,

$$\langle \log t_\star \rangle_L = \sum_{i=1}^{N_\star} \gamma_i \,.\, \log t_i, \tag{2.6}$$

$$\langle \log t_\star \rangle_M = \sum_{i=1}^{N_\star} \mu_i \,.\, \log t_i, \tag{2.7}$$

where t_i is the age of the i$^{\rm th}$ SSP element and γ_i and μ_i are its light- and mass-fractions, respectively. Meanwhile, if Z_i is the metallicity of the i$^{\rm th}$ SSP element then the logarithmic mean stellar metallicity weighted by both light and mass can be written as, respectively,

$$\log \langle Z_\star \rangle_L = \log \sum_{i=1}^{N_\star} \gamma_i \,.\, Z_i, \tag{2.8}$$

$$\log \langle Z_\star \rangle_M = \log \sum_{i=1}^{N_\star} \mu_i \,.\, Z_i, \tag{2.9}$$

On the one hand, Figure 2.3.4 shows the difference in the *light-weighted mean stellar age* $\langle \log t_\star \rangle_L$ (*top row panels*) and *mean stellar metallicity* $\log \langle Z_\star \rangle_L$ (*bottom row panels*) between STARLIGHT and REBETIKO values as a function of CSP age t for instantaneous burst (*left-hand side panels*) and continuous

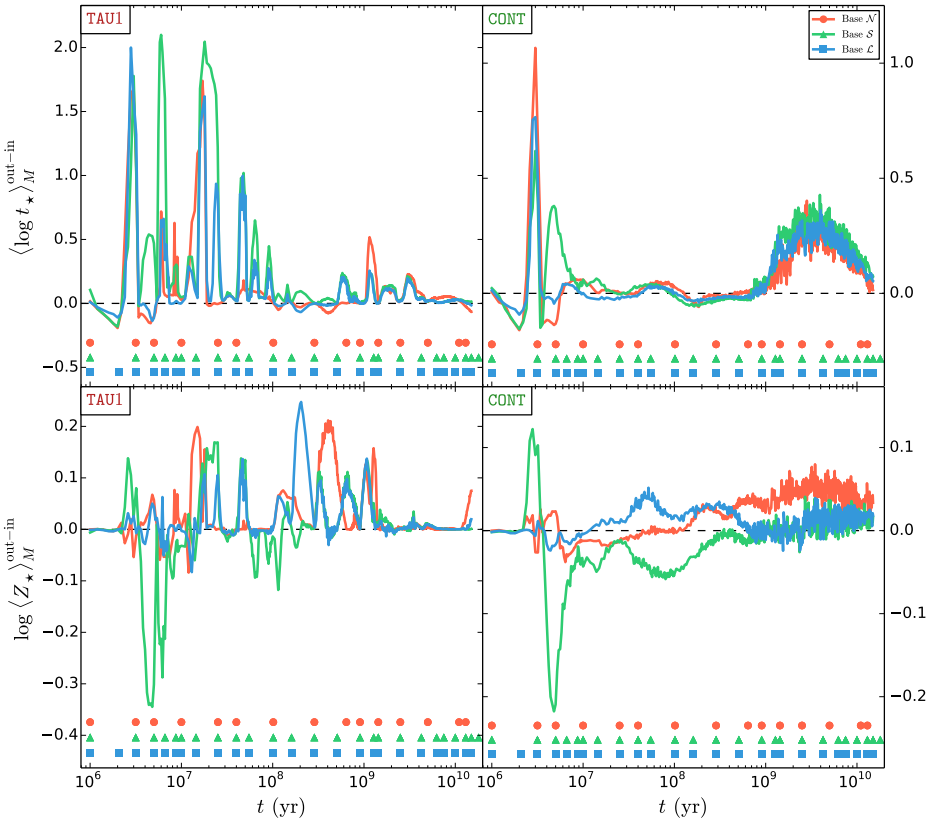

Figure 2.3.5: Difference in the mass-weighted mean stellar age $\langle \log t_\star \rangle_M$ (top row panels) and mean stellar metallicity $\log\langle Z_\star \rangle_M$ (bottom row panels) between STARLIGHT (out) and REBETIKO (in) values as a function of CSP age t for instantaneous burst (left-hand side panel) and continuous SFHs (right-hand side panel). Legend details are identical those in Figure 2.3.3.

SFHs (*right-hand side panels*) with the same colour coding as in Figure 2.3.3. The results show that the estimated age and metallicity can have uncertainties peaks of up to ∼0.3 and 0.25 dex, respectively, and that these more prominent for an instantaneous burst SFH. These peaks seem linked with evolutionary stages not properly covered by the adopted bases. However, it is worth noting that the uncertainties in both quantities are roughly consistent with the precision of ∼0.2 dex of STARLIGHT (CF2005; Mateus *et al.* 2006). Moreover, the mean stellar age and metallicity are closest to their true values when adopting Base $\mathcal{L}$. Overall, age underestimations seem correlated with metallicity overestimations for both SFHs, which is particularly clear for the continuous SFH for $2 \times 10^5 \lesssim t \lesssim 15 \times 10^9$ yr and all adopted base libraries. This a typical example of the age-metallicity degeneracy issue (e.g. Faber 1972; Worthey 1994) briefly mention in Section 1.2.

On the other hand, Figure 2.3.5 shows the difference in the *mass-weighted mean stellar age* $\langle \log t_\star \rangle_M$ (*top row panels*) and *mean stellar metallicity* $\log\langle Z_\star \rangle_M$ (*bottom row panels*) between the STARLIGHT and REBETIKO values as a function of CSP age t for instantaneous burst (*left-hand side panels*) and continuous SFHs (*right-hand side panels*) with the same colour coding as in Figure 2.3.3. The results show that the age and metallicity are estimated within an uncertainty of up to ∼2 and 0.35 dex, respectively. These uncertainties seem again to be correlated to poorly covered evolutionary stages by the adopted base libraries. Overall, uncertainties in mass-weighted age and metallicity are larger than those from light-weighted determinations. This can be understood considering that (**a**) young stars are more luminous than old stars and (**b**) small light variations of old stellar populations result in considerable mass variations when applying the M/L ratio to recover mass-related stellar population properties with PSS.

The spectral synthesis results illustrated in Figures 2.3.2–2.3.5 show that the reduced chi-squared and mean absolute percentage error, although important for assessing the relative goodness of the synthesis

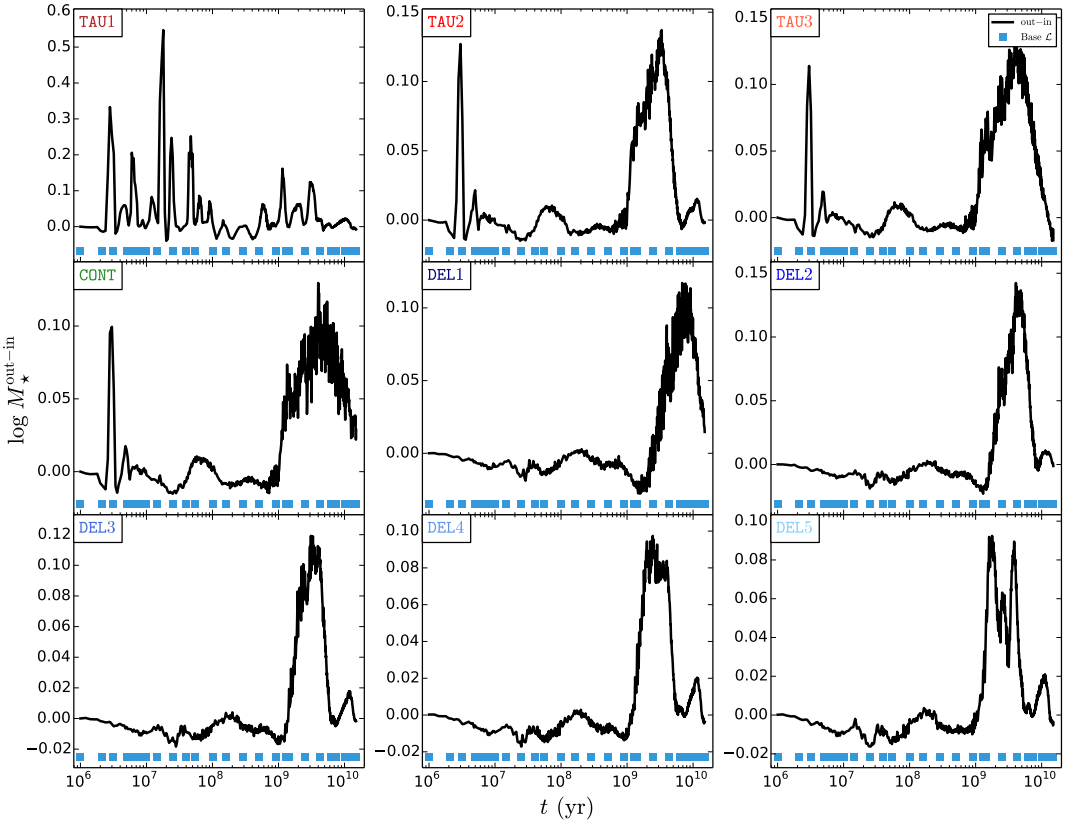

Figure 2.3.6: Difference in the total stellar mass $M_\star$ between STARLIGHT (out) and REBETIKO (in) values as a function of CSP age t. Panels from left- to right-hand side and top to bottom represent the exponentially declining, continuous and delayed SFHs displayed in Figure 2.1.1. Blues squares represent the age coverage of the Base $\mathcal{L}$.

solution, do not necessarily quantify in a reliable manner the likeness between the estimated physical properties and their true values. This fact is particularly important when interpreting synthesis results of real spectra for which a simple visual inspection might suggest a particularly good spectral fit. In these cases, it is expected low values for standard measures of the goodness of the spectral fit. However, the results obtained here show that these are not sufficient to guarantee that the derived physical properties can be taken as reliable without a critical interpretation of the minimisation procedure or any other method that was adopted to extract physical information from the spectrum of the galaxy.

The results presented in this section also show that Base $\mathcal{L}$ is best suited to reduce the uncertainties on derived physical properties for the particular set of spectra computed with REBETIKO. Indeed, Base $\mathcal{L}$ is a good compromise between computational time cost and accuracy of the estimated physical properties when compared to the other adopted base libraries. Therefore, spectral synthesis results presented and discussed hereafter are based solely in Base $\mathcal{L}$.

2.3.2 Dependence on the star formation history

It is also important to understand how the recovery of stellar population properties using PSS depends on the SFH and CEH of the CSPs. Although the synthesis results should still depend on the adopted base library to a large extent, such analysis should provide valuable insight to the application of PSS to large samples of galaxies with known morphological classification.

Figure 2.3.6 shows the difference in the *total stellar mass* $M_\star$ between STARLIGHT and REBETIKO values as a function of CSP age t. Panels from *left-* to *right-hand side* and *top* to *bottom* display results for CSPs with exponentially declining, continuous and delayed SFHs labeled according to the nomenclature adopted in Figure 2.1.1. The age coverage of the SSPs in Base $\mathcal{L}$ is represented by the *blue squares*.

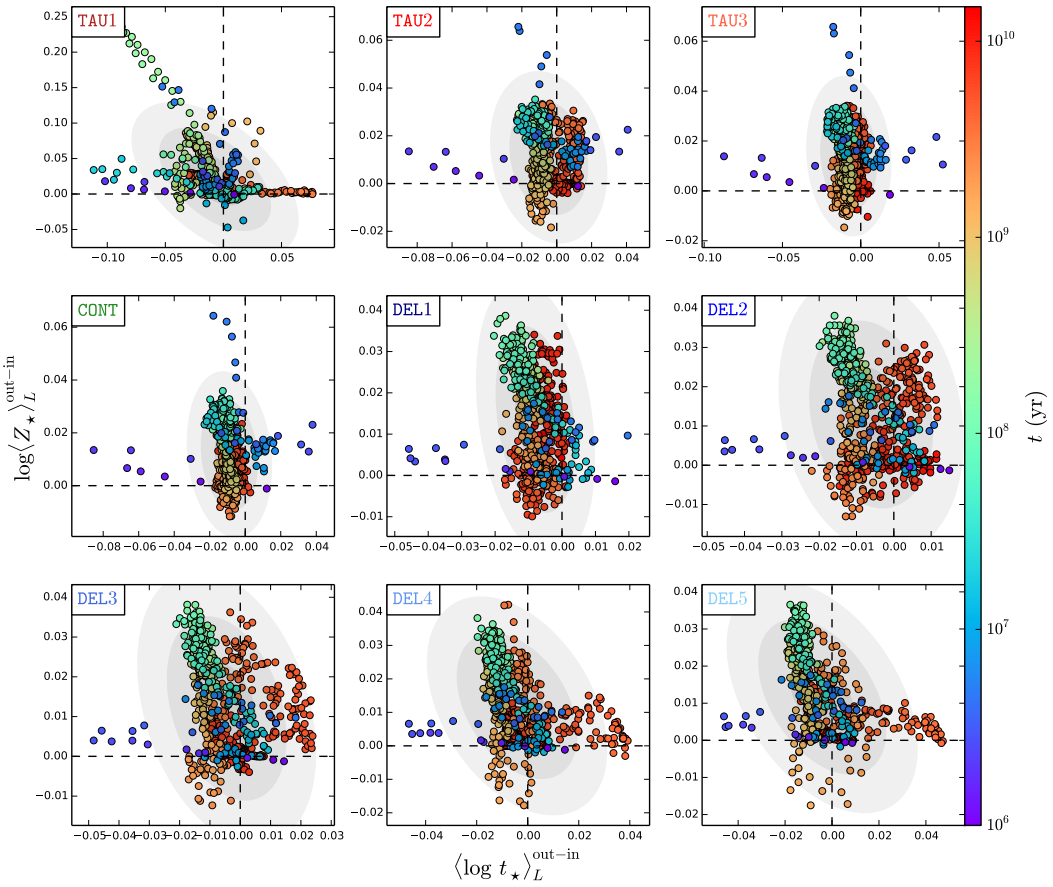

Figure 2.3.7: Difference in the light-weighted mean stellar age $\langle \log t_\star \rangle_L$ as a function of the difference in the mean stellar metallicity $\log\langle Z_\star \rangle_L$ between STARLIGHT (out) and REBETIKO (in) values colour coded according to the CSP age t. Panel display configuration is identical to that in Figure 2.3.6. Light- to dark-grey ellipses represent 1σ, 2σ and 3σ 2-dimensional standard deviations, respectively.

Overall, the results show that the stellar mass is estimated within an uncertainty of to ∼0.13 dex, except for the instantaneous burst SFH, where it can reach up to ∼0.55 dex. The mass overestimation bump of up to ∼0.13 dex when $10^9 \lesssim t \lesssim 15 \times 10^{10}$ yr seen in Figure 2.3.3 for the continuous SFH that can be attributed to algebraic degeneracies between the older SSPs is present roughly for each SFHs. The instantaneous burst SFH does not present this feature but contains a maximum overestimation peak around 2×10^7 yr of ∼0.55 dex surrounded by other peaks up of ∼0.2 dex that appear to be linked to a poor age coverage of the adopted base.

On the one hand, Figure 2.3.7 shows the relation between the difference in the *light-weighted mean stellar age* $\langle \log t_\star \rangle_L$ and *mean stellar metallicity* $\log\langle Z_\star \rangle_L$ between STARLIGHT and REBETIKO values colour coded according to the CSP age t. Panels display configuration is identical to that in Figure 2.3.6. The results show a typical maximum uncertainty of up to ∼0.05 dex for both age and metallicity for the majority of SFHs, with the exception being once again the instantaneous burst. For this SFH the age can be under or overestimated by up to ∼0.12 and ∼0.08 dex, respectively, whereas the metallicity can be under or overestimated up to ∼0.045 and ∼0.23 dex, respectively. On the one hand, age underestimation for most SFHs is predominantly linked to evolutionary models with ages roughly in $10^6 \lesssim t \lesssim 10^7$ yr, except for an instantaneous burst where this range extends to $10^6 \lesssim t \lesssim 10^8$ yr. The most significant age overestimation is connected to models with ∼10^9 yr, which is particularly striking for an instantaneous burst. On the other hand, metallicity underestimation is more prominent for $10^9 \lesssim t \lesssim 10^{10}$ yr and its overestimation is most apparent at ∼10^6 and 10^8 yr. These biases are also present in Figure 2.3.4. These results point once again to the inherent age-metallicity degeneracy issue due to the confusion of old

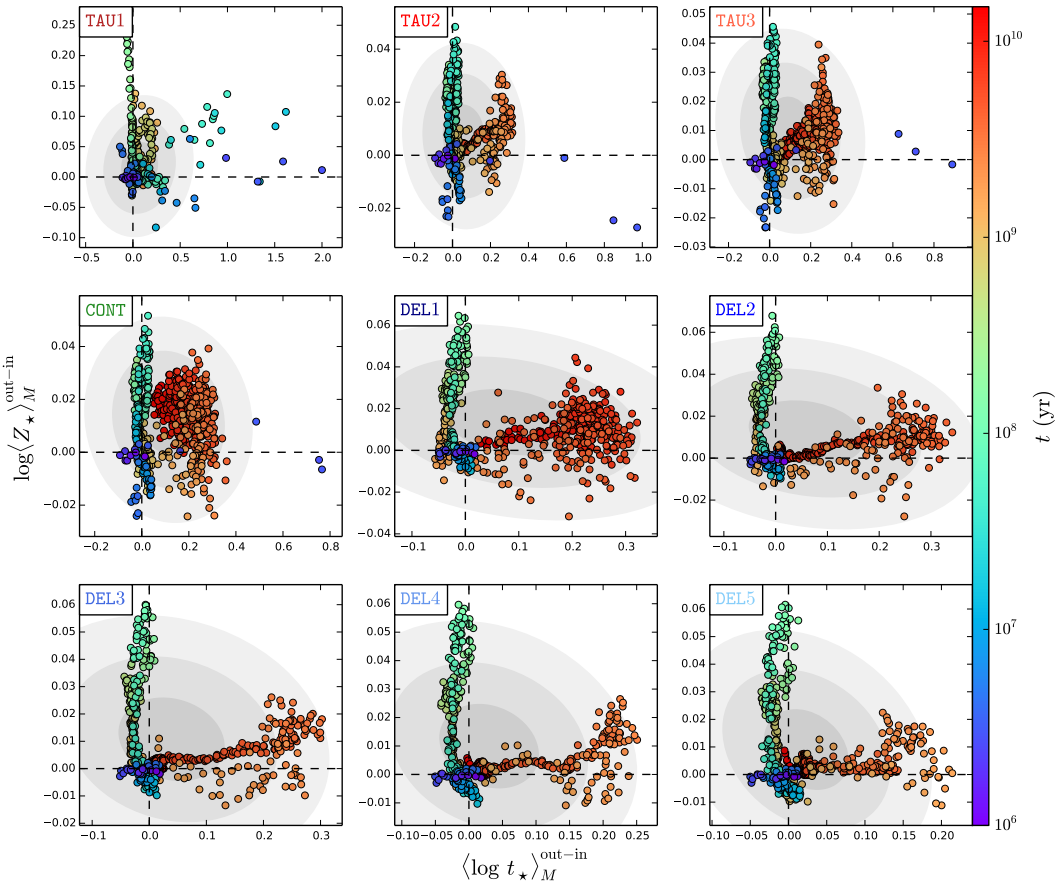

Figure 2.3.8: Difference in the mass-weighted mean stellar age $\langle\log t_\star\rangle_M$ as a function of the difference in the mean stellar metallicity $\log\langle Z_\star\rangle_M$ between STARLIGHT (out) and REBETIKO (in) values colour coded according to the CSP age t. Panel display configuration is identical to that in Figure 2.3.6. Light- to dark-grey ellipses represent 1σ, 2σ and 3σ 2-dimensional standard deviations, respectively.

metal-poor with young metal-rich galaxies. This issue is particularly clear for the instantaneous burst SFH and is represented by the diagonal line showing an increasing metallicity with decreasing age and vice versa.

On the other hand, Figure 2.3.8 shows the relation between the difference in the *mass-weighted mean stellar age* $\langle\log t_\star\rangle_M$ and *mean stellar metallicity* $\log\langle Z_\star\rangle_M$ between STARLIGHT and REBETIKO values colour coded according to the CSP age t. Panels display configuration is identical to that in Figure 2.3.6. The results show that the age can be under or overestimated for most of SFHs by up to $\sim$0.05 and 0.3 dex, respectively. Moreover, the metallicity can be under and overestimated by up to $\sim$0.02 and 0.045 dex, respectively. The exception to this is trend is found for the instantaneous burst SFH, for which the age and metallicity show overestimations of up to $\sim$0.25 and $\sim$0.2 dex, respectively, which are more pronounced for $10^6 \lesssim t \lesssim 10^8$ and $10^8 \lesssim t \lesssim 10^{10}$ yr, as also apparent from Figure 2.3.5. On average, mass-weighted age and metallicity uncertainties are larger than their light-weighted counterparts.

Overall, these results show that the recovery of stellar population properties with PSS strongly depends on the characteristics of the stellar continuum (e.g. shape, prominence of the absorption features). This inherent caveat of PSS is aggravated by a generally non-optimal age coverage by the base library used for spectral modelling, which can lead to significant uncertainties on mass, mean age and mean metallicity at evolutionary stages between successive young SSPs in the base library. Moreover, degeneracies between older SSPs in the base can lead to systematic biases on the mass, age and metallicity for each of the considered SFHs, with the exception for an instantaneous burst. These results suggest that tailored-made base libraries should probably be produced to model the CSPs of each SFH in order to optimally account

for the different stellar spectral characteristics and thus retrieve better synthesis results. However, although this approach might be feasible when applying PSS to synthetic galaxies, it appears impractical and rather unfeasible for automated PSS application to real galaxy spectra. Moreover, it is important to note that the uncertainties found are roughly within those reported for STARLIGHT (Cid Fernandes *et al.* 2005).

3 Active galaxy models

Synthetic spectra of *active galaxies* (AGs) were created by adding a simple AGN FC continuum model to CSPs. A subsequent analysis of these spectra with PSS helps defining an AGN detection threshold in a Lyman-continuum-leaking galaxy with an evolved CSP. Moreover, an investigation of the impact of an AGN continuum on the estimation of fundamental stellar population properties was performed with PSS while using multiple modelling approaches to handle the AGN spectral contribution. Results show that a purely-stellar PSS modelling approach of AG can lead to severe systematic biases on the estimated total stellar mass, mean stellar age and mean stellar metallicity, which can be mitigated when adopting an adequate approach of modelling the AGN continuum.

This chapter is organised as follows. Section 3.1 describes the addition of an AGN continuum defined as a PL to CSPs. Section 3.2 presents the methodology and results after applying PSS to these synthetic AG spectra while adopting different approaches for the handling of the AGN continuum. One one hand, Subsection 3.2.1 details the synthesis results of synthetic spectra with a CSP with 10 Gyr and varying AGN fractional contribution simulating an Lyman-continuum-leaking AG with an evolved stellar component. This case study provides an AGN fractional contribution value under which state-of-the-art PSS codes do not reliably detect a PL spectral contribution (Cardoso, Gomes & Papaderos 2016). On the other hand, Subsection 3.2.2 explores the impact of the AGN FC continuum to the estimation of fundamental stellar properties of galaxies with different SFHs (Cardoso, Gomes & Papaderos 2017).

3.1 Synthetic spectra of AGs

The optical AGN FC is commonly assumed to be well approximated by a PL represented as $F_\nu \propto \nu^{-\alpha} \Leftrightarrow F_\lambda \propto \lambda^{\alpha-2}$ (e.g. Oke, Neugebauer & Becklin 1970; Oke & Gunn 1974; O'Connell 1976; Koski 1978; Ferland & Netzer 1983; Bergvall, Johansson & Olofsson 1986; Marcha *et al.* 1996; Kraemer & Crenshaw 2000; Hao *et al.* 2013; Kügler *et al.* 2014) with the PL index α in the range $\alpha = 0.5$–2 for different types of AGN (e.g. Oke, Neugebauer & Becklin 1970; Koski 1978; Heckman 1980; Malkan & Filippenko 1983; Stasińska 1984a,b; Veilleux & Osterbrock 1987; Marcha & Browne 1996;; Goerdt & Kollatschny 1998; Vega *et al.* 2009). This approximation is often made in spectral synthesis (e.g. Goerdt & Kollatschny 1998; Schmitt, Storchi-Bergmann & Cid Fernandes 1999; Kauffmann *et al.* 2003c; Cid Fernandes *et al.* 2004; Vega *et al.* 2009 Benítez *et al.* 2013) and photoionisation studies (e.g. Heckman 1980; Ferland & Netzer 1983; Stasińska 1984a,b; Veilleux & Osterbrock 1987). However, the nature of this FC component in radio quiet galaxies, particularly in Seyfer 2, has been source of debate for several decades (e.g. Koski 1978; Ho, Filippenko & Sargent 1995; Ho, Filippenko & Sargent 1997; Cid Fernandes, Storchi-Bergmann & Schmitt 1998; Storchi-Bergmann *et al.* 1998; Schmitt, Storchi-Bergmann & Cid Fernandes 1999; Eracleous & Halpern 2001; Ho, Filippenko & Sargent 2003; Cid Fernandes *et al.* 2004; Garcia-Rissmann *et al.* 2005; Ho 2008; Vega *et al.* 2009). An overview of this debate is referred to Cardoso, Gomes & Papaderos (2017)

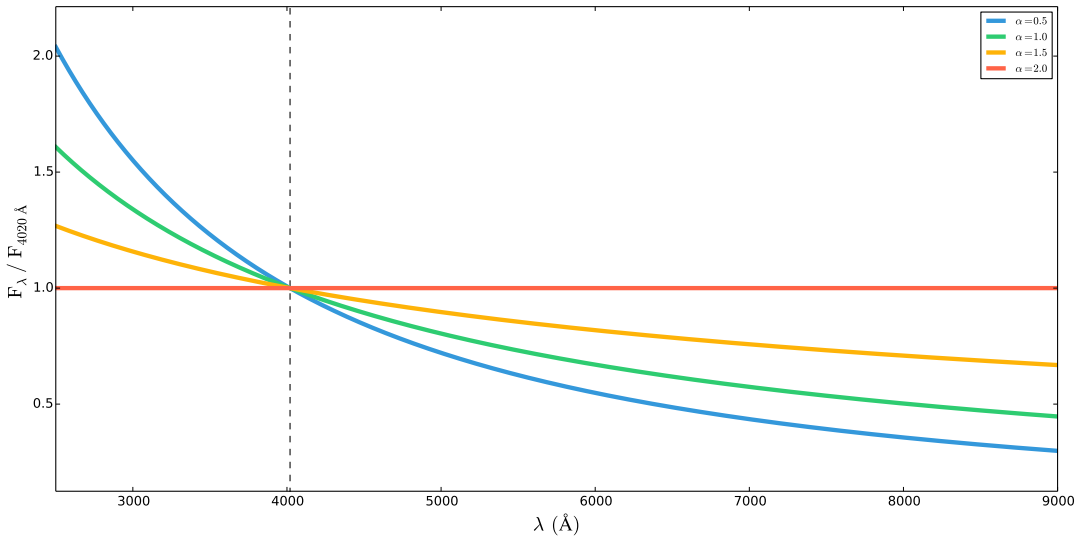

Figure 3.1.1: AGN FCs parameterised by a PL function as $F_\nu \propto \nu^{-\alpha} \Leftrightarrow F_\lambda \propto \lambda^{\alpha-2}$ normalised at $\lambda_0 = 4020$ Å (black dashed line) as a function of wavelength λ. Blue, green, yellow and red lines represent PLs with $\alpha = 0.5$, 1, 1.5 and 2, respectively.

included in Appendix B and, for the sake of conciseness, the following discussion focus only on some of the reported fractional contributions of this optical spectral component in AGs.

Koski (1978) used spectrophotometric scans of 20 Seyfert, 3 intermediate Seyfert and 5 narrow-line radio galaxies to study the emission-line, stellar and non-thermal spectral contributions. The stellar continuum and absorption lines were subtracted using an elliptical galaxy spectrum as template for the nuclear stellar populations. It was found that the typical amount of non-stellar PL continuum is ∼29% at λ4861 with $\alpha = 0.2$–0.8. In turn, Heckman (1980) studied 90 bright galaxies with optical and radio data and concluded that ∼90% of the monochromatic flux at 3600 Å was stellar in nature. Thus, it was concluded that any blue FC in *low-ionisation nuclear emission-line region* (LINER) galaxies should have a negligible contribution to the continuum. Moreover, Malkan & Filippenko (1983) studied the nuclei of 9 Seyfert galaxies with extreme weak stellar absorption lines and found that stars could contribute between 17% and 60% to the visual continuum. The remaining non-stellar continuum could be approximated as a PL with $\alpha = 1.1$–1.2 from the visual to 10 μm. In turn, Schmitt, Storchi-Bergmann & Cid Fernandes (1999) investigated the contributions of AGN and stellar populations to absorption-line EWs and continuum ratios in the 3500–7000 Å range of 20 Seyfert 2 galaxies and concluded that the contributions of stars younger than 10 Myr and of an AGN FC should rarely exceed ∼5 %. Eracleous & Halpern (2001) characterised NGC 3065 as a LINER with broad Balmer emission lines coming from an accretion disk. The continuum was modelled as a linear combination of a non-stellar component and starlight described by spectra of S0 galaxies. It was found that the spectrum of NGC 4339 when used as a template provides an good match to the continuum of NGC 3065 without a need for a non-stellar component. However, other galaxy templates lead to a non-stellar continuum that can contribute up to ∼10% of the continuum flux at Hα and Hβ and up to ∼15% at [OII]λ3727. Moreover, Cid Fernandes *et al.* (2004) studied the stellar population properties of a sample of 79 mostly Seyfert 2 galaxies. This was accomplished by applying full-spectrum PSS modelling with an early version of STARLIGHT in the spectral region 3500–5200 Å while allowing for variations of a PL spectral component in the base library. This work found stellar populations of all ages and a PL component with a mean contribution within ∼20–30% and a maximum contribution of ∼63% to the monochromatic flux at 4020 Å, which could either describe the scatter starlight of an hidden AGN or a young and dusty starburst. Finally, Vega *et al.* (2009) analysed a sample of 64 Seyfert, 9 normal and 5 starburst galaxies with STARLIGHT, estimated the fractional contribution of multiple FCs with $\alpha = 1$–2 and found that the PL fractional contribution can be as high as ∼90% in Seyfert 1, ∼50% in Seyfert 2 and ∼32% in normal galaxies. The results of these different studies show that there is no clear trend of AGN PL fractional contribution with AGN

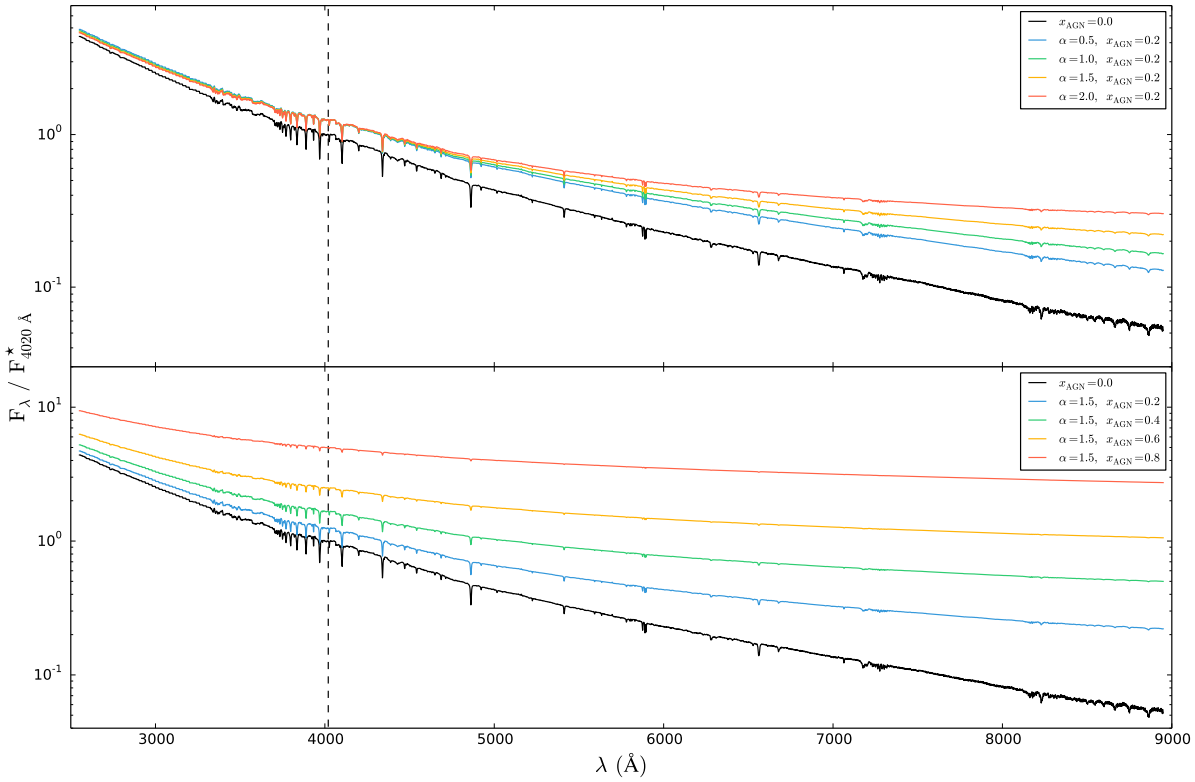

Figure 3.1.2: AG synthetic spectra created by combining a CSP with 1 Myr, solar metallicity and instantaneous burst SFH with AGN PLs with variations on the PL index α (*top panel*) and fractional contributions x_{AGN} (bottom panel) to the monochromatic flux at $\lambda_0 = 4020$ Å (black dashed line). Black lines represent the CSP spectra and blue, green, yellow and red lines represent the spectra of AGs with $\alpha = 0.5$, 1, 1.5 and 2 for $x_{AGN} = 0.4$ on the top panel and with $x_{AGN} = 0.8$, 0.6, 0.4 and 0.2 for $\alpha = 1.5$ on the bottom panel, respectively.

type. Moreover, the contribution of this FC component can empirically be as high as 90% for radio quiet galaxies such as Seyfert. This points to the importance of quantifying potential biases on the estimated physical properties when applying PSS to AGs without a specific strategy to account for the AGN PL.

The optical AGN FC was assumed in this work to be well represented by a PL as $F_\nu \propto \nu^{-\alpha}$. The AGN continuum model is fully parameterised by the PL index α and its fractional contribution x_{AGN} to the monochromatic flux at the normalisation wavelength $\lambda_0 = 4020$ Å. It were adopted values of $\alpha = 0.5$, 1, 1.5 and 2 and $x_{AGN} = 0.2$, 0.4, 0.6 and 0.8 to study the impact of different AGN continua shapes and contributions on the estimation of physical properties with PSS. Such wide range of values ensures that no strong prior assumptions are made regarding the AGN spectral shape and fractional contribution. Figure 3.1.1 shows PLs normalised at $\lambda_0 = 4020$ Å (*black dashed line*) with $\alpha = 0.5$, 1, 1.5 and 2 represented by *blue*, *green*, *yellow* and *red lines*, respectively. This figure shows that the PL continuum becomes bluer with decreasing α.

Evidence has shown that several local spheroidal galaxies display signs of extreme nuclear Lyman-continuum leakage (Papaderos *et al.* 2013; Gomes *et al.* 2016c). Indeed, Papaderos *et al.* (2013) analysed IFU spectroscopy of a sample of 32 spheroidals from the CALIFA survey with STARLIGHT and found that the nuclear Lyman continuum escape fraction in several of these objects can be has high as ∼70–95%. Papaderos *et al.* (2013) suggested that this could help reconcile the fact that many of these galaxies display strong AGN activity in the radio and X-ray wavelengths but only weak optical emission-lines characteristic of LINERs. The optical spectrum is expected in these cases to consist essentially of stellar emission and an AGN FC. Indeed, the continuum should lack strong absorption features and NE in the limiting case of complete Lyman-continuum leakage, thus superficially resembling that of a BL Lac (e.g. Oke & Gunn 1974; Marcha *et al.* 1996; Kügler *et al.* 2014). These results motivated the creation in this

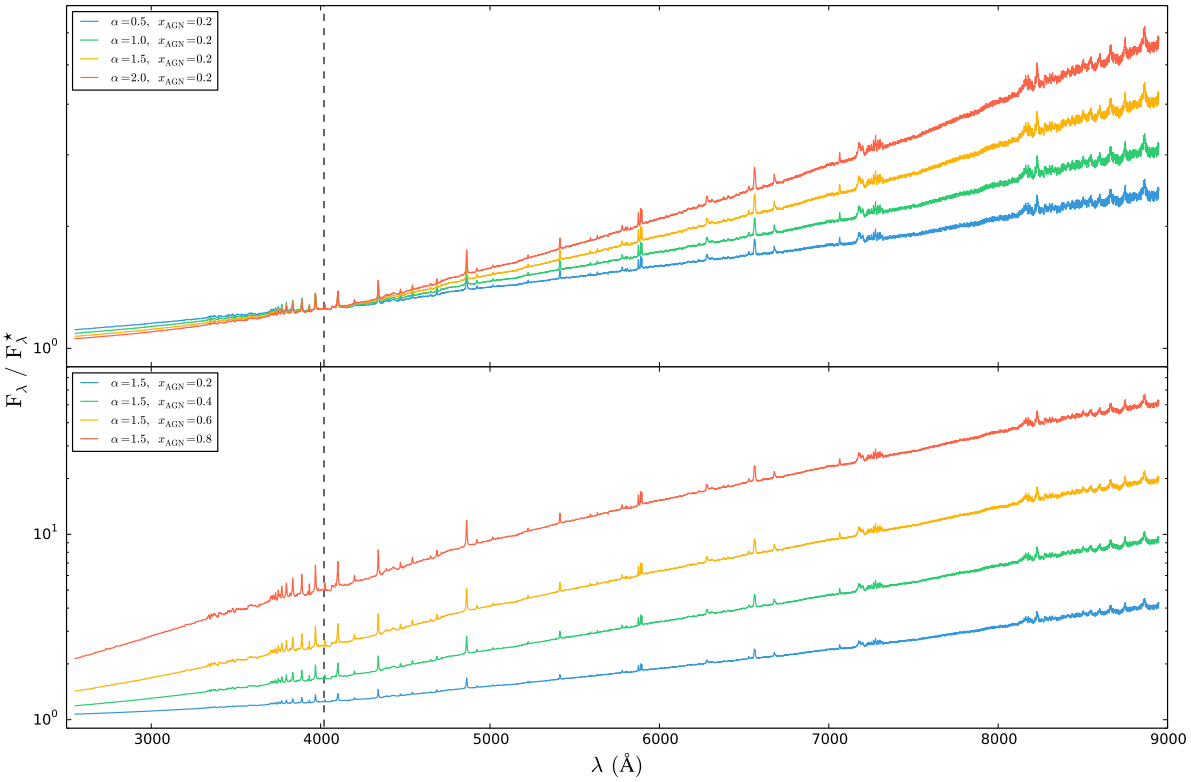

Figure 3.1.3: AG synthetic spectra with a CSP with 1 Myr, solar metallicity and instantaneous burst SFH with AGN PLs with variations on α (*top panel*) and $x_{\rm AGN}$ (bottom panel) divided by their stellar spectral component. Blue, green, yellow and red lines represent AGs with $\alpha = 0.5$, 1, 1.5 and 2 for $x_{\rm AGN} = 0.4$ on the top panel and with $x_{\rm AGN} = 0.8$, 0.6, 0.4 and 0.2 for $\alpha = 1.5$ on the bottom panel, respectively, and black dashed line represents λ_0=4020 Å.

work of synthetic AG spectra containing only stellar and AGN spectral components.

The flux F_λ of a synthetic AG normalised at wavelength λ_0 is the linear combination of CSP $F^\star_\lambda$ and AGN $F^{\rm AGN}_\lambda$ spectral fluxes,

$$\frac{F_\lambda}{F_{\lambda_0}} = x_\star \frac{F^\star_\lambda}{F^\star_{\lambda_0}} + x_{\rm AGN} \frac{F^{\rm AGN}_\lambda}{F^{\rm AGN}_{\lambda_0}}, \tag{3.1}$$

where $x_\star$ and $x_{\rm AGN}$ are, respectively, the stellar and AGN fractional contributions to F_{λ_0} following the normalisation condition $x_\star + x_{\rm AGN} = 1$ at $\lambda_0 = 4020$ Å. Equation 3.1 can be rewritten so that the stellar flux and related stellar population properties are conserved during the addition of the AGN PL continuum,

$$F_\lambda = F^\star_\lambda + \frac{x_{\rm AGN}}{1 - x_{\rm AGN}} F^\star_{\lambda_0} \left(\frac{\lambda}{\lambda_0}\right)^{\alpha-2}, \tag{3.2}$$

considering $F^{\rm AGN}_\lambda \propto \lambda^{\alpha-2}$ and the normalisation condition at λ_0. Synthetic spectra of AGs were created following Equation 3.2 by adding 16 AGN PLs for the different values of α and $x_{\rm AGN}$ to the CSPs presented in Section 2.2 and illustrated in Figures A.1.1–A.1.9 in Appendix A.

Figure 3.1.2 shows the combination of the continuum of a CSP with 1 Myr, solar metallicity and instantaneous burst SFH with AGN FCs with variations in α (*top panel*) and $x_{\rm AGN}$ (*bottom panel*). The purely-stellar spectra are represented by *black lines*. Moreover, AG spectra with $\alpha = 0.5$, 1, 1.5 and 2 for $x_{\rm AGN} = 0.4$ and with $x_{\rm AGN} = 0.8$, 0.6, 0.4 and 0.2 for $\alpha = 1.5$ are represented on the *top* and *bottom panels* by the *blue*, *green*, *yellow* and *red lines*, respectively. This figure illustrates two important facts resulting from the addiction of the FC to a purely-stellar spectrum. On the one hand, the top panel shows that the final spectrum F_λ becomes steeper with decreasing α, as also illustrated in Figure 3.1.1. This would be

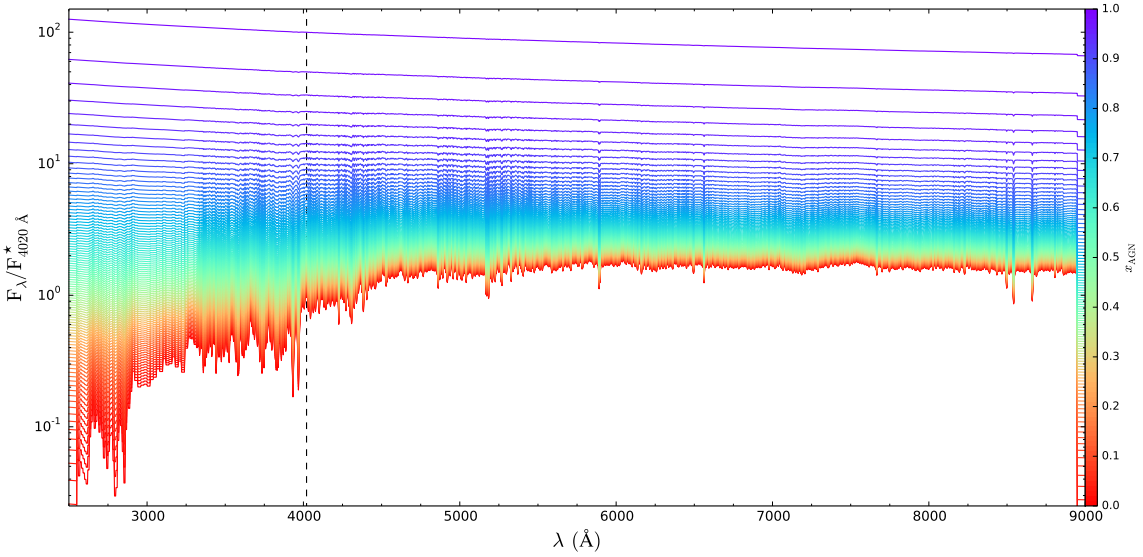

Figure 3.1.4: AG synthetic spectra with S/N = 1000 created with the combination of a CSP with 10 Gyr, solar metallicity and instantaneous burst SFH with an AGN PL with $\alpha = 1.5$. Colour coding represents the AGN fractional flux contribution $x_{\rm AGN}$ at $\lambda_0 = 4020$ Å in $x_{\rm AGN} \in [0, 1[$ in steps of 0.01.

in principal similar to adding the continua of increasingly young SSPs with washed-out absorption-line features to the purely-stellar spectrum $F^\star_\lambda$ as a function of decreasing α (e.g. Moultaka 2005). On the other hand, the bottom panel shows that the dilution of stellar absorption features is directly proportional to $x_{\rm AGN}$ and stronger with increasing wavelength diverging from λ_0. This fact is clearer observed in Figure 3.1.3 that shows the same AG spectra divided by their stellar spectral component. Evidence shows that a non-stellar continuum is indeed responsible for the dilution of stellar absorption lines (e.g. Koski 1978; Serote Roos *et al.* 1998; Moultaka & Pelat 2000; Kauffmann *et al.* 2003c).

A smaller set of synthetic AG spectra was created by combining the continuum of a CSP with 10 Gyr, solar metallicity and instantaneous burst SFH with a AGN PL with $\alpha = 1.5$ and varying AGN fractional contribution of $x_{\rm AGN} \in [0, 1[$ in steps of 0.01. Noise was then added to these spectra assuming S/N = 5, 10, 25, 50, 75, 100, 250, 500, 750 and 1000 at λ_0. Figure 3.1.4 shows the resulting spectra for S/N = 1000. This set of spectra was used to investigate if the AGN spectral contribution can be reliable estimated with state-of-the-art PSS in a galaxy with an old stellar component and leaking all of its Lyman-continuum photons.

3.2 Analysis of stellar properties with PSS

The PSS code STARLIGHT was applied to the synthetic spectra following a modelling procedure similar to that detailed in Section 2.3. However, the base library was modified to include different approaches for handling an PL spectral contribution. This is particularly important since the majority of PSS studies of the nuclear region of Seyferts often do not account for the AGN continuum as relevant spectral component (e.g. Kauffmann *et al.* 2003c; Cid Fernandes *et al.* 2005; Coziol *et al.* 2011). With this in mind, it was considered the following modelling configurations:

- `npl`: no AGN PL continuum is included in the base library;
- `spl`: an AGN PL continuum with the same value of α as the one adopted for each synthetic spectrum is included in the base library, and
- `mpl`: AGN PL continua with $\alpha = 0.5$, 1, 1.5 and 2 are included in the base library.

The first configuration corresponds to the *worst-case scenario* where no attempt is made to account for the AGN continuum. This means that the input spectrum can only be decomposed into stellar building blocks (e.g. Mateus *et al.* 2006; Stasińska *et al.* 2006; Cid Fernandes *et al.* 2011; Coziol *et al.* 2011). The second approach represents the *best-case scenario* in which the base library contains a single PL that is

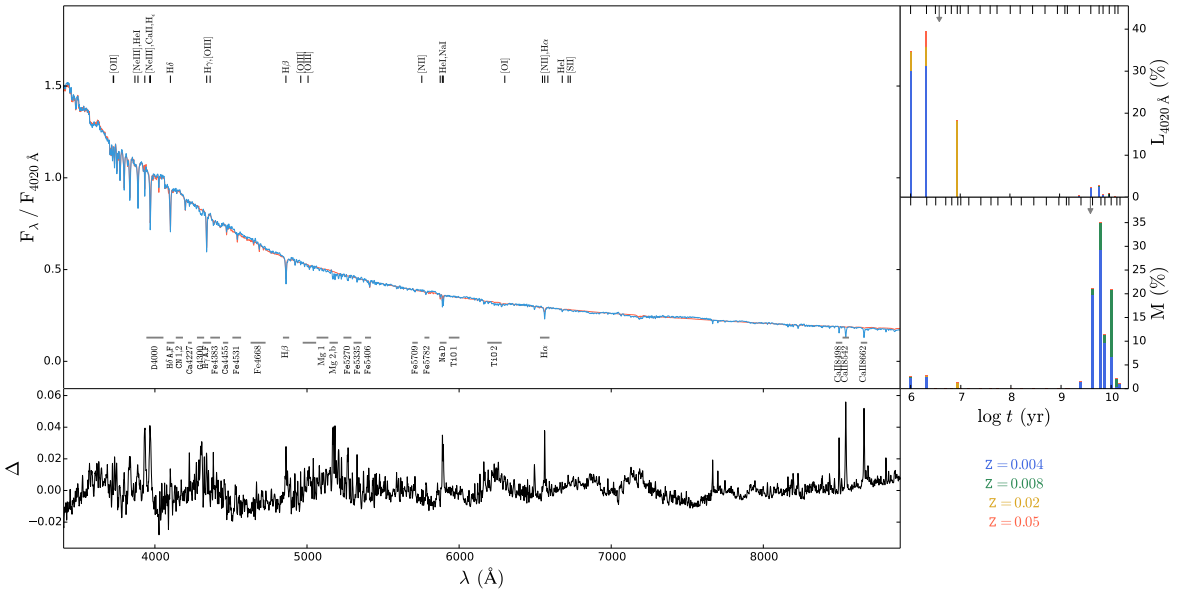

Figure 3.2.1: STARLIGHT spectral modelling results of a an AG with a CSP with 1 Myr, solar metallicity and instantaneous burst SFH and an AGN PL with $\alpha = 1.5$ and $x_{\rm AGN} = 0.2$. Panel display configuration and legend details are identical to those in Figure 2.3.1.

identical to the one embedded in the input spectrum. An approximation to this configuration setup is in theory possible if the optical AGN continuum shape can be constrained for example with ancillary observations in the UV and/or NIR. The third approach aims to represent a *conservative scenario* in which the exact AGN continuum shape is unknown and, hence, the spectral fit is performed including multiple AGN continua in the base library with α in a range supported by evidence (e.g. Garcia-Rissmann *et al.* 2005; Mezcua *et al.* 2011; Roche *et al.* 2016). This approach bears the risk of finding an AGN solution that includes multiple PLs, which could lead to an unphysical model of the AGN continuum. In turn, this could introduce complex biases to the estimated stellar properties (e.g. A_V, mean age, mean metallicity). This hypothesis is tested with the spectra presented in Figure 3.1.4 assuming A_V as a free parameter between -1 and 4 when employing PSS.

As an example of an application of STARLIGHT to a AG spectrum, Figure 3.2.1 shows the average results of 10 STARLIGHT spectral fits to a synthetic AG spectrum with a CSP with 1 Myr, solar metallicity and instantaneous burst SFH and an AGN PL with $\alpha = 1.5$ and $x_{\rm AGN} = 0.2$. Panel display configuration and legend details are identical to those in Figure 2.3.1. The results show relatively large residuals indicating that the best-fit spectral model found by STARLIGHT differs considerably from the input spectrum. Moreover, estimated total stellar mass $\log M_\star = 7.19\ M_\odot$, mean stellar age $\langle \log t_\star \rangle \simeq 6.64$ yr and mean stellar metallicity $\log\langle Z_\star \rangle \simeq -1.99$ clearly differ from input values of $\log M_\star = 5.73\ M_\odot$, $\langle \log t_\star \rangle = 6$ yr and $\log\langle Z_\star \rangle = -1.70$. These results show that the AGN PL is responsible for a considerable mass and age overestimation and metallicity underestimation for this particular AG model.

On the one hand, Subsection 3.2.1 presents results synthesis for the synthetic spectra presented in Figure 3.1.4 while adopting modelling setups `spl` and `mpl`. Presented in Cardoso, Gomes & Papaderos (2016), this analysis was performed to place an AGN detection threshold in an AG with an old stellar spectral component and to gain a first impression of potential biases on stellar population properties induced by the added AGN PL component. On the other hand, Subsection 3.2.2 presents the synthesis results as in Cardoso, Gomes & Papaderos (2017) for all modelling configurations and different SFHs, as presented in for an instantaneous burst SFH, with synthesis results for other SFHs mentioned when appropriate.

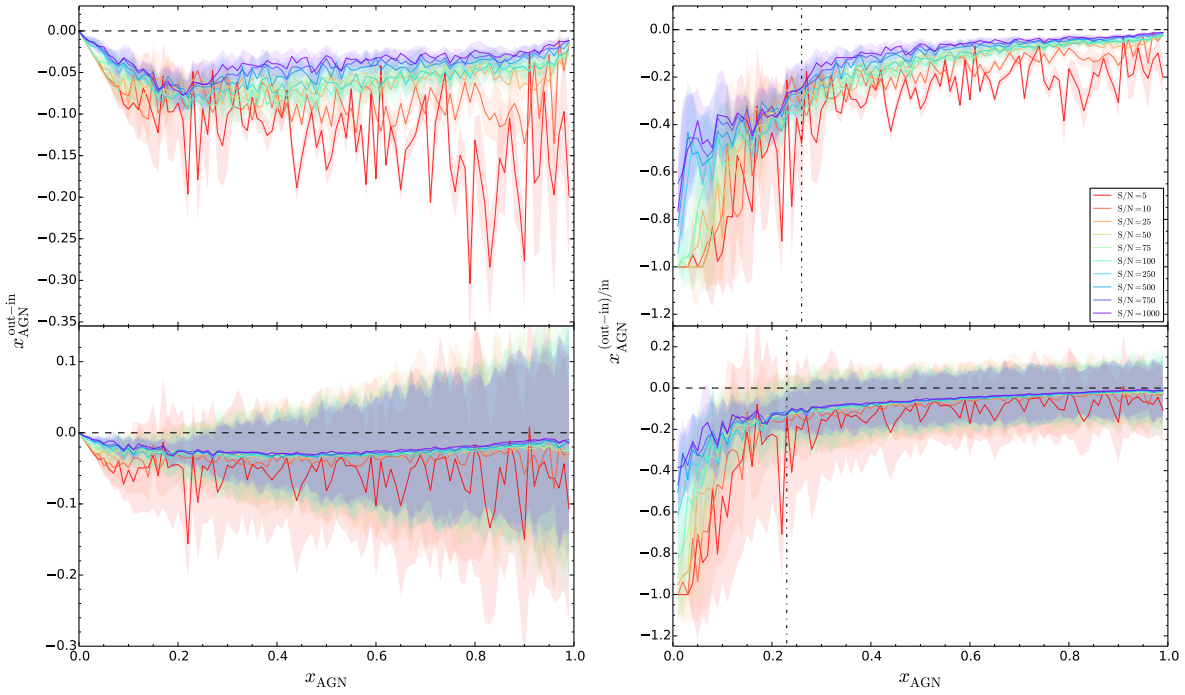

Figure 3.2.2: Difference in the AGN fractional flux contribution $x_{\rm AGN}$ (*left-hand side panels*) and fractional error (right-hand side panels) between STARLIGHT (out) and (in) as a function of $x_{\rm AGN}$ for `spl` (top panels) and `mpl` (bottom panels). Dark red, light red, orange, olive, light green, turquoise, cyan, blue, dark blue and violet lines represent results for S/N = 5, 10, 25, 50, 75, 100, 250, 500, 750 and 1000, respectively. Shaded areas represent $\pm 1\sigma$ standard deviations around the mean computed from ten fits to each synthetic spectrum. Vertical dash-dotted lines represent the value of $x_{\rm AGN}$ for each the Gelman & Rubin (1992) convergence criterion is satisfied.

3.2.1 Case study: Lyman-continuum-leaking AG with old stellar population

Figure 3.2.2 shows the $x_{\rm AGN}$ difference (*left-hand side panels*) and *fractional error* (*right-hand side panels*) between STARLIGHT (*out*) and REBETIKO (*in*) values as a function of $x_{\rm AGN}$ for `spl` (*top row panels*) and `mpl` (*bottom row panels*). Results for S/N = 5, 10, 25, 50, 75, 100, 250, 500, 750 and 1000 are represented by *dark red*, *light red*, *orange*, *olive*, *light green*, *turquoise*, *cyan*, *blue*, *dark blue* and *violet lines*, respectively. Moreover, shaded areas correspond to 1σ standard deviation around each line representing the mean of the 10 spectral fits for each input spectrum. The results on left-hand-side panels show that the accuracy with which $x_{\rm AGN}$ is recovered increases with S/N as $x_{\rm AGN} \to 0$ or 1 for both `spl` and `mpl`. The $x_{\rm AGN}$ is on average underestimated by $\sim$0.06 and $\sim$0.03 and has a maximum average of up to $\sim$0.11 and $\sim$0.05 for `spl` and `mpl`, respectively. Moreover, the uncertainty with which $x_{\rm AGN}$ is estimated is larger for `mpl`, as seen by the large 1σ standard deviations around the mean. Moreover, right-hand side panel results show on average a $\sim$0.11 fractional error difference between `spl` and `mpl`. Assuming that the lines for each S/N can be interpreted as analogues of independent chains in a random-walk Monte Carlo simulation, the application of the Gelman & Rubin (1992) convergence criterion finds a variance ratio $\hat{R} < 1.1$ for $x_{\rm AGN} \geq 0.26$ and 0.23 (*vertical dash-dotted lines*) for `spl` and `mpl`, respectively. Thus, an effective AGN detection threshold can be placed at $x_{\rm AGN}^{\rm threshold} \simeq 0.26$.

Figure 3.2.3 shows the difference in the *total stellar mass* $M_\star$ between STARLIGHT and REBETIKO values (*left-hand side panels*) and *V-band extinction* A_V estimated with STARLIGHT (*right-hand side panels*) as a function of $x_{\rm AGN}$ for `spl` (*top row panels*) and `mpl` (*bottom row panels*). Legend details are identical to those in Figure 3.2.2. The results show that the mass is overestimated roughly by $\sim$0.02 dex for $x_{\rm AGN} \lesssim 0.7$ and can be underestimated by up to $\sim$0.7 and 1.2 dex when $x_{\rm AGN} \gtrsim 0.9$ for `spl` and `mpl`, respectively. Moreover, the mass is on average systematically underestimated with decreasing S/N and increasing$x_{\rm AGN}$.

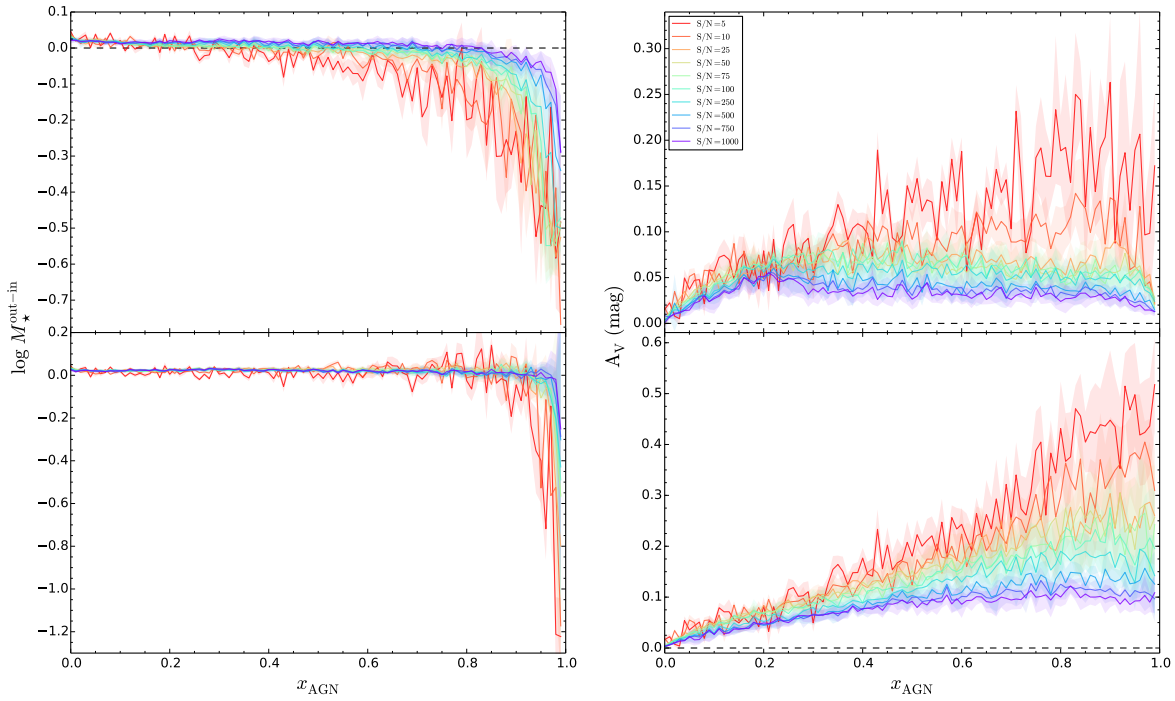

Figure 3.2.3: Difference in the total stellar mass $M_\star$ between STARLIGHT (out) and REBETIKO (in) values (left-hand side panels) and V-band extinction A_V estimated with STARLIGHT (right-hand side panels) as a function of x_{AGN} for `spl` (top panels) and `mpl` (bottom panels). Legend details are identical to those in Figure 3.2.2.

Meanwhile, estimated extinction increases with decreasing S/N for both `spl` and `mpl` and roughly with x_{AGN} for `mpl`. The extinction reaches a maximum of $\sim$0.075 at $x_{\mathrm{AGN}} \sim 0.4$ for `spl` and of $\sim$0.2 at $x_{\mathrm{AGN}} \gtrsim 0.8$ for `mpl`. The overall trend of A_V in both panels looks like a rough mirrored version along the x-axis of results found for the x_{AGN} difference displayed on left-hand side panels of Figure 3.2.2. This visual trend suggests that the estimation of the extinction and AGN fractional contribution are somehow connected. This was corroborated with an alternative set of synthesis tests made with the same synthetic spectra fixing A_V to zero when applying PSS. These alternative results show that the stellar mass is systematically overestimated $\sim$0.02 dex roughly for the whole x_{AGN} range for both `spl` and `mpl`. Moreover, results indicate that x_{AGN} is estimated within an uncertainty of $\sim$0.025 for both `spl` and `mpl` and the application of the Gelman & Rubin (1992) yields convergence of the AGN fractional error when $x_{\mathrm{AGN}} \geq 0.32$ and 0.13 for `spl` and `mpl`, respectively. Therefore, it can be concluded that the effective AGN detection threshold $x_{\mathrm{AGN}}^{\mathrm{threshold}} \simeq 0.26$ does not depend significantly on A_V for `spl`.

Figure 3.2.4 shows the difference in the *light-* (*left-hand side panels*) and *mass-weighted mean stellar age* $\langle \log t_\star \rangle$ (*right-hand side panels*) between STARLIGHT and REBETIKO values as a function of x_{AGN} for `spl` (*top row panels*) and `mpl` (*bottom row panels*). Legend details are identical to those in Figure 3.2.2. The results show a systematic age underestimation with increasing x_{AGN} and decreasing S/N for both `spl` and `mpl`. This underestimation can reach up to $\sim$3 dex and 1 dex for the light- and mass-weighted ages, respectively. Moreover, the light-weighted age is on average underestimated by $\sim$0.3 and $\sim$0.09 dex for `spl` and `mpl`, respectively, whereas the mass-weighted age is overestimated $\sim$0.02 and $\sim$0.005 dex for `spl` and `mpl`, respectively.

Finally, Figure 3.2.5 shows the difference in the *light-* (*left-hand side panels*) and *mass-weighted mean stellar metallicity* $\log\langle Z_\star \rangle$ (*right-hand side panels*) between STARLIGHT and REBETIKO values as a function of x_{AGN} for `spl` (*top row panels*) and `mpl` (*bottom row panels*). Legend details are again identical to those in Figure 3.2.2. The results show with increasing x_{AGN} that there is a systematic overestimation of the light-weighted metallicity for $x_{\mathrm{AGN}} \lesssim 0.6$ of up to $\sim$0.1 dex and a systematic underestimation for $x_{\mathrm{AGN}} \gtrsim 0.8$ of up to $\sim$0.4 dex for both `spl` and `mpl`. Meanwhile, mass-weighted metallicity is roughly well

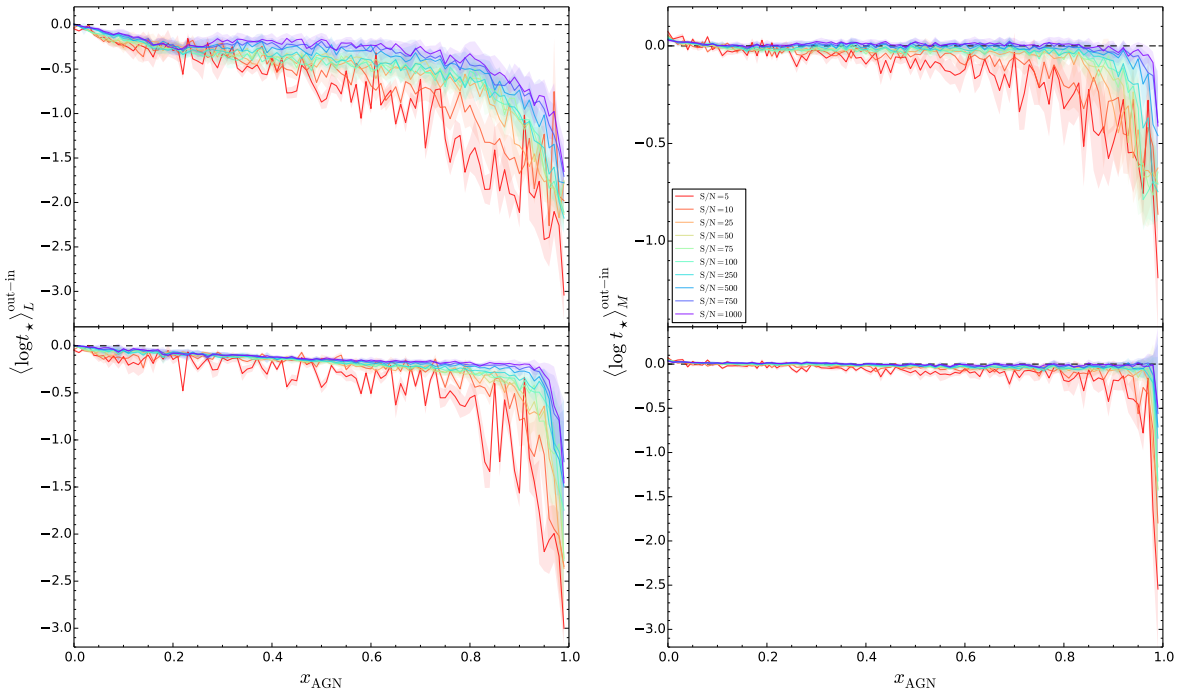

Figure 3.2.4: Difference in the mean stellar age $\langle \log t_\star \rangle$ between STARLIGHT (out) and REBETIKO (in) values weighted by light (left-hand side panels) and mass (right-hand side panels) as a function of $x_{\rm AGN}$ for `spl` (top panels) and `mpl` (bottom panels). Legend details are identical to those in Figure 3.2.2.

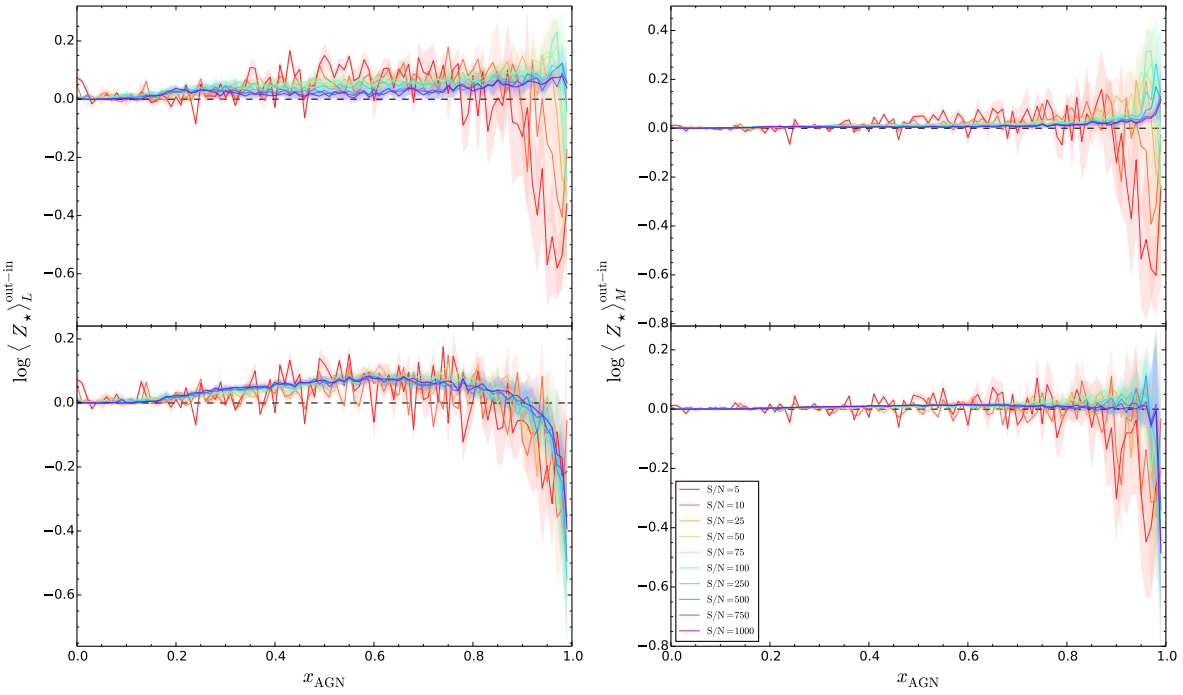

Figure 3.2.5: Difference in the mean stellar metallicity $\log\langle Z_\star \rangle$ between STARLIGHT (out) and REBETIKO (in) values weighted by light (left-hand side panels) and mass (right-hand side panels) as a function of $x_{\rm AGN}$ for `spl` (top panels) and `mpl` (bottom panels). Legend details are identical to those in Figure 3.2.2.

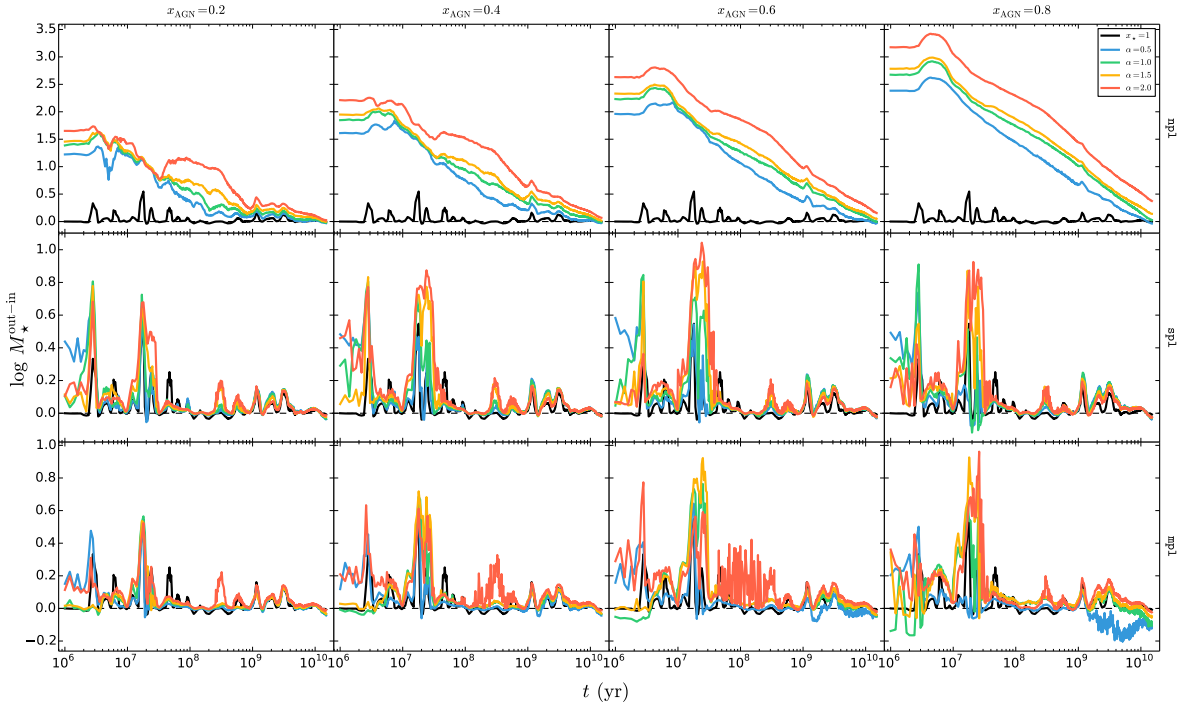

Figure 3.2.6: Difference in the total stellar mass $M_\star$ between STARLIGHT (out) and REBETIKO (in) values as a function of CSP age t for an instantaneous burst SFH. Top, middle and bottom rows display results adopting a base library without any AGN PL (`npl`), with a PL with the same index α as the input values (`spl`) and with PLs with $\alpha = 0.5$, 1, 1.5 and 2 (`mpl`), respectively. Left- to right-hand side panels represent increasing $x_{\rm AGN}$ from 0.2 to 0.8 in steps of 0.2, respectively. Black, blue, green, yellow and red points and lines represent results for CSPs and AGs with a PL with $\alpha = 0.5$, 1.0, 1.5 and 2.0, respectively.

recovered for $x_{\rm AGN} \lesssim 0.8$ and is systematically under or overestimated by up to $\sim$0.1 and 0.4 dex with increasing $x_{\rm AGN}$ when $x_{\rm AGN} \gtrsim 0.9$ for `spl` and `mpl`, respectively. Moreover, light-weighted metallicity is on average overestimated by $\sim$0.03 and $\sim$0.02 dex for `spl` and `mpl`, respectively, whereas its mass-weighted counterpart is overestimated by up to $\sim$0.007 and $\sim$0.004 dex for `spl` and `mpl`, respectively.

Overall, these results show that an effective AGN detection threshold can be tentatively placed at an AGN fractional contribution $x_{\rm AGN}^{\rm threshold} \simeq 0.26$. Moreover, the light-weighted mean stellar age and metallicity can be under and overestimated at this AGN spectral contribution by as much as $\sim$0.3 and $\sim$0.03 dex, respectively, for the *best-case scenario* in which it is known the exact shape of AGN continuum. Meanwhile, the total stellar mass and mass-weighted age and metallicity are well recovered within a $\sim$0.02 dex uncertainty at the same AGN fractional contribution.

3.2.2 Dependence on the star formation history and AGN modelling approach

Figure 3.2.6 shows the difference in the *total stellar mass* $M_\star$ between the STARLIGHT and REBETIKO values as a function of CSP age t. Results for `npl`, `spl` and `mpl` are represented on the *top*, *middle* and *bottom row panels*, respectively. Moreover, results with increasing AGN fraction fraction $x_{\rm AGN}$ are displayed from *left-* to *right-hand side panels* going from $x_{\rm AGN} = 0.2$ to 0.8 in steps of 0.2, respectively, and synthesis results for $x_\star = 1$ (purely-stellar) and $\alpha = 0.5$, 1, 1.5 and 2 are represented by *black*, *blue*, *green*, *yellow* and *red points and lines*, respectively. The top row results show a systematic mass overestimation with decreasing t that can reach a maximum of $\sim$3.5 dex around 4×10^6 yr. This trend is accentuated with increasing α and $x_{\rm AGN}$. Moreover, variations on α and $x_{\rm AGN}$ translate into variations in mass of up to $\sim$1 and 3 dex, respectively. Figure A.2.1 in Appendix A shows similar trends for the other SFHs.

The middle row results show that the mass can be overestimated up to $\sim$1 dex at evolutionary

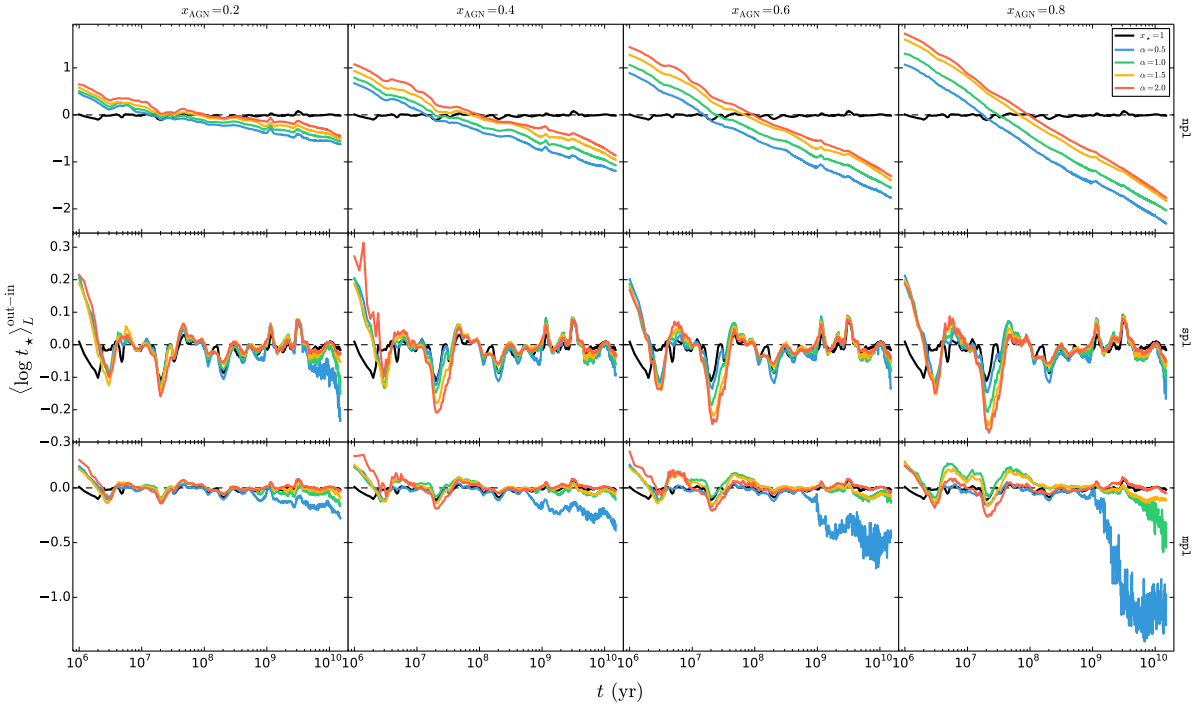

Figure 3.2.7: Difference in the light-weighted mean stellar age $\langle \log t_\star \rangle_L$ between STARLIGHT (out) and REBETIKO (in) values as a function of CSP age t for AGs with instantaneous burst SFH. Panel display and legend details are analogous to those of Figure 3.2.6.

stages associated with considerable mass uncertainties on purely-stellar spectra. Results in Section 2.3 showed that these are likely due to an non-optimal age coverage of the adopted base library for synthetic spectra with an instantaneous burst SFH. Moreover, it is worth noting the existence of significant mass overestimation peaks reaching up to ∼1 dex around 3×10^6 and 2×10^7 yr that increase significantly with increasing $x_{\rm AGN}$. Results also show that variations in α have small impact on the recovery of the stellar mass. The bottom row illustrates overall similar results. Indeed, there is an overall mass overestimation peak around 2×10^7 yr that can reach up to ∼1 dex and that increases with $x_{\rm AGN}$. Moreover, results show a peculiar feature of mass underestimation for $t \gtrsim 10^9$ yr with decreasing α and $x_{\rm AGN}$ that is best understood when analysing the synthesis results of other physical properties.

Figure 3.2.7 shows the difference in the *light-weighted mean stellar age* $\langle \log t_\star \rangle_L$ between STARLIGHT and REBETIKO values as a function of CSP age t. Panels configuration and legend details are identical to those in Figure 3.2.6. The top row results show a systematic age overestimation of up to ∼1.5 dex with decreasing age for $t \lesssim 5 \times 10^7$ yr and underestimation of up to ∼2 dex with increasing age for $t \gtrsim 5 \times 10^7$ yr. These trends are clearly accentuated with increasing $x_{\rm AGN}$ and can be understood considering that the AGN continuum dilutes the Balmer absorption lines that naturally become weaker with age, thus leading to a stellar age overestimation for $t \lesssim 5 \times 10^7$ yr. Meanwhile, the same AGN continuum also dilutes the strength of $D_n(4000)$ that becomes stronger with age, therefore leading to an age underestimation for $t \gtrsim 5 \times 10^7$ yr. Results also show that the age is systematically overestimated with increasing α. This in turn can be understood considering that STARLIGHT has to introduce a significant fraction of old SSPs to the best-fit solution in order to reproduce the flattening of the featureless AGN continuum with increasing α. Figure A.2.2 in Appendix A shows similar trends for the other SFHs.

The middle row results show an age uncertainty within ∼0.2 dex, consistent with the uncertainty found for the CSP illustrated in the black lines. However, results show a significant age underestimation of up to ∼0.2 dex for $\sim 5 \times 10^7$ yr that is accentuated with increasing α and $x_{\rm AGN}$. Moreover, the age is systematic overestimated by up to ∼0.2 dex with decreasing age for $t \lesssim 3 \times 10^6$ yr and underestimated by up to ∼0.15 dex with increasing age for $t \gtrsim 3 \times 10^9$ yr. The bottom row display similar results, albeit with a few peculiar differences. For instance, the age is systematically over and underestimation for $t \lesssim 3 \times 10^6$

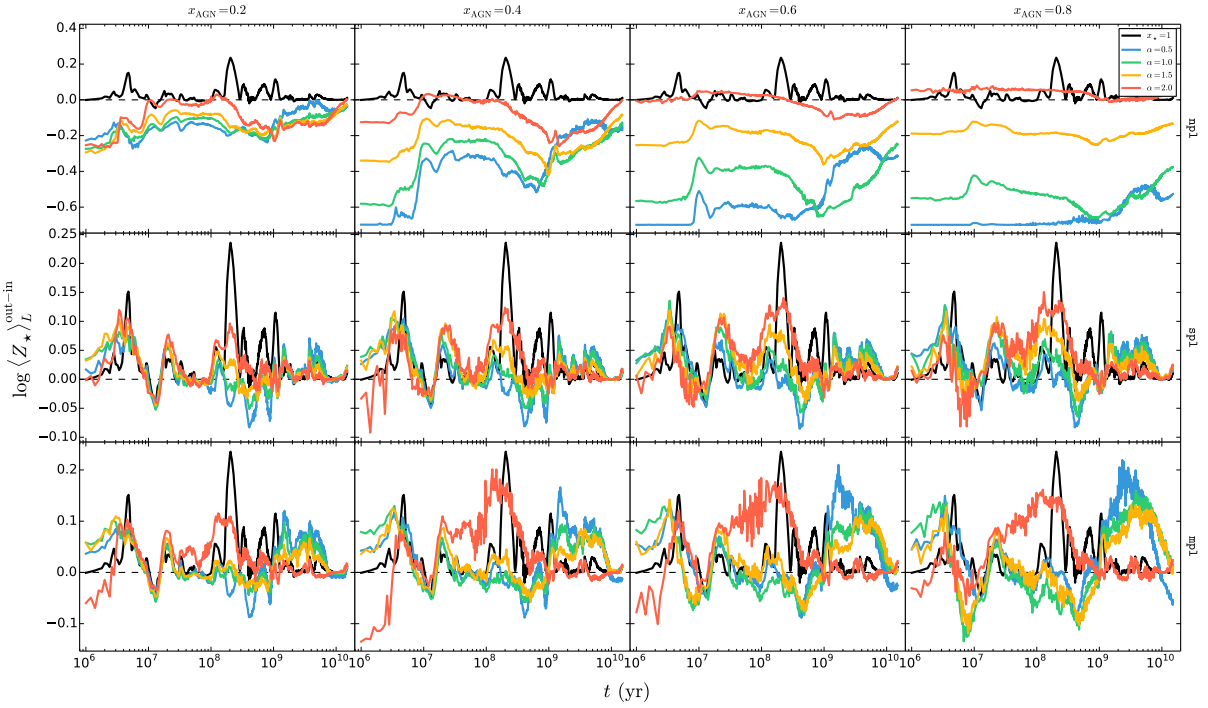

Figure 3.2.8: Difference in the light-weighted mean stellar age $\log\langle Z_\star\rangle_L$ between STARLIGHT (out) and REBETIKO (in) values as a function of CSP age t for AGs with instantaneous burst SFH. Panel display and legend details are analogous to those of Figure 3.2.6.

and $t \gtrsim 3 \times 10^9$ yr, respectively, with increasing $x_{\rm AGN}$ and decreasing α. The latter trend is of particular significance because it illustrates the degeneracy between young SSPs and an AGN with a strong blue continuum.

Figure 3.2.8 shows the difference in the *light-weighted mean stellar metallicity* $\log\langle Z_\star\rangle_L$ between STARLIGHT and REBETIKO value as a function of CSP age t. Panels configuration and legend details are identical to those in Figure 3.2.6. The top row results show a systematic metallicity underestimation of up to $\sim$0.7 with decreasing t and increasing $x_{\rm AGN}$. This trend is somewhat offset by an increasing metallicity overestimation with increasing α. It is important to note that the metallicity underestimation plateau of $\sim$0.7 dex for $\alpha = 0.5$ and $x_{\rm AGN} = 0.8$ corresponds to lowest metallicity value in the adopted base library which is $Z = 0.004$. Therefore, this result has no intrinsic physical meaning since it is due to bounding limits of the base library. Figure A.2.5 in Appendix A shows similar trends for the other SFHs.

The middle row results show that the metallicity is recovered well within the typical uncertainties of $\sim$0.2 dex found for the CSPs. Moreover, metallicity uncertainties increase with α and $x_{\rm AGN}$. The bottom row results show metallicity uncertainties also within $\sim$0.2 dex which become more prominent with increasing $x_{\rm AGN}$. These are correlated with evolutionary stages for which CSP synthesis results also show considerable uncertainties. Moreover, there is a metallicity overestimation with decreasing α for $t \gtrsim 10^9$ yr that somewhat mirrors that of age underestimation seen in Figure 3.2.7.

Figure 3.2.9 shows the difference in the *mass-weighted mean stellar age* $\langle\log t_\star\rangle_M$ between STARLIGHT and REBETIKO values as a function of CSP age t. Panels configuration and legend details are identical to those in Figure 3.2.6. The top row results show a systematic age overestimation of up to $\sim$4 dex with decreasing age and increasing α. Despite being somewhat independent of $x_{\rm AGN}$, this trend is similar to that found for the mass illustrated on the top row panels of Figure 3.2.6. Results also show that mass-weighted age uncertainties are larger than those found for the light-weighted age (e.g. Torres-Papaqui *et al.* 2013). Figure A.2.4 in Appendix A shows similar trends for the other SFHs.

The middle row results show that the age can be overestimated by up to $\sim$3 dex for $t \sim 3 \times 10^6$ and $t \sim 2 \times 10^7$ yr. The later peak correlates with a mass overestimation, as illustrated on the middle row panels of Figure 3.2.6. Moreover, age uncertainties are somewhat independent of α and $x_{\rm AGN}$. The

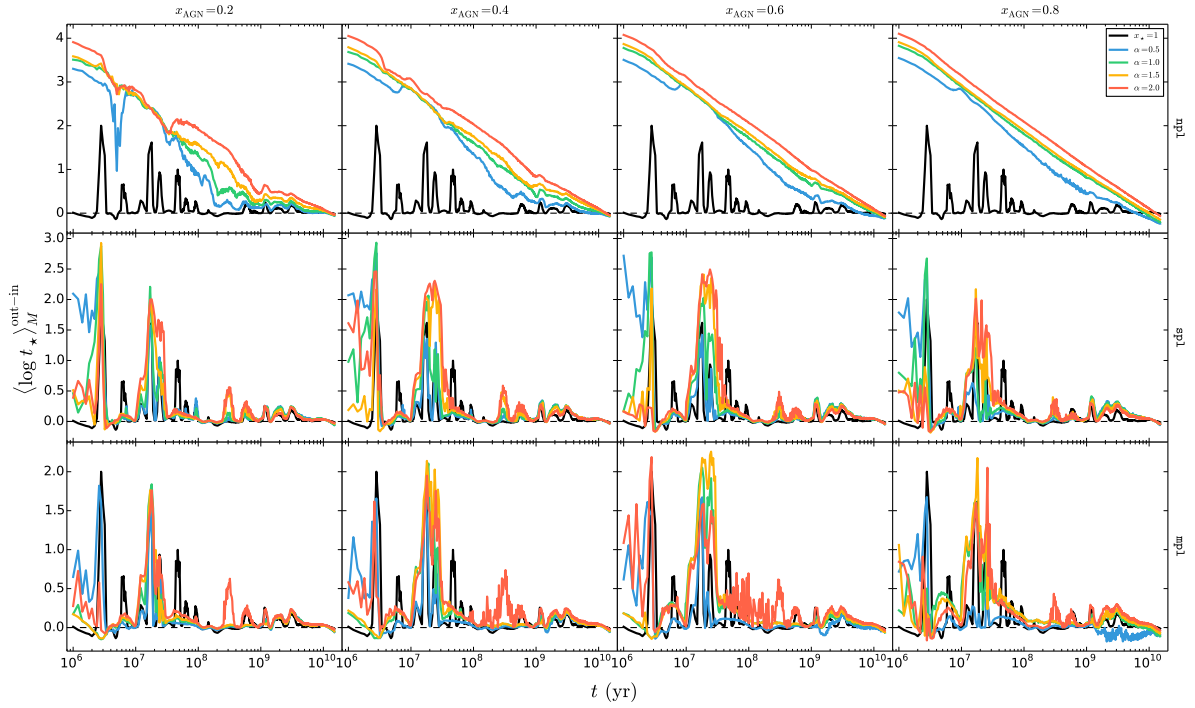

Figure 3.2.9: Difference in the mass-weighted mean stellar age $\langle \log t_\star \rangle_M$ between STARLIGHT (out) and REBETIKO (in) values as a function of CSP age t for AGs with instantaneous burst SFH. Panel display and legend details are analogous to those of Figure 3.2.6.

bottom row results show similar overall trends and uncertainties. Indeed, the age can be overestimated by up to ∼2 dex for $t \sim 3 \times 10^6$ and $t \sim 2 \times 10^7$ yr.

Figure 3.2.10 shows the difference in the *mass-weighted mean stellar metallicity* $\log\langle Z_\star \rangle_M$ between STARLIGHT and REBETIKO value as a function of CSP age t. Panels configuration and legend details are identical to those in Figure 3.2.6. The top row results show a systematic metallicity underestimation of up to ∼0.7 dex with decreasing age and increasing $x_{\rm AGN}$. This underestimation reaches a plateau at ∼0.7 dex for $\alpha = 0.5$ and $x_{\rm AGN} = 0.8$, as in Figure 3.2.8. Moreover, mass-weighted metallicity uncertainties are consistently larger that light-weighted uncertainties, similarly to the results found for the mean stellar age. Figure A.2.5 in Appendix A shows similar trends for the other SFHs.

The middle row results show metallicity uncertainties within ∼0.4 dex. Moreover, metallicity is systematically underestimated by up to ∼0.4 for $t \lesssim 10^7$ yr with decreasing α. The bottom row results show similar trends and uncertainties. However, results also show a metallicity overestimation feature for $t \gtrsim 10^9$ yr which increases with $x_{\rm AGN}$ and with decreasing α, somewhat mirroring along the x-axis the age underestimation seen in Figure 3.2.9.

Finally, Figure 3.2.11 shows the difference in the AGN *fractional contribution* $x_{\rm AGN}$ between STARLIGHT and REBETIKO values as a function of CSP age t. Results for `spl` and `mpl` are represented on the *top* and *bottom row panels*, respectively. The $x_{\rm AGN}$ in the `mpl` modelling configuration is the sum the light-fractions of each of the 4 PLs in the base library. Legend details are identical to those in Figure 3.2.6. The top row results show a systematic $x_{\rm AGN}$ underestimation of up to ∼0.06 with increasing α and decreasing $x_{\rm AGN}$. Meanwhile, the bottom row results show that the $x_{\rm AGN}$ is systematic over and underestimated for $t \lesssim 10^8$ and $t \gtrsim 10^9$ yr, respectively. These trends become more accentuated with decreasing α and increasing $x_{\rm AGN}$. Moreover, $x_{\rm AGN}$ is strongly underestimated for $t \gtrsim 10^9$ yr and $\alpha = 0.5$ and $x_{\rm AGN} = 0.8$, which is likely due to the degeneracy between young and blue SSPs and the AGN blue continuum for $\alpha = 0.5$. This helps explaining the mass and age underestimation bumps and metallicity overestimation bump for these evolutionary stages seen on the bottom rows of Figures 3.2.6–3.2.10.

Figures A.2.6–A.2.11 in Appendix A show synthesis results for a continuous SFH. Results show trends roughly similar to those found for an instantaneous burst SFH, although with considerable smaller

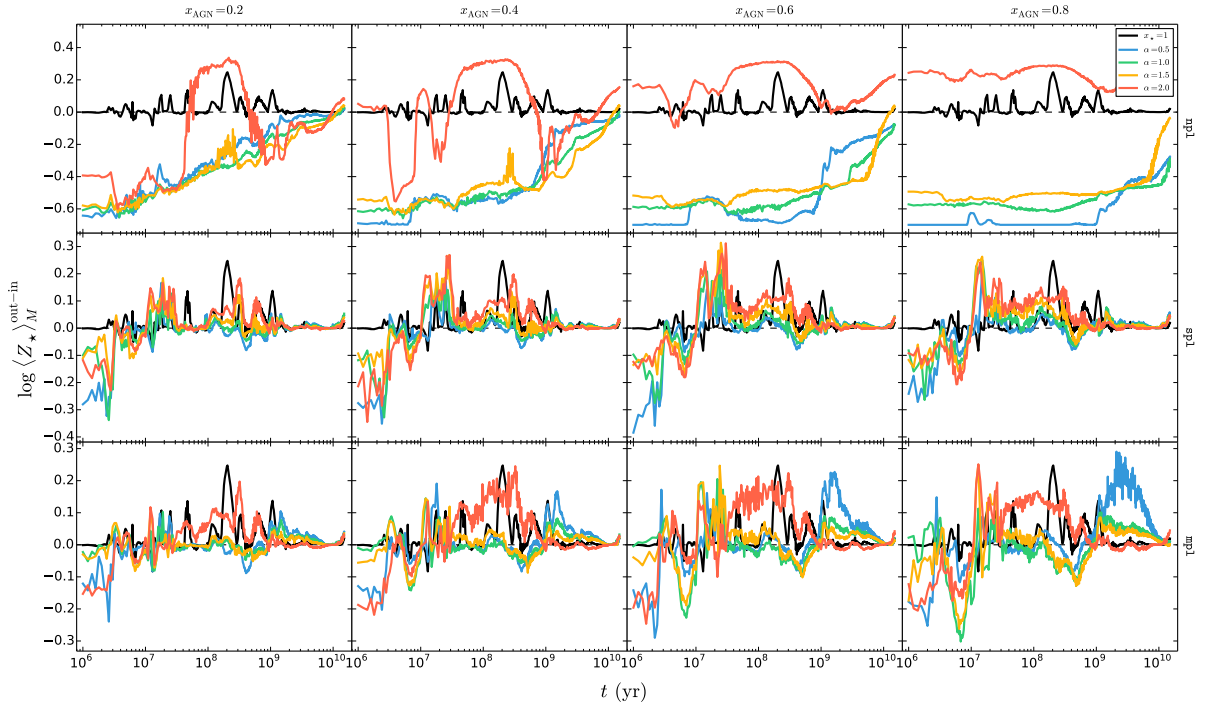

Figure 3.2.10: Difference in the mass-weighted mean stellar age $\log\langle Z_\star\rangle_M$ between STARLIGHT (out) and REBETIKO (in) values as a function of CSP age t for AGs with instantaneous burst SFH. Panel display and legend details are analogous to those of Figure 3.2.6.

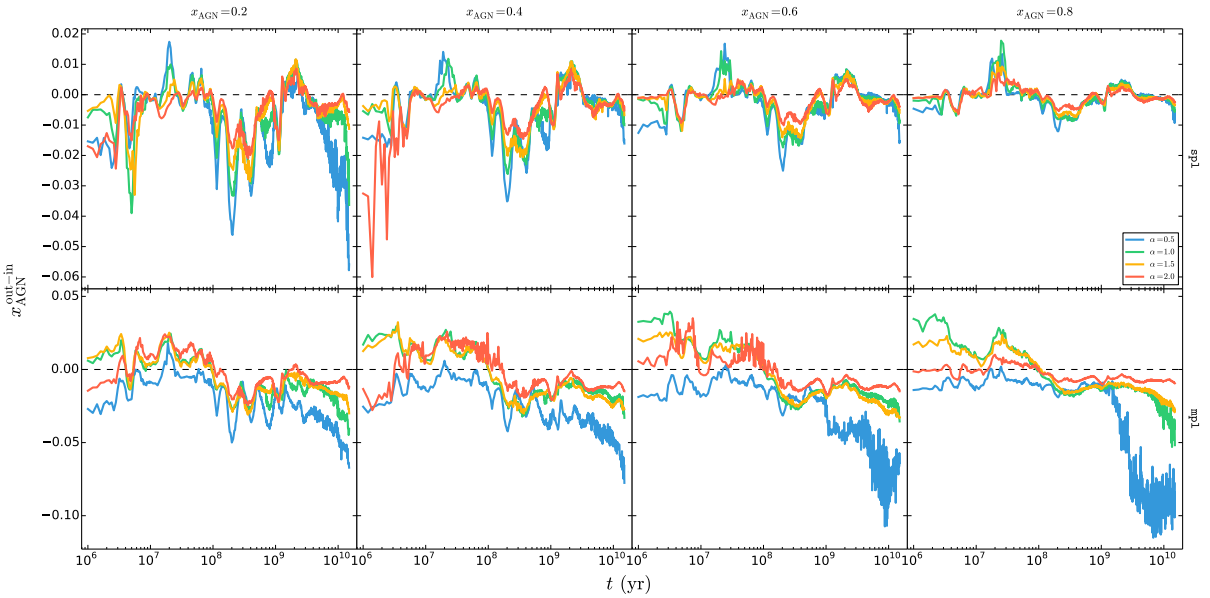

Figure 3.2.11: Difference in the AGN fractional contribution $x_{\rm AGN}$ between STARLIGHT (out) and REBETIKO (in) values as a function of CSP age t for AGs with instantaneous burst SFH. Top and bottom rows display results for `spl` and `mpl`, respectively. Left- to right-hand side panels represent increasing $x_{\rm AGN}$ from 0.2 to 0.8 in steps of 0.2. Legend details are analogous to those of Figure 3.2.6.

uncertainties in all physical properties. Overall, these results show that the biases on stellar properties correlate on first order with $x_{\rm AGN}$ and on second order with α. This is mainly due to the combined

effect of the dilution of stellar absorption features by the AGN continuum and degeneracies between the continua of the AGN and the young SSPs, respectively. Moreover, results show that the estimated total stellar mass, mean age and mean metallicity with the PSS code STARLIGHT show uncertainties of up to ∼2, 4 and 0.7 dex, respectively, at the AGN detection threshold $x_{\rm AGN}^{\rm threshold} \simeq 0.26$ when applying a purely-stellar modelling approach. In addition, uncertainties within ∼0.8, 2.5 and 0.3 dex for the same stellar population properties are found even when including in the base library a single of multiple AGN continua. Therefore, it can be concluded that the adopted state-of-the-art PSS code cannot robustly discriminate between AGN PL and stellar spectral components, at the expense of considerable biases on the stellar properties of the galaxy.

4

Nebular emission models

Synthetic spectra with NE were created by conducting photoionisation simulations using the CSP and AG evolutionary models described on previous chapters. These models aim to a realistic description and PSS modelling of galaxy spectra that consistently include NE excited by a mixture of stellar and AGN radiation. This set of synthetic spectra was used to investigate the impact of NE on the estimation of stellar population properties with PSS. Synthesis results show that the estimated stellar properties can be affected by significant biases that may limit the understanding of the role of AGN feedback and NE on the evolutionary history of galaxies.

This chapter is organised as follows. Section 4.1 details how NE was added to the CSP and AG synthetic spectra using a photoionisation code. Subsection 4.1.1 starts by describing the main physical ingredients in a NLR adopted as an illustrative photoionisation simulation. Subsection 4.1.2 then presents simulations assuming typical gas physical conditions in HIIRs and NLRs in order to incorporate NE into the CSP and AG synthetic spectra, respectively. Section 4.2 describes the methodology and results after applying PSS to these synthetic spectra and investigates the impact of NE to the estimated stellar properties. On the one hand, Subsection 4.2.1 focus on NE only due to the ionising starlight of a CSP. On the other hand, Subsection 4.2.2 investigates the NE arising from the combined ionising radiation from a CSP and an AGN and the combined impact of AGN and NE on the estimated stellar properties. Section 4.3 presents a brief conceptional overview of the PSS code FADO and its application to synthetic star-forming galaxies created with REBETIKO. A comparison of the synthesis results between STARLIGHT and FADO illustrates the importance of accounting for the nebular continuum with the latter for an improved determination of the SFH of these galaxies.

4.1 Synthetic spectra of galaxies with nebular emission

The emission of astrophysical plasmas (e.g. planetary nebulae, HIIRs, NLRs, BLRs) can be interpreted with the help of photoionisation codes (e.g. Sutherland & Dopita 1993; Gruenwald *et al.* 1997 Ferland *et al.* 1998). The main ingredients of state-of-the-art photoionisation codes usually are the physical properties of a radiation field and a gaseous cloud, for which the ionisation and thermal equilibrium equations are solved while taking into account processes such as photoionisation, recombination, free-free radiation and collisional excitation. For example, CLOUDY (Ferland *et al.* 1998) considers the shape and brightness of the radiation field illuminating the cloud, the total H density and various details of the chemical composition of the gas (e.g. abundances, dust grains), some parameters describing the geometry of the environment (e.g. thickness of the cloud, distance between cloud and radiative source) and computes, among other things, a detailed predicted spectrum. A subsequent comparison between simulations and observations helps to constrain the gas excitation mechanisms and other physical characteristics of the emitting source (e.g. electron density and temperature, ionisation parameter).

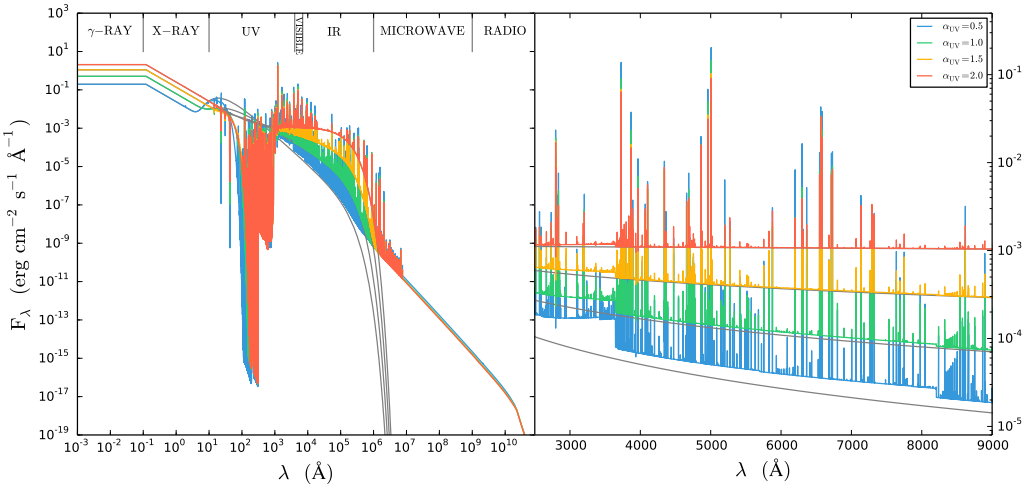

Figure 4.1.1: SEDs NLR photoionisation simulations computed with the CLOUDY assuming an AGN radiation field as defined in Equation 4.1 and the following physical conditions: open plane-parallel geometry; solar composition gas; no dust; constant H density of $n_{\rm H} = 10^3$ cm^{-3}; ionisation parameter of $\log U = -3$; $T_{\rm BB} = 5 \times 10^6$ K; $kT_{\rm IR} = 0.01$ Ryd; $\alpha_{\rm X} = 1$; $\alpha_{\rm OX} = 1.4$, and case B recombination. Blue, yellow, green and red lines represent $\alpha_{\rm UV} = 0.5, 1, 1.5, 2$ and the grey lines represent the underlying incident radiation fields.

4.1.1 Illustrative photoionisation simulation of a NLR

Valuable insight on photoionisation modelling can be gathered considering as an illustrative case a NLR simulation computed with CLOUDY (version C13.03, last described in Ferland *et al.* 2013). For this purpose, it was considered an AGN incident radiation field embedded in the code which is defined as,

$$F_\nu = \nu^{-\alpha_{\rm UV}} e^{-\frac{h\nu}{kT_{\rm BB}}} e^{-\frac{kT_{\rm IR}}{h\nu}} + A\nu^{-\alpha_{\rm X}}, \tag{4.1}$$

where $T_{\rm BB}$ is the cut-off temperature of the blue bump, $T_{\rm IR}$ is the infrared cut-off temperature, $\alpha_{\rm UV}$ and $\alpha_{\rm X}$ are the power-law indices in the UV and in the X-ray wavelength ranges, respectively, and the coefficient A is adjusted to produce the correct value of the X-ray to UV ratio $\alpha_{\rm OX}$. The hardness of this field can be parameterised by the ionisation parameter U as,

$$U = \frac{1}{4\pi c n_{\rm H} r^2} \int_{\nu_0}^{\infty} \frac{L_\nu}{h\nu} {\rm d}\nu = \frac{Q({\rm H})}{4\pi c n_{\rm H} r^2} \quad , \tag{4.2}$$

where c is the speed of light, r is the distance between the radiative source and the illuminated face of the cloud, L_ν is the luminosity at frequency ν, h is the Planck constant, and Q(H) is the number of H-ionising photons. Therefore, the variable U represents in a single parameter the amount of ionising photons reaching the illuminated face of cloud per unit area. Regarding the spacial distribution, two main geometries can be adopted in CLOUDY: closed (spheric-symmetric) or open (plane-parallel). The former is applicable to planetary nebula simulations, whereas the latter is more adequate in NLR simulations, given that the ionising source is far from the illuminated face of the cloud (e.g. Stasińska 1984b; Martín-Manjón *et al.* 2010; Groves, Dopita & Sutherland 2004).

NLR models were computed assuming an open geometry, where plane-parallel slabs are perpendicular to the incident radiation field, as well as typical NLR physical conditions: a constant H density of $n_{\rm H} = 10^3$ cm^{-3} (e.g. Ferland & Netzer 1983; Groves, Dopita & Sutherland 2004; Osterbrock & Ferland 2006; Stasińska *et al.* 2006; Kewley *et al.* 2006) and an ionisation parameter of $\log U = -3$ (e.g. Ferland & Netzer 1983; Stasińska 1984a,b; Bergvall, Johansson & Olofsson 1986;VO1987; Kewley *et al.* 2006; Stasińska *et al.* 2006). The incident radiation field follows the AGN radiation field defined in Equation 4.1 assuming the following parameter values: $T_{\rm BB} = 5 \times 10^6$ K (Bregman 1990; Meléndez *et al.* 2011; Roos *et al.* 2015); $kT_{\rm IR} = 0.01$ Ryd, so that the cutoff is located at 10 μm; $\alpha_{\rm X} = 1$ (Mathews & Ferland 1987); $\alpha_{\rm UV} = 0.5, 1, 1.5, 2$ (following the values adopted in Section 3.1), and $\alpha_{\rm OX} = 1.4$ (Zamorani *et al.* 1981).

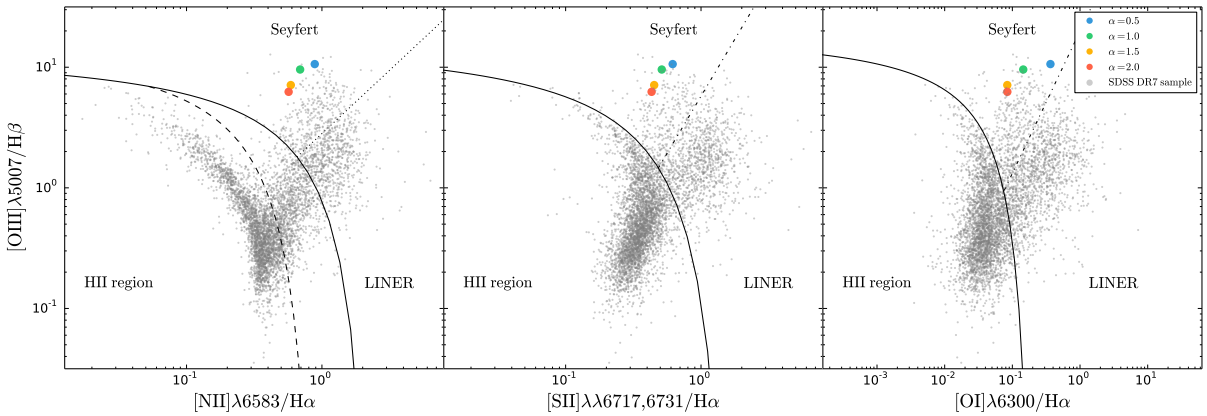

Figure 4.1.2: Emission-line flux ratios [NII]λ6583/Hα (left-hand side panel), [SII]$\lambda\lambda$6717,6731/Hα (central panel) and [OI]λ6300/Hα (right-hand side panel) as a function of [OIII]λ5007/Hβ for the spectra represented in Figure 4.1.1. Blue, green, yellow and red circles represent $\alpha_{\rm UV} = 0.5$, 1, 1.5 and 2, respectively. Full, dashed, dot-dashed and dotted black lines represent the demarcation lines proposed by Kewley *et al.* (2001), Kauffmann *et al.* (2003c), Kewley *et al.* (2006) and Schawinski *et al.* (2007), respectively. Grey points represent a sample of 5000 galaxies randomly selected from the SDSS DR 7 (Abazajian *et al.* 2009).

No dust obscuration was considered in this simulation in order to simplify the modelling and analysis of gas emission characteristics. Moreover, simulations assume that the gas has solar chemical abundances (Grevesse & Sauval 1998) and case B recombination (Zanstra 1961).

Figure 4.1.1 shows NLR emitted spectra over the whole electromagnetic spectral (*left-hand side panel*) and optical ranges (*right-hand side panel*) as a function of wavelength λ in Å. Incident spectra are represented as *grey lines* and emitted spectra for $\alpha_{\rm UV} = 0.5, 1, 1.5$ and 2 are represented as *blue*, *green*, *yellow* and *red* lines, respectively. Results on the right-hand side panel show that the relative strength of the nebular continuum and line emission increases with decreasing $\alpha_{\rm UV}$ in the optical. This follows from the increasing number of ionising photons Q(H) as the UV continuum becomes steeper with decreasing $\alpha_{\rm UV}$.

The physical conditions of astrophysical plasmas can be constrained by comparing the results of simulations with observables such emission-line ratios involving optical emission lines (e.g. BPT1981; VO1987). The main ionisation mechanism responsible for the observed emission-line strengths can then be categorised with aid of different theoretical and empirical demarcation lines separating the different regions in the diagrams. Some of the most widely used demarcation lines in the traditional BPT1981 and VO1987 diagnostic diagrams are those proposed by Kewley *et al.* (2001, 2006), Kauffmann *et al.* (2003c) and Schawinski *et al.* (2007). Kewley *et al.* (2001) proposed the following *theoretical demarcation lines* to isolate star-forming galaxies located on the left-hand side and bottom corner of the BPT1981 and VO1987,

$$\log\left(\frac{[\mathrm{OII}]\lambda5007}{\mathrm{H}\beta}\right) = \frac{0.61}{\log([\mathrm{NII}]\lambda6583/\mathrm{H}\alpha) - 0.47} + 0.19, \tag{4.3}$$

$$\log\left(\frac{[\mathrm{OII}]\lambda5007}{\mathrm{H}\beta}\right) = \frac{0.72}{\log([\mathrm{SII}]\lambda\lambda6717,6731/\mathrm{H}\alpha) - 0.32} + 1.30, \tag{4.4}$$

$$\log\left(\frac{[\mathrm{OII}]\lambda5007}{\mathrm{H}\beta}\right) = \frac{0.73}{\log([\mathrm{OI}]\lambda6300/\mathrm{H}\alpha) + 0.59} + 1.33. \tag{4.5}$$

In turn, Kauffmann *et al.* (2003c) proposed an *empirical line* to isolate star-forming galaxies in the BPT1981 diagram using SDSS DR 1 galaxies (Abazajian *et al.* 2003) defined as,

$$\log\left(\frac{[\mathrm{OII}]\lambda5007}{\mathrm{H}\beta}\right) = \frac{0.61}{\log([\mathrm{NII}]\lambda6583/\mathrm{H}\alpha) - 0.05} + 0.13. \tag{4.6}$$

The objects in the region between Equations 4.3 and 4.6 are usually referred to as *composite* or

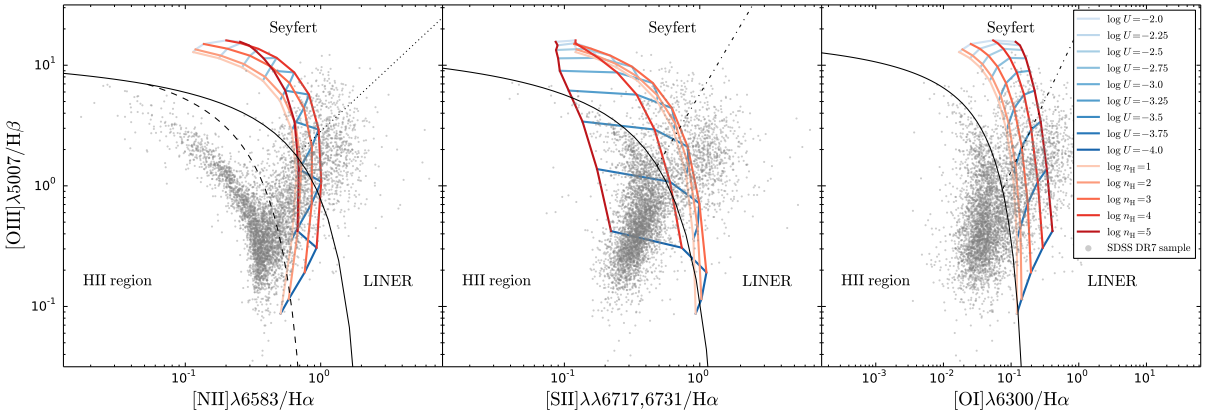

Figure 4.1.3: Emission-line flux ratios [NII]λ6583/Hα (left-hand side panel), [SII]$\lambda\lambda$6717,6731/Hα (central panel) and [OI]λ6300/Hα (right-hand side panel) as a function of [OIII]λ5007/Hβ for $\alpha_{\rm UV} = 1.5$ and physical conditions identical to those adopted in Figure 4.1.2. Light to dark blue lines represent ionisation parameter variations of $\log U = -2.00$, -2.25, -2.50, -2.75, -3.00, -3.25, -3.50, -3.75 and -4.00 and light to dark red lines represent H density variations of $\log n_{\rm H} = 1$, 2, 3, 4 and 5 cm^{-3}. Remaining legend details are identical to those in Figure 4.1.2.

transient galaxies, as it is thought that the emission of these objects can be due to ionising radiation from, among others, young stars, AGN and/or post-main sequence stars (e.g. post-AGB stars, white dwarfs). Later, Kewley *et al.* (2006) presented *empirical lines* to segregate Seyfert and LINERs in the right-hand side and top corner of the VO1987 diagrams with SDSS DR 4 galaxies (Adelman-McCarthy *et al.* 2006) that are defined as,

$$\log\left(\frac{[\text{OII}]\lambda5007}{\text{H}\beta}\right) = 1.89 \times \log(\text{SII}]\lambda\lambda6717,6731/\text{H}\alpha) + 0.76, \tag{4.7}$$

$$\log\left(\frac{[\text{OII}]\lambda5007}{\text{H}\beta}\right) = 1.18 \times \log(\text{OI}]\lambda6300/\text{H}\alpha) + 1.30. \tag{4.8}$$

Moreover, Schawinski *et al.* (2007) proposed an analogous *empirical line* to separate Seyfert and LINERs in the BPT1981 diagram also using SDSS DR 4 galaxies,

$$\log\left(\frac{[\text{OII}]\lambda5007}{\text{H}\beta}\right) = 1.05 \times \log(\text{NII}]\lambda6583/\text{H}\alpha) + 0.45. \tag{4.9}$$

Figure 4.1.2 shows the emission-line flux ratios [NII]λ6584/Hα (*left-hand side panel*), [SII]$\lambda\lambda$6717,6731 /Hα (*central panel*) and [OI]λ6300/Hα (*right-hand side panel*) as a function of [OIII]λ5007/Hβ for the spectra illustrated in Figure 4.1.1. The Kewley *et al.* (2001), Kauffmann *et al.* (2003c), Kewley *et al.* (2006) and Schawinski *et al.* (2007) are represented by the *full*, *dashed*, *dot-dashed* and *dotted black lines*, respectively. The emission-line ratio distribution of a sample of randomly selected 5000 galaxies from the SDSS DR 7 (Abazajian *et al.* 2009) is represented as *grey points*. This figure shows that the spectra presented in Figure 4.1.1 fall in the Seyfert locus and that the emission-line ratios of these models roughly increase with decreasing $\alpha_{\rm UV}$ (e.g. Stasińska 1984a,b; Groves *et al.* 2004).

More insight can be gain by analysing the impact of variations on fundamental parameters such as $n_{\rm H}$ or U on the predicted emission-line ratios. Figure 4.1.3 shows emission-line ratios for $\log U = -2.00$, -2.25, -2.50, -2.75, -3.00, -3.25, -3.50, -3.75 and -4.00 (*blue lines*) and $\log n_{\rm H} = 1$, 2, 3, 4 and 5 cm^{-3} (*red lines*) for $\alpha_{\rm UV} = 1.5$, with the remaining physical conditions and legend details being identical to those adopted in the models of Figure 4.1.2. The results show that the emission-line ratios roughly increase with $n_{\rm H}$ and that variations in Seyfert and LINER loci are well mapped by $\log U \gtrsim -3$ and $\log U \lesssim -3$, respectively (e.g. Ferland & Netzer 1983; Kraemer & Crenshaw 2000; Kewley *et al.* 2006). The drawback of using U as a variable in these simulations it is also its main appeal, in that in a single parameter is incorporated the hardness of the radiation field, H density of the gas and distance between the radiative source and

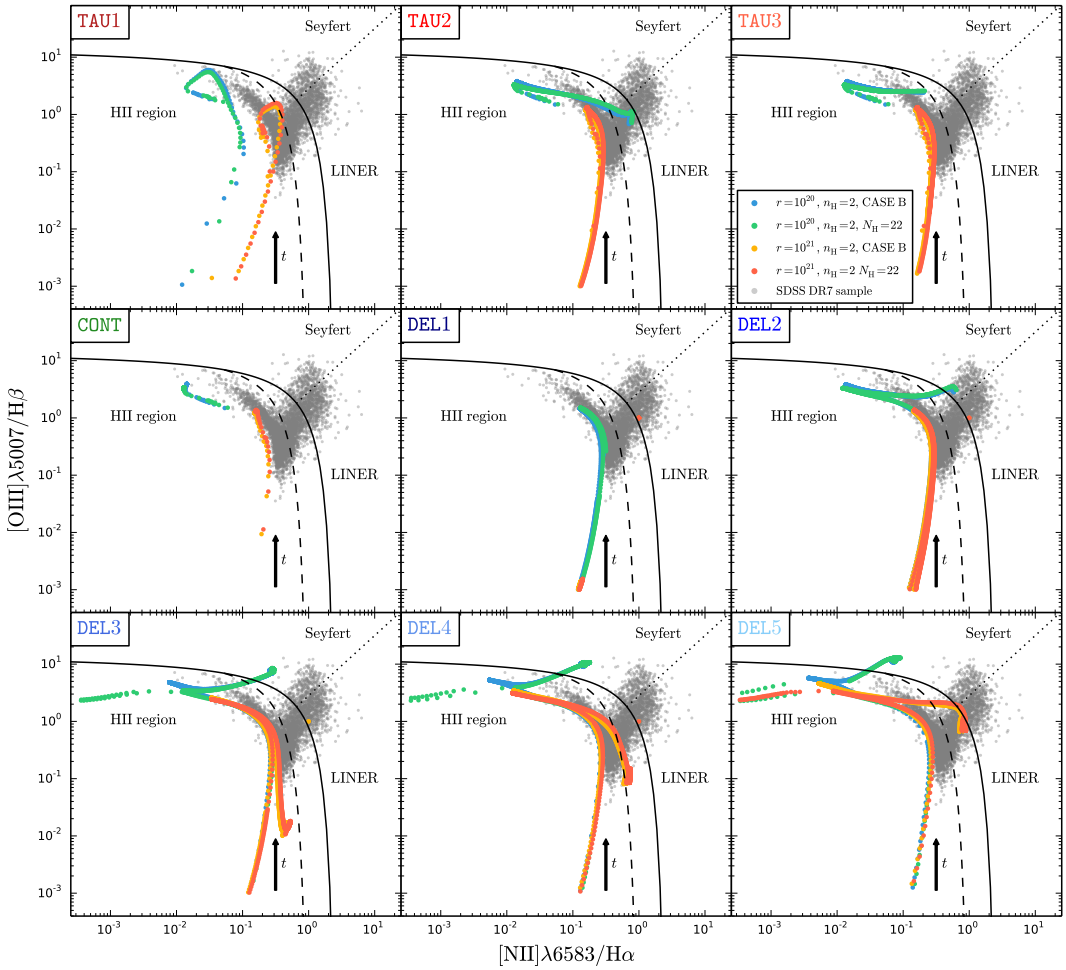

Figure 4.1.4: Emission-line flux ratio [NII]λ6583/Hα as a function of [OIII]λ5007/Hβ of CSP simulations computed with CLOUDY. Panels from left- to right-hand side and top to bottom represent the exponentially declining, continuous and delayed SFHs displayed in Figure 2.1.1. Blue, green, yellow and red points represent simulations with $n_{\rm H} = 10^2$ cm^{-2} and $r = 10^{20}$ cm and case B recombination, $r = 10^{20}$ cm and $N_{\rm H} = 10^{22}$ cm^{-2}, $r = 10^{21}$ cm and case B recombination, $r = 10^{21}$ cm and $N_{\rm H} = 10^{22}$ cm^{-2}, respectively. Remaining legend details are identical to those in Figure 4.1.2.

the cloud. More realistic photoionisation simulations usually treat these as free parameters and fine-tune them to match the observations, even at the risk of such approach being arbitrarily complex.

4.1.2 Synthetic spectra of CSPs and AGs with nebular emission

Several studies have shown that NE significantly contributes to optical photometric passbands (e.g. Krüger, Fritze-v. Alvensleben & Loose 1995; Papaderos *et al.* 1998; Anders & Fritze-v. Alvensleben 2003; Zackrisson *et al.* 2008; Papaderos & Östlin 2012; Pacifici *et al.* 2015). With this in mind, a library of synthetic spectra with NE was computed with CLOUDY to study the impact of NE on the estimated stellar population properties using full-spectrum purely-stellar PSS. The NE is calculated considering as input radiation fields the CSP and AG spectra presented in Sections 2.2 and 3.1, respectively, and assuming typical physical conditions observed in HIIRs and NLRs, respectively. The number of ionising photons for each input spectrum is computed by CLOUDY considering the radiation in the range $91 \leq \lambda \leq 911.76$ Å, with 91 Å corresponding to the lower limit in the BC2003 SSP evolutionary models. The PSS analysis of CSPs with NE was made in order to evaluate the impact of NE in the estimated properties of star-forming galaxies when adopting a purely-stellar base library (e.g. Asari *et al.* 2007). Moreover, the analysis of

AGs with NE aims to investigate potential biases on the estimated stellar properties of Seyfert galaxies with circumnuclear star-formation. In the following is discussed typical physical conditions of HIIRs and NLRs adopted to produce synthetic spectra with physically motivated emission-line ratios. The traditional optical diagnostic diagrams were then employed to evaluate the validity of the assumed physical conditions.

Various studies indicate that a H density of $n_{\rm H} = 10$ cm^{-3} adequately represents small-to-medium isolated HIIRs (e.g. Veilleux & Osterbrock 1987; Castellanos *et al.* 2002), $n_{\rm H} = 10^2$ cm^{-3} describes HII galaxies (e.g. Hägele *et al.* 2008; Stasińska *et al.* 2006) and large circumnuclear HIIRs (e.g. García-Vargas *et al.* 1997) and that $n_{\rm H} = 10^3$ cm^{-3} is commonly associated to NLRs (e.g. Ferland & Netzer 1983; Groves, Dopita & Sutherland 2004; Osterbrock & Ferland 2006; Stasińska *et al.* 2006; Kewley *et al.* 2006). Taking these results into consideration, it was assumed constant H densities of $n_{\rm H} = 10^2$ cm $^{-3}$ and 10^3 cm^{-3} for the HIIR and NLR simulations, respectively. Moreover, although a spherical geometry might be physical meaningful in simulations of stellar clusters, such a geometry does not seem appropriate for a simulation of a galaxy as a whole. Indeed, a more realistic approach is to consider a gaseous layer located between the ionising source and the observer. Therefore, simulations were made assuming open plane-parallel geometry (e.g. Stasińska 1984b; Martín-Manjón *et al.* 2010; Groves, Dopita & Sutherland 2004). The clouds are additionally assumed to have solar abundances (Grevesse & Sauval 1998). It is important to note that the solar metallicity of $Z_{\odot} = 0.017$ in Grevesse & Sauval (1998) differs from that of $Z_{\odot} = 0.02$ in BC2003. However, it can be considered as a reasonable first-order approximation that the stellar populations and the gas have similar chemical compositions (Martín-Manjón *et al.* 2010). Dust was not included in these models to assure that the subsequent PSS analysis is focused on the gas emission as the only additional spectral component.

Garcia-Vargas *et al.* (1995) conducted HIIR simulations with ageing stellar clusters with a fixed distance $r = 10^{20.84}$ cm between the cluster and the cloud. Moreover, Bennert *et al.* (2006) studied the properties of the NLR in the Seyfert 2 NGC 1386 with photoionisation models computed with CLOUDY and considered $r = 50$, 100 and 250 pc ($\sim$1.5, 3.1 and 7.7×10^{20} cm) while investigating variations of different physical quantities (e.g. ionisation parameter, metal abundances, density). Both studies showed that these distances can adequately reproduce observed emission-line ratios in HIIRs and NLRs, respectively. Following these results, in this work it was considered fixed distances between the radiation sources and the inner face of the cloud of $r = 10^{20}$ or 10^{21} cm ($\sim$32.4 and 324 pc) for both HIIR and NLR simulations. Moreover, simulations were performed assuming case B recombination or a H column density $N_{\rm H} = 10^{22}$ cm^{-2}, based on Seyfert 2 observations (e.g. Kraemer & Crenshaw 2000; Alonso-Herrero *et al.* 2006; Corral *et al.* 2011; Meléndez *et al.* 2014). These different configurations were adopted to enable a comparison between the predicted emission-line ratios based on theoretical- and empirical-founded assumptions and to evaluate the impact of the distance on the strength of the predicted emission-lines.

Figure 4.1.4 shows results for CSP simulations on the BPT1981 diagram. Panels from *left-* to *right-hand side* and *top* to *bottom* display results for CSPs with exponentially declining, continuous and delayed SFHs labeled according to nomenclature introduced in Figure 2.1.1. Moreover, simulations with $r = 10^{20}$ cm and case B recombination, $r = 10^{20}$ cm and $N_{\rm H} = 10^{22}$ cm^{-2}, $r = 10^{21}$ cm and case B recombination, $r = 10^{21}$ cm and $N_{\rm H} = 10^{22}$ cm^{-2} are represented by *blue*, *green*, *yellow* and *red points*, a sequence of which can be interpreted as a *photoionisation evolutionary track*. *Black arrows* represent the direction of increasing CSP age t. The remaining legend details are identical to those in Figure 4.1.2. The results confirm that the distance between the ionising source and the illuminated face of the nebulae strongly affects the emission line fluxes, since an increasing distance between the source and the cloud leads to a stronger geometrical dilution and thus to a decrease of ionising photons per unit area reaching the nebula. Moreover, the results show that simulations with case B recombination and $N_{\rm H} = 10^{22}$ produce similar emission-line ratios. Moreover, photoionisation evolutionary tracks of delayed SFHs are capable of reaching at later evolutionary stages the regions of Seyfert (`DEL2`, `DEL3`, `DEL4` and `DEL5`) and LINERs (`DEL5`). Similar results are found for the VO1987 diagrams represented on Figures A.3.1 and A.3.2 in the Appendix A.

Figure 4.1.5 shows results of simulations of AGs in the BPT1981 diagram for $r = 10^{21}$ cm, case B recombination and continuous SFH. Results for AGs with $\alpha = 0.5$, 1, 1.5 and 2 for $x_{\rm AGN} = 0.8$ and $x_{\rm AGN} = 0.8$, 0.6, 0.4 and 0.2 for $\alpha = 0.5$ are represented as *blue*, *green*, *yellow* and *red lines* on the *left-* and *right-hand side* panels, respectively. The remaining legend details are identical to those in Figure 4.1.2. It is apparent from both diagrams that the CSP age t roughly increases from the bottom-middle to the top-left-hand side, as in Figure 4.1.4. The photoionisation evolutionary tracks traverse with increasing t

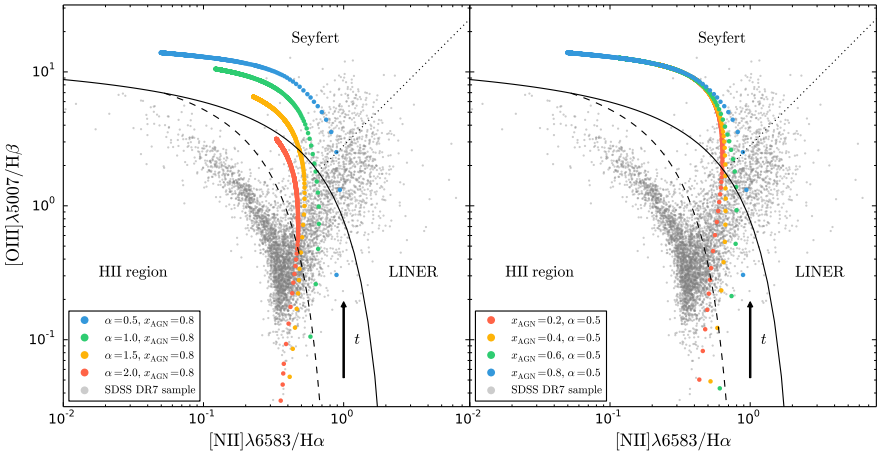

Figure 4.1.5: Emission-line flux ratio [NII]λ6583/Hα as a function of [OIII]λ5007/Hβ of a AG simulations with continuous SFH computed with CLOUDY. Blue, green, yellow and red points represent $\alpha = 0.5$, 1, 1.5 and 2 for $x_{\rm AGN}$ on the left-hand side panel and $x_{\rm AGN} = 0.8$, 0.6, 0.4 and 0.2 for $\alpha = 0.5$ on the *right-hand side panel*, respectively. Remaining legend details are identical to those in Figure 4.1.2.

the star-forming, composite and Seyfert regions, respectively. Interestingly, tracks for $x_{\rm AGN} = 0.6$ and 0.8 on right-hand side panel pass through the LINER regime before reaching the Seyfert region. Results also show that the emission-line ratios roughly increase with decreasing α and increasing $x_{\rm AGN}$, indicating an increasing number of ionising photons. Kewley *et al.* (2001) illustrated this fact showing that pure-starburst photoionisation models go from the bottom-right-hand-side tip of the *extreme starburst demarcation line* (Equation 4.3) towards the AGN regime. Indeed, Kewley *et al.* (2001) showed that star-forming galaxies with an AGN contributing only 20% to the optical emission would be classified as AGN-hosts in the traditional BPT1981 and VO1987 diagnostic diagrams. This was empirically corroborated by Kauffmann *et al.* (2003c) with SDSS DR 1 galaxies (Abazajian *et al.* 2003).

The simulations of CSPs and AGs with NE indicate that the resulting spectra are capable of reproducing emission-line ratios of star-forming and Seyfert galaxies, respectively. This lends empirical support to the assumptions made on the physical conditions of the HIIRs and NLRs simulations. Spectra with NE were renormalised relative to the monochromatic flux at $\lambda_0 = 995$ Å of their counterparts without NE in order to avoid stellar absorption features and NE (continuum and lines). Figure 4.1.6 shows the normalisation procedure considering the same spectra as in Figure 3.1.2. The CSP spectrum with 100 Myr , solar metallicity for an instantaneous burst SFH is represented by *black lines*. Moreover, AG spectra with variations of the PL index $\alpha = 0.5$,1, 1.5 and 2 for fixed $x_{\rm AGN} = 0.4$ and variations of the AGN fractional contribution $x_{\rm AGN} = 0.8$, 0.6, 0.4, 0.2 for fixed $\alpha = 1.5$ are represented in the *top* and *bottom panels* as *blue*, *green*, *yellow* and *red lines*, respectively. The underlying spectra without NE are represented by grey lines. This renormalisation procedure ensures that the synthesis results of the synthetic spectra of CSP and AGs with NE can be properly compared to the results obtained for their counterparts without NE presented in Sections 2.3 and 3.2, respectively.

4.2 Analysis of stellar properties with PSS

PSS was applied to this library of synthetic spectra following a modelling procedure similar to that detailed in Section 2.3. The only noteworthy difference is that the spectra with NE where fitted while masking the most prominent emission lines, which is common practice in PSS applications to spectra with clear NE (Asari *et al.* 2007). This was achieved by adopting a 3σ clipping method and masking the emission lines using the composite mask that comes with the distribution package of STARLIGHT created from the analysis of SDSS spectra. Results obtained from PSS modelling of CSPs and AGs spectra with NE are presented in Subsections 4.2.1 and 4.2.2, respectively. The analysis of the synthesis results for CSPs with NE encompass the 4 simulation configurations detailed in Subsection 4.1.2, whereas those for the AGs

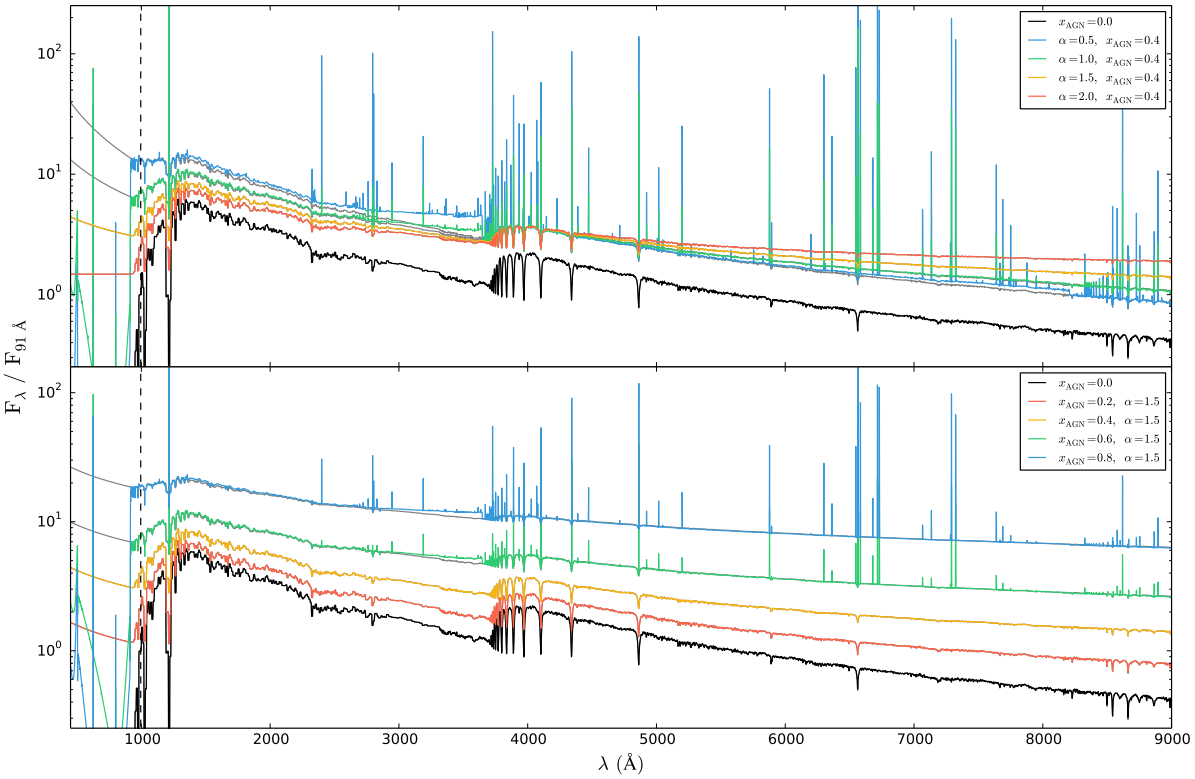

Figure 4.1.6: Renormalisation procedure of synthetic AG spectra with nebular emission (NE), a CSP with 1 Myr, solar metallicity and instantaneous burst SFH (black lines) and AGN PLs with variations on α (top panel) and $x_{\rm AGN}$ (bottom panel). Blue, green, yellow and red lines represent AGs with $\alpha = 0.5$, 1, 1.5 and 2 for $x_{\rm AGN} = 0.4$ and $x_{\rm AGN} = 0.8$, 0.6, 0.4 and 0.2 for $\alpha = 1.5$ on the top and bottom panels, respectively. Grey lines represent AGN spectra without NE and the black dashed line represent the normalisation wavelengths $\lambda_0 = 995$ Å.

with NE consider only the configuration with $r = 10^{21}$ cm and case B recombination as an illustrative case. However, similar trends and uncertainties were found for the remaining sets of simulations.

As an example of an application of STARLIGHT to an AG spectrum with NE, Figure 4.2.1 shows the average results of the 10 STARLIGHT best-fits to a AG with NE, a CSP with 1 Myr, solar metallicity and instantaneous burst SFH and an AGN PL with $\alpha = 1.5$ and $x_{\rm AGN} = 0.2$ for $r = 10^{21}$ cm and case B recombination. It can be seen that STARLIGHT accounts for the nebular continuum with significantly bluer stellar continuum than the input. The results show that the estimated total stellar mass $\log M_\star = 7.88\ M_\odot$, mean stellar age $\langle \log t_\star \rangle \simeq 7.25$ yr and mean stellar metallicity $\log\langle Z_\star \rangle \simeq -2.16$ are significantly different from their input values of $\log M_\star = 5.73\ M_\odot$, $\langle \log t_\star \rangle = 6$ yr and $\log\langle Z_\star \rangle = -1.70$. Indeed, these results show that the NE leads to a severe mass and age overestimation and metallicity underestimation. This is visually represented by the SFHs that comprise a mixture of very young ($t < 10^7$ Myr) and old SSPs ($t > 10^{10}$ Gyr) accounting for the bulk of light and stellar mass, respectively, leading to a severe age and mass overestimation. Moreover, visual inspection of the fit reveals that the fitted blue stellar continuum has stellar absorption features dimmer than in the input spectrum, which reflects the metallicity underestimation. More striking is arguably the inability of the best-fit model to reproduce the Balmer and Paschen discontinuities.

4.2.1 Dependence on the star formation history and simulation models in CSPs

Figure 4.2.2 shows the difference in the *total stellar mass* $M_\star$ between STARLIGHT (*out*) and REBETIKO (*in*) values as a function of CSP age t for all SFHs. The panel display configuration and legend details are

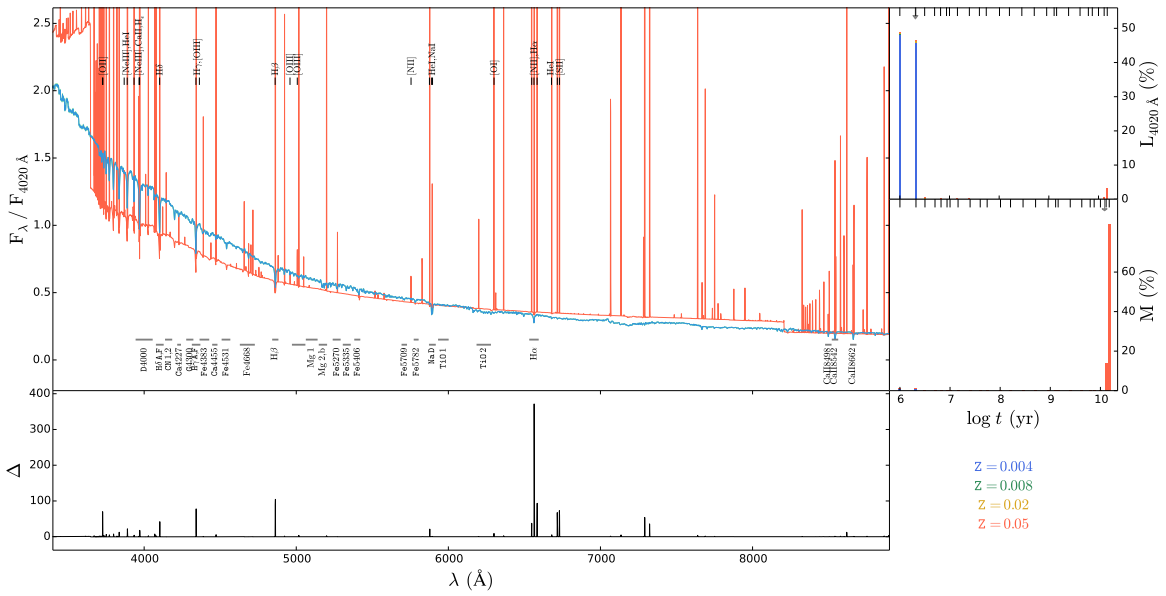

Figure 4.2.1: STARLIGHT spectral modelling results of an AG model with NE, a CSP with 1 Myr, solar metallicity and instantaneous burst SFH and an AGN PL with $\alpha = 1.5$ and $x_{\rm AGN} = 0.2$. Panel display configuration and legend details are identical to those in Figure 2.3.1.

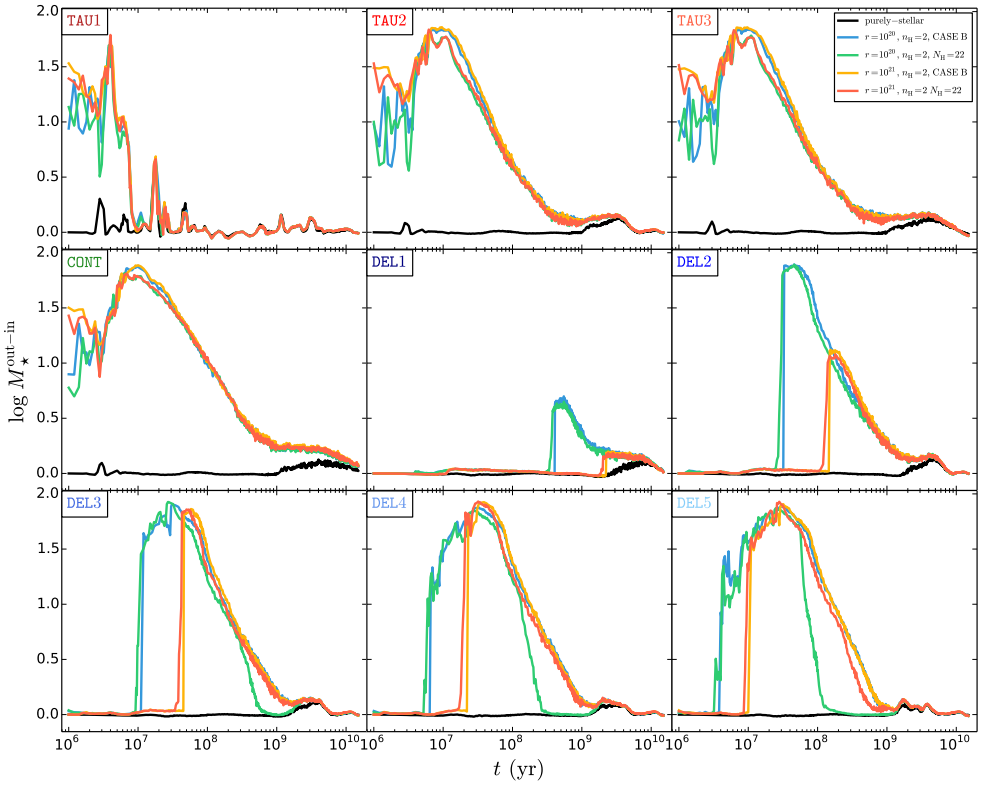

Figure 4.2.2: Difference in the total stellar mass $M_\star$ between STARLIGHT (out) and REBETIKO (in) values as a function of CSP age t. Panel display configuration and legend details are identical to that in Figure 4.1.4

identical to those in Figures 2.3.6 and 4.1.4, respectively. The results show that the stellar mass can be

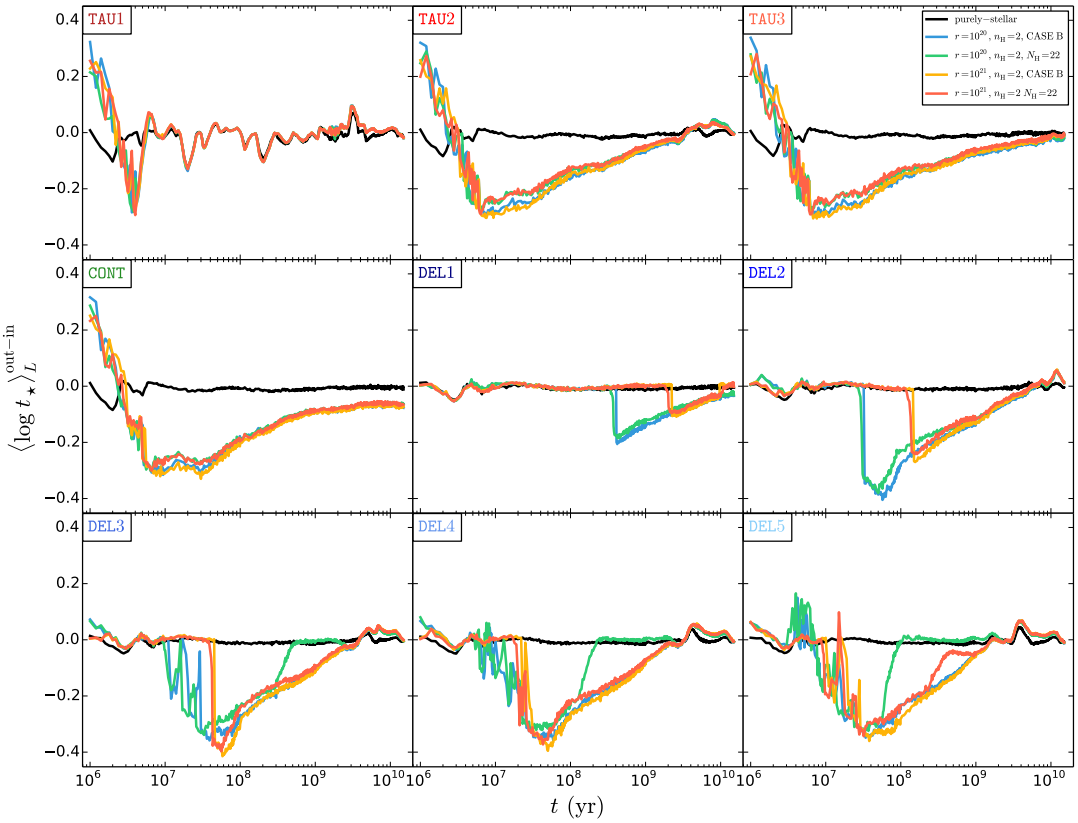

Figure 4.2.3: Difference in the light-weighted mean stellar age $\langle \log t_\star \rangle_L$ between STARLIGHT (out) and REBETIKO (in) values as a function of CSP age t. Panel display configuration and legend details are identical to those in Figure 4.1.4.

overestimated by up to ∼2 dex at $10^6 \lesssim t \lesssim 10^9$ yr, which is connected to the star-formation peaks of the different SFHs. Young stellar populations during these stages contribute with a significant amount of ionising photons that are responsible for the nebular emission illustrated in Figure 4.1.4. Overall, similar results are found for case B recombination and $N_{\rm H} = 10^{22}$ for the same distance. However, larger mass biases are found for $r = 10^{20}$ cm, a fact that can be attributed to the larger amount of ionising photons reaching the cloud, as illustrated in the emission-line rations in Figure 4.1.4. The overall low SFR values and consequently lower NE contribution in the delayed SFH `DEL1` prevent large mass biases such as those seen, for instance, for `DEL5`.

Figure 4.2.3 shows the difference in the *light-weighted mean stellar age* $\langle \log t_\star \rangle_L$ between STARLIGHT and REBETIKO values as a function of CSP age t for all SFHs. The panel display configuration and legend details are identical to those in Figure 4.2.2. The results show an overall age overestimation of up to ∼0.4 at $t \lesssim 3 \times 10^6$ yr for which the SFHs display relative high star-formation. This is due to the fact that the input CSP and nebular continua must be modelled with a mixture of young SSPs. However, this trend soon is inverted with increasing t as the underlying input stellar spectrum becomes redder, although the nebular continuum demands a significant contribution of young SSPs. This leads to a severe age underestimation by up to ∼0.4 dex for $3 \times 10^6 \lesssim t \lesssim 10^{10}$ yr. As with the mass biases, this age underestimation bump occurs at the peak of star formation for each SFH.

Figure 4.2.4 shows the difference in the *light-weighted mean stellar metallicity* $\log\langle Z_\star \rangle_L$ between STARLIGHT and REBETIKO values as a function of CSP age t for all SFHs. The panel display configuration and legend details are identical to those in Figure 4.2.2. The results show that the metallicity can be underestimated by up to ∼0.6 dex when $3 \times 10^6 \lesssim t \lesssim 10^{10}$ yr, which are evolutionary stages associated with the peak of star formation for each SFH. As shown in Figure 4.2.1, the nebular continuum leads STARLIGHT to fit SSPs with the lowest metallicities in an attempt to account for the slope of the input

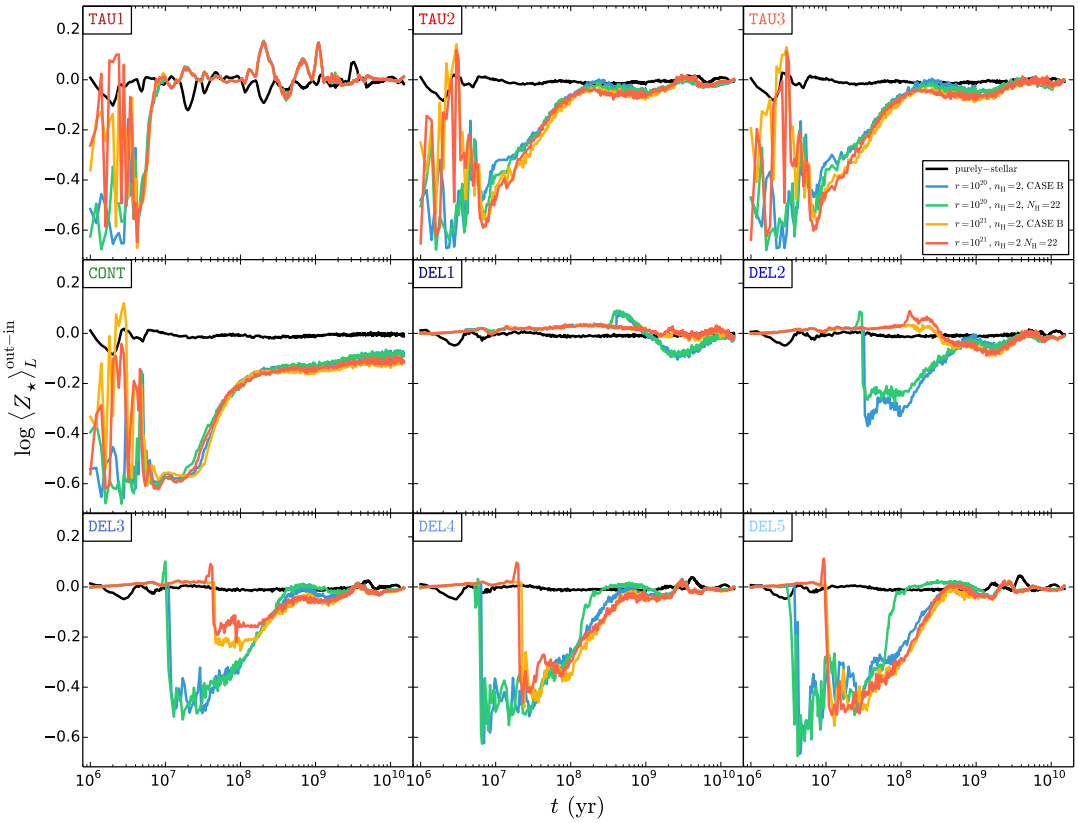

Figure 4.2.4: Difference in the light-weighted mean stellar metallicity $\log\langle Z_\star\rangle_L$ between STARLIGHT (out) and REBETIKO (in) values as a function of CSP age t. Panel display configuration and legend details are identical to those in Figure 4.1.4.

spectrum around the Balmer and Paschen jumps and its overall blue continuum, thus leading to a significant metallicity underestimation. As for the mass and age, most significant metallicity biases are observed for configurations with $r = 10^{21}$ cm.

Figure 4.2.5 shows the difference in the *mass-weighted mean stellar age* $\langle \log t_\star\rangle_M$ between STARLIGHT and REBETIKO values as a function of CSP age t for all SFHs. The panel display configuration and legend details are identical to those in Figure 4.2.2. The results show an overall systematic age overestimation of up to ∼3.5 dex with decreasing t during the evolutionary stages near the star-formation peaks of each SFH. The observed trend is similar to that found for the mass illustrated in Figure 4.2.2. It is interesting to note that this trend is also similar to the one shown on the top row panels of Figure 3.2.9, for the which the main source of bias was the AGN PL. This suggests that a PSS code such STARLIGHT is unable to distinguish between AGN PL and the nebular continuum when employing a purely-stellar modelling as adopted here, even though the differences between these spectral components is quite noticeable by eye. This fact, once again, highlights the inherent risk of adopting a purely-stellar PSS modelling approach in an automated manner to large samples of galaxies with heterogeneous spectral components.

Figure 4.2.6 shows the difference in the *mass-weighted mean stellar metallicity* $\log\langle Z_\star\rangle_M$ between STARLIGHT and REBETIKO values as a function of CSP age t for all SFHs. The panel display configuration and legend details are identical to those in Figure 4.2.2. The results show an overall metallicity overestimation of up to ∼0.4 dex during evolutionary stages associated with strong star formation activity for the each SFH. The observed metallicity overestimation is linked to a strong mass overestimations observed in Figure 4.2.2. However, the strength of the nebular continuum overturns this metallicity overestimation after the peak of star formation, since the blue input continuum can only be fitted with SSPs with the lowest-metallicity SSPs, as seen in Figure 4.2.1. Thus, the evolutionary models present a metallicity underestimation trend similar to that found in Figure 4.2.4 after the star-formation peak.

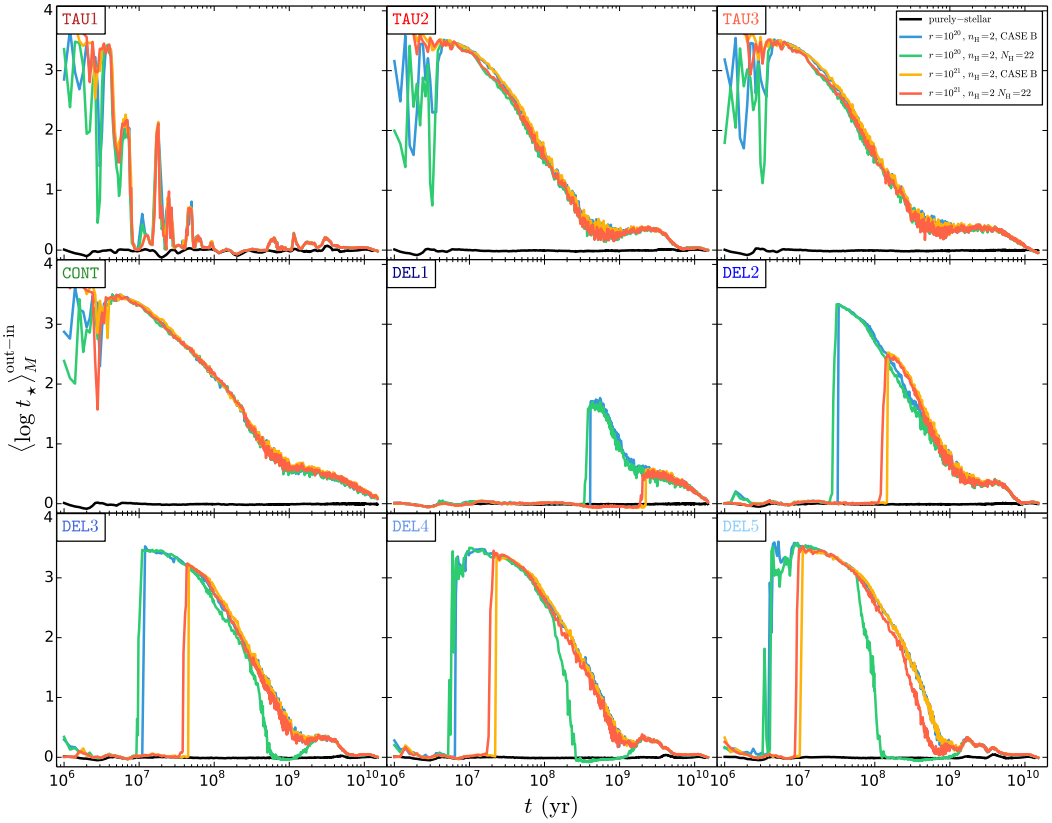

Figure 4.2.5: Difference in the mass-weighted mean stellar age $\langle \log t_\star \rangle_M$ between STARLIGHT (out) and REBETIKO (in) values as a function of CSP age t. Panel display configuration and legend details are identical to those in Figure 4.1.4.

In summary, these results show that a strong NE contribution during star-formation activity can lead to mass, age and metallicity systematic biases of up to ∼2, 4 and 0.6 dex, respectively, when employing a purely-stellar modelling PSS approach. Results also show that the nebular continuum artificially increases the total stellar mass, dilutes stellar absorption features that mimic a strongly sub-solar metallicity and either greatly rejuvenates or ages the stellar content of a galaxy when the age is either weighted by light or mass, respectively.

4.2.2 Dependence on the star formation history in AGs

Figure 4.2.7 shows the difference in the *total stellar* $M_\star$ between STARLIGHT and REBETIKO values as a function of CSP age t for an instantaneous burst (*top row*) and continuous SFHs (*bottom row*). Moreover, results with increasing AGN fraction fraction $x_{\rm AGN}$ are displayed from *left-* to *right-hand side panels* going from $x_{\rm AGN} = 0.2$ to 0.8 in steps of 0.2, respectively. Results for CSPs with and without NE are presented by *violet* and *black lines*, respectively, and synthesis results of AGs with NE for $\alpha = 0.5$, 1, 1.5 and 2 are represented by *blue*, *green*, *yellow* and *red lines*, respectively. The results show a systematic mass overestimation of up to ∼3.5 dex with decreasing t and α and with increasing $x_{\rm AGN}$. This trend is similar to the one displayed on the top row of Figure 3.2.6 for a purely-stellar modelling approach of AGs without NE. However, nebular emission from both stellar populations and AGN accentuate the mass overestimation for models with $t \lesssim 10^8$ yr. This is particularly noticeable at $\sim 3 \times 10^6$ yr for the instantaneous burst SFH at the lower $x_{\rm AGN}$ values. These overestimation peaks seem to be linked to a incomplete age coverage of the SSPs in the adopted base library, given that results for the CSPs display uncertainties by up to ∼0.5 dex near these evolutionary stages. Results presented in Subsection 4.2.1 showed that the biases in stellar properties that are induced by the NE disappear after the decline of star-forming activity. Notwithstanding, the ever-present AGN continuum in these spectra leads to an

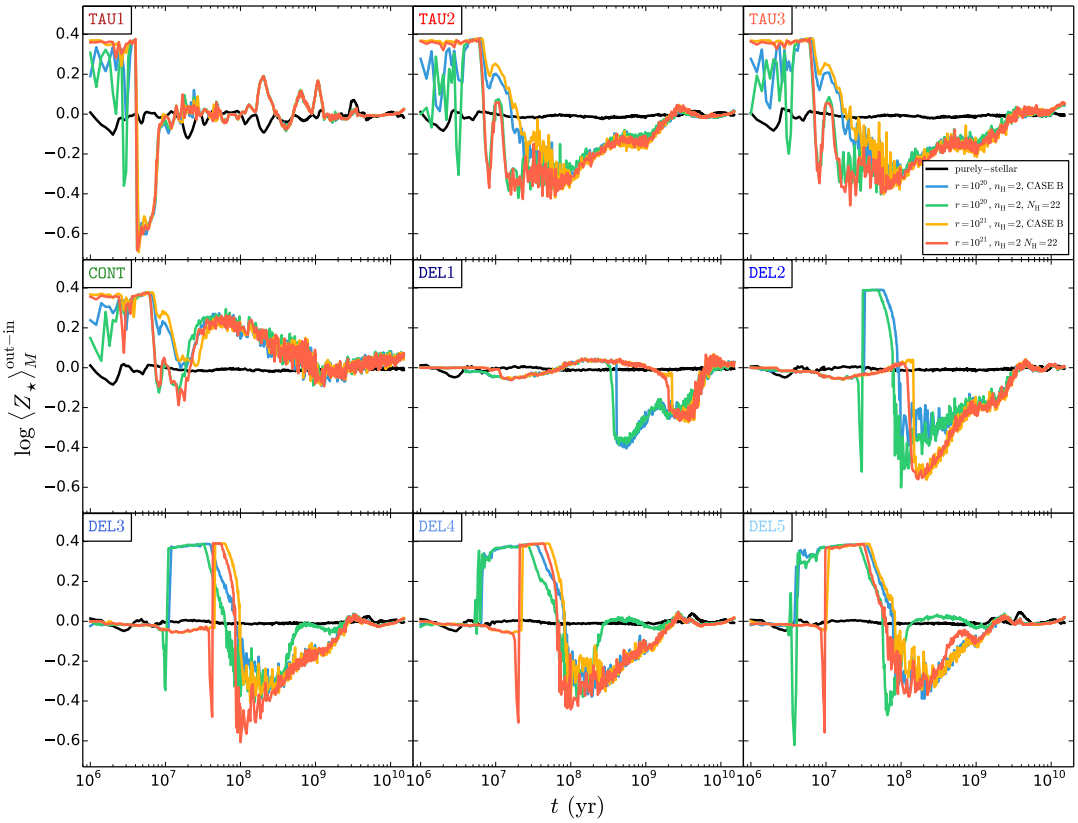

Figure 4.2.6: Difference in the mass-weighted mean stellar metallicity $\log\langle Z_\star\rangle_M$ between STARLIGHT (out) and REBETIKO (in) values as a function of CSP age t. Panel display configuration and legend details are identical to those in Figure 4.1.4.

underlying NE contribution throughout the galaxy evolution. This explains the fact that larger mass biases are found for AGs with NE than without NE. Overall, the AGN PL continuum seems to be the main source of mass biases for all evolutionary stages and SFHs. Figure A.3.3 in Appendix A shows roughly similar trends for the other SFHs.

Figure 4.2.8 shows the difference in the *light-weighted mean stellar age* $\langle\log t_\star\rangle_L$ between STARLIGHT and REBETIKO values as a function of CSP age t. The panel display configuration and legend details are identical to those in Figure 4.2.7. The results show that the age is systematically under and overestimated by up to ∼1.5 and 1 dex for $t \lesssim 10^8$ and $t \gtrsim 10^9$ yr, respectively. This trend is similar to the one apparent on the top row of Figure 3.2.7 for AGs without NE. However, results show that NE leads to a systematic age underestimation of up to ∼0.5 dex for evolutionary stages associated with strong star-formation activity. Biases in age that primarily stem from the NE due to the AGN become increasingly prominent with decreasing α. This trend results from the fact that the nebular continuum must be accounted for by young low-metallicity SSPs. Regardless, the AGN continuum seems to be the main source of age biases. Figure A.3.4 in Appendix A shows roughly similar trends for the other SFHs.

Figure 4.2.9 shows the difference in the *light-weighted mean stellar metallicity* $\log\langle Z_\star\rangle_L$ between STARLIGHT and REBETIKO values as a function of CSP age t. The panel display configuration and legend details are identical to those in Figure 4.2.7. The results for the instantaneous burst SFH reveal that the metallicity is systematically underestimated by up to ∼0.7 dex with decreasing CSP age t and α and with increasing $x_{\rm AGN}$. This systematic metallicity underestimation increases with t in the case of an continuous SFH. Moreover, this underestimation suffers an offset with increasing α which can lead to a metallicity overestimation up to ∼0.1 dex for $x_{\rm AGN} = 0.8$ and $\alpha = 2$. The pronounced plateau of -0.7 dex metallicity underestimation corresponds once again to the lowest metallicity value in the adopted base library. Overall, this trend is similar to that illustrated on the top row of Figure 3.2.8. Moreover, NE

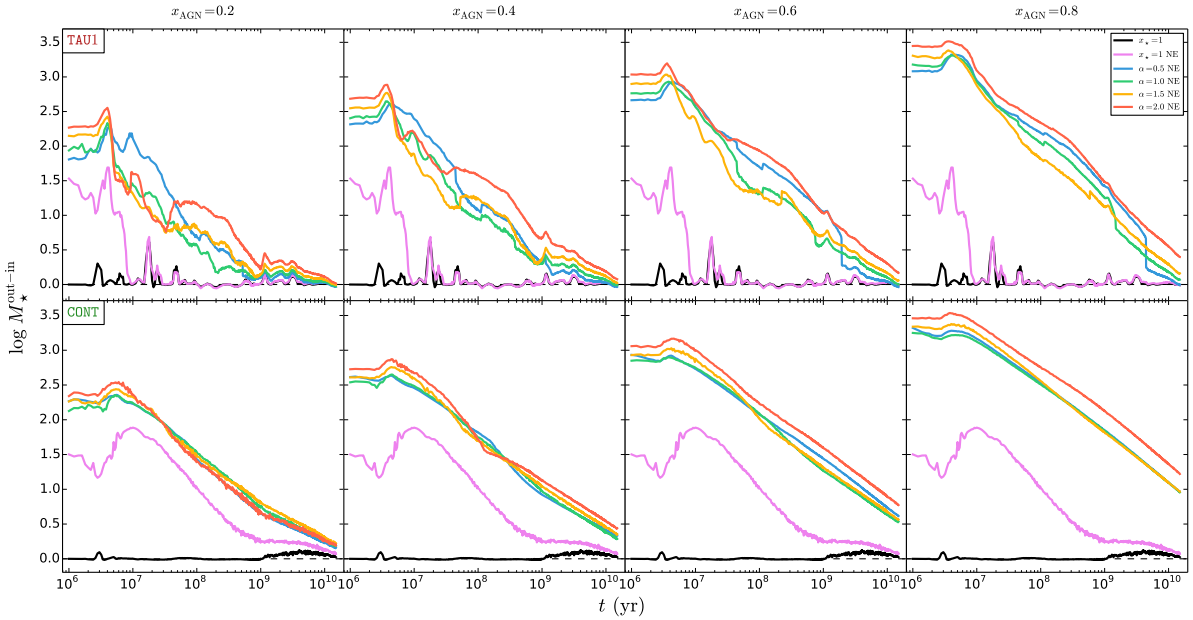

Figure 4.2.7: Difference in the total stellar mass $M_\star$ between STARLIGHT (out) and REBETIKO (in) values as a function of CSP age t. Top and bottom rows display results for instantaneous burst and continuous SFHs. Left- to right-hand side panels represent increasing $x_{\rm AGN}$ from 0.2 to 0.8 in steps of 0.2, respectively. Black and violet lines represent results of CSPs without and with NE, respectively. Blue, green, yellow and red lines represent results for AGs with NE and $\alpha = 0.5$, 1, 1.5 and 2, respectively.

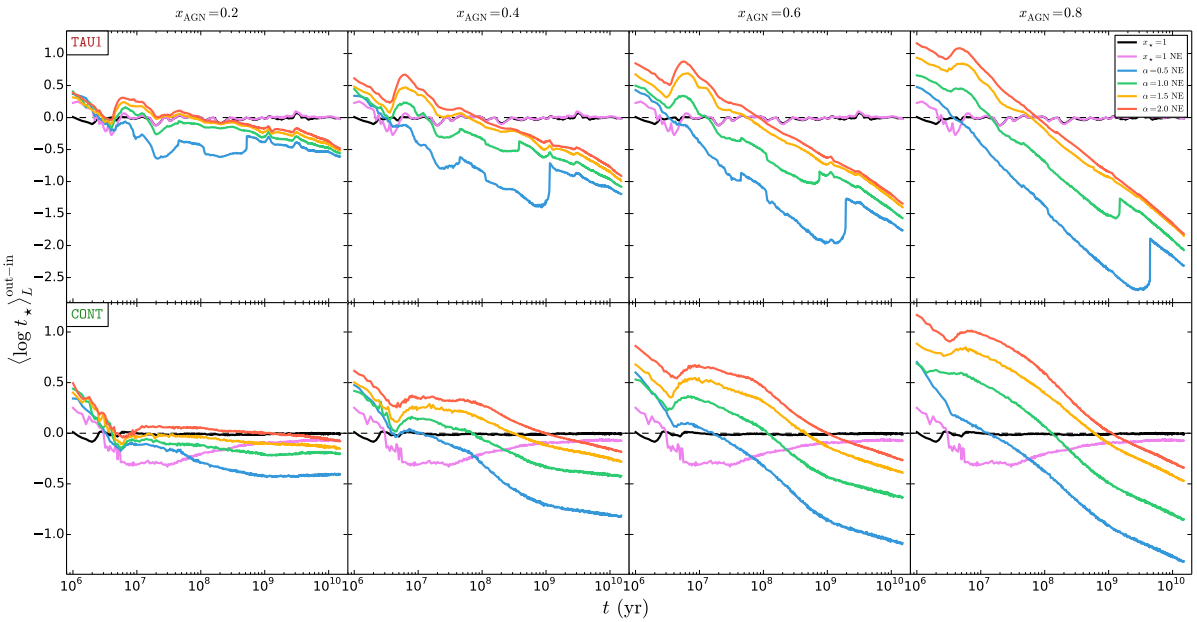

Figure 4.2.8: Difference in the light-weighted mean stellar age $\langle \log t_\star \rangle_L$ between STARLIGHT (out) and REBETIKO (in) values as a function of CSP age t. Panel display configuration and legend details are identical to those in Figure 4.2.7.

leads to a systematic metallicity underestimation up to ∼0.5 dex for $t \lesssim 10^7$ yr and $x_{\rm AGN} = 0.2$, a trend which is mitigated with increasing $x_{\rm AGN}$. Figure A.3.5 in Appendix A shows roughly similar trends for the other SFHs.

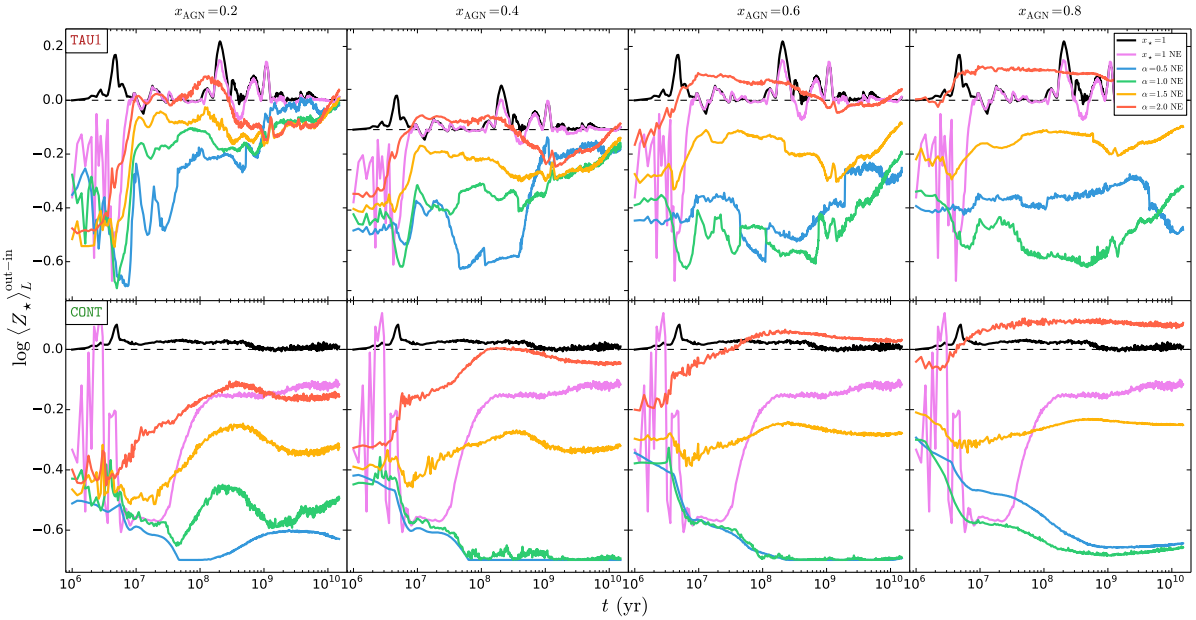

Figure 4.2.9: Difference in the light-weighted mean stellar metallicity $\log\langle Z_\star\rangle_L$ between STARLIGHT (out) and REBETIKO (in) values as a function of CSP age t. Panel display configuration and legend details are identical to those in Figure 4.2.7.

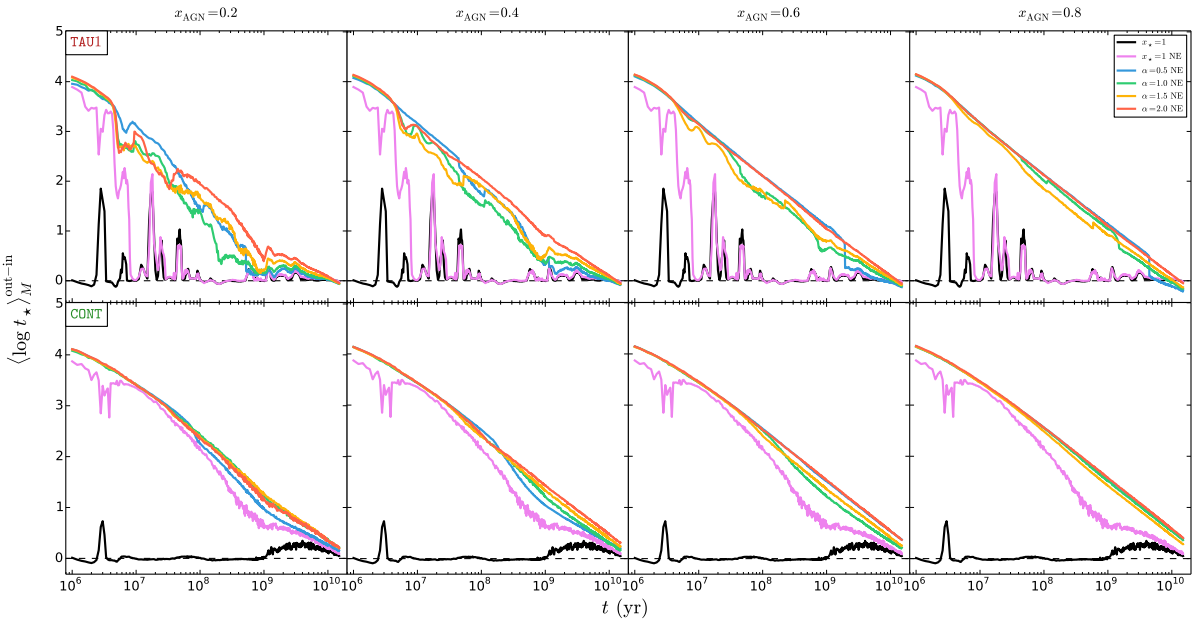

Figure 4.2.10: Difference in the mass-weighted mean stellar age $\langle \log t_\star \rangle_M$ between STARLIGHT (out) and REBETIKO (in) values as a function of CSP age t. Panel display configuration and legend details are identical to those in Figure 4.2.7.

Figure 4.2.10 shows the difference in the *mass-weighted mean stellar age* $\langle \log t_\star \rangle_M$ between STARLIGHT and REBETIKO values as a function of CSP age t. The panel display configuration and legend details are identical to those in Figure 4.2.7. The results show a systematic age overestimation of up to ∼4 dex with decreasing t and increasing α. This bias is similar to that displayed on the top row of Figure 3.2.9 and on Figure 4.2.5. Moreover, age is systematically overestimated by up to ∼0.5 dex for $x_{AGN} = 0.2$ due to the

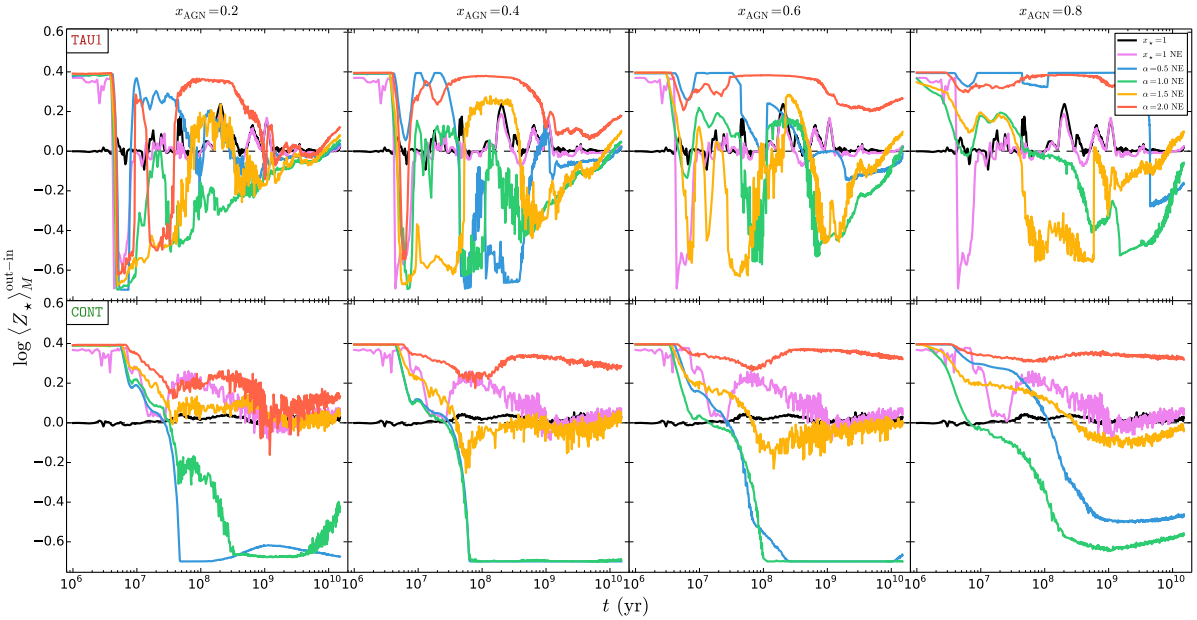

Figure 4.2.11: Difference in the mass-weighted mean stellar metallicity $\log\langle Z_\star\rangle_M$ between STARLIGHT (out) and REBETIKO (in) values as a function of CSP age t. Panel display configuration and legend details are identical to those in Figure 4.2.7.

NE related to star-formation activity for each SFH. However, this trend is washed out with increasing $x_{\rm AGN}$, indicating that the underlying AGN continuum is the main source of of mass-weighted age biases. The same conclusion is reached from the analysis of Figure 4.2.7, in which the biases induced by the NE are mitigated with increasing $x_{\rm AGN}$. Figure A.3.6 in Appendix A shows roughly similar trends for the other SFHs.

Finally, Figure 4.2.11 shows the difference in the *mass-weighted mean stellar metallicity* $\log\langle Z_\star\rangle_M$ between STARLIGHT and REBETIKO values as a function of CSP age t. The panel display configuration and legend details are identical to those in Figure 4.2.7. The metallicity is systematically underestimated with decreasing t and α and with increasing $x_{\rm AGN}$ for the instantaneous burst SFH, whereas this bias increases with t in the case of a continuous SFH. Overall, results are similar to those illustrated in Figure 4.2.9 for the light-weighted metallicity. However, mass-weighted metallicity can also be systematically overestimated by up to ∼0.4 dex with increasing $x_{\rm AGN}$ for both SFHs, in particular for $\alpha = 2$. It is worth noting that this overestimation plateau of ∼0.4 dex corresponds to the highest metallicity value in the adopted base library which is $Z = 0.05$. Figure A.3.7 in Appendix A shows roughly similar trends for the other SFHs.

Coupled with the findings discussed in Subsection 4.2.1, these results indicate that the stellar mass, mean age and mean metallicity inferred from PSS can be plagued by uncertainties of up to ∼3.5, 4 and 0.7 dex, respectively. These uncertainties depend on the age of the CSP t, AGN fractional contribution $x_{\rm AGN}$, PL index α and on the relative contribution of NE. Moreover, it is important to keep in mind that, in some instances, the inferred properties can be biased towards the boundaries imposed by the construction of the base library. This fact was clearly illustrated by the metallicity under and overestimation plateaus at ∼-0.7 and 0.4 dex corresponding to the lower and upper metallicity values in the adopted base library, respectively.

Above all, these results suggest that an unsupervised application of PSS to star-forming and/or active galaxies can result in strong biases in the determination of fundamental stellar properties of galaxies (e.g. mass, mean age and mean metallicity), which could in turn significantly impact the understanding of the mass assembly history of both star-forming galaxies and those additionally hosting an AGN. As an illustrative case, a purely-stellar PSS analysis of a star-forming AGN-host galaxy older than 1 Gyr may readily lead to the erroneous conclusion of this system to be particularly massive and composed of predominately old and metal-poor stellar populations. The same holds even for a star-forming galaxy

sustaining merely moderate star formation deprived of an AGN, given that the NE excited by starlight is in itself sufficient to lead to significant biases in the inferred stellar properties. Taken at face value, such results could lead to the conclusion that high-mass and metal-poor star-forming galaxies are common at high redshifts, which in turn might be taken as evidence against the hierarchical galaxy growth scenario (Lacey & Cole 1993).

In summation, a thorough understanding of galaxy formation and evolution requires a quantitative knowledge of biases introduced by the AGN and NE spectral contributions to the observed spectrum of a galaxy when applying a purely-stellar PSS approach. A way to mitigate this issue would be to explore the assembly history of galaxies with next generation PSS codes, such as FADO, that aim to account for all relevant physical ingredients of the optical continuum.

4.3 PSS code FADO

The PSS code *Fitting Analysis using Differential evolution Optimisation* (FADO, Gomes & Papaderos 2017) has the ability of ensuring consistency between the best-fit population vector (i.e. SFH, intrinsic extinction and kinematics) and the observed nebular characteristics of a star-forming galaxy (e.g. H Balmer-line luminosities and EWs, continuum shape around the Balmer and Paschen jumps). Moreover, the code determines emission-line fluxes and EWs, allows for the visualisation of the modelling results and can handle up to 2000 base elements with up to 24000 wavelength elements each, which is an important advantage towards future work with higher-resolution SSP libraries. FADO employs genetic *differential evolution optimisation* (Storn & Price 1996, 1997; Price, Storn & Lampinen 2005). This optimisation approach is specially suited for multi-objective programming over continuous spaces, automatically adapted for parallel computation and, most importantly, reliably converging at an affordable expense of computational time. This results in significant improvements with respect to the uniqueness of spectral fits and the overall efficiency of the convergence schemes integrated in the code when modelling galaxies with strong nebular emission contribution. FADO currently offers three modelling schemes:

1. **full-consistency mode**: spectral modelling aiming at consistency between observed and predicted continuum (stellar plus nebular) and Balmer emission-line luminosities and EWs;
2. **nebular-continuum mode**: similar to the prior mode but without the requirement for consistency between predicted and observed Balmer-line luminosities and EWs, and
3. **stellar mode**: spectral modelling with only purely-stellar spectral elements.

Other distinctive conceptual improvements of FADO over currently available PSS codes include: (**a**) computation and inclusion of the nebular continuum contribution to the best-fit solution and identification of the population vector (e.g. mass, age and metallicity of individual SSPs, intrinsic extinction) that best reproduces the nebular characteristics of a galaxy; (**b**) automatic characterisation of the input spectrum for the sake of optimisation of the SSP library and spectral modelling strategy using artificial intelligence; (**c**) computation of uncertainties both for the information encoded in the best-fit population vector and secondary products (e.g. light- and mass-weighted mean stellar age and mean stellar metallicity); (**d**) automated spectroscopic classification based on optical emission-line ratios after correction for underlying stellar absorption; (**e**) determination of the electron temperature and density of the ionised gas whenever meaningful, and (**f**) computation of the intrinsic extinction in the stellar and nebular component.

A set of synthetic spectra with NE were modelled with STARLIGHT and the first public version of FADO (version v01) in order to evaluate the ability of the latter to robustly infer the main stellar properties in its full-consistency mode. The synthetic spectra were computed with REBETIKO following Equation 2.1 and adopting BC2003 SSPs with Padova 1994 evolutionary tracks (Alongi *et al.* 1993; Bressan *et al.* 1993; Fagotto *et al.* 1994a,b; Girardi *et al.* 1996) and a Chabrier (2003) IMF. The NE was computed assuming case B recombination ($n_e = 100$ cm^{-3} and $T_e = 1,000$ K) and assuming $A_V = 0$ mag. Moreover, the spectra were convolved with a Guassian kernel to simulate a line broadening due to a line-of-sight stellar dispersion of 50 km/s. Figures A.3.8 and A.3.9 in Appendix A show the synthetic spectra of CSPs with NE and other spectrophotometric properties for instantaneous burst and continuous SFHs, respectively.

These spectra were fitted with both PSS codes between 3400 and 8900 Å while masking the strongest emission lines. Figure 4.3.1 shows the STARLIGHT and FADO spectral fits for a CSP with NE, 1 Myr, solar metallicity and instantaneous burst SFH. The input, STARLIGHT and FADO best-fit spectra are represented by the *black*, *red* and *blue lines* in the *main panel*, respectively. The residuals spectra resulting from subtracting the best-fit models found by STARLIGHT and FADO from the input spectrum are represented

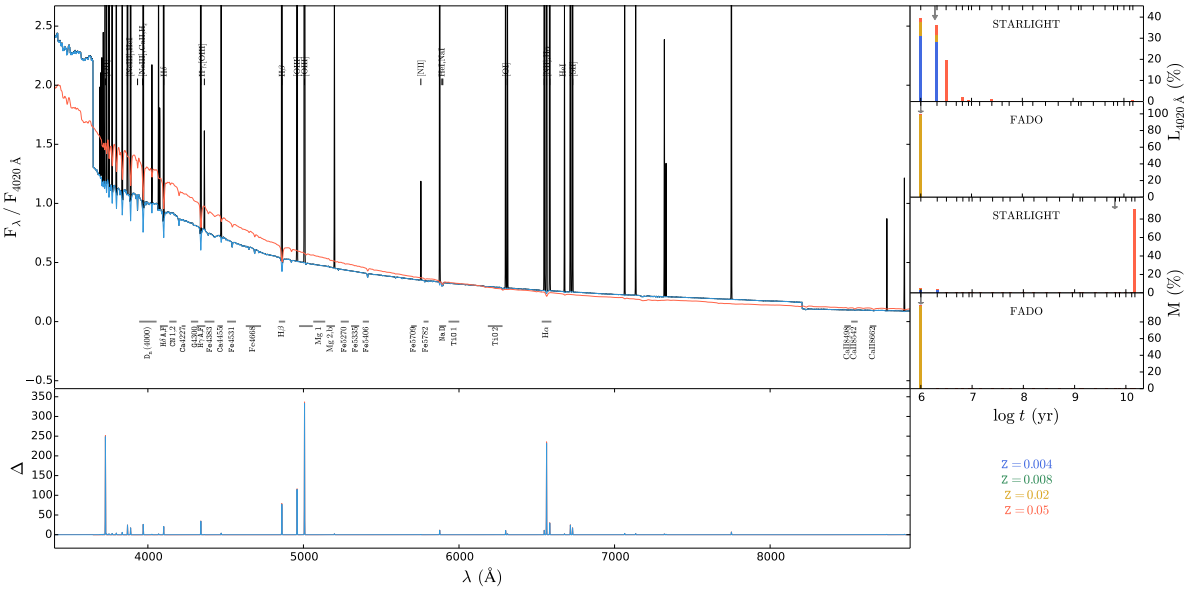

Figure 4.3.1: STARLIGHT and FADO spectral modelling results of a CSP with NE, 1 Myr, solar metallicity and instantaneous burst SFH. Main panel: Black, red and blue lines represent the input and fitted spectra by STARLIGHT and FADO, respectively. Bottom panel: Red and blue lines represents the residuals spectrum resulting from subtracting the STARLIGHT and FADO best-fits from the input spectrum. Top right-hand side panels: SFH in light fractions for STARLIGHT (top) and FADO (bottom). Bottom right-hand side panels: SFH in mass fractions for STARLIGHT (top) and FADO (bottom).

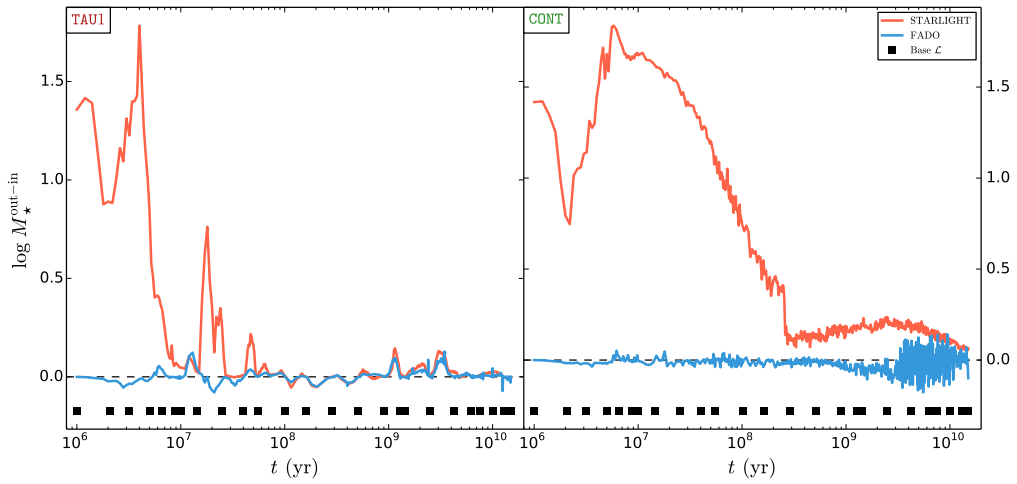

Figure 4.3.2: Difference in the total stellar mass $M_\star$ between STARLIGHT/FADO (out) and REBETIKO (in) values as a function of CSP age t for instantaneous burst (left panel) and continuous SFHs (right panel). Red and blue lines represent results with STARLIGHT and FADO, respectively.

by the *red* and *blue lines* in the *bottom panel*, respectively. Moreover, the estimated SFHs in light and mass fractions are represented on the *top* and *bottom right-hand side panels*, respectively. The stellar properties with STARLIGHT were found to be $\log M_\star = 7.23\ M_\odot$, $\langle \log t_\star \rangle \simeq 7.21$ yr and $\log\langle Z_\star \rangle \simeq -1.68$, which differ significantly from the input values of $\log M_\star = 5.73\ M_\odot$, $\langle \log t_\star \rangle = 6$ yr and $\log\langle Z_\star \rangle = -1.70$. Meanwhile, FADO estimates $\log M_\star = 5.74\ M_\odot$, $\langle \log t_\star \rangle = 6$ yr and $\log\langle Z_\star \rangle = -1.70$, which are in good agreement with the input values. This is visually corroborated by a good fit and well recovered SFHs.

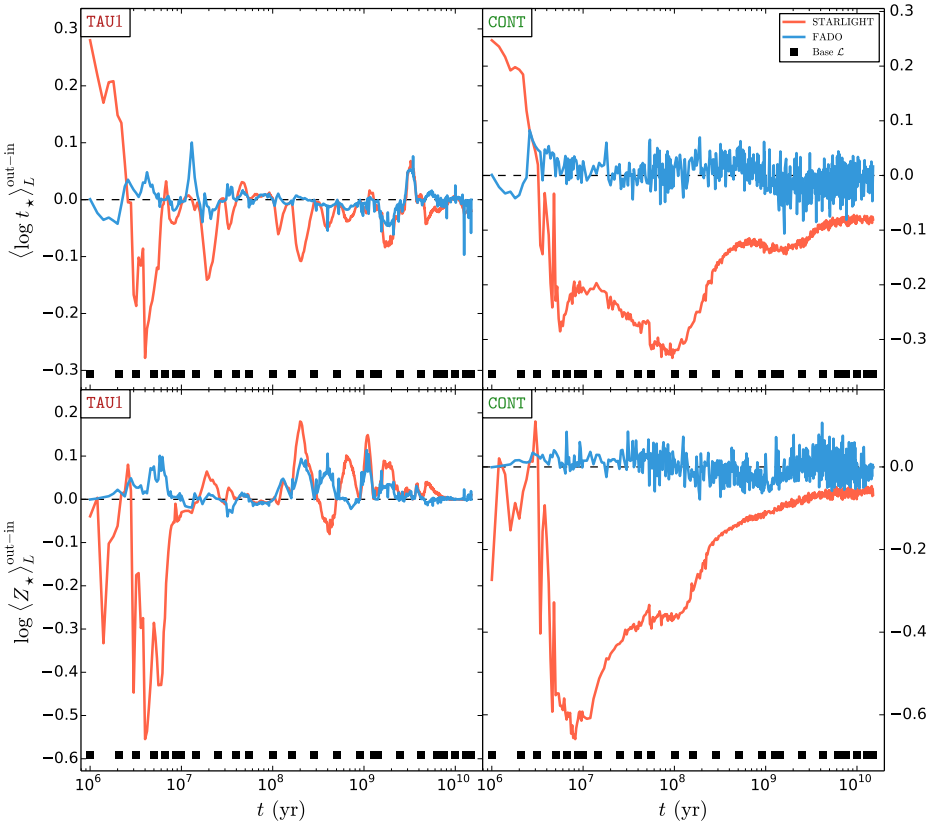

Figure 4.3.3: Difference in the light-weighted mean stellar age $\langle \log t_\star \rangle_L$ (top row panels) and mean stellar metallicity $\log \langle Z_\star \rangle_L$ (bottom row panels) between STARLIGHT/FADO (out) and REBETIKO (in) values as a function of CSP age t for instantaneous burst (left-hand side panel) and continuous SFHs (right-hand side panel). Legend details are identical to those in in Figure 4.3.2.

Figure 4.3.2 shows the difference in the *total stellar mass* $M_\star$ between the STARLIGHT/FADO (out) and REBETIKO (in) values as a function of CSP age t for instantaneous burst (*left-hand side*) and continuous (*right-hand side*) SFHs. Synthesis results obtained with STARLIGHT and FADO are represented by *red* and *blue lines*, respectively. Overall, the STARLIGHT results for both SFHs are similar to those presented in Figure 4.2.2. Meanwhile, the results from FADO show that the mass is estimated within an uncertainty of up to ~ 0.2 dex for both SFHs. Moreover, FADO results show a slight mass overestimation hump of up to $\sim$0.1 dex for $t \gtrsim 10^9$ yr and continuous SFH. This trend seems to be analogous to that presented in Figure 2.3.3 for the analysis of CSP with STARLIGHT.

Figure 4.3.3 shows the difference in the *light-weighted mean stellar age* $\langle \log t_\star \rangle_L$ (*top row panels*) and *mean stellar metallicity* $\log \langle Z_\star \rangle_L$ (*bottom row panels*) between the STARLIGHT/FADO and REBETIKO values as a function of CSP age t. The panel display configuration and legend details are identical to those in Figure 4.3.2. The results obtained with STARLIGHT for both SFHs are again similar to those presented in Figures 4.2.3 and 4.2.4. However, the FADO results show that the age and metallicity are recovered within uncertainties of up to $\sim$0.1. The estimated age for the instantaneous burst SFH displays an overestimation peak of up to $\sim$0.1 dex for $t \lesssim 2 \times 10^7$ yr that is correlated with a poor age coverage of the base library. Moreover, there is also a small age underestimation bump of up to $\sim$0.1 dex for $10^9 \lesssim t \lesssim 10^{10}$ yr for a continuous SFH. Metallicity uncertainties in FADO seem also to correlate with poorly covered evolutionary stages by the SSPs in the base library.

Finally, Figure 4.3.4 shows the difference in *mass-weighted mean stellar age* $\langle \log t_\star \rangle_M$ (*top row panels*) and *mean stellar metallicity* $\log \langle Z_\star \rangle_M$ (*bottom row panels*) between the STARLIGHT/FADO and REBETIKO values as a function of CSP age t. The panel display configuration and legend details are identical to those in Figure 4.3.2. The results obtained with STARLIGHT for both SFHs show trends similar to those

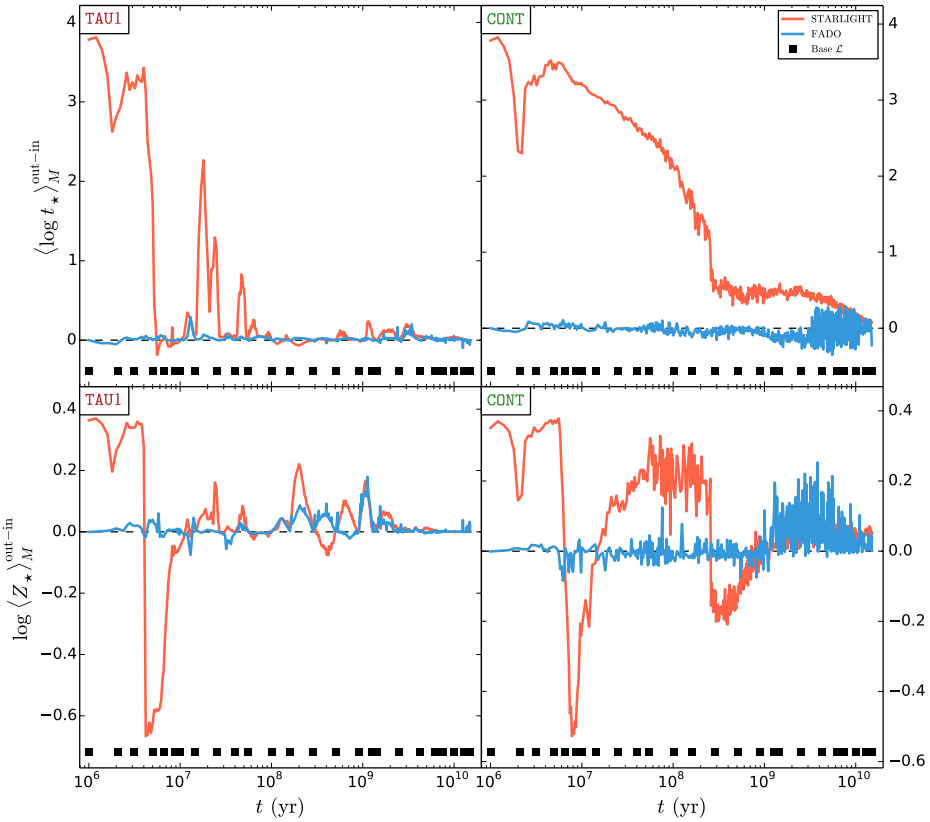

Figure 4.3.4: Difference in the mass-weighted mean stellar age $\langle \log t_\star \rangle_M$ (*top row panels*) and mean stellar metallicity $\log \langle Z_\star \rangle_M$ (bottom row panels) between STARLIGHT/FADO (out) and REBETIKO (in) values as a function of CSP age t for instantaneous burst (left-hand side panel) and continuous SFHs (right-hand side panel). Legend details are identical to those in in Figure 4.3.2.

presented in Figures 4.2.5 and 4.2.6. Meanwhile, the FADO results show that the age and metallicity are estimated within uncertainties of up to ∼0.2. Both age and metallicity results show an overestimation bump of up to ∼0.2 dex for $10^9 \lesssim t \lesssim 10^{10}$ yr for a continuous SFH.

Overall, the stellar properties estimated with this preliminary version of FADO show a significant improvement when compared to those inferred by STARLIGHT. This fact stresses the importance of estimating in a self-consistent manner both the stellar and nebular continuum in oder to recover a good approximation of the true SFH of a star-forming galaxy. Evolutionary stages for which FADO displays noteworthy uncertainties seem to be correlated with a non-optimal age coverage by the adopted base library, as seen for mass, age and metallicity for $10^7 \lesssim t \lesssim 3 \times 10^7$ yr and continuous SFH. Indeed, these results are likely due to the likeness of the SSPs with $t \gtrsim 10^9$ yr in the adopted library, as similar results were found on Section 2.3 during the analysis with STARLIGHT of purely-stellar synthetic spectra assuming different base libraries.

5 Conclusion

Spectral synthesis was applied to synthetic galaxies in order to quantify the impact of AGN and NE to the estimation of physical properties when adopting purely-stellar or more complex modelling strategies. CSPs evolutionary models of galaxies with synthetic spectra and other spectrophotometric properties were computed with the ESS code REBETIKO (Papaderos & Gomes in prep.) using SSPs convolved with different SFR functions aiming to approximate the SFHs of different Hubble-type galaxies. Radiation for an AGN and excited gas was then incrementally added to these models to recreate the optical SED of active star-forming galaxies. These synthetic spectra were modelled with a full-spectrum state-of-the-art PSS code in order to quantify the effect of AGN and NE to the estimation of fundamental stellar properties (e.g. SFH, total mass, mean age, mean metallicity) encoded in the spectral continuum of galaxies.

The analysis initially focused on the estimated stellar properties when employing a purely-stellar PSS approach to CSPs. Results showed that the estimated stellar properties strongly depend on the age coverage of the adopted base library of SSPs and that the total stellar mass, mean stellar age and mean stellar metallicity can be recovered within an uncertainty of up to $\sim$0.2 dex for different SFHs, which is the typical value for the adopted state-of-the-art PSS code STARLIGHT. Results suggest that taylor-made base libraries should be adopted to model different Hubble-type galaxies in order to assure a robust determination of their stellar properties. Although possible when dealing with synthetic spectra, this approach might ultimately be unfeasible in a application of PSS to large samples of real galaxies. Moreover, it is important to bare in mind that similar stellar evolutionary ingredients were used to create the synthetic CSPs with ESS and in the subsequent decomposition of these into elementary spectral building blocks with PSS. Therefore, the observed uncertainties for the estimated stellar properties are lower limits of the real uncertainties when applying a similar approach to real spectra of galaxies. The same holds for the PSS analysis of more complex spectra presented in this work.

Synthetic spectra of Lyman-continuum-evacuated AGs including a CSP and a simple AGN FC represented by PL defined as $F_\nu \propto \nu^{-\alpha} \Leftrightarrow F_\lambda \propto \lambda^{\alpha-2}$ where then analysed with PSS. Three modelling configurations where adopted in order to handle the AGN spectral contribution: (**a**) neglecting any AGN continuum model in the base library; (**b**) including a single AGN PL model in the base library with the same slope as the one considered in the input AG spectrum, and (**c**) including AGN PL models with $\alpha = 0.5$, 1, 1.5 and 2 in the base library. Results showed that an effective AGN detection threshold can be placed at an AGN fractional contribution of $x_{\rm AGN} \simeq 0.26$ to the monochromatic flux at 4020 Å in an Lyman-continuum-evacuated AG with a CSP with 10 Gyr, solar metallicity and instantaneous burst SFH and an AGN with $\alpha = 1.5$ (Cardoso, Gomes & Papaderos 2016). Moreover, a PSS modelling analysis for multiple SFHs under a purely-stellar spectral decomposition showed that the total stellar mass and mean age can be overestimated by up to $\sim$3.5 and 4 dex, respectively, and that the mean metallicity can be underestimated by least up to $\sim$0.7 dex. The biases in these stellar properties show non-trivial correlations with CSP age, roughly increase with α and $x_{\rm AGN}$ and seem independent of the SFH of the galaxy. Moreover, a PSS modelling approach including SSPs and AGN PLs in the base

library can lead to stellar mass, mean age and mean metallicity uncertainties of up to ∼1, 3 and 0.3 dex, respectively, depending on the CSP age, α and $x_{\rm AGN}$. These results stress the importance of modelling the AGN spectral contribution when applying PSS to active galaxies without strong NE (Cardoso, Gomes & Papaderos 2017).

NE was then added to the CSP and AG synthetic spectra using photoionisation simulations and assuming typical physical conditions of HIIRs and NLRs, respectively. A subsequent purely-stellar PSS approach showed that the inferred stellar mass, mean age and mean metallicity can be plagued by uncertainties of up to ∼3.5, 4 and 0.7 dex, respectively. These biases depend of the CSP age, α, $x_{\rm AGN}$ and on the adopted SFH, as NE during star-formation leads to significant stellar properties uncertainties. These different results point to the fact that current PSS codes are lacking fundamental physical ingredients needed for a robust spectral modelling of active and/or star-forming galaxies. Moreover, they also highlight the inherent danger of an unsupervised PSS application to spectra of galaxies with significant non-stellar spectral components. A brief analysis of CSPs with NE using the PSS code FADO (Gomes & Papaderos 2017) illustrates the importance of simultaneously estimating the stellar and nebular continua in order to robustly estimate the SFH and other stellar properties of star-forming galaxies.

The systematic biases on fundamental physical properties of galaxies presented in this work show above all the potential for obtaining systematically biased estimates of stellar population properties when applying a purely-stellar PSS approach to active and/or star-forming galaxies. For instance, results showed this approach can lead to the mischaracterisation of a star-forming galaxy older than 1 Gyr hosting an AGN as being particularly massive, composed by a majority of old and metal-poor stellar populations. The same is true for a star-forming galaxy or a Lyman-continuum-leaking AGN-host. Moreover, these results can also lead to the characterisation of galaxies with roughly the age of the universe to be composed mainly of young and metal-poor stellar populations. This interpretation in turn might lead to the conclusion that these objects provide strong evidence against the hierarchical growth scenario for galaxy formation and evolution. The next-generation PSS should be able to disentangle the most important spectral components (e.g. stellar, AGN, NE and dust emission) in the different Hubble-type galaxies so to guarantee a coherent assessment of the mass assembly history of the Universe.

Among many other avenues, the analysis presented in this thesis can be expanded by investigating potential biases on stellar properties using currently available SS codes when considering SSPs with different IMFs and/or CSPs with different metallicities. Indeed, it would be also interesting to apply a chemically consistent ESS code and study the impact on the same physical properties of a realistic metallicity evolution of the SSPs composing the stellar continuum. Moreover, an important question not addressed in this work relates the impact of dust absorption and reemission and its interplay with other spectral contributions to the study of galaxy formation and evolution with state-of-the-art SS. For instance, it is to be expected to some extent a correlation between the dust model and the estimated V-band extinction. However, it is not clear how the combined impact of AGN, dust and NE might have on the physical properties estimated with PSS.

Recent studies show signs of the current transition towards a panchromatic full-spectrum SS approach. For instance, Röck *et al.* 2016 presented the first SPS models base on empirical stellar spectra covering the optical and infrared between 3500 and 50000 Å. These models can be particular useful in distinguishing the underlying stellar continuum in this spectral range from the remaining relevant spectral components (e.g. AGN, NE, dust). Moreover, López Fernández *et al.* (2016) presented an extended version of STARLIGHT which can perform spectral analysis using full-spectrum optical and UV photometric data and showed that the inclusion of UV can help constraining the mean stellar age and mean metallicity in star-forming disk galaxies. Meanwhile, FADO is expected to play a significant role in the self-consistent interpretation of the SFH of star-forming galaxies by analysing both the stellar and gas characteristics encoded in their spectra. Improvements on the treatment of the optical AGN FC are expected to play equally an important role in advancing the current understanding of galaxy formation and evolution of active galaxies.

In summation, this work reaffirms the idea that the analysis of galaxy observations under the preview of theoretical astrophysics remains largely an untraveled road. This realisation remains both humbling and exciting.

A

Additional Resources

A.1 Analysis of purely-stellar galaxy models

Figures A.1.1–A.1.9 present synthetic CSP spectra and other spectrophotometric properties of evolutionary models created with the ESS code REBETIKO for the SFHs displayed on Figure 2.1.1.

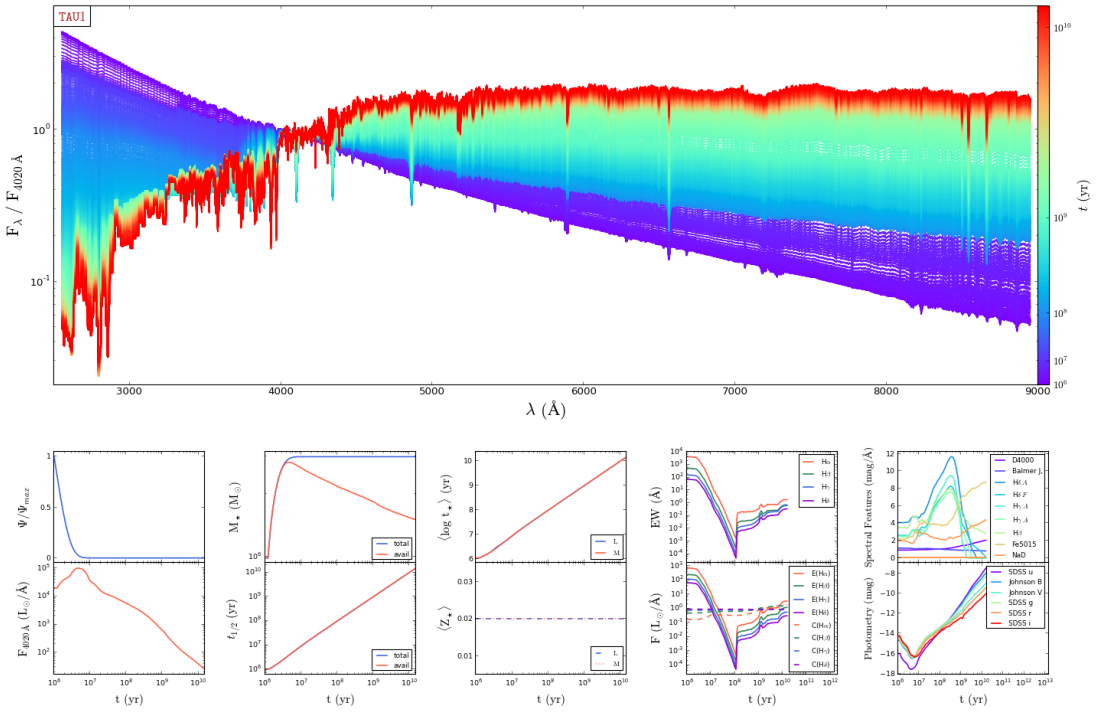

Figure A.1.1: Synthetic CSP spectra normalised at $\lambda_0 = 4020$ Å and other spectrophotometric quantities computed with REBETIKO for the SFH labeled as `TAU1` in Figure 2.1.1. Panel display configuration and legend details are identical to those in Figure 2.2.1.

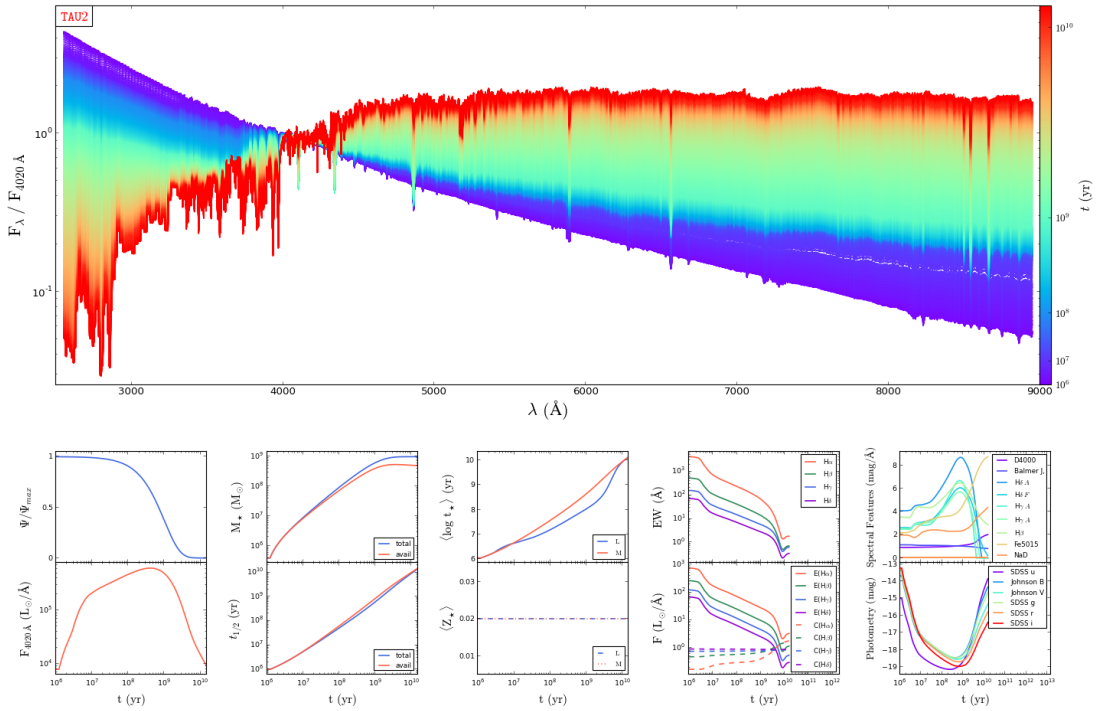

Figure A.1.2: Synthetic CSP spectra normalised at $\lambda_0 = 4020$ Å and other spectrophotometric quantities computed with REBETIKO for the SFH labeled as `TAU2` in Figure 2.1.1. Panel display configuration and legend details are identical to those in Figure 2.2.1.

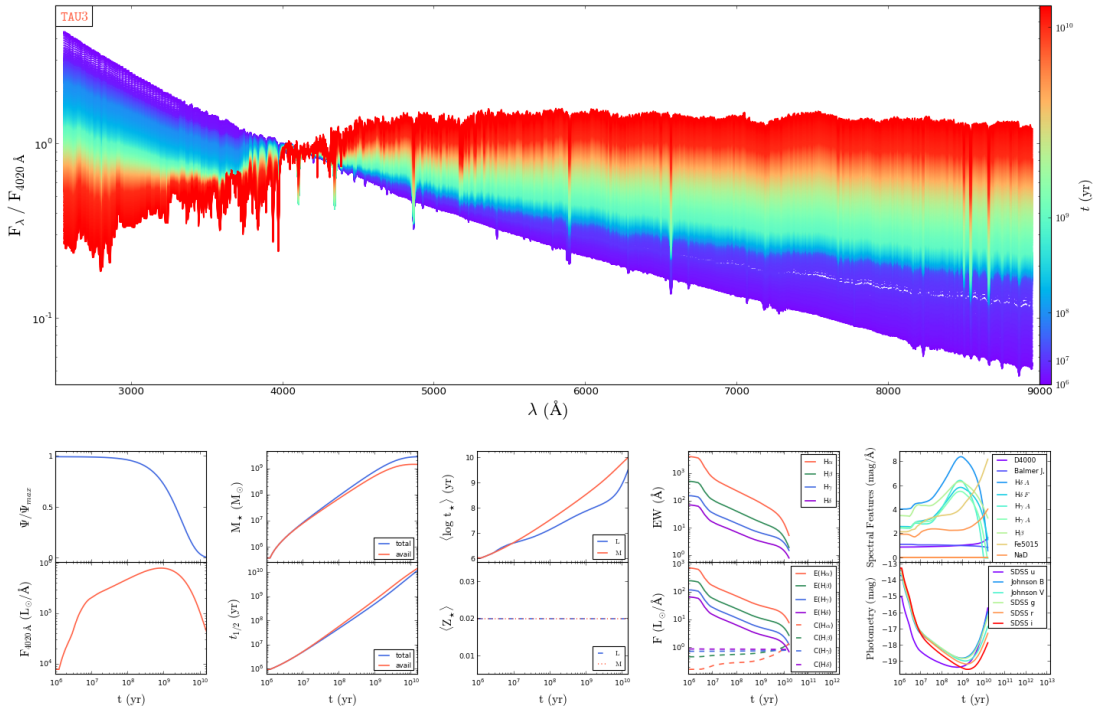

Figure A.1.3: Synthetic CSP spectra normalised at $\lambda_0 = 4020$ Å and other spectrophotometric quantities computed with REBETIKO for the SFH labeled as `TAU3` in Figure 2.1.1. Panel display configuration and legend details are identical to those in Figure 2.2.1.

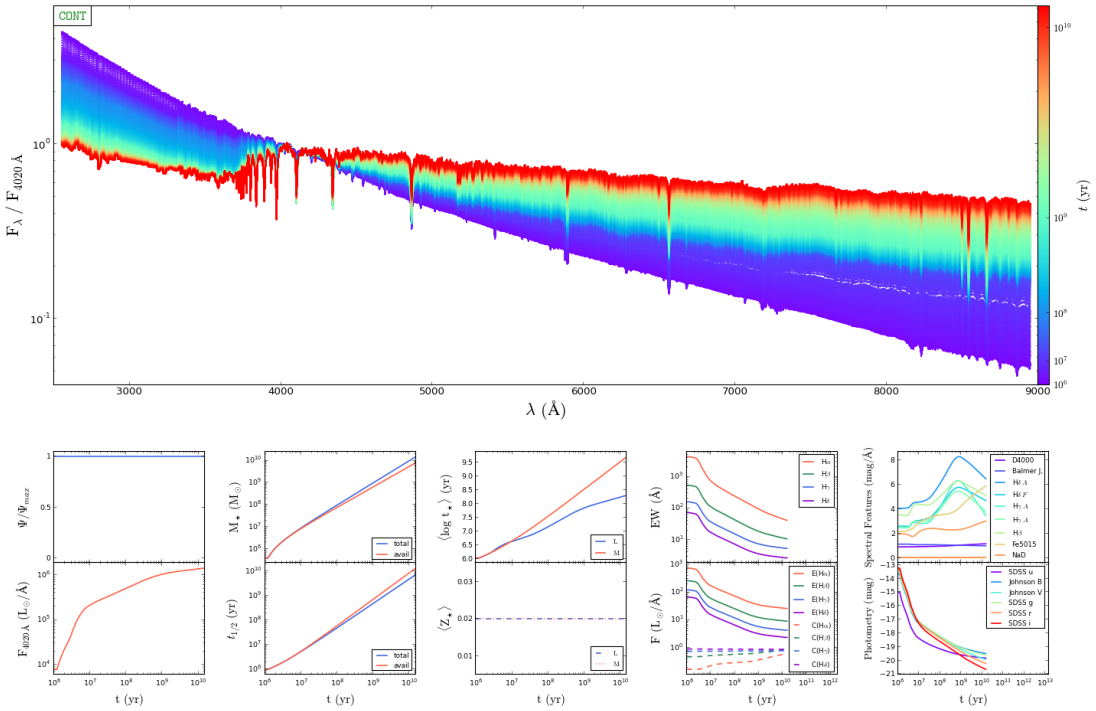

Figure A.1.4: Synthetic CSP spectra normalised at $\lambda_0 = 4020$ Å and other spectrophotometric quantities computed with REBETIKO for the SFH labeled as `CONT` in Figure 2.1.1. Panel display configuration and legend details are identical to those in Figure 2.2.1.

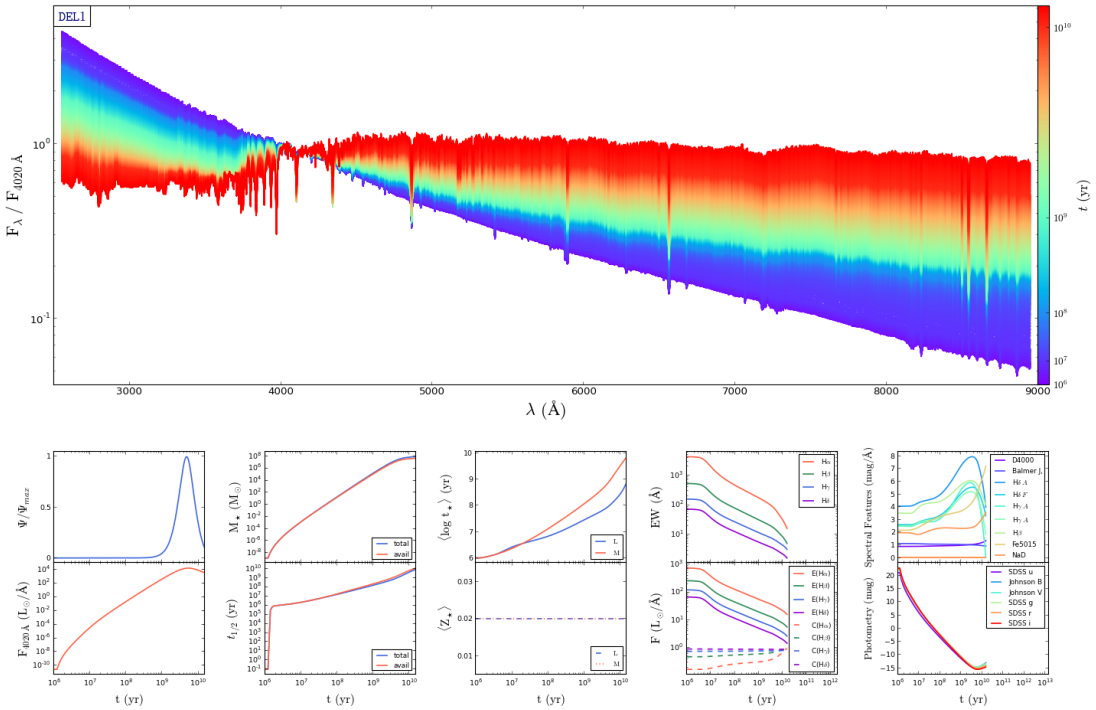

Figure A.1.5: Synthetic CSP spectra normalised at $\lambda_0 = 4020$ Å and other spectrophotometric quantities computed with REBETIKO for the SFH labeled as `DEL1` in Figure 2.1.1. Panel display configuration and legend details are identical to those in Figure 2.2.1.

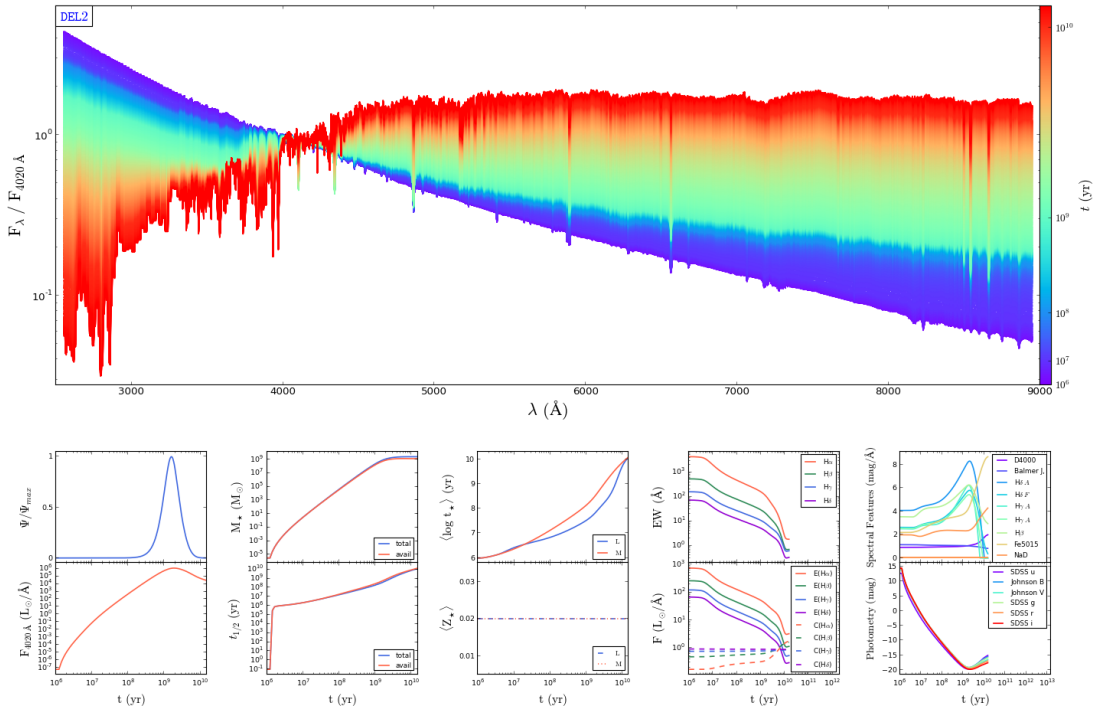

Figure A.1.6: Synthetic CSP spectra normalised at $\lambda_0 = 4020$ Å and other spectrophotometric quantities computed with REBETIKO for the SFH labeled as `DEL2` in Figure 2.1.1. Panel display configuration and legend details are identical to those in Figure 2.2.1.

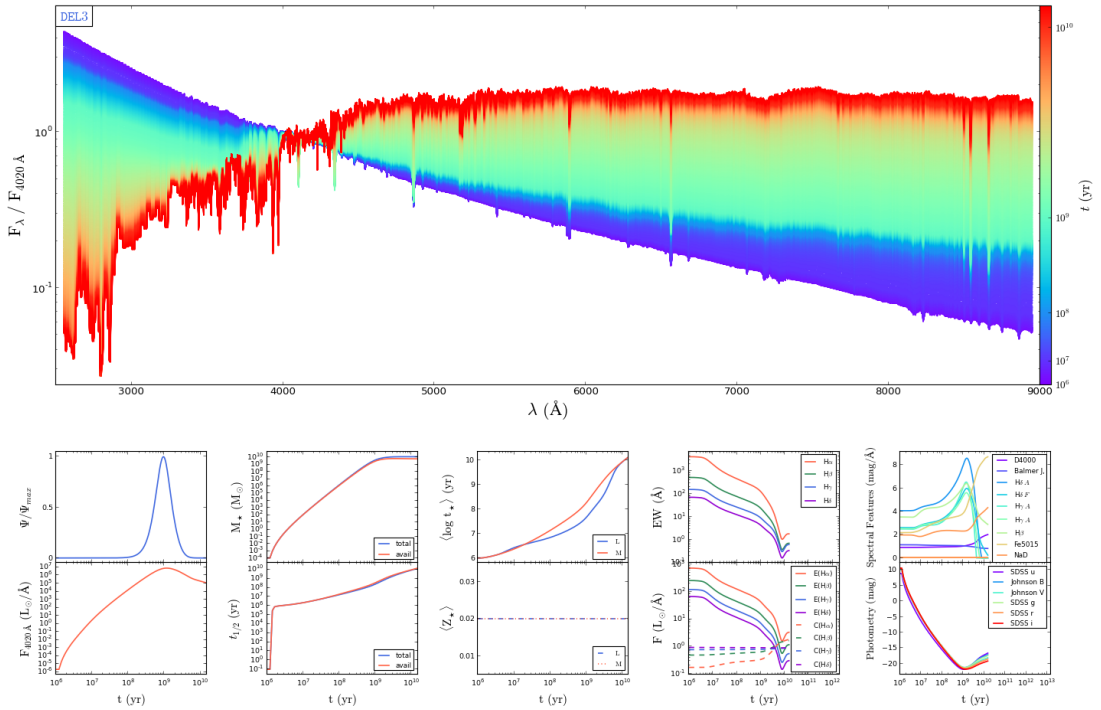

Figure A.1.7: Synthetic CSP spectra normalised at $\lambda_0 = 4020$ Å and other spectrophotometric quantities computed with REBETIKO for the SFH labeled as `DEL3` in Figure 2.1.1. Panel display configuration and legend details are identical to those in Figure 2.2.1.

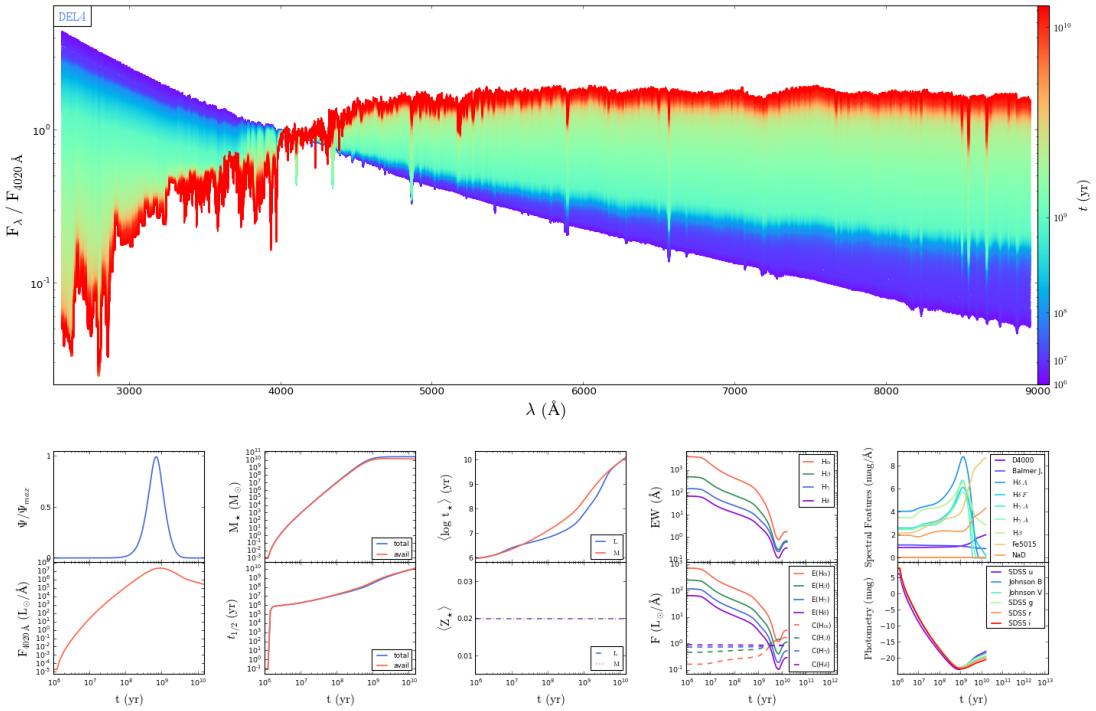

Figure A.1.8: Synthetic CSP spectra normalised at $\lambda_0 = 4020$ Å and other spectrophotometric quantities computed with REBETIKO for the SFH labeled as `DEL4` in Figure 2.1.1. Panel display configuration and legend details are identical to those in Figure 2.2.1.

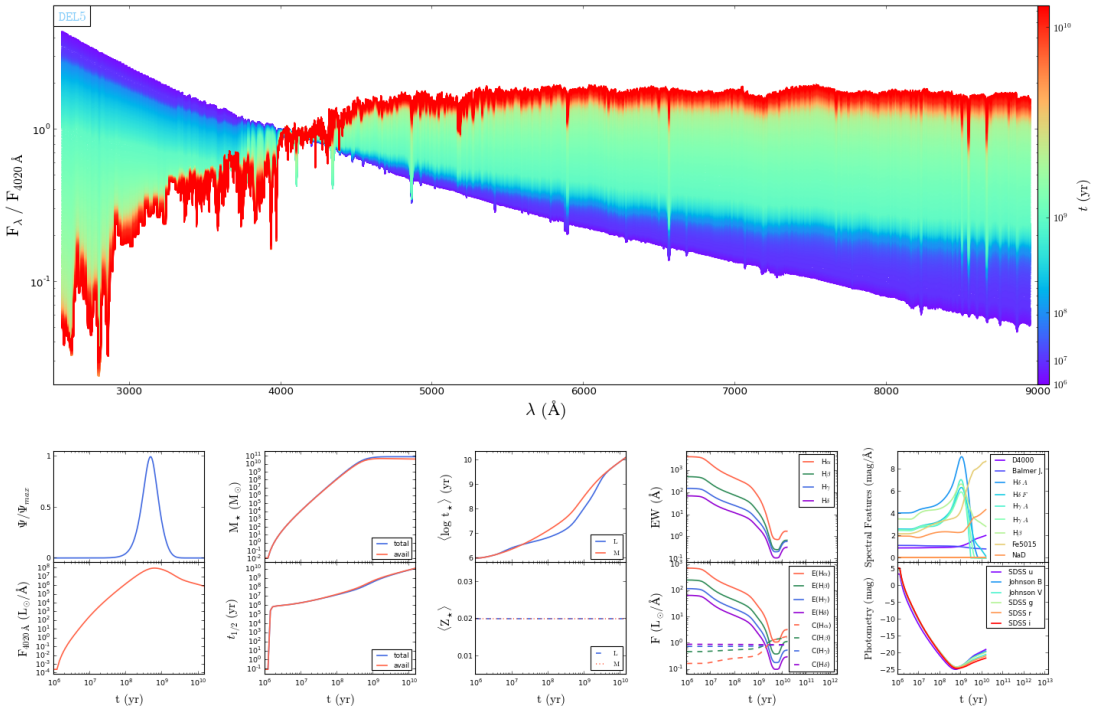

Figure A.1.9: Synthetic CSP spectra normalised at $\lambda_0 = 4020$ Å and other spectrophotometric quantities computed with REBETIKO for the SFH labeled as `DEL5` in Figure 2.1.1. Panel display configuration and legend details are identical to those in Figure 2.2.1.

A.2 Analysis of active galaxy models

Figures A.2.1–A.2.5 presents PSS results for AG synthetic spectra for the SFHs presented in Figure 2.1.1 considering a purely-stellar modelling approach. Moreover, Figures A.2.6–A.2.11 present results for CSPs with continuous SFH similar to the Figures 3.2.6–3.2.11 displayed synthesis results an instantaneous burst SFH, respectively.

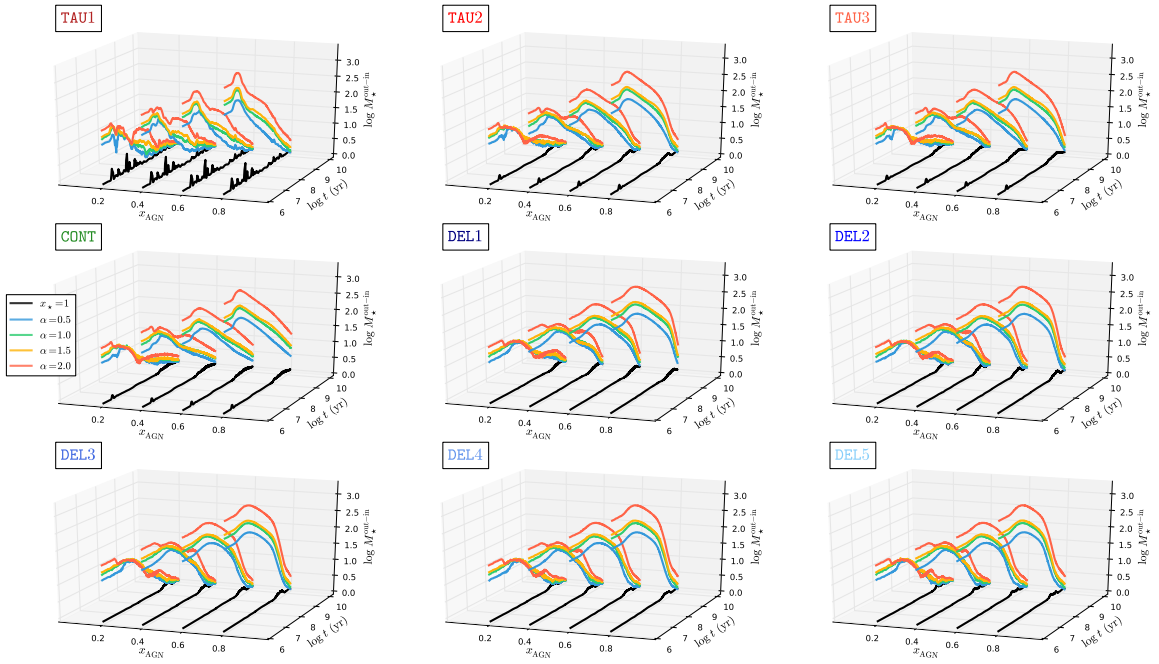

Figure A.2.1: Difference in the total stellar mass $M_\star$ between STARLIGHT (out) and REBETIKO (in) values (z axis) as a function of CSP age t (y axis) and AGN fractional contribution $x_{\rm AGN}$ (x axis). Panels from left- to right-hand side and top to bottom represent the exponentially declining, continuous and delayed SFHs displayed in Figure 2.1.1. Black, blue, green, yellow and red lines represent purely-stellar CSPs ($x_\star = 1$) and AGs with $\alpha = 0.5$, 1.0, 1.5 and 2.0, respectively.

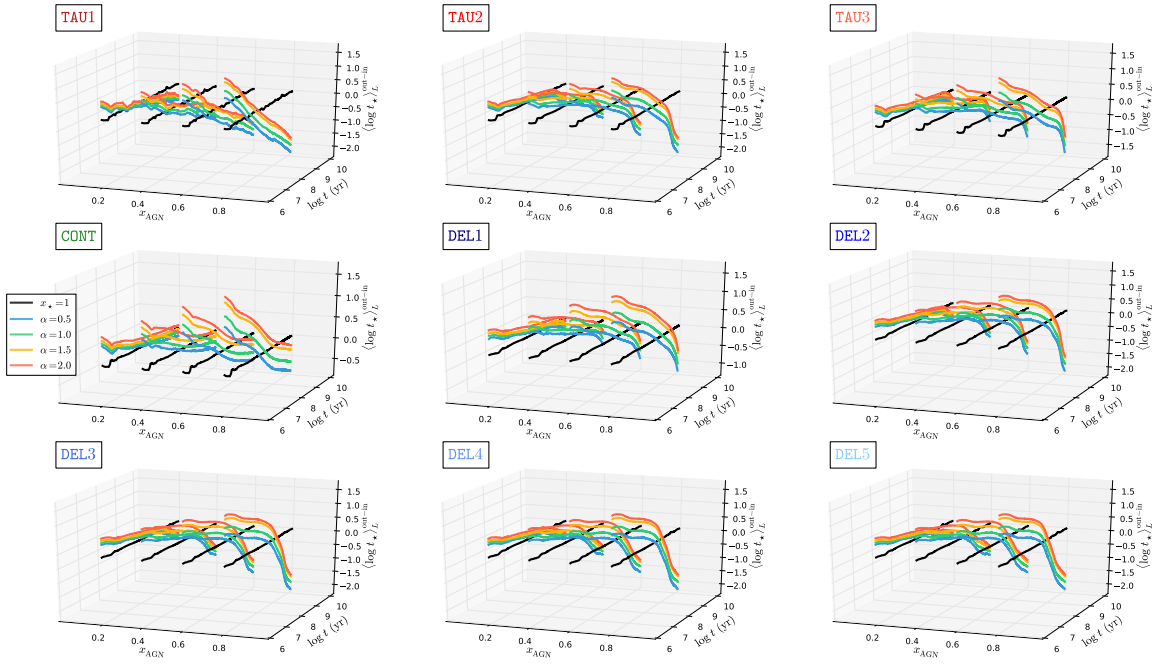

Figure A.2.2: Difference in the light-weighted mean stellar age $\langle \log t_\star \rangle_L$ between STARLIGHT and REBETIKO values (z axis) as a function of CSP age t (y axis) and AGN fractional contribution (x axis). Panel display configuration and legend details are identical to those in Figure A.2.1.

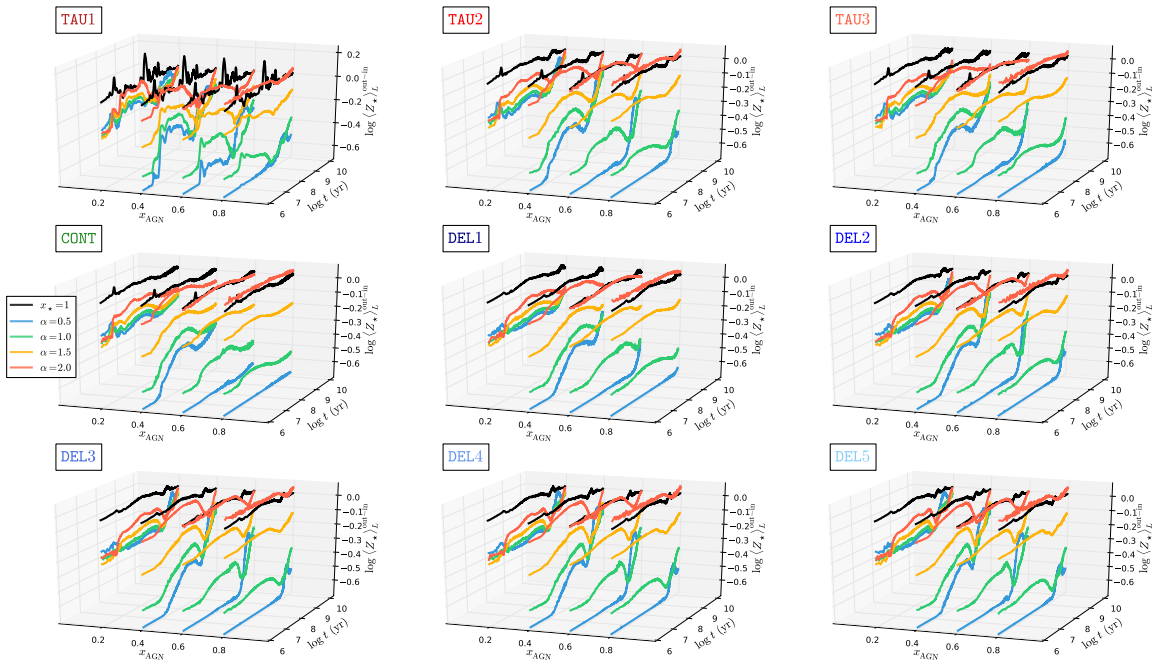

Figure A.2.3: Difference in the light-weighted mean stellar metallicity $\log \langle Z_\star \rangle_L$ between STARLIGHT and REBETIKO values (z axis) as a function of CSP age t (y axis) and AGN fractional contribution (x axis). Panel display configuration and legend details are identical to those in Figure A.2.1.

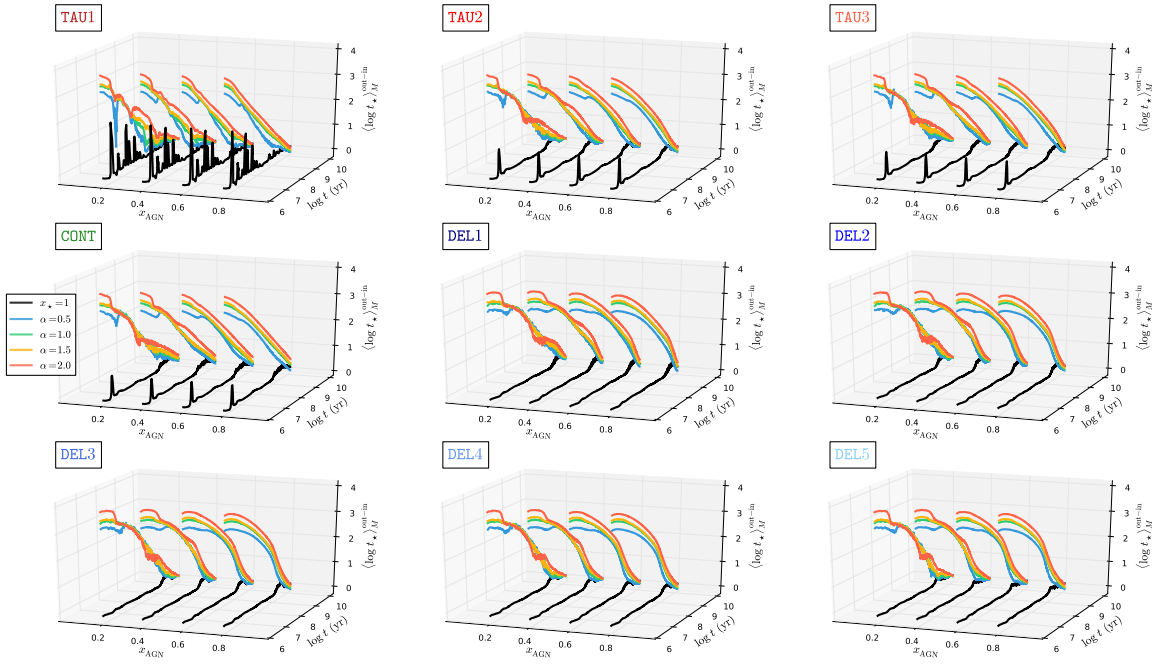

Figure A.2.4: Difference in the mass-weighted mean stellar age $\langle \log t_\star \rangle_M$ between STARLIGHT and REBETIKO values (z axis) as a function of CSP age t (y axis) and AGN fractional contribution (x axis). Panel display configuration and legend details are identical to those in Figure A.2.1.

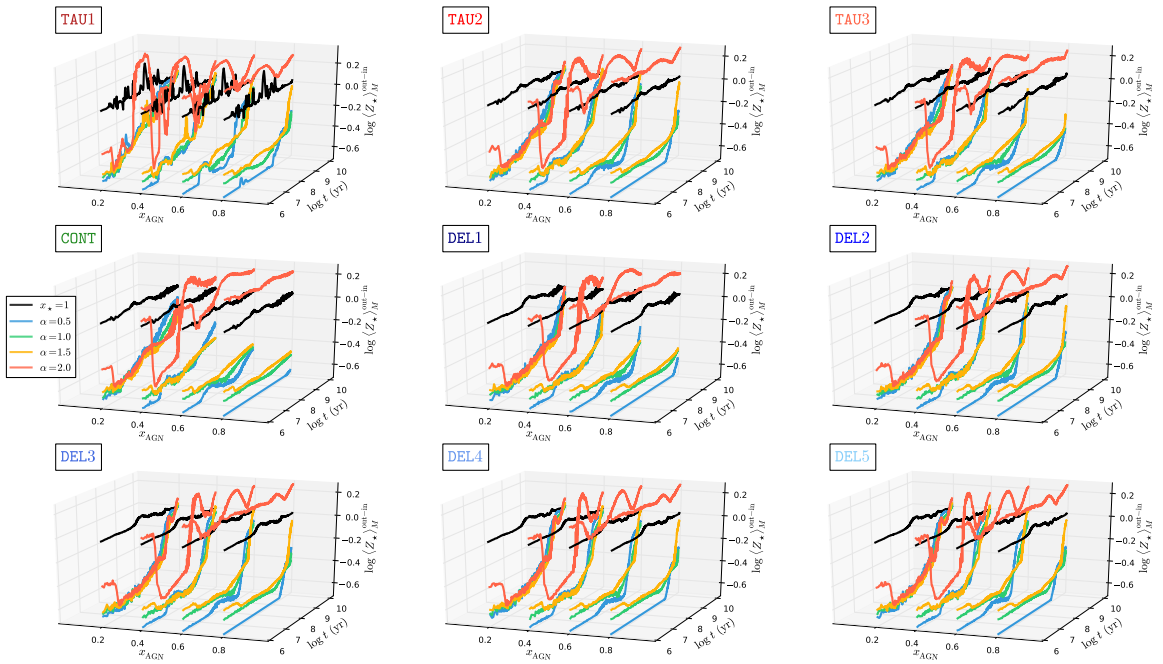

Figure A.2.5: Difference in the mass-weighted mean stellar metallicity $\log \langle Z_\star \rangle_M$ between STARLIGHT and REBETIKO values (z axis) as a function of CSP age t (y axis) and AGN fractional contribution (x axis). Panel display configuration and legend details are identical to those in Figure A.2.1.

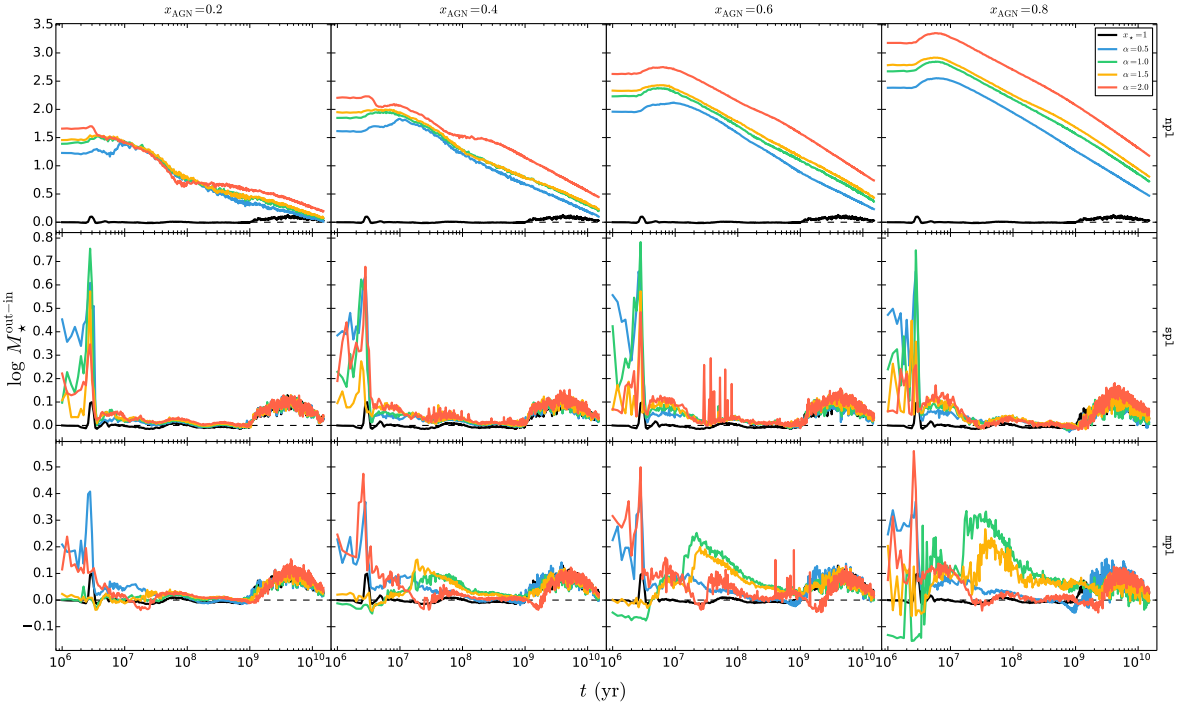

Figure A.2.6: Difference in the total stellar mass $M_\star$ between STARLIGHT (out) and REBETIKO (in) values as a function of CSP age t for CSPs with continuous SFH. Panel display and legend details are identical to those in Figure 3.2.6.

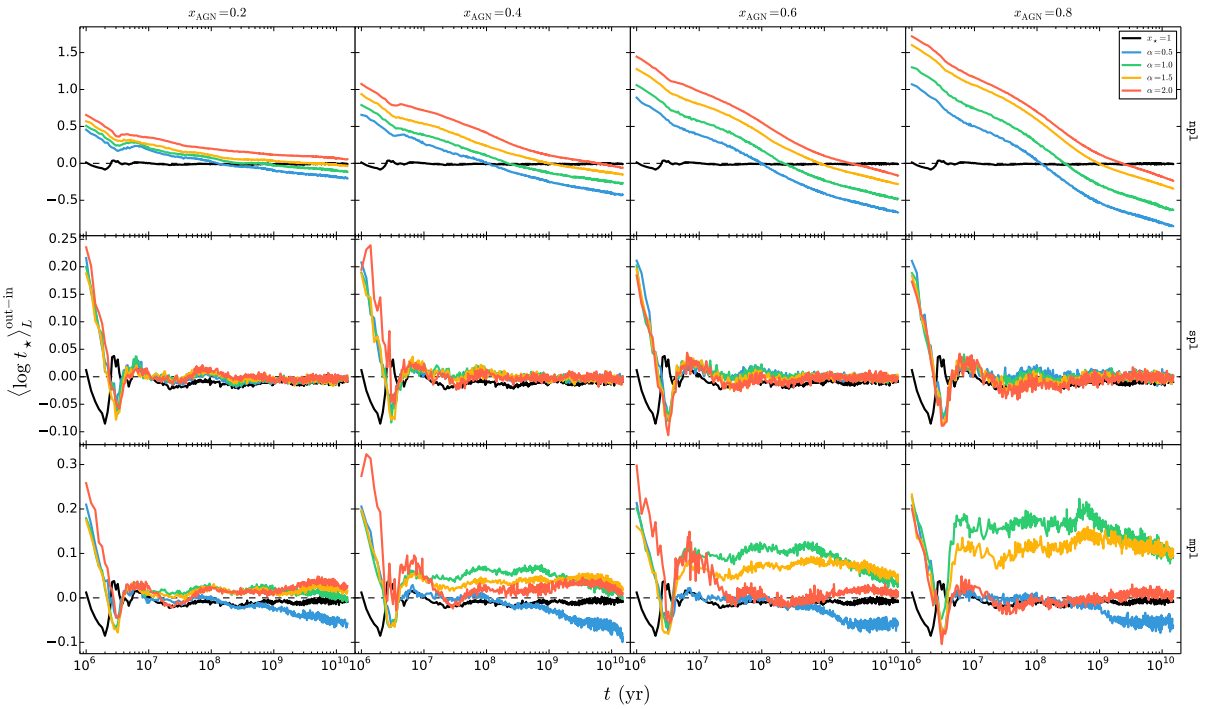

Figure A.2.7: Difference in the light-weighted mean stellar age $\langle \log t_\star \rangle_L$ between STARLIGHT (out) and REBETIKO (in) values as a function of CSP age t for CSPs with continuous SFH. Panel display and legend details are identical to those in Figure 3.2.6.

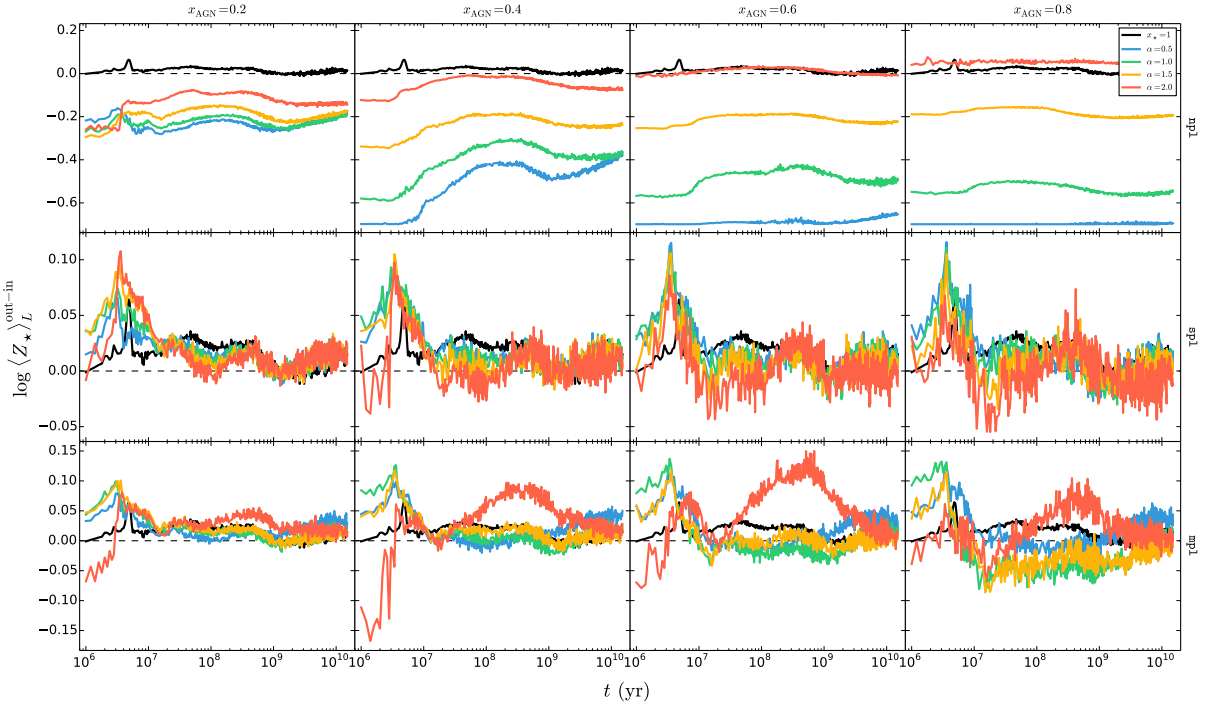

Figure A.2.8: Difference in the light-weighted mean stellar metallicity $\log\langle Z_\star\rangle_L$ between STARLIGHT (out) and REBETIKO (in) values as a function of CSP age t for CSPs with continuous SFH. Panel display and legend details are identical to those in Figure 3.2.6.

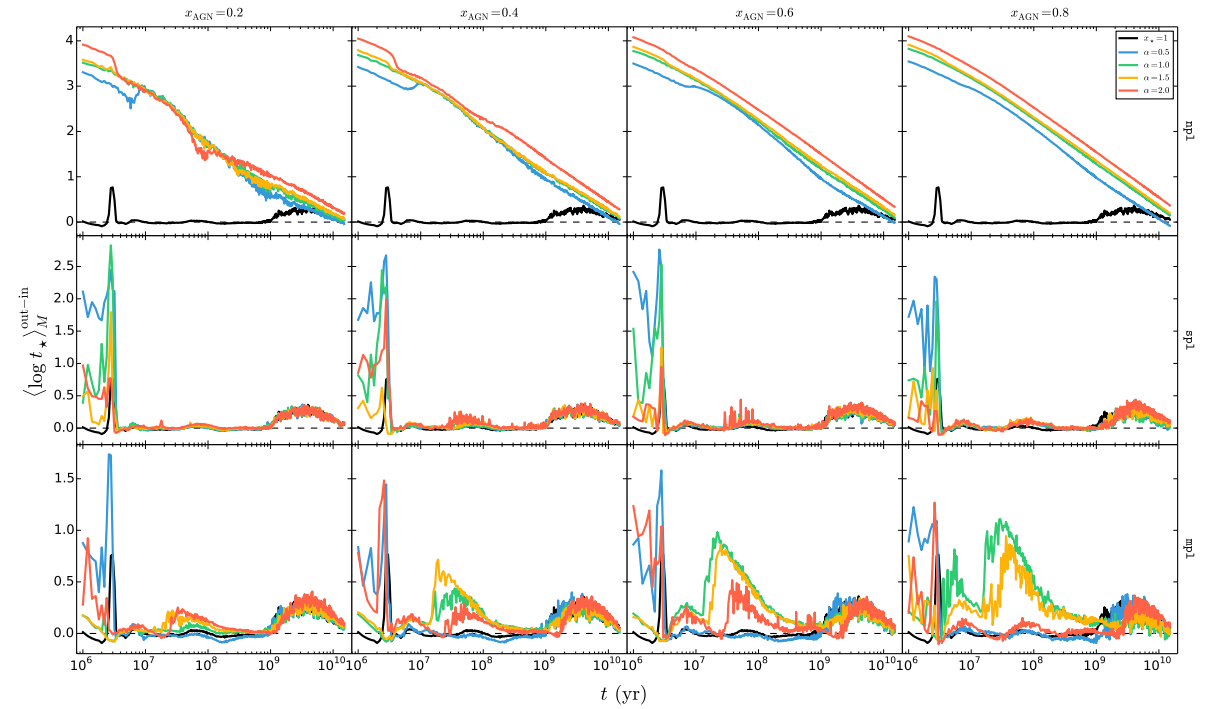

Figure A.2.9: Difference in the mass-weighted mean stellar age $\langle \log t_\star\rangle_M$ between STARLIGHT (out) and REBETIKO (in) values as a function of CSP age t for CSPs with continuous SFH. Panel display and legend details are identical to those in Figure 3.2.6.

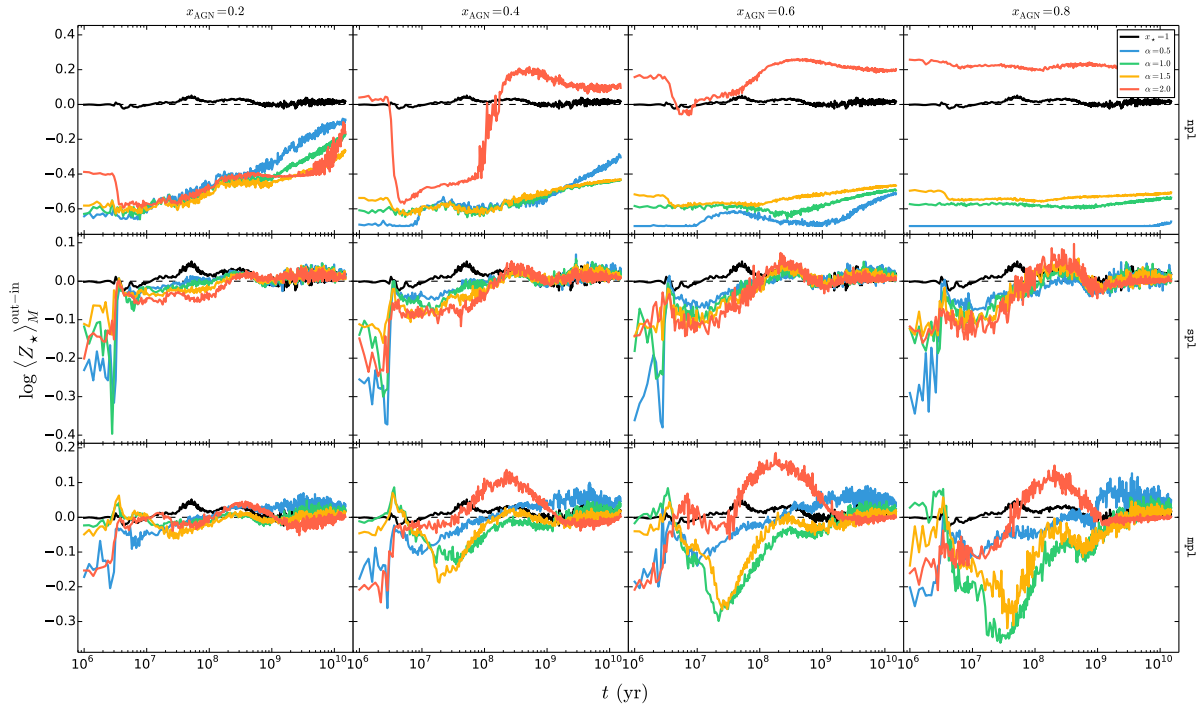

Figure A.2.10: Difference in the mass-weighted mean stellar metallicity $\log\langle Z_\star\rangle_M$ between STARLIGHT (out) and REBETIKO (in) values as a function of CSP age t for CSPs with continuous SFH. Panel display and legend details are identical to those in Figure 3.2.6.

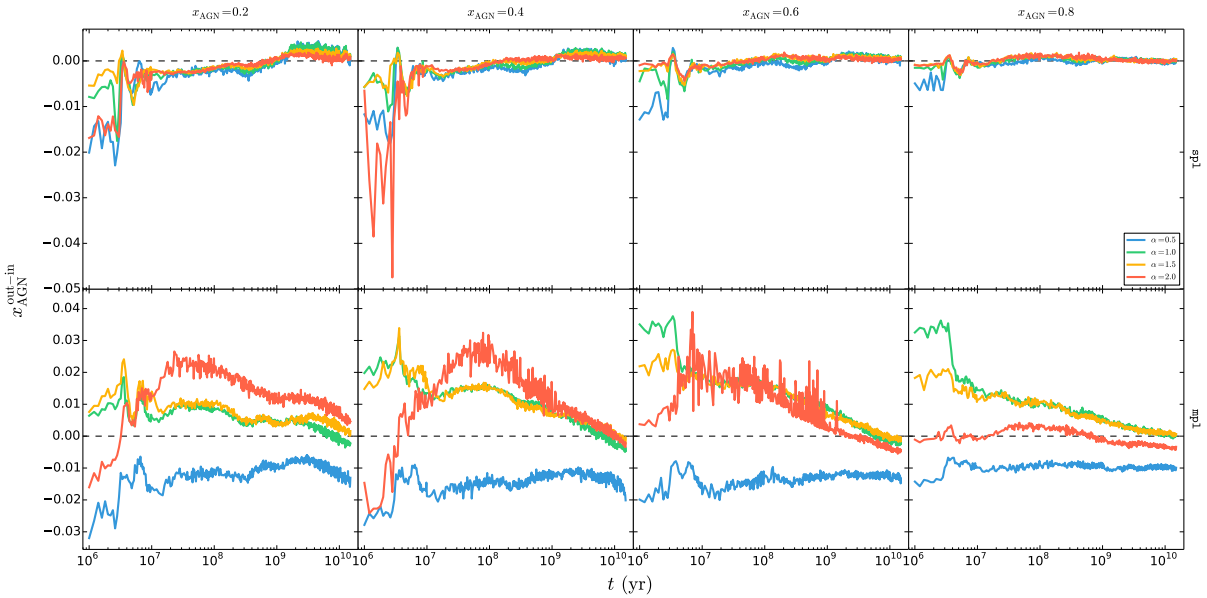

Figure A.2.11: Difference in the AGN fractional contribution $x_{\rm AGN}$ between STARLIGHT (out) and REBETIKO (in) values as a function of CSP age t for CSPs with continuous SFH. Panel display and legend details are identical to those in Figure 3.2.6.

A.3 Analysis of nebular emission models

Figures A.3.1 and A.3.2 show results for CSP photoionisation simulations on the VO1987 diagrams. Moreover, Figures A.3.3–A.3.7 presents PSS results for AGs with NE. Finally, Figures A.3.8–A.3.9 present synthetic CSP spectra with NE and other spectrophotometric properties of evolutionary models created with the ESS code REBETIKO for instantaneous burst and continuous SFHs.

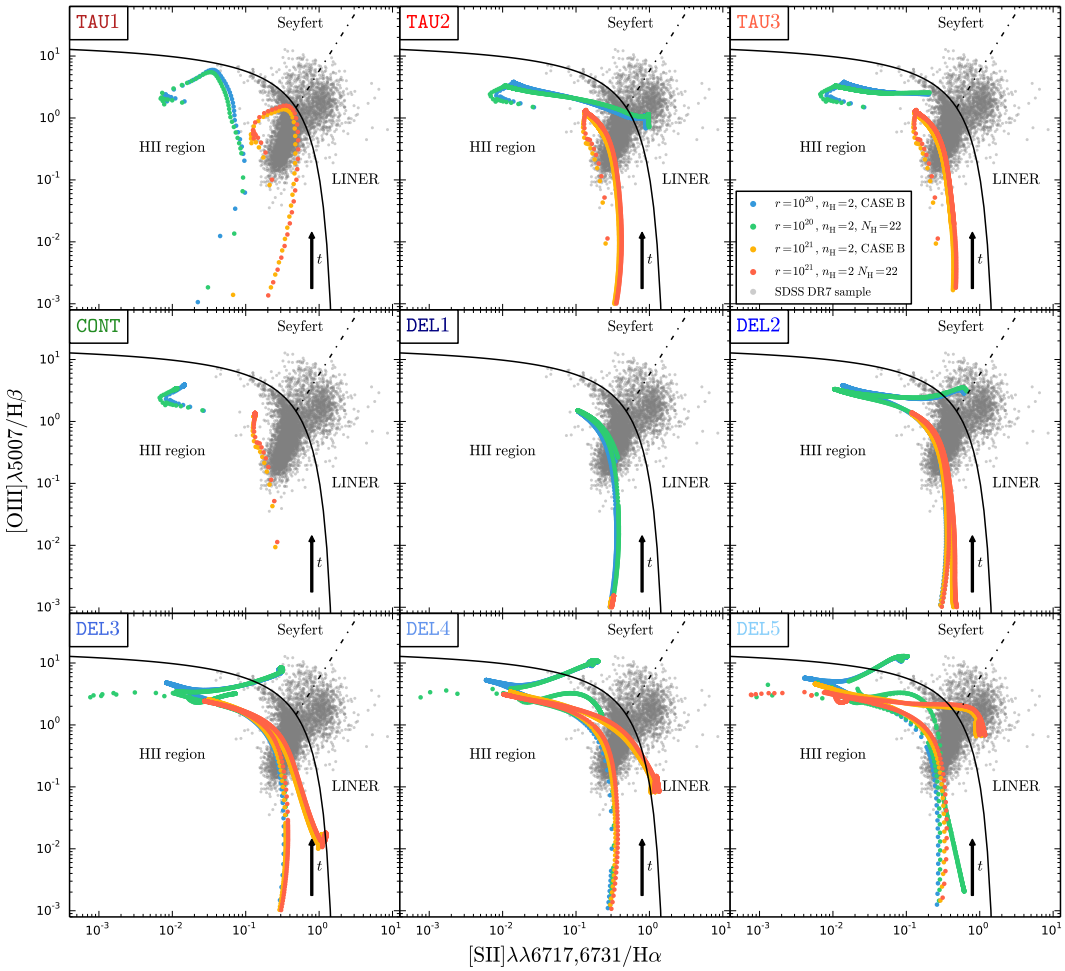

Figure A.3.1: Emission-line flux ratio [SII]$\lambda\lambda$6717,6731/Hα as a function of [OIII]λ5007/Hβ for CSP simulations computed with CLOUDY. Panel display configuration and legend details are identical to those in Figure 4.1.4.

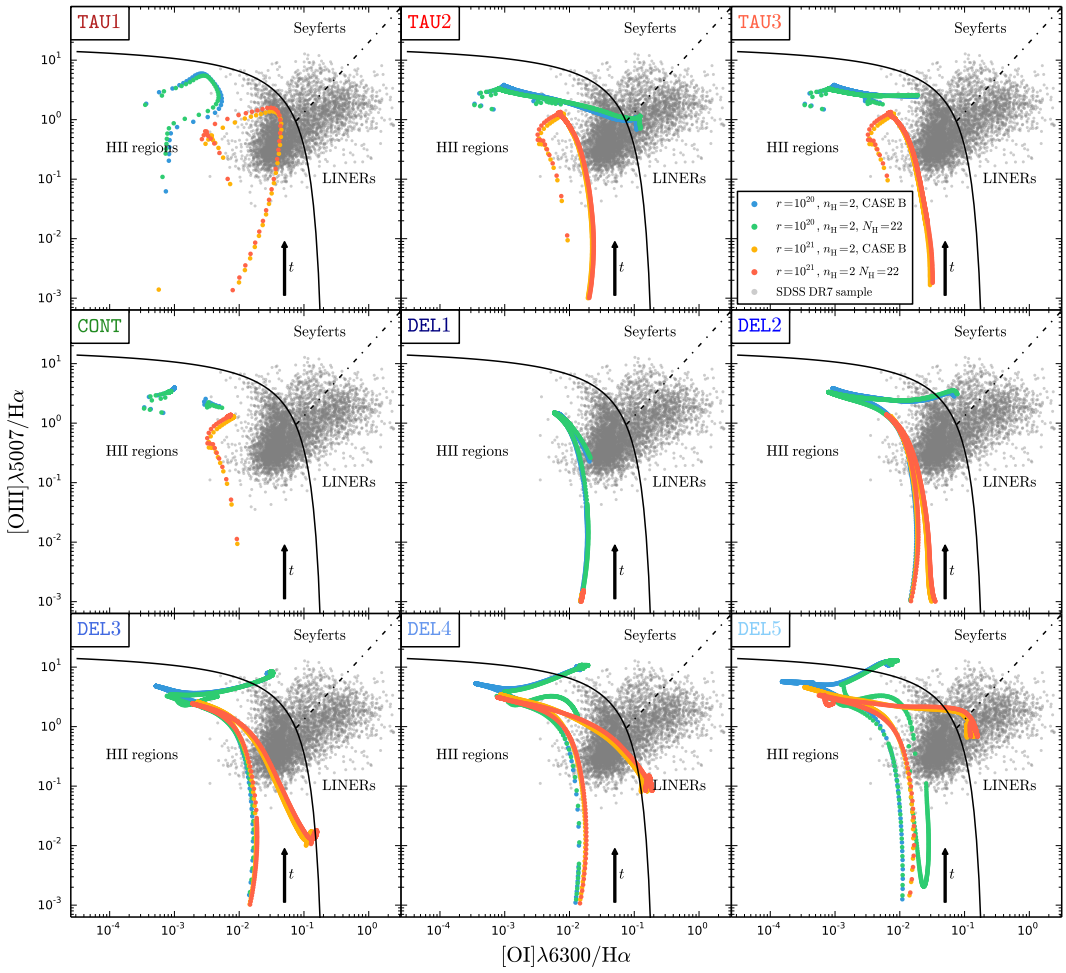

Figure A.3.2: Emission-line flux ratio [OI]λ6300/Hα as a function of [OIII]λ5007/Hβ for CSP simulations computed with CLOUDY. Panel display configuration and legend details are identical to those in Figure 4.1.4.

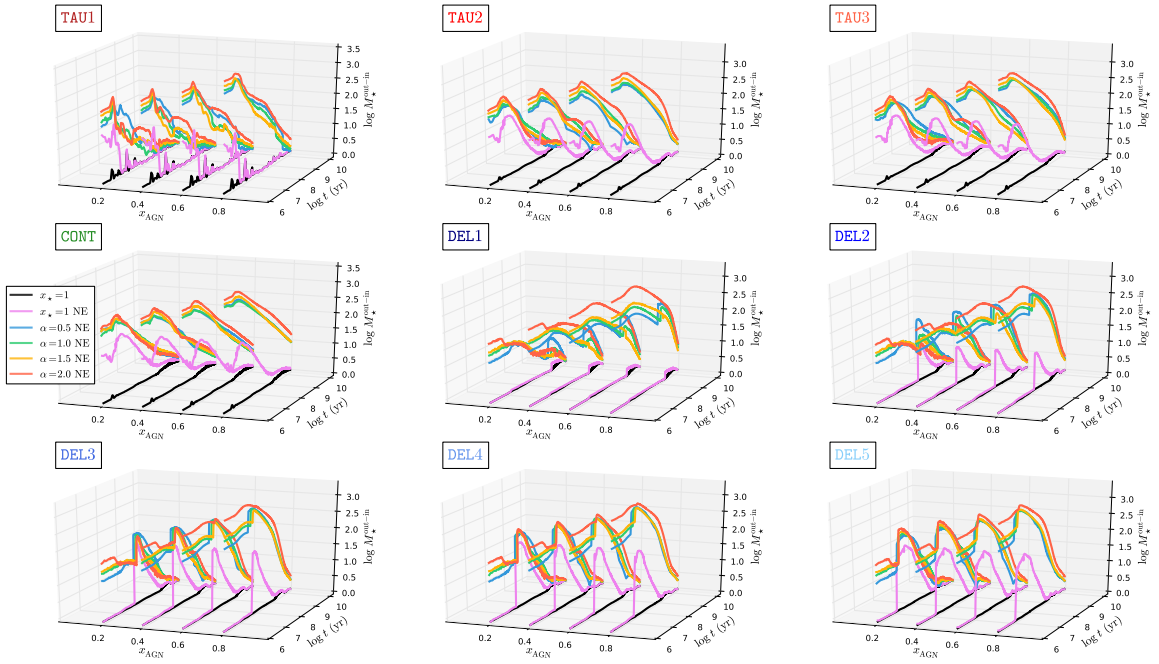

Figure A.3.3: Difference in the total stellar mass $M_\star$ between STARLIGHT (out) and REBETIKO (in) values (z axis) as a function of CSP age t (y axis) and AGN fractional contribution $x_{\rm AGN}$ (x axis) for AGs with NE. Panels from left- to right-hand side and top to bottom represent the exponentially declining, continuous and delayed SFHs displayed in Figure 2.1.1. Black and violet lines represent results of CSPs without and with NE, respectively. Blue, green, yellow and red lines represent results for AGs with NE and $\alpha = 0.5$, 1, 1.5 and 2, respectively.

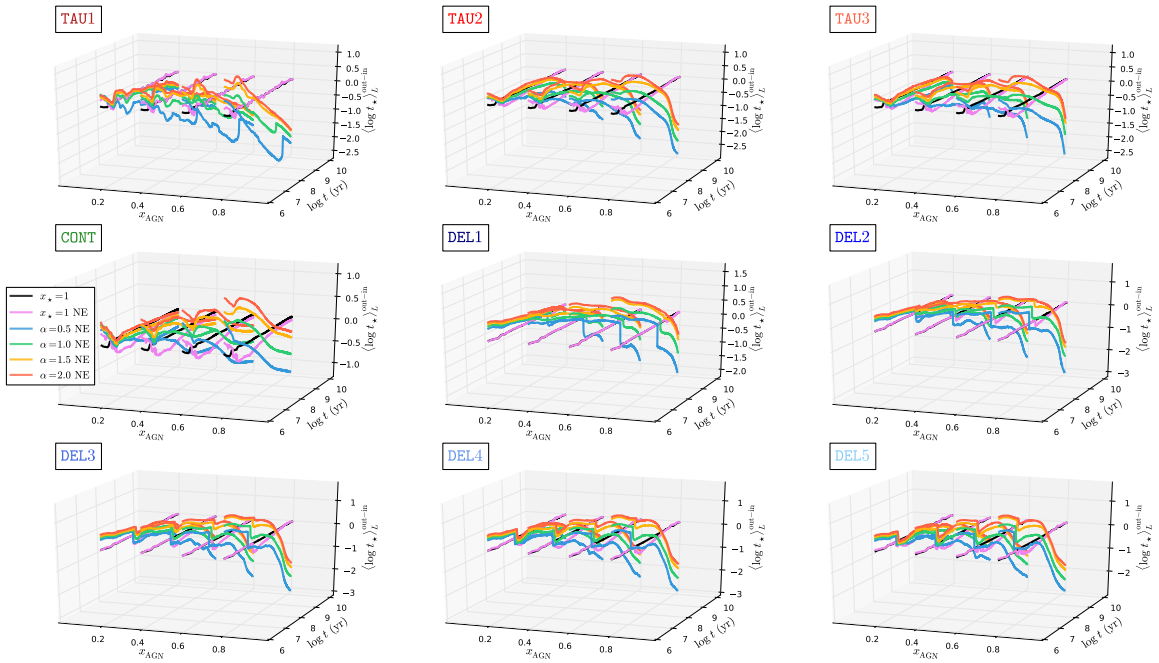

Figure A.3.4: Difference in the light-weighted mean stellar age $\langle \log t_\star \rangle_L$ between STARLIGHT and REBETIKO values (z axis) as a function of CSP age t (y axis) and AGN fractional contribution (x axis) for AGs with NE. Panel display configuration and legend details are identical to those in Figure A.3.3.

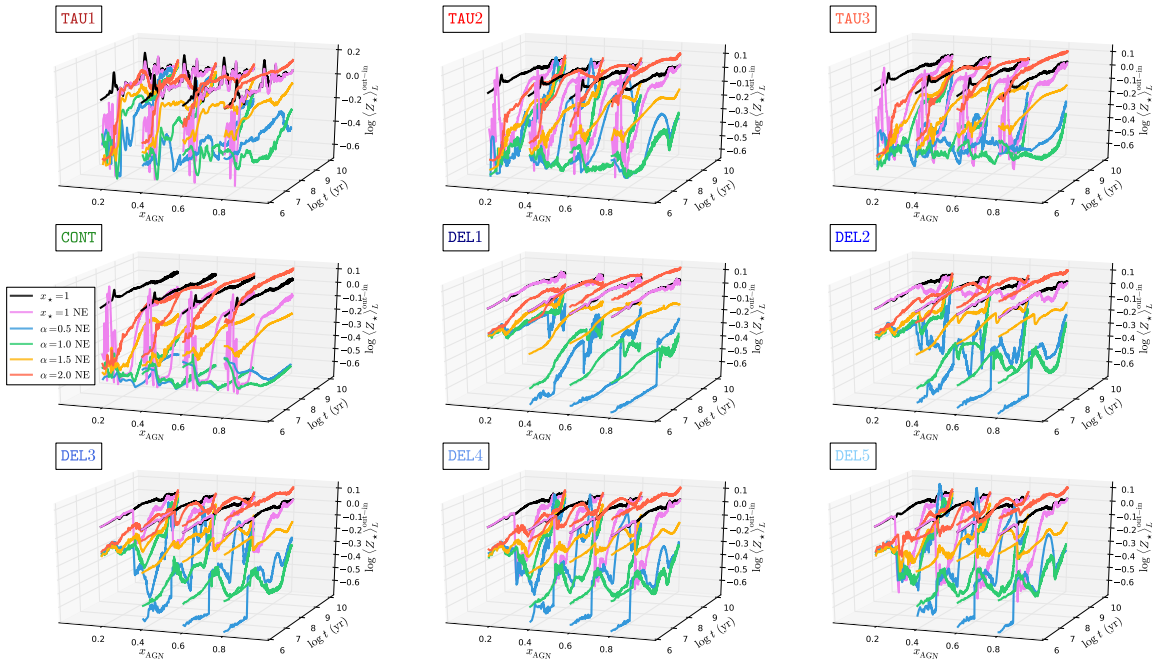

Figure A.3.5: Difference in the light-weighted mean stellar metallicity $\log\langle Z_\star\rangle_L$ between STARLIGHT and REBETIKO values (z axis) as a function of CSP age t (y axis) and AGN fractional contribution (x axis) for AGs with NE. Panel display configuration and legend details are identical to those in Figure A.3.3.

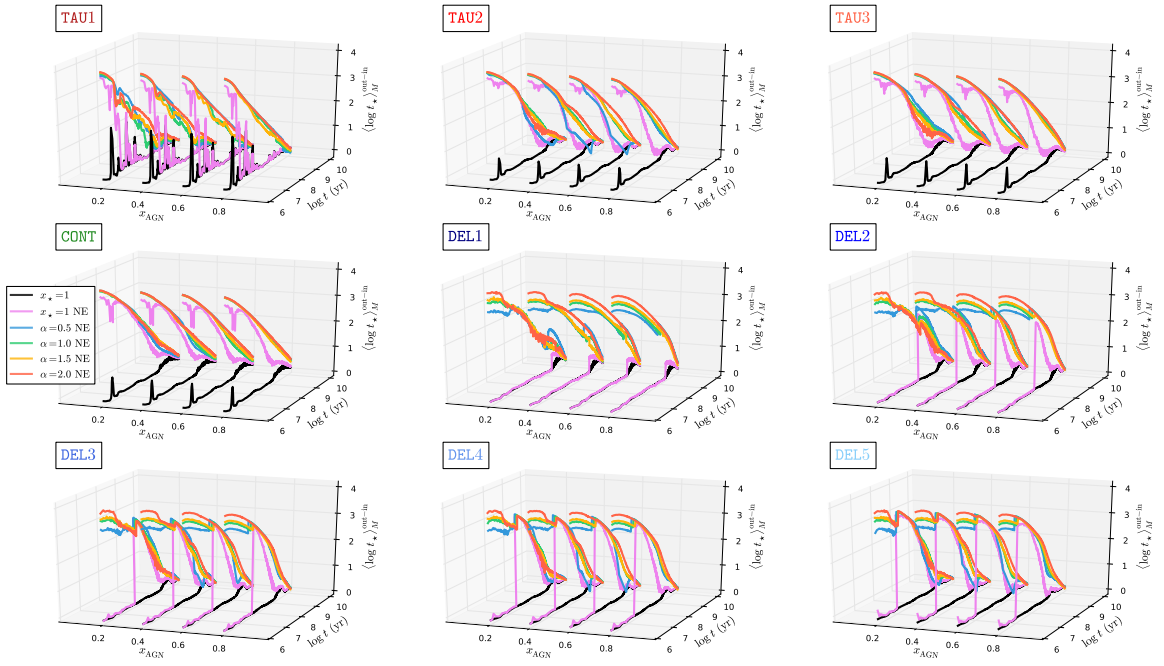

Figure A.3.6: Difference in the mass-weighted mean stellar age $\langle\log t_\star\rangle_M$ between STARLIGHT and REBETIKO values (z axis) as a function of CSP age t (y axis) and AGN fractional contribution (x axis) for AGs with NE. Panel display configuration and legend details are identical to those in Figure A.3.3.

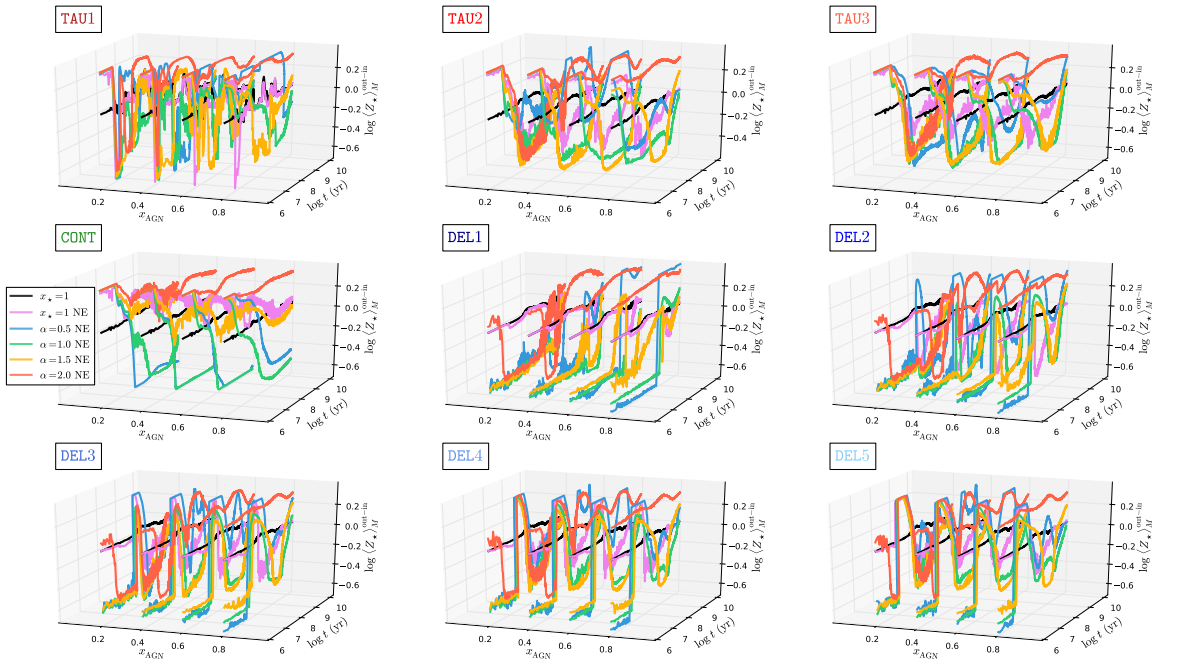

Figure A.3.7: Difference in the mass-weighted mean stellar metallicity $\log\langle Z_\star\rangle_M$ between STARLIGHT and REBETIKO values (z axis) as a function of CSP age t (y axis) and AGN fractional contribution (x axis) for AGs with NE. Panel display configuration and legend details are identical to those in Figure A.3.3.

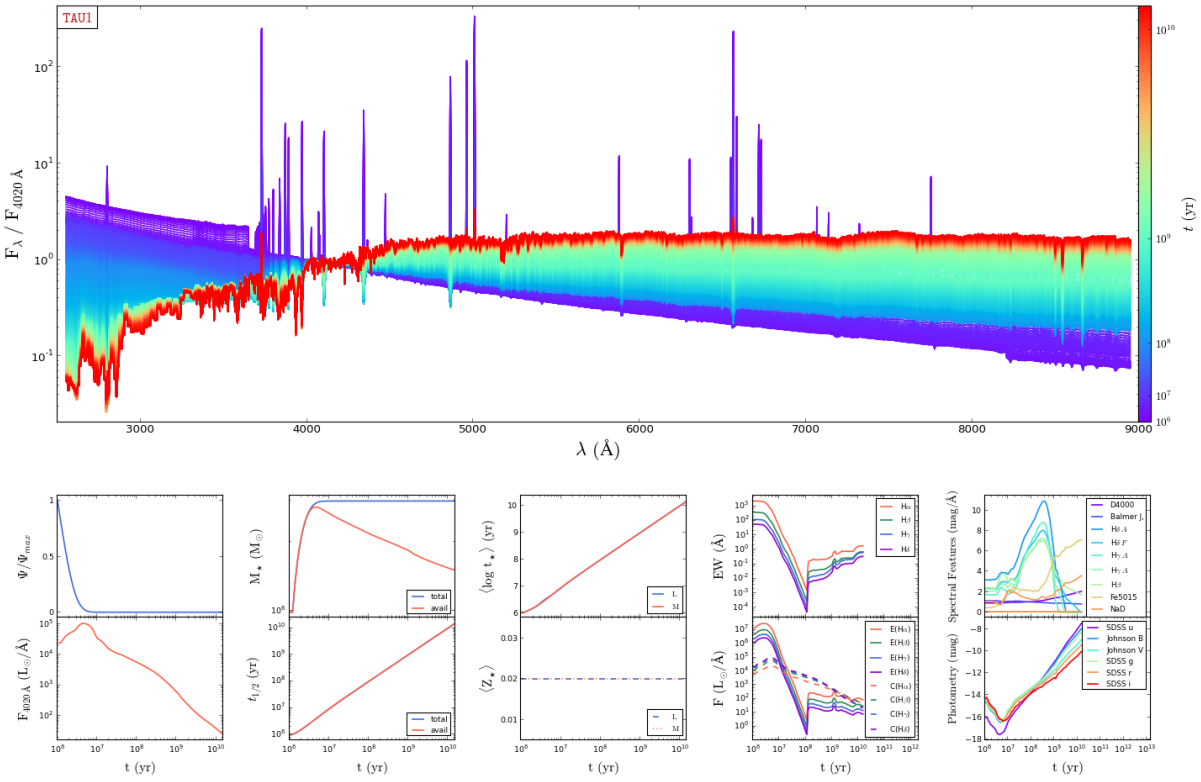

Figure A.3.8: Synthetic CSP spectra with NE normalised at $\lambda_0 = 4020$ Å and other spectrophotometric quantities computed with REBETIKO for the SFH labeled as `TAU1` in Figure 2.1.1. Panel display configuration and legend details are identical to those in Figure 2.2.1.

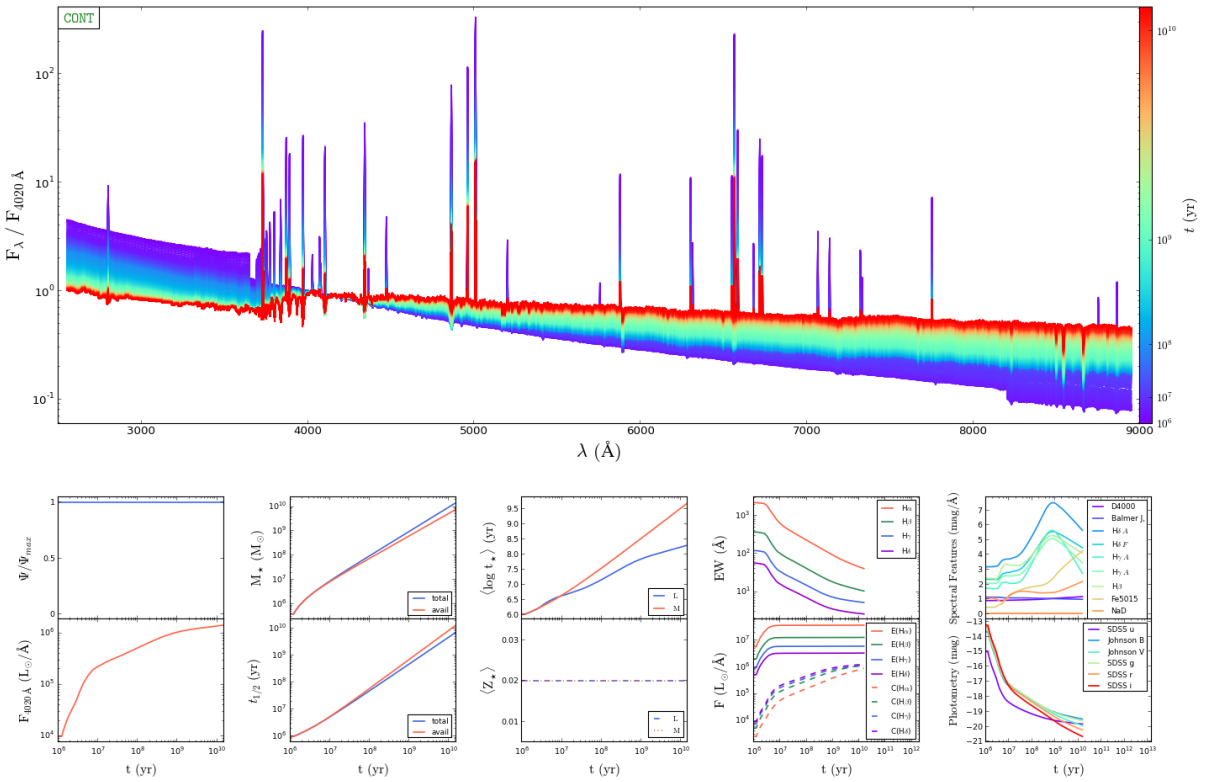

Figure A.3.9: Synthetic CSP spectra with NE normalised at $\lambda_0 = 4020$ Å and other spectrophotometric quantities computed with REBETIKO for the SFH labeled as `CONT` in Figure 2.1.1. Panel display configuration and legend details are identical to those in Figure 2.2.1.

B

Publications & Communications

Refereed Publications

- Roche, N., Humphrey, A., Lagos, P., Papaderos, P., Silva, M., Cardoso, L. S. M., Gomes, J. M., 2016 "*MUSE 3D Spectroscopy and Kinematics of the gigahertz peaked spectrum Radio Galaxy PKS 1934-63: Interaction, Recently Triggered AGN and Star Formation*", MNRAS, 459, 4259, arXiv: 1604.00309
- Cardoso, L. S. M., Gomes, J. M., and Papaderos, P., 2016 "*Semi-empirical AGN detection threshold in spectral synthesis studies of Lyman-continuum-leaking early-type galaxies*", A&A, 594, L2, arXiv: 1609.08792
- Cardoso, L. S. M., Gomes, J. M., and Papaderos, P., 2016 "*Impact of an AGN featureless continuum on the estimation of stellar population properties*", A&A, arXiv: 1705.04224

Conference Proceedings

- Cardoso, L. S. M., Gomes, J. M., and Papaderos, P., "*Evaluating the robustness of state-of-the-art spectral synthesis when applied to Active Galaxies*" – XXIV Encontro Nacional de Astronomia e Astrofísica (ENAA), Porto, Portugal, 2014
- Cardoso, L. S. M., Gomes, J. M., and Papaderos, P., "*Quantifying the impact of AGN and nebular emission on stellar population properties with REBETIKO*" – The interplay between local and global processes in galaxies, Cozumel, México, 2016

Scientific Presentations

– "*Evaluating the robustness of state-of-the-art spectral synthesis when applied to Active Galaxies*" (*contributed presentation*) – XXIV Encontro Nacional de Astronomia e Astrofísica (ENAA), Porto, Portugal, 18^{th} of June 2014

– "*Impact of a toy AGN model in stellar population properties with state-of-the-art spectral synthesis*" (*contributed talk*) – X Estallidos Workshop, Granada, Spain, 12^{th} of May 2015

– "*Quantifying the impact of AGN and nebular emission on stellar population properties with REBETIKO*" (*poster presentation*) – The interplay between local and global processes in galaxies, Cozumel, México, 11^{th}–15^{th} of April 2016

– "*Spectral synthesis studies of accretion-powered nuclear activity in galaxies in the presence of extensive Lyman continuum photon escape*" (*contributed talk*) – Escape of Lyman radiation from galactic labyrinths, Crete, Greece, 22^{nd}–26^{th} of April 2016

A&A 594, L2 (2016)
DOI: 10.1051/0004-6361/201629278

Astronomy & Astrophysics

Letter to the Editor

Semi-empirical AGN detection threshold in spectral synthesis studies of Lyman-continuum-leaking early-type galaxies

Leandro S. M. Cardoso[1,2], Jean-Michel Gomes[1], and Polychronis Papaderos[1]

[1] Instituto de Astrofísica e Ciências do Espaço, Universidade do Porto, CAUP, Rua das Estrelas, 4150-762 Porto, Portugal
e-mail: Leandro.Cardoso@astro.up.pt
[2] Departamento de Física e Astronomia, Faculdade de Ciências, Universidade do Porto, Rua do Campo Alegre 687, 4169-007 Porto, Portugal

Received 8 July 2016 / Accepted 19 September 2016

ABSTRACT

Various lines of evidence suggest that the cores of a large portion of early-type galaxies (ETGs) are virtually evacuated of warm ionised gas. This implies that the Lyman-continuum (LyC) radiation produced by an assumed active galactic nucleus (AGN) can escape from the nuclei of these systems without being locally reprocessed into nebular emission, which would prevent their reliable spectroscopic classification as Seyfert galaxies with standard diagnostic emission-line ratios. The spectral energy distribution (SED) of these ETGs would then lack nebular emission and be essentially composed of an old stellar component and the featureless power-law (PL) continuum from the AGN. A question that arises in this context is whether the AGN component can be detected with current spectral population synthesis in the optical, specifically, whether these techniques effectively place an AGN detection threshold in LyC-leaking galaxies. To quantitatively address this question, we took a combined approach that involves spectral fitting with STARLIGHT of synthetic SEDs composed of stellar emission that characterises a 10 Gyr old ETG and an AGN power-law component that contributes a fraction $0 \leq x_{\rm AGN} < 1$ of the monochromatic luminosity at $\lambda_0 = 4020$ Å. In addition to a set of fits for PL distributions $F_\nu \propto \nu^{-\alpha}$ with the canonical $\alpha = 1.5$, we used a base of multiple PLs with $0.5 \leq \alpha \leq 2$ for a grid of synthetic SEDs with a signal-to-noise ratio of 5–10^3. Our analysis indicates an effective AGN detection threshold at $x_{\rm AGN} \simeq 0.26$, which suggests that a considerable fraction of ETGs hosting significant accretion-powered nuclear activity may be missing in the AGN demographics.

Key words. galaxies: active – galaxies: nuclei – galaxies: stellar content – galaxies: evolution

1. Introduction

The build-up of super-massive black holes (SMBHs) and co-evolution with their galaxy hosts is a central question in extragalactic astronomy. In this regard, comprehensive multi-wavelength studies of matter accretion onto SMBHs and the associated active galactic nuclei (AGN) phenomenon are fundamental for elucidating the interplay between SMBH growth and galaxy assembly history. Accretion-powered activity in galaxies is mostly being addressed in the optical through emission-line ratio diagnostics, which allow distinguishing between, for instance, gas photoionisation by an AGN and OB stars (e.g. Baldwin et al. 1981; Veilleux & Osterbrock 1987). The diagnostic power of such methods presumably vanishes, however, when galactic nuclei are mostly evacuated of gas (e.g. permeated by hot and tenuous plasma), thereby allowing the bulk of the Lyman continuum (LyC) output from an AGN to escape without being locally reprocessed as nebular emission. In those cases the optical spectral energy distribution (SED) is expected to essentially consist of stellar emission and a featureless AGN continuum. In the limiting case of a dominant AGN and high LyC-photon escape fraction, the optical SED of a galaxy is therefore expected to entirely lack both nebular (continuum and line) emission and stellar absorption features and superficially somewhat resemble that of a BL Lac (e.g. Oke & Gunn 1974; Marchã et al. 1996; Kügler et al. 2014).

The situation of an AGN leaking LyC radiation envisaged here may apply to many early-type galaxy (ETG) nuclei. Papaderos et al. (2013) have first estimated the LyC escape fraction from ETG nuclei to be 70–95% (see also Gomes et al. 2016) and pointed out that LyC photon escape may constitute a key element in understanding why many of these systems, despite evidence of a strong AGN energy source in radio or X-ray wavelengths, show only weak optical emission-lines typical of low-ionization nuclear emission-line regions (LINERs, Heckman 1980). Several questions naturally arise from such considerations. For instance, to which extent can an AGN be recovered from the optical SED of such LyC-leaking ETGs using currently available spectral fitting techniques? More specifically, do these techniques effectively place a detection threshold on the featureless AGN continuum, and are they capable of recovering its main characteristics (e.g. luminosity contribution, spectral slope) simultaneously with those of the stellar component in the host galaxy?

Spectral population synthesis (SPS, also referred to as the inverse or semi-empirical approach; Faber 1972) has been applied over the past decades to optical Seyfert galaxy spectra with the goal of evaluating the AGN power-law (PL) featureless continuum and how this might affect the retrieved star formation history (e.g. Koski 1978; Schmitt et al. 1999; Cid Fernandes et al. 2004; Benítez et al. 2013). However, none of these works have

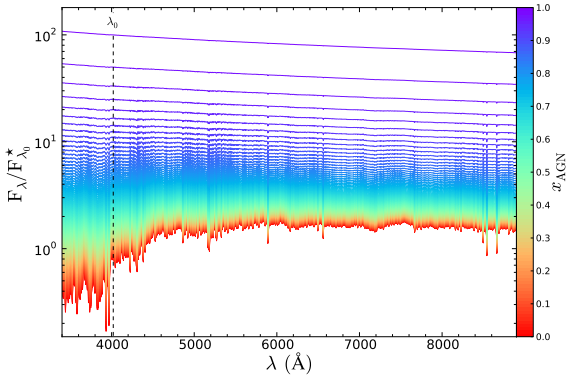

Fig. 1. Synthetic galaxy spectra resulting from the combination of a 10 Gyr old solar-metallicity stellar population with a power-law AGN continuum defined as $F_\nu \propto \nu^{-1.5}$. The colour coding represents the AGN fractional flux contribution $x_{\rm AGN}$ at $\lambda_0 = 4020$ Å.

attempted to quantitatively infer an AGN detectability threshold for LyC-leaking ETGs, which is the goal of this study.

2. Method and results

The approach taken here involves computing and subsequently modelling synthetic SEDs with an SPS code. For the first task we computed a synthetic optical spectrum with our evolutionary synthesis code REBETIKO (Papaderos & Gomes, in prep.) that represents an ETG that has formed monolithically 10 Gyr ago. For this, we adopted simple stellar population (SSP) spectra of solar metallicity ($Z_\odot = 0.02$) from Bruzual & Charlot (2003), with a Chabrier (2003) initial mass function (IMF) between 0.1 and 100 $M_\odot$ and Padova evolutionary tracks (Alongi et al. 1993; Bressan et al. 1993; Fagotto et al. 1994a,b,c; Girardi et al. 1996), and zero intrinsic extinction in the V-band ($A_V = 0$ mag). The featureless AGN continuum, which was added to the stellar SED, was parameterised by a PL defined as $F_\nu \propto \nu^{-\alpha}$ (e.g. Oke et al. 1970; O'Connell 1976; Koski 1978) with the canonical spectral index $\alpha = 1.5$ for Seyfert galaxies (e.g. Ferland & Netzer 1983; Schmitt et al. 1999; Kauffmann et al. 2003; Cid Fernandes et al. 2004). Afterwards, we attempted to recover the AGN characteristics (α, light fraction) by fitting the synthetic SEDs with the most recent publicly available version of the SPS code STARLIGHT (Cid Fernandes et al. 2005, public distribution v04).

The continuum flux F_λ at the normalisation wavelength λ_0 resulting from the superposition of the AGN PL $F^{\rm AGN}_\lambda$ to the stellar SED $F^\star_\lambda$ can be written as

$$F_\lambda = F^\star_\lambda + \frac{x_{\rm AGN}}{x_\star} F^{\rm AGN}_\lambda = F^\star_\lambda + \frac{x_{\rm AGN}}{x_\star} F^\star_{\lambda_0} \left(\frac{\lambda}{\lambda_0}\right)^{\alpha-2}, \quad (1)$$

where $x_\star$ and $x_{\rm AGN}$ are the fractional stellar and AGN flux contributions, respectively, constrained by the normalisation condition $x_\star + x_{\rm AGN} = 1$ at $\lambda_0 = 4020$ Å. Equation (1) ensures that the stellar physical properties (e.g. flux, mass) computed with REBETIKO are conserved by the addition of the AGN component.

In this work we adopted a PL index $\alpha = 1.5$ and a range for the AGN relative contribution of $x_{\rm AGN} \in [0, 1[$ in steps of 0.01 to create synthetic spectra, as shown in Fig. 1. We note that SEDs with $x_{\rm AGN} \geq 0.5$ are only included for the sake of completeness, given that already an $x_{\rm AGN} \gtrsim 0.4$ corresponds to conspicuously featureless spectra that would normally be excluded from SPS modelling upon visual inspection. Finally, the set of synthetic SEDs comprises ten signal-to-noise (S/N) ratios between 5 and 10^3 at λ_0 in order to study how the AGN recovery depends on the quality of input spectra.

The synthetic SEDs were then fitted with STARLIGHT using a base with SSPs from Bruzual & Charlot (2003) for 25 ages from 1 Myr to 13 Gyr and 4 metallicities ($Z = 0.2$, 0.4, 1 and 2.5 $Z_\odot$) with a Chabrier (2003) IMF and Padova evolutionary tracks. Additionally, the base contains a single PL with $\alpha = 1.5$, as the one embedded in the input SED. The spectral fitting was performed between 3400 and 8900 Å following common practice in studies of local galaxy samples from SDSS (e.g. Asari et al. 2007; Ribeiro et al. 2016), with A_V kept as a free parameter between −1 and 4 mag. Moreover, Starlight was applied ten times for each spectrum assuming different initial guesses in the parameter space (i.e. seed numbers in the fitting procedure) to better evaluate formal uncertainties.

A second set of fits was computed using seven PLs in the base with an α between 0.5 and 2 in steps of 0.25, within the range of values commonly adopted both in spectral synthesis (e.g. Goerdt & Kollatschny 1998; Schmitt et al. 1999; Kauffmann et al. 2003; Cid Fernandes et al. 2004; Moultaka 2005; Benítez et al. 2013) and photoionisation models (e.g. Ferland & Netzer 1983; Stasińska 1984a,b; Mathews & Ferland 1987; Veilleux & Osterbrock 1987). The motivation behind this experiment was to check whether STARLIGHT can choose the PL with the correct slope, a test which is of relevance to its unsupervised application to large spectroscopic data sets without a priori knowledge of α. The allowance for multiple PLs of different α obviously bears the risk that an eventual inclusion of more than one PL in the best-fitting solution would lead to a non-PL distribution, which in turn might affect the properties inferred for the stellar component (e.g. A_V). These two series of fits are referred to in the following as `spl` (single PL) and `mpl` (multiple PLs), respectively.

For both `spl` and `mpl`, it is important to bear in mind that the results presented below correspond to a best-case scenario where the ingredients used to compute the input SEDs (i.e. SSPs and PLs) are also included in the base that is subsequently used for spectral fitting. This, and the fact that synthetic SEDs are composed of only a single-age stellar component, instead of the rather general case of a composite stellar population, further simplifies the framework of this study and facilitates the recovery of the AGN characteristics. Thus, the following analysis probably yields a generous estimate on the true capability of STARLIGHT for recovering an AGN hosted within a LyC-leaking ETG.

The first step in our analysis is to examine to which extent STARLIGHT can recover the AGN contribution. Figure 2 shows the difference between the output and input luminosity contribution $x^{\rm out}_{\rm AGN} - x^{\rm in}_{\rm AGN}$ of the AGN as a function of $x^{\rm in}_{\rm AGN}$ for ten S/N values (see legend for details). The accuracy on the estimation of $x_{\rm AGN}$ slightly increases with increasing AGN contribution, despite several local deviations from the true value, especially for lower-S/N ($\lesssim$25) spectra. A salient feature in both panels is that STARLIGHT on average underestimates the fractional contribution of the PL by ~6.2% (~3.0%) for `spl` (`mpl`) models, and that this offset, even though subtle, is apparent over the entire $x_{\rm AGN}$ range.

This bias is best visible in Fig. 3, which shows the relative deviation $(x^{\rm out}_{\rm AGN} - x^{\rm in}_{\rm AGN})/x^{\rm in}_{\rm AGN}$. The AGN contribution is systematically underestimated, reaching ~35.4% and ~14.9% at $x_{\rm AGN} = 0.2$ for `spl` and `mpl`, respectively. Interestingly, the deviation is

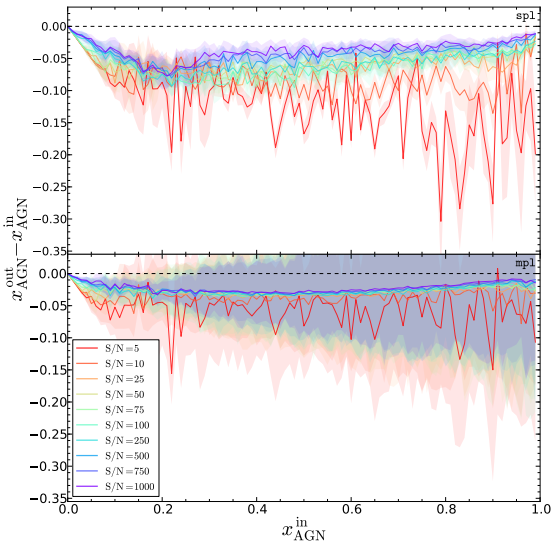

Fig. 2. Difference between output and input AGN fractional flux contribution $x^{\rm out}_{\rm AGN} - x^{\rm in}_{\rm AGN}$ at λ_0 as a function of $x^{\rm in}_{\rm AGN}$ for ten S/N values. Results obtained by fitting synthetic spectra with STARLIGHT with a single (`spl`) and multiple (`mpl`) AGN power-law components in the base library are shown in the *upper and lower panels*, respectively. The shaded area corresponds to the $\pm 1\sigma$ standard deviation around the mean, as computed from ten STARLIGHT fits to each synthetic spectrum.

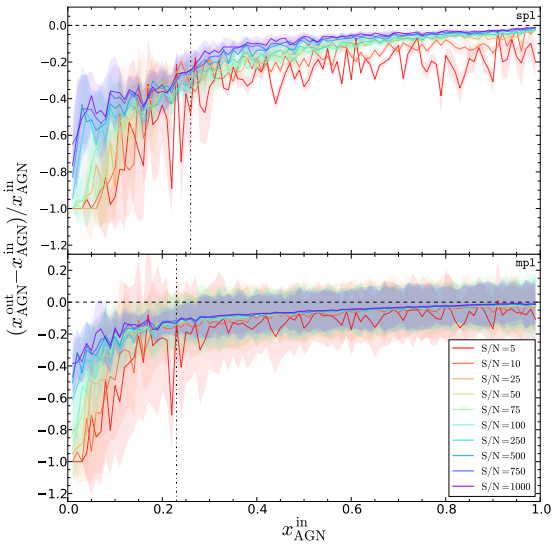

Fig. 3. Relative error of the fractional flux contribution of the AGN $(x^{\rm out}_{\rm AGN} - x^{\rm in}_{\rm AGN})/x^{\rm in}_{\rm AGN}$ as a function of $x^{\rm in}_{\rm AGN}$ for `spl` and `mpl` fits (*upper and lower panels*, respectively). The vertical dash-dotted lines mark the AGN detection threshold inferred from the Gelman & Rubin (1992) convergence test (see discussion for details).

on average by ∼10.7% higher for `spl` fits, although these employ the single PL component embedded in the input SED. Assuming that the lines inferred for each S/N in Fig. 3 are analogues of independent chains in a random-walk Monte Carlo simulation, we can estimate an AGN detection threshold from the Gelman & Rubin (1992) convergence criterion. This yields a variance ratio $\hat{R} < 1.1$ for $x_{\rm AGN} \geq 0.26$ and 0.23 (dash-dotted lines) for `spl` and `mpl` fits, respectively. These values reflect the empirical insight from Fig. 1 that traces of a diluting AGN continuum are barely recognisable by eye for a $x_{\rm AGN} \lesssim 0.2$. Automated application of STARLIGHT on large spectroscopic data sets (e.g. SDSS, 6dF, GAMA) would thus underestimate or entirely miss the AGN contribution, potentially leading to the erroneous classification of LyC-leaking AGNs as lineless *passive* galaxies, in the notation by Cid Fernandes et al. (2011). It is also noteworthy that the stellar mass $M_\star$ is recovered in either case at a level better than ∼10% for $x^{\rm in}_{\rm AGN} \lesssim 0.5$ (shaded area in Fig. 4).

One question that arises from the foregoing is whether the underestimation of the AGN contribution despite almost unbiased $M_\star$ estimates could come at the price of biases in other quantities of relevance, such as the luminosity-weighted mean stellar age $\langle t_\star \rangle_L$ and the intrinsic extinction A_V. This is indeed the case judging from Figs. 5 and 6, which reveal a trend for a S/N-dependent underestimation of the age and overestimation of A_V over the considered $x_{\rm AGN}$ range. Specifically, the luminosity-weighted mean stellar age computed with STARLIGHT is underestimated by ∼1.7 and 0.8 Gyr at $x_{\rm AGN} = 0.26$ and 0.23 for `spl` and `mpl`, respectively. At the AGN detection threshold this bias is apparently partly compensated for by an artificial reddening by $A_V \sim 0.07$ mag. Indirect evidence of a coupling between extinction and age at the expense of $x_{\rm AGN}$ comes from the fact that the latter is accurately retrieved by STARLIGHT when A_V is fixed to 0 mag.

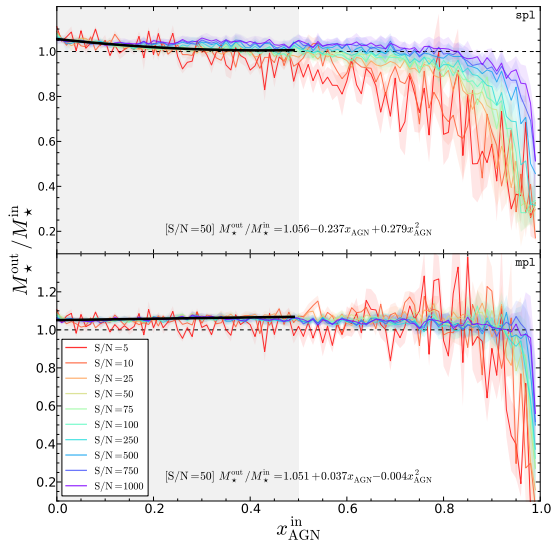

Fig. 4. Ratio between output and input total stellar mass $M_\star$ as a function of $x^{\rm in}_{\rm AGN}$ for `spl` and `mpl` fits (*upper and lower panels*, respectively). Thick black lines represent second-order polynomial fits for $x^{\rm in}_{\rm AGN} \leq 0.5$ and a $S/N = 50$.

3. Summary and conclusions

The aim of this study was to examine whether there is an AGN detectability threshold in optical spectral synthesis studies of LyC-leaking early-type galaxies (ETGs) hosting accretion-powered nuclear activity. To address this question, we took a combined approach that involved spectral fitting with

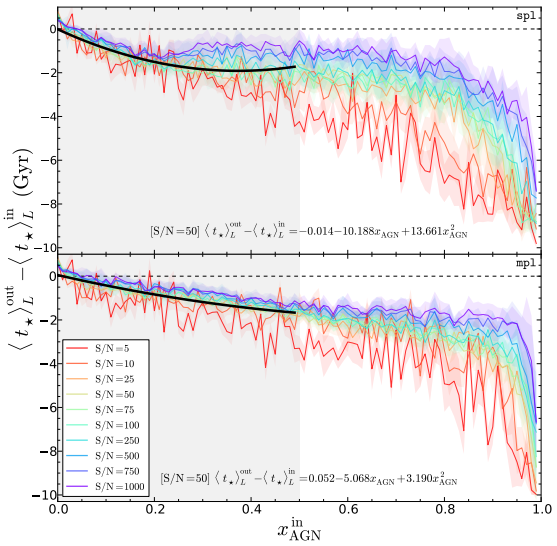

Fig. 5. Difference between the output and input luminosity-weighted mean stellar age $\langle t_\star\rangle_L$ as a function of $x_{\rm AGN}^{\rm in}$ for `spl` and `mpl` models (*upper and lower panels*, respectively). Thick black lines have the same meaning as in Fig. 4.

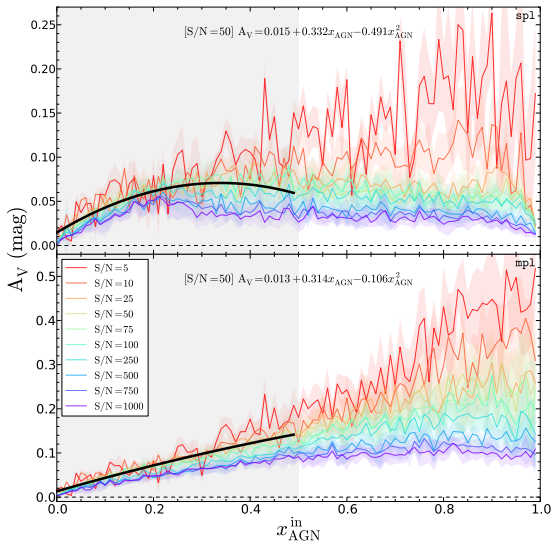

Fig. 6. Inferred intrinsic extinction A_V (mag) in the V-band as a function of $x_{\rm AGN}^{\rm in}$ for `spl` and `mpl` fits (*upper and lower panels*, respectively). The input SEDs are computed for an $A_V = 0$. Thick black lines have the same meaning as in Fig. 4.

STARLIGHT of synthetic SEDs that are composed of an instantaneously formed 10 Gyr old stellar component *plus* an AGN power-law component providing a fraction $0 \leq x_{\rm AGN} < 1$ of the monochromatic luminosity at $\lambda_0 = 4020$ Å. For this set of models, we find that STARLIGHT recovers the stellar mass to within ∼10%, but systematically overestimates the intrinsic extinction and underestimates the luminosity-weighted stellar age and $x_{\rm AGN}$. Our analysis indicates an effective AGN detection threshold at $x_{\rm AGN} \simeq 0.26$, which suggests that a considerable fraction of ETGs hosting significant accretion-powered nuclear activity may be missing in the AGN demographics.

Acknowledgements. We thank the anonymous referee for valuable comments and suggestions. L.S.M.C. acknowledges support by Fundação para a Ciência e a Tecnologia (FCT) (Ref. UID/FIS/04434/2013) through national funds and by FEDER funding through the program Programa Operacional de Factores de Competitividade (COMPETE) 2020 (Ref. POCI-01-0145- FEDER-007672). J.M.G. acknowledges support by FCT through the Fellowship SFRH/BPD/66958/2009 and POPH/FSE (EC) by FEDER funding through the program COMPETE. P.P. is supported by FCT through the Investigador FCT Contract No. IF/01220/2013 and POPH/ FSE (EC) by FEDER funding through the program COMPETE. L.S.M.C., J.M.G. and P.P. acknowledge support by FCT under project FCOMP-01-0124-FEDER-029170 (Ref. FCT PTDC/FIS-AST/3214/2012), funded by FCT-MEC (PIDDAC) and FEDER (COMPETE). L.S.M.C., J.M.G. and P.P. also acknowledge the exchange programme "Study of Emission-Line Galaxies with Integral-Field Spectroscopy" (SELGIFS, FP7-PEOPLE-2013-IRSES-612701), funded by the EU through the IRSES scheme.

References

Alongi, M., Bertelli, G., Bressan, A., et al. 1993, A&AS, 97, 851
Asari, N. V., Cid Fernandes, R., Stasińska, G., et al. 2007, MNRAS, 381, 263
Baldwin, J. A., Phillips, M. M., & Terlevich, R. 1981, PASP, 93, 5
Benítez, E., Méndez-Abreu, J., Fuentes-Carrera, I., et al. 2013, ApJ, 763, 36
Bressan, A., Fagotto, F., Bertelli, G., & Chiosi, C. 1993, A&AS, 100, 647
Bruzual, G., & Charlot, S. 2003, MNRAS, 344, 1000
Chabrier, G. 2003, PASP, 115, 763
Cid Fernandes, R., Gu, Q., Melnick, J., et al. 2004, MNRAS, 355, 273
Cid Fernandes, R., Mateus, A., Sodré, L., Stasińska, G., & Gomes, J. M. 2005 MNRAS, 358, 363
Cid Fernandes, R., Stasińska, G., Mateus, A., & Vale Asari, N. 2011, MNRAS, 413, 1687
Faber, S.M. 1972, A&A, 20, 361
Fagotto F., Bressan A., Bertelli G., & Chiosi C. 1994a, A&AS, 104, 365
Fagotto F., Bressan A., Bertelli G., & Chiosi C. 1994b, A&AS, 105, 29
Fagotto F., Bressan A., Bertelli G., & Chiosi C. 1994c, A&AS, 105, 39
Ferland, G. J., & Netzer, H. 1983, ApJ, 264, 105
Gelman, A., & Rubin, D. B. 1992, Statist. Sci., 7, 457
Girardi L., Bressan A., Chiosi C., Bertelli G., & Nasi E. 1996, A&AS, 117, 113
Goerdt, A., & Kollatschny, W. 1998, A&A, 337, 699
Gomes, J. M., Papaderos, P., Kehrig, C., et al. 2016, A&A, 588, A68
Heckman, T. M. 1980, A&A, 87, 152
Kauffmann, G., Heckman, T. M., Tremonti, C., et al. 2003, MNRAS, 346, 1055
Koski, A. T. 1978, ApJ, 223, 56
Kügler, S. D., Nilsson, K., Heidt, J., Esser, J., & Schultz, T. 2014, A&A, 569, A95
Marchã, M. J. M., Browne, I. W. A., Impey, C. D., & Smith, P. S. 1996, MNRAS, 281, 425
Mathews, W. G., & Ferland, G. J. 1987, ApJ, 323, 456
Moultaka, J. 2005, A&A, 430, 95
O'Connell, R. W. 1976, ApJ, 206, 370
Oke, J. B., & Gunn, J. E. 1974, ApJ, 189, L5
Oke, J. B., Neugebauer, G., & Becklin, E. E. 1970, ApJ, 159, 341
Papaderos, P., Gomes, J. M., Vílchez, J. M., et al. 2013, A&A, 555, L1
Ribeiro, B., Lobo, C., Antón, S., Gomes, J. M., & Papaderos, P. 2016, MNRAS, 456, 3899
Schmitt, H. R., Storchi-Bergmann, T., & Cid Fernandes, R. 1999, MNRAS, 303, 173
Stasińska, G. 1984a, A&AS, 55, 15
Stasińska, G. 1984b, A&A, 135, 341
Veilleux, S., & Osterbrock, D. E. 1987, ApJS, 63, 295

Astronomy & Astrophysics manuscript no. output
May 11, 2017

Impact of an AGN featureless continuum on estimation of stellar population properties

Leandro S. M. Cardoso[1,2], Jean Michel Gomes[1], and Polychronis Papaderos[1]

[1] Instituto de Astrofísica e Ciências do Espaço, Universidade do Porto, CAUP, Rua das Estrelas, PT4150-762 Porto, Portugal
e-mail: leandro.cardoso@astro.up.pt, jean@astro.up.pt, or papaderos@astro.up.pt
[2] Departamento de Física e Astronomia, Faculdade de Ciências, Universidade do Porto, Rua do Campo Alegre 687, PT4169-007, Porto, Portugal

Received ?? ; Accepted ??

ABSTRACT

The effect of the featureless power-law (PL) continuum of an active galactic nucleus (AGN) on the estimation of physical properties of galaxies with optical population spectral synthesis (PSS) remains largely unknown. With the goal of a quantitative examination of this issue, we fit synthetic galaxy spectra representing a wide range of galaxy star formation histories (SFHs) and including distinct PL contributions of the form $F_\nu \propto \nu^{-\alpha}$ with the PSS code STARLIGHT to study to which extent various inferred quantities (e.g. stellar mass, mean age, and mean metallicity) match the input. The synthetic spectral energy distributions (SEDs) computed with our evolutionary spectral synthesis code include an AGN PL component with $0.5 \leq \alpha \leq 2$ and a fractional contribution $0.2 \leq x_{\rm AGN} \leq 0.8$ to the monochromatic flux at 4020 Å. At the empirical AGN detection threshold $x_{\rm AGN} \simeq 0.26$ that we previously inferred in a pilot study on this subject, our results show that the neglect of a PL component in spectral fitting can lead to an overestimation by ∼2 dex in stellar mass and by up to ∼1 and ∼4 dex in the light- and mass-weighted mean stellar age, respectively, whereas the light- and mass-weighted mean stellar metallicity are underestimated by up to ∼0.3 and ∼0.6 dex, respectively. These biases, which become more severe with increasing $x_{\rm AGN}$, are essentially independent of the adopted SFH and show a complex behaviour with evolutionary time and α. Other fitting set-ups including either a single PL or multiple PLs in the base reveal, on average, much lower unsystematic uncertainties of the order of those typically found when fitting purely stellar SEDs with stellar templates, however, reaching locally up to ∼1, 3 and 0.4 dex in mass, age and metallicity, respectively. Our results underscore the importance of an accurate modelling of the AGN spectral contribution in PSS fits as a minimum requirement for the recovery of the physical and evolutionary properties of stellar populations in active galaxies. In particular, this study draws attention to the fact that the neglect of a PL in spectral modelling of these systems may lead to substantial overestimates in stellar mass and age, thereby leading to potentially significant biases in our understanding of the co-evolution of AGN with their galaxy hosts.

Key words. galaxies: active – galaxies: Seyfert – galaxies: stellar content – galaxies: evolution

1. Introduction

The mass assembly, star formation and chemical evolution history of galaxies are fundamental to the understanding of the physical and spectrophotometric properties of galaxies in the local universe. In recent decades, numerous studies have employed spectral synthesis with the aim of addressing these issues. This technique saw its initial realisation with the works by Whipple (1935) and Baade (1944a,b). They have attempted to categorise groups of stars within local galaxies according to their spectral types and found that, predominantly, O and B stars were in the disk and G, K, and M stars were in the bulge. This was later recognised to be a signature of the different stellar populations (population I, II, and III stars) composing distinct structural components in galaxies. These works planted the seed of the modern concept for modelling the spectral continuum of galaxies as due to the linear superposition of individual star spectra or star clusters in galaxies. Historically, spectral synthesis has followed two main approaches: population spectral synthesis (PSS) and evolutionary spectral synthesis (ESS).

On the one hand, also known as population synthesis or inversion technique, PSS aims at decomposing the observed spectrum of a galaxy into its main elementary building blocks, such as individual stars and/or groups of stars of a given age, metallicity, and stellar initial mass function (IMF). Per definition, this technique yields a discretised approximation to the star formation and chemical evolution history (SFH and CEH, respectively) of a galaxy. The PSS approach saw its inception with the works by Morgan (1956), Wood (1966), and Faber (1972) and has over the years been subject to significant development (e.g. Bica 1988; Pelat 1997, 1998; Moultaka et al. 2004; Heavens, Jimenez & Lahav 2000; Heavens et al. 2004; Cid Fernandes et al. 2005; Ocvirk et al. 2006a,b; Tojeiro et al. 2007; MacArthur et al. 2009; Koleva et al. 2009). In the last two decades, spectral synthesis has transitioned from the modelling of a few observables, such as colours, fluxes, and/or equivalent widths (EWs) of absorption lines (e.g. Wood 1966; Faber 1972; Worthey 1994; Kauffmann et al. 2003) to the more powerful pixel-by-pixel (λ-by-λ) fitting technique that exploits the full information in current medium- to high-resolution spectroscopic data (e.g. Cid Fernandes et al. 2005; Koleva et al. 2009; Tojeiro et al. 2007).

On the other hand, also known as the direct approach, ESS allows for the estimation of physical properties of galaxies, such as the stellar mass, age, and metallicity, on the basis of empirically founded assumptions on the IMF, chemical evolution, and star formation rate (SFR). This approach was pioneered by Tinsley (1968) and Spinrad & Taylor (1972) and since then has been a thriving topic of research with the creation of increas-

ingly sophisticated models (e.g. Krüger, Fritze-v. Alvensleben & Loose 1995; Fioc & Rocca-Volmerange 1997; Leitherer et al. 1999; Zackrisson et al. 2001; Bruzual & Charlot 2003; Anders et al. 2004; Le Borgne et al. 2004; Maraston 2005; Coelho et al. 2007; Mollá et al. 2009; Kotulla et al. 2009; Vazdekis et al. 2010).

Whereas there is broad consensus that these techniques have led in the past decade to a great leap forward in our understanding of the assembly history of normal galaxies, their application to active galactic nucleus (AGN) remains controversial and problematic. As a matter of fact, the chief goal of spectral modelling of AGN spectra in the 70s and 80s has been the recovery of the AGN emission after fitting and removal of the underlying stellar spectral energy distribution (SED). The main assumption behind this approach was that the underlying host galaxy was composed solely of old and metal-rich stellar populations that are in general well represented by an elliptical galaxy spectral template. For instance, the original work by Koski (1978) showed, using photometric scans of a sample of Seyferts (named after Carl Keenan Seyfert; Seyfert 1943) and narrow-line radio galaxies, that a non-stellar component could be approximated by a featureless continuum (FC) with a power-law (PL) function $F_\nu \propto \nu^{-\alpha}$ in the UV-optical range with α between 0.2 and 2.8 and an average value of $\langle\alpha\rangle = 1.0 \pm 0.5$. In this study, the AGN was found to provide on average ∼30% of the continuum at the Hβ wavelength.

The accuracy of these methods for removing the underlying stellar SED has generally been limited by various sources of uncertainty (as extensively discussed in Ho, Filippenko & Sargent 1997, and more recently in Ho 2008) and, from the spectral synthesis point of view, the techniques employed were not meant to investigate, or were not capable of exploring, the SFH and CEH of galaxies. As a consequence, it might be questioned whether these studies could accurately retrieve the pure SED of the AGN, in particular for galaxies where stellar emission dominates. Even though more elaborate methods were developed for the starlight removal, such as off-nuclear spectrum subtraction within the same galaxy (Storchi-Bergmann, Baldwin & Wilson, 1993) or a linear combination of the spectra of different galaxies (Ho, Filippenko & Sargent, 1997, 2003; Storchi-Bergmann, Cid Fernandes & Schmitt, 1998), they generally did not have the reconstruction of the stellar mass assembly history of active galaxies as prime objective.

Concerning the PL contribution, it is well-established in the framework of the AGN unified model (Antonucci 1993; Netzer 2015) that it constitutes the dominant component in the SED optical continuum of type 1 AGNs, such as quasars and Seyfert 1 galaxies. However, its relative contribution to the UV-optical in type 2 AGN, such as Seyfert 2 and low-ionisation nuclear emission-line region (LINER) galaxies (Heckman 1980), remained controversial, largely owing to the limited capability of current spectral fitting codes.

Indeed, even though a substantial body of work has been devoted to this subject, a review of the literature reveals a wide set of discordant conclusions, in some cases drawn using similar methods. Part of the confusion might be attributed to poorly described or justified methodological assumptions and the assessment of the propagation of uncertainties in the physical properties of both the estimated stellar and AGN contribution, besides sample selection effects.

For example, observations of the optical stellar features, such as the Mgb band (∼5200Å), have shown in some cases a certain degree of dilution in these regions by a PL component (e.g. Koski 1978; Dressler 1984; Nelson & Whittle 1995; Serote Roos et al. 1998; Cid Fernandes, Storchi-Bergmann & Schmitt 1998; Boisson et al. 2000; Moultaka & Pelat 2000; Kauffmann et al. 2003; Garcia-Rissmann et al. 2005; Vega et al. 2009). Conversely, it was pointed out that the EWs of the infrared Ca II triplet (hereafter CaT at 8498, 8542, and 8662 Å) were similar or even larger than in normal galaxies (e.g. Terlevich, Díaz & Terlevich 1990; Nelson & Whittle 1995), as they are more suitable for a stellar population and kinematical analysis. Vega et al. (2009) applied the PSS code STARLIGHT to active galaxies and found that Seyfert 1 galaxies have EW(CaT) between ∼1.5 and ∼7.5 Å with a median value of 4.8 Å and that Seyfert 2 lie between ∼1.5 and ∼10.5 Å with a median value of 6.5 Å. Their results suggest that Seyfert 2 show no sign of dilution of EW(CaT) as compared to normal galaxies, even though optical absorption lines such as the CaII K (CaK) band at 3933 Å are much weaker than in old, bulge-like stellar populations. Evolutionary models in an EW(CaT)–EW(CaK) diagram suggest that young stellar populations are responsible for the dilution of optical lines in active galaxies. However, the authors concluded that non-stellar contributions can reach ∼85% in Seyfert 1, ∼50 % in Seyfert 2 and starburst galaxies, and ∼32% even for normal galaxies by applying STARLIGHT with multiple PLs with α = 1–2.

The controversy on the PL contribution to type 2 objects remains until today. For example, in studies by Ho, Filippenko & Sargent (1995, 1997, 2003) and Ho (2008) it was argued that samples analysed by some other groups were, in general, not large enough and unbiased, preventing an accurate separation of nuclear from global properties. Even though other surveys, such as SDSS (York et al. 2000), have surpassed statistically the number of galaxies of smaller surveys (e.g. the Palomar sample; Ho, Filippenko & Sargent 1995), these larger surveys have the disadvantage of large projected aperture sizes, where the continuum emission in type 2 AGN could be significantly diluted by star formation (Kauffmann et al. 2003). This might explain why some works have found almost no PL contribution in type 2 AGN (Cid Fernandes, Storchi-Bergmann & Schmitt 1998; Schmitt, Storchi-Bergmann & Cid Fernandes 1999, while others found that a PL could account for up ∼90% of the optical flux (e.g. Koski 1978; Vega et al. 2009).

For instance, Cid Fernandes, Storchi-Bergmann & Schmitt (1998) have studied the stellar content of active galaxies with long-slit spectroscopy of 38 active and 4 normal galaxies with the goal of detecting the fractional contribution of a FC relative to the stellar emission. This study detected dilution of stellar absorption lines by a PL in most of the galaxies with broad-line emission, whereas almost no PL contribution was found for most of the type 2 Seyferts in their sample. Likewise, a follow-up study in Schmitt, Storchi-Bergmann & Cid Fernandes (1999) investigated the contribution by an AGN PL to the optical using flux continuum ratios and absorption-line EWs on spectra of nuclear regions of 20 local Seyfert 2 galaxies. The conclusions drawn was that the contribution from stars younger than 10 Myr and a PL rarely exceeds 5% and that the high FC contribution (up to ∼70%) found by Koski (1978) was likely overestimated because of the use of an elliptical template spectrum for the nuclear stellar population.

More recently, Cid Fernandes et al. (2004) applied a λ-by-λ spectral synthesis approach with an early version of the PSS code STARLIGHT (Cid Fernandes et al. 2005) to constrain the SFH of 79 Seyfert 2 galaxies in the 3500–5200 Å range while simultaneously fitting an additional PL continuum with varying spectral index α. The authors found stellar populations of all ages and a PL mean contribution of ∼20–30% and maximum contribution of ∼63% to the monochromatic flux at 4020 Å. Although the au-

thors warned that the PL component might be due to scattered light from a hidden AGN or a young and dusty starburst, its importance was clearly documented in this PSS modelling study. Likewise, Benítez et al. (2013) found that a PL component provides up to ∼30% to the monochromatic luminosity at 5100 Å by applying STARLIGHT on 10 nearby intermediate-type AGN from SDSS.

Some contradictory results were also found by Eracleous & Halpern (2001), who characterised NGC 3065 as a LINER with broad Balmer emission lines coming from an accretion disk. The authors modelled the continuum of that galaxy with a linear combination of a PL non-stellar component with starlight described by different spectra of elliptical S0 galaxies. This work found that the SED continuum of NGC 3065 can be modelled without the need for a PL if the spectrum of NGC 4339 is taken as a template for subtracting the stellar contribution, whereas other templates would imply a non-stellar component contributing up to ∼10% of the SED continuum at Hα and Hβ and $\lesssim$15% at [OII]λ3727.

As many of the results obtained by fitting a mixture of stellar and PL templates to observed spectra remain divergent and the estimation of stellar population properties with this technique is still largely uncharted territory[1], it appears to be worthwhile to supplement existing work with modelling of synthetic composite spectra with stellar and AGN components of known constitution for the sake of evaluating the capability of SED fitting codes to retrieve the input physical and evolutionary characteristics of a galaxy (e.g. SFH, CEH, and AGN contribution). The very few works existing in this regard (e.g. Bon, Popović & Bon 2014; Hayward & Smith 2015; Ciesla et al. 2015; Cardoso, Gomes & Papaderos 2016) yield a variety of conclusions.

Bon, Popović & Bon (2014) simulated a mock galaxy sample of 7000 integrated spectra of Seyfert 2 galaxies and used the PSS code ULySS (Koleva et al. 2009) to recover the underlying stellar contribution and PL component. Their main results show that the stellar populations characteristics can be retrieved whenever the signal-to-noise ratio is higher than 20 and if the stellar contribution is more than 10% of the total flux.

A different methodology was adopted by Hayward & Smith (2015), where hydrodynamical simulations with full radiative transfer modelling were used to create mock SEDs with known observational and physical characteristics (e.g. photometric bands, V-band extinction, stellar mass, dust luminosity and mass, and SFR). The authors in turn applied the MAGPHYS code (da Cunha, Charlot & Elbaz 2008) with ultraviolet to millimetre photometry in an attempt to recover the stellar population properties. Overall, results showed that most physical parameters are well estimated, although it was found that in certain cases (e.g. major mergers) AGN contamination leads to a stellar mass overestimation of ∼0.03 dex at AGN activity peaks.

At variance to the previous studies, a strong dependence on the estimated stellar properties on the specifics of SED fitting was reported by Ciesla et al. (2015). These authors fitted broad-band photometric SEDs with CIGALE (Noll et al. 2009) assuming exponentially decreasing and delayed SFHs, solar-metallicity Maraston (2005) SSPs, Calzetti et al. (2000) dust extinction law, and dust remission. Their results showed that exclusion of AGN optical templates from the fit can lead to the overestimation of the stellar mass by up to ∼150% and of the SFR by up to ∼300%, depending on AGN spectral type and SFH. Both overestimations increase with the AGN overall contribution to the total infrared luminosity $x_{\rm AGN}^{\rm IR}$. Inclusion of AGN templates in the fit can lead to the overestimation of the AGN light fraction up to ∼100%, depending on the AGN spectral shape and $x_{\rm AGN}^{\rm IR}$. However, the estimated AGN light fraction tends roughly to its true value with increasing $x_{\rm AGN}^{\rm IR}$. Quite importantly, the authors found uncertainties in mass up to ∼40% (∼0.15 dex) and ∼40–50% on the SFR, depending on the AGN spectral shape and $x_{\rm AGN}^{\rm IR}$.

Our work builds upon and extends a pilot investigation of biases in optical PSS modelling of early-type active galaxies showing a high Lyman continuum (LyC) photon escape fraction presented in Cardoso, Gomes & Papaderos (2016) (hereafter CGP16). The observational motivation behind this study comes from the estimation of a high (>90%) LyC photon escape fraction in early-type active galaxies by Papaderos et al. (2013) and Gomes et al. (2016), which, according to our current knowledge, host a super-massive black hole in their nuclei with expected accretion-powered activity. More generally, it is conceivable that the model framework adopted in this study is applicable to any other galaxy spheroid or spheroidal component (e.g. classical bulges), where, in the absence of absorbing gas of sufficient density, the bulk of the LyC radiation from the AGN accretion disk may escape without producing in situ optical nebular emission. Motivated by such considerations, the main objective of this study is to shed further light into the assembly history of active galaxies by quantifying potential uncertainties in the recovery of their SFHs and CEHs and characteristic stellar population properties with state-of-the-art PSS.

This paper is organised as follows. Section 2 presents our library of synthetic spectra with stellar and AGN components (Subsection 2.1) and the adopted PSS modelling approach (Subsection 2.2). Sections 3 and 4 provide an overview and discussion of our results. Finally, Section 5 summarises the main findings and conclusions of this work.

2. Methodology

2.1. Synthetic spectra library

A library of synthetic SEDs was computed with the ESS code REBETIKO (Papaderos & Gomes, in prep.; hereafter PG). These SEDs are a time- and metallicity-dependent linear combination of coeval and chemically homogeneously groups of stars known as simple stellar populations (SSPs), which is a term introduced by Renzini (1981). The flux of a composite stellar population (CSP) $F_\lambda^{\rm CSP}(t)$ representing the overall stellar content of a galaxy of age t can be computed by linearly combining SSPs of different ages and metallicities according to an assumed SFR $\Psi(t) = {\rm d}M_\star/{\rm d}t$,

$$F^{\rm CSP}(\lambda, t, Z) = \int_0^t \Psi(t - t') F^{\rm SSP}(\lambda, t', Z)\, {\rm d}t', \qquad (1)$$

where $F^{\rm SSP}(\lambda, t', Z)$ represents the SSP spectral library as a function of the wavelength λ, age t', and metallicity Z (see e.g. Tinsley 1980; Walcher et al. 2011; Cerviño 2013; Conroy 2013 for reviews on spectral synthesis).

This work adopts Bruzual & Charlot (2003) solar-metallicity ($Z_\odot$ = 0.02) SSPs with a Chabrier (2003) IMF to create synthetic CSP spectra for a fixed metallicity and a wide range of

[1] Whether a second and dominant blue featureless continuum (FC2) is present in type 2 AGNs due to compact starbursts (e.g. Cid Fernandes & Terlevich 1995; Heckman et al. 1995; Tran 1995), instead of coming only from the AGN synchrotron emission, is irrelevant to our work, which focusses on the recovery of the stellar population properties (e.g. SFHs and CEHs) of the host galaxy in case a PL (or AGN-like) contribution is present.

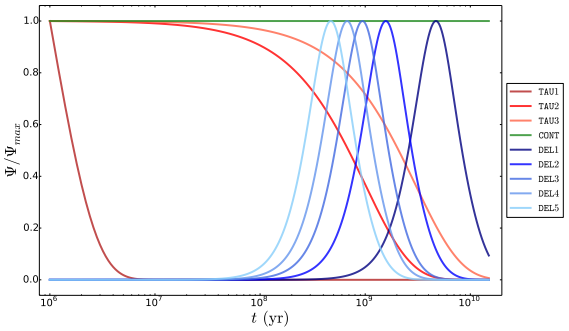

Fig. 1. SFR functions $\Psi(t)$ adopted in the ESS code Rebetiko for the assembly of purely-stellar evolutionary models. Red, green, and blue lines represent exponentially declining, continuous, and delayed SFR functions, respectively.

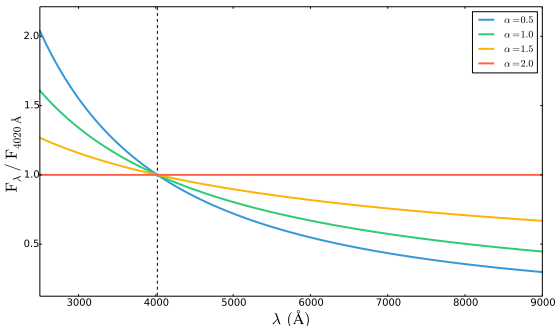

Fig. 2. Featureless PL AGN continua parameterised as $F_\nu \propto \nu^{-\alpha}$ normalised at $\lambda_0 = 4020$ Å (dashed vertical line) as a function of wavelength λ. Blue, green, yellow, and red lines represent PLs with $\alpha = 0.5$, 1, 1.5, and 2, respectively.

SFH parameterisations that are generally assumed to approximate those of the different Hubble types (e.g. Rocca-Volmerange & Guiderdoni 1988; Gavazzi et al. 2002; Bruzual & Charlot 2003). Figure 1 shows the adopted SFR functions: exponentially declining (red lines) with e-folding timescales of 0.001, 1, and 3 Gyr from left to right, respectively; continuous (green line), and delayed (blue lines) with different star formation peaks as a function of the look-back time (e.g. Gavazzi et al. 2002; PG).

The library comprises 716 spectra with ages between 1 Myr and 15 Gyr for each SFH complemented with a wide range of physical properties, such as SFHs weighted by light and mass and CEHs with constant solar metallicity. These purely stellar models are used in this work to provide baseline results to which active galaxy models are compared to when applying PSS.

Another library of more complex models was created by adding simple AGN continua models to the CSPs. The optical AGN FC is assumed to be well represented by a PL defined as $F_\nu \propto \nu^{-\alpha}$ (e.g. Oke, Neugebauer & Becklin 1970; O'Connell 1976; Koski 1978). This approximation has been widely adopted in spectral synthesis (e.g. Goerdt & Kollatschny 1998; Schmitt, Storchi-Bergmann & Cid Fernandes 1999; Kauffmann et al. 2003; Cid Fernandes et al. 2004; Moultaka 2005) and photoionisation studies (e.g. Ferland & Netzer 1983; Stasińska 1984a,b; Mathews & Ferland 1987; Veilleux & Osterbrock 1987), in which the PL index is commonly within $\alpha = 0.5$–2.

The flux F_λ normalised at wavelength λ_0 is the linear combination of purely stellar model $F^\star_\lambda$ and AGN $F^{\rm AGN}_\lambda$ continua,

$$F_\lambda = x_\star \frac{F^\star_\lambda}{F^\star_{\lambda_0}} + x_{\rm AGN} \frac{F^{\rm AGN}_\lambda}{F^{\rm AGN}_{\lambda_0}}, \quad (2)$$

where $x_\star$ and $x_{\rm AGN}$ are the fractional contributions of stellar and AGN monochromatic fluxes at $\lambda_0 = 4020$ Å, respectively. Equation 2 is constrained by the normalisation condition $x_\star + x_{\rm AGN} = 1$ at λ_0.

It is useful to rewrite Equation 2 as

$$F_\lambda = F^\star_\lambda + \frac{x_{\rm AGN}}{x_\star} F^\star_{\lambda_0} \left(\frac{\lambda}{\lambda_0}\right)^{\alpha-2}, \quad (3)$$

where the total stellar flux $F^\star_\lambda$ is unchanged and it is assumed that $F^{\rm AGN}_\lambda \propto \lambda^{\alpha-2}$, following $F^{\rm AGN}_\nu \propto \nu^{-\alpha}$. We adopted AGN PL continua with $\alpha = 0.5$, 1, 1.5 and 2 and $x_{\rm AGN} = 0.2$, 0.4, 0.6 and 0.8 to study the effects of AGN PL index and fractional contribution variations in the estimation of stellar population properties with PSS. These wide ranges assure us that no strong prior assumptions are made concerning the AGN optical shape and relative contribution. Figure 2 shows the adopted AGN PL continua with $\alpha = 0.5$, 1, 1.5, and 2 corresponding to blue, green, yellow, and red lines, respectively. This figure shows that the AGN PL becomes bluer with decreasing α.

As an example, Fig. 3 shows SEDs resulting from combining an instantaneously formed stellar population with 100 Myr and solar metallicity with AGN PLs with α and $x_{\rm AGN}$ variations. Purely stellar spectra are represented by black lines and models with AGN PLs with $\alpha = 0.5$, 1, 1.5, and 2 for $x_{\rm AGN} = 0.4$ (top panel) and $x_{\rm AGN} = 0.2$, 0.4, 0.6, and 0.8 for $\alpha = 1.5$ (bottom panel) are represented by blue, green, yellow, and red lines, respectively.

This figure illustrates two facts of special relevance to this study. Firstly, the normalisation wavelength λ_0 defines how the AGN continuum shape affects the underlying stellar continuum since Eq. 3 implies a flux increase when $\alpha < 2$ larger than $F_{\star,\lambda_0}$ for $\lambda < \lambda_0$ and smaller than $F_{\star,\lambda_0}$ for $\lambda > \lambda_0$. Thus, adopting typical values of λ_0 such as 4020 Å (e.g. Cid Fernandes et al. 2004) or 5050 Å (e.g. Goerdt & Kollatschny 1998) means that the AGN continuum approximated as a PL for $\alpha < 2$ has a slope similar to that of young SSPs. Secondly, the dilution effect of absorption-line features due to the addition of a FC (e.g. Koski 1978; Serote Roos et al. 1998; Moultaka & Pelat 2000; Kauffmann et al. 2003) depends on adopted λ_0, α, and $x_{\rm AGN}$.

Figure 4 illustrates this last point by presenting SEDs normalised at λ_0 for an instantaneous burst SFH with 100 Myr and solar metallicity (black line) combined with AGN continua for fixed $\alpha = 1.5$ and $x_{\rm AGN} = 0.2$, 0.4, 0.6, and 0.8 (blue, green, yellow, and red lines, respectively). This figure shows that λ_0 defines a demarcation point in the spectra that separates regions suffering from blueing or reddening. Moreover, the dilution of the underlying stellar continuum induced by the AGN PL increases with increasing $x_{\rm AGN}$.

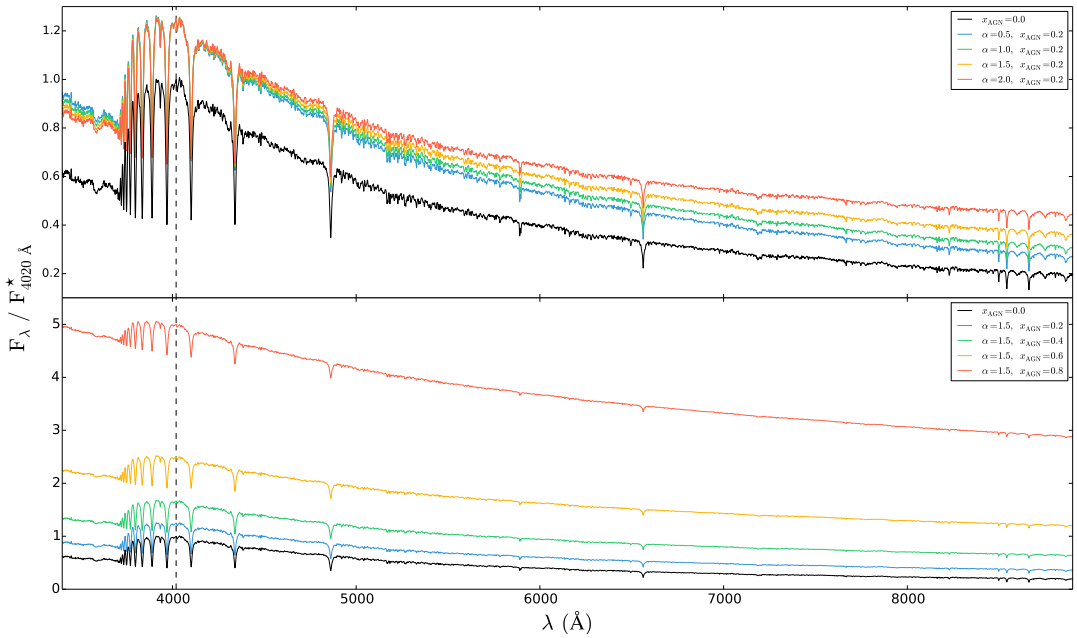

Fig. 3. Combination of a CSP SED for an instantaneously formed stellar population of age 100 Myr and solar metallicity with AGN PLs for different values of α and fractional contribution x_{AGN} to the monochromatic flux at λ_0 = 4020 Å (black dashed line). Black lines represent purely stellar SEDs and blue, green, yellow, and red lines represent active galaxy SEDs with α = 0.5, 1, 1.5, and 2 for x_{AGN} = 0.4 (top panel) and x_{AGN} = 0.2, 0.4, 0.6, and 0.8 for α = 1.5 (bottom panel), respectively.

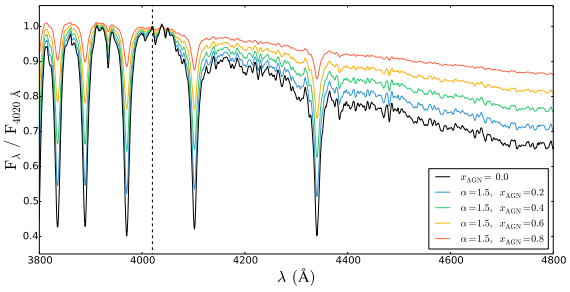

Fig. 4. Synthetic SEDs normalised at λ_0 (black dashed line) with the contributions of an instantaneously formed solar-metallicity stellar population of age 100 Myr and an AGN PL with fixed α = 1.5. The black line represents the purely stellar continuum and the blue, green, yellow, and red lines represent active galaxy SEDs with x_{AGN} = 0.2, 0.4, 0.6, and 0.8, respectively.

2.2. Application of population synthesis

Both purely stellar and active galaxy SEDs were modelled with the latest public distribution[2] of STARLIGHT (Cid Fernandes et al. 2005) to investigate the ability of PSS to infer the SFHs and CEHs of mock galaxies. The code STARLIGHT is widely used (e.g. Mateus et al. 2006; Stasińska et al. 2008; Cid Fernandes et al. 2010, 2011; Kehrig et al. 2012; Benítez et al. 2013; Papaderos et al. 2013; Cid Fernandes et al. 2014; Stasińska et al. 2015; Gomes et al. 2016) and can be regarded as a good representative of the state of the art. It is important to bear in mind the main objective of this work is to quantify potential biases on fundamental physical properties of active galaxies estimated with purely-stellar PSS that might rise owing to the introduction of a simple AGN model, as in Ciesla et al. (2015).

The adopted base library comprises Bruzual & Charlot (2003) SSPs with 25 ages (illustrated as the vertical black lines on the top of the right-hand side panels of Fig. 5) and 4 metallicities (Z = 0.2, 0.4, 1 and 2.5 $Z_\odot$). This library is similar to that adopted by Asari et al. (2007) with the following notable differences: first, better coverage of the younger evolutionary stages and, second, without the two lowest metallicities that are not expected to contribute significantly to the intrinsic degeneracies. A base library with a finer age and metallicity coverage would in principle help reduce uncertainties associated with poorly sampled evolutionary stages, although at a high computational cost. For instance, base libraries with 100 and 300 SSPs (i.e. the maximum number of base elements that STARLIGHT can handle) take ~110 and 1000 seconds to perform a single fit to one of these synthetic spectra in a Intel® Core™ i7 CPU 870 @ 2.93GHz workstation desktop. Thus, the adopted base library should be regarded as a compromise between computational time and a fine age and metallicity coverage. The spectral fitting is made between 3400 and 8900 Å, following common practice in local galaxy studies (e.g. Asari et al. 2007; Ribeiro et al. 2016) and to take advantage of the wavelength coverage of the STELIB stellar library (Le Borgne et al. 2003) adopted in the Bruzual & Charlot (2003) evolutionary models.

[2] STARLIGHTV04: http://astro.ufsc.br/starlight/

Moreover, the stellar kinematics and V-band extinction A_V were fixed to zero and no pixel clipping method was adopted. The reason for keeping stellar kinematics and extinction fixed to input values in the STARLIGHT fits is to facilitate an easier comparison between fits to purely stellar and active galaxy SEDs and to better isolate the potential PSS biases owing to the addition of the AGN PL continuum.

The AGN models were processed by STARLIGHT for three fitting set-ups:

(i) without any PL contribution in the base
(ii) including in the base a single PL with same α as that embedded in the input spectra
(iii) including in the base PLs with α = 0.5, 1, 1.5 and 2, leaving to STARLIGHT the choice to pick up the PL which best matches the data.

Set-ups (*i*) and (*ii*) may be regarded as special cases in PSS modelling. The former corresponds to the worst-case scenario where fitting of an active galaxy SED is attempted with purely stellar templates, whereas the latter represents the ideal situation of the base library containing a single PL that is identical to that integrated in the input spectrum. Conversely, set-up (*iii*) can be viewed as a conservative fitting approach in the situation of not having prior knowledge of the AGN optical continuum shape (e.g. Ho & Kim 2009; Roche et al. 2016). Hereafter, these approaches are referred to as no power law (`npl`), single power law (`spl`), and multiple power laws (`mpl`). In the following, focus is given to results derived for an instantaneous burst SFH. However, similar trends are seen for the other SFHs, results for which are discussed when appropriate.

As an example, Figure 5 shows the average results for 10 STARLIGHT fits for `npl` with the best fit (blue line) to the input synthetic active galaxy spectrum (red line) with an stellar population instantaneously formed with 100 Myr and solar metallicity (green line) and an AGN PL with α = 1.5 and $x_{\rm AGN}$ = 0.2 (yellow line) in the main panel. The bottom panel presents the residuals after subtracting the fit from the input spectrum and the right-hand side panels show the estimated SFHs in terms of the light and mass fraction (top and bottom, respectively).

3. Results

Figure 6 shows the ratio in the currently available total stellar mass $M_\star$ between the PSS (output) and ESS (input) values as a function of age t, with increasing $x_{\rm AGN}$ from left- to right-hand side panels, respectively. The results from `npl`, `spl`, and `mpl` are presented on the top, middle, and bottom rows, respectively (subsequent figures follow a similar panel configuration, except when explicitly stated otherwise). Moreover, PSS results for purely stellar spectra results are represented by black lines, while active galaxy spectra with α = 0.5, 1, 1.5, and 2 are represented by blue, green, yellow, and red lines, respectively. The results for purely stellar models show a maximum mass overestimation up to ∼0.5 dex, which are likely linked to a poor age coverage of the SSPs in the adopted base library.

The results in Fig. 6 for `npl` show a systematic mass overestimation up to ∼3.5 dex correlated with increasing α and $x_{\rm AGN}$ and with decreasing age t, with a maximum at $t \sim 10$ Myr. Figure A.2 in Appendix A shows similar results for other SFHs. Results for `spl` and `mpl` reveal local mass overestimations within ∼1 dex. This overestimation increases with increasing $x_{\rm AGN}$, is somewhat independent from α and becomes more severe in models with ages where spectral synthesis of purely stellar spectra also show considerable uncertainties.

One question of considerable interest concerns the origin of this severe stellar mass overestimation. Results show that STARLIGHT has to compensate for the lack of the PL component in the base in a purely stellar modelling configuration. This leads to a nearly bimodal mixture of young and old stellar populations, as illustrated in the SFH panels of Fig. 5. It is to be expected that in such a modelling approach the blue AGN continuum is accounted for by a non-realistic mixture of stellar populations, where very young SSPs would always dominate the light, whereas the contribution of old SSPs is almost negligible in terms of light. Notwithstanding this fact, these old SSPs provide the bulk of stellar mass, thus leading to the observed mass overestimation.

Figure 7 shows the difference in the light-weighted mean stellar age $\langle \log t_\star \rangle_L$ between PSS and ESS values as a function of age t. The results of purely stellar models show mean stellar age uncertainties within ∼0.1 dex. Cid Fernandes et al. (2005) showed that both light-weighted mean stellar age and metallicity could be recovered with STARLIGHT within a typical uncertainty of ∼0.2 dex using mock data with S/N=10. This uncertainty is considered in this work to be a fiducial value.

The results in Fig. 7 for `npl` show a systematic age over- and underestimation of up to ∼1.5 and ∼2 dex for young ($t \lesssim 100$ Myr) and old ($t \gtrsim 100$ Myr) evolutionary models, respectively. This trend is accentuated with increasing $x_{\rm AGN}$ and originates from an increasing dilution of stellar absorption features, as seen in Fig. 4. Figure A.3 shows similar results for other SFHs. Moreover, the results for `spl` show an age over- and underestimation of up to ∼0.3 dex, which appear to be correlated with ages where purely stellar fits also show considerable uncertainties. In addition, there is a clear age underestimation at ∼20 Myr that increases with increasing α and $x_{\rm AGN}$. The results for `mpl` show uncertainties and trends similar to those found for `spl`. However, the age of old evolutionary models ($t > 1$ Gyr) can be underestimated by as much as ∼1.5 dex. This feature becomes more prominent with increasing $x_{\rm AGN}$ for α = 0.5. The results in Fig A.1 suggest that this trend is due to a poor estimation of $x_{\rm AGN}$ for this fitting set-up, which also explains the slight mass underestimation for this age and AGN contribution.

Figure 8 illutrating results for mass-weighted mean stellar age $\langle \log t_\star \rangle_M$ show overall uncertainties that are larger than their light-weighted counterparts. Synthesis results of purely stellar models show a maximum age overestimation up to ∼2 dex. Moreover, the results for `npl` show a systematic age overestimation up to ∼4 dex with α and decreasing t. Figure A.4 shows similar results for other SFHs. This trend is similar to that found in the top row of Fig. 6. Results for `spl` and `mpl` show age overestimations up to ∼3 and 2 dex, respectively, in ages where purely stellar models display considerable uncertainties, similarly to total stellar mass results in Fig. 6.

Figure 9 shows the difference in the light-weighted mean stellar metallicity $\log\langle Z_\star \rangle_L$ between PSS and ESS values as a function of age t. The results for the purely stellar models show metallicity over- and underestimations within ∼0.2 dex correlated with evolutionary ages with light-weighted age under- and overestimations, respectively. This is likely due to age-metallicity degeneracies that prevent a clear distinction between young metal-rich and old metal-poor stellar populations or vice versa (Faber 1972; O'Connell 1980; Renzini & Buzzoni 1986; Bressan, Chiosi & Tantalo 1996; Pelat 1997, 1998; Cid Fernandes et al. 2005). This problem arises after changes of absorption line features induced by variations in both age and

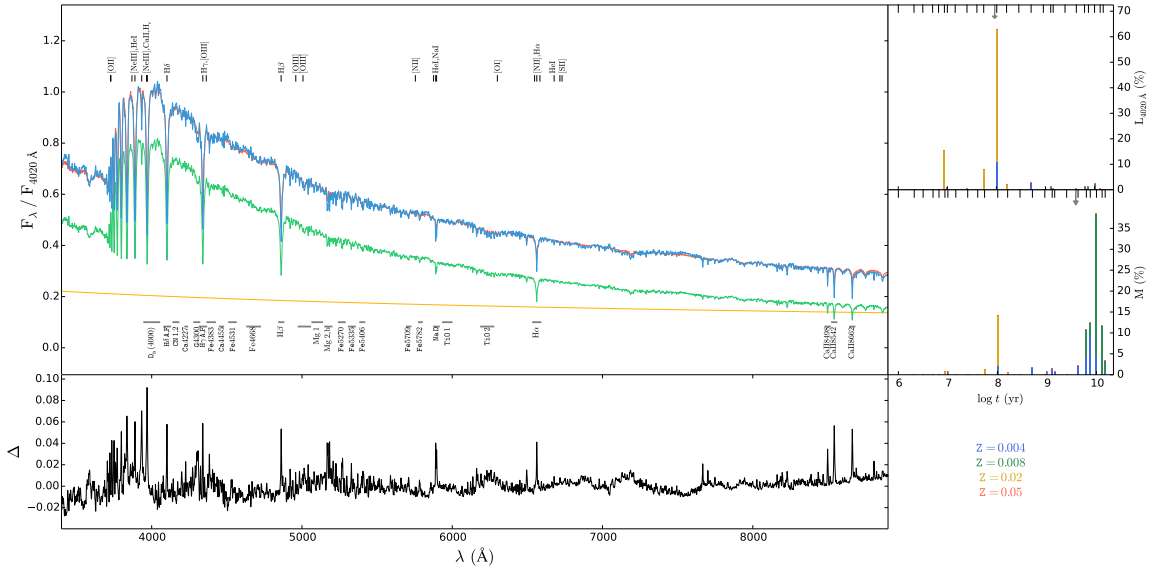

Fig. 5. Mean results of 10 STARLIGHT fits to a SED with a CSP with 100 Myr, solar metallicity, and an instantaneous burst SFH (green line) and an AGN PL with $\alpha = 1.5$ and $x_{\rm AGN} = 0.2$ (yellow line). Main panel: The red and cyan lines correspond to the input and and fitted spectra, respectively. The top and bottom annotations represent the wavelength range of several emission and absorption lines, respectively. Bottom panel: The residuals spectrum (black line) after subtracting the best fit from the input SED is shown. Top right panel: The SFHs in stellar light fractions is shown. Different colours correspond to different metallicities (see text below x-axis for label details). Lines on the top x-axis denote the age of the adopted base of SSPs. Bottom right panel: The SFHs in mass fractions are shown.

metallicity (e.g. Worthey 1994), which is aggravated in this case by the dilution of the absorption features by the PL.

The results in Fig. 9 for `npl` show a systematic underestimation of metallicity by up to ∼0.7 dex with decreasing α and age t and increasing $x_{\rm AGN}$. Figure A.5 shows similar results for other SFHs. The metallicity underestimation plateau at -0.7 dex seen for $\alpha = 2$ and $x_{\rm AGN} = 0.8$ when $t < 1$ Gyr corresponds to a metallicity of $0.2\,Z_{\odot}$, which is the lowest metallicity found in the base. Thus, this result is due to the construction of the base library and has no physical meaning. In addition, this result is due to an increasing dilution of the absorption features with increasing $x_{\rm AGN}$, which artificially makes the stellar continuum increasingly metal poorer. The results for `spl` display random metallicity uncertainties up to ∼0.15 dex predominately located around ages where purely stellar synthesis results also show considerable uncertainties. These roughly increase with increasing α and $x_{\rm AGN}$. Moreover, the results for `mpl` show an increasing metallicity overestimation up to ∼0.2 dex with increasing α and $x_{\rm AGN}$ for $t \gtrsim 1$ Gyr, mirroring the age underestimation at the same evolutionary stages shown in Fig. 7.

Figure 10 illustrating results for the mass-weighted mean stellar metallicity $\log\langle Z_{\star}\rangle_M$ show that light- and mass-weighted metallicities display similar trends with t, α and $x_{\rm AGN}$ for all setups. Indeed, the results for `npl` show again that the metallicity can be underestimated by up to ∼0.7 dex. Figure A.5 shows similar results for other SFHs. Results also show that the mass-weighted properties tend to have larger uncertainties than their light-weighted counterparts. The reason for this is that small light variations translate into large mass variations when applying the mass-to-light ratio to the light fractions vector of the SSPs to determine mass related properties.

Figures A.7–A.11 in Appendix A show plots of spectral synthesis results for a continuous SFH analogous to those presented in Figures 6–10. These results show that stellar uncertainties induced by the added AGN PL component are relatively lower for a continuous SFH than those estimated for an instantaneous burst SFH. This happens because short phases of significant spectrophotometric evolution in the first few hundred Myr are largely washed out in the case of continuous star formation when looking at the time evolution of light- and mass-weighted stellar properties. With respect to an instantaneous burst of a given age and metallicity, the SSP that best approximates this evolutionary stage is not necessarily included in the base library. In this case, and assuming the best case scenario in which there are almost no degeneracies among the stellar populations, adjacent SSPs in age and/or metallicity would have to be used, which unavoidably induces strong local deviations between the true and estimated evolutionary quantities. Thus, results obtained for the instantaneous burst SFH should be viewed as upper limits to the uncertainties on the analysed stellar properties.

4. Discussion

A substantial body of work devoted to the exploration of the assembly history of galaxies relies on automated PSS modelling of large extragalactic data sets (e.g. Kauffmann et al. 2003; Asari et al. 2007; Cid Fernandes et al. 2010). A common practice in these studies is the prior exclusion from the PSS modelling of galaxies classified as Seyfert on the basis of BPT emission-line

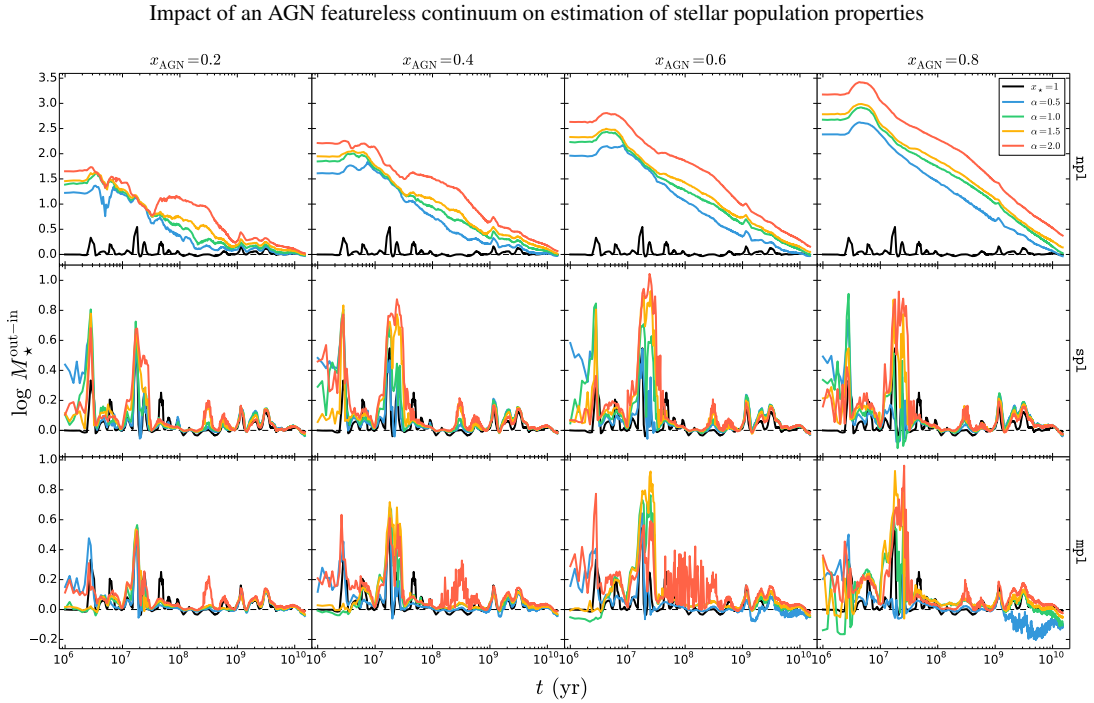

Fig. 6. Difference in the total stellar mass $M_\star$ between PSS (out) and ESS (in) values as a function of model age t for a instantaneous burst SFH. Results adopting a base library without any AGN PL (`npl`), with a PL with the same index value as the input values (`spl`) and with PLs with α = 0.5, 1, 1.5, and 2 (`mpl`) are presented on top, middle, and bottom rows, respectively. Increasing AGN flux fractional contribution $x_{\rm AGN}$ at λ_0 = 4020 Å are represented from left- to right-hand side panels. Results from purely stellar models and models with PLs with α = 0.5, 1.0, 1.5, and 2.0 are represented by black, blue, green, yellow, and red lines, respectively.

diagnostics, since both the spectroscopic characteristics of these systems (e.g. broad emission lines and dilution of stellar features by the featureless AGN PL) and code-specific limitations generally hinder a reliable separation of the non-thermal and stellar SEDs and the extraction from the latter of key physical and evolutionary properties (e.g. stellar mass, mean stellar age and metallicity, and SFH). However, as pointed out in Papaderos et al. (2013) and Gomes et al. (2016) (see also CGP16), standard BPT classification diagnostics become inapplicable in the case of virtually gas-evacuated galaxies where the bulk of the Lyman continuum radiation from an AGN eventually escapes without locally producing detectable optical line emission. This, together with dilution of nuclear emission-line EWs by the stellar component along the line of sight, may readily prevent detection of accretion-powered nuclear activity in an early-type galaxy (Papaderos et al. 2013; Gomes et al. 2016), which is then classified as retired/passive and included in automated PSS studies. The same may obviously apply to old classical bulges, many of which show faint nebular emission despite hosting a super-massive black hole whose accretion-powered energy release may result in significant contamination of the optical spectrum by an AGN PL component. Our pilot study in CGP16 has first addressed the question of the detectability of an AGN PL embedded within an old instantaneously formed Lyman-photon leaking galaxy and explored the effect that this PL component may have on optical PSS modelling studies. This analysis has revealed that a PL contributing up to ∼26% (≡ $x_{\rm AGN}^{\rm threshold}$) of the monochromatic luminosity at 4020 Å generally evades detection both from visual inspection and PSS modelling of a galaxy spectrum and introduces a substantial bias in the physical properties of the stellar component obtained through spectral synthesis. Here, we extend this study by modelling with the PSS code STARLIGHT an extensive grid of synthetic stellar SEDs that trace the spectral evolution of galaxies for a wide range of SFHs over an age span between 1 Myr and 15 Gyr. A comparison of the physical properties obtained for the stellar component from PSS modelling with the input values constrained by the synthetic SEDs has allowed to examine in detail potential biases in PSS modelling for different fitting set-ups (Sect. 3).

Of special importance is the fact that, regardless of the spectral index α of the PL component integrated in the synthetic input SEDs, PSS fitting with purely stellar templates yields at $x_{\rm AGN}^{\rm threshold}$ an overestimation of stellar mass $M_\star$ by up to two orders of magnitude for instantaneously formed stellar populations of age $\lesssim 10^8$ yr. Even though this bias is becoming gradually smaller with increasing age of the input SEDs, it still impacts $M_\star$ estimates by a factor of ∼2 over several Gyr of galactic evolution. For the same set of synthetic SEDs, PSS fits overestimate (underestimate) the light-weighted stellar age by up to ∼1 dex of stellar populations younger (older) than 10 Myr, whereas the mass-weighted stellar age is overestimated by up to ∼3 dex for young ages and a factor ≥2 for old (∼5 Gyr) stellar populations. As for the mass-weighted stellar metallicity, our study indicates a systematic underestimation by a factor of ∼3 for young ages with this bias decreasing yet still present beyond an age of ∼1 Gyr. Such biases are also well documented for SFHs involving a prolonged star formation process (e.g. continuous or exponentially decreasing), suggesting a principal trend for purely stellar

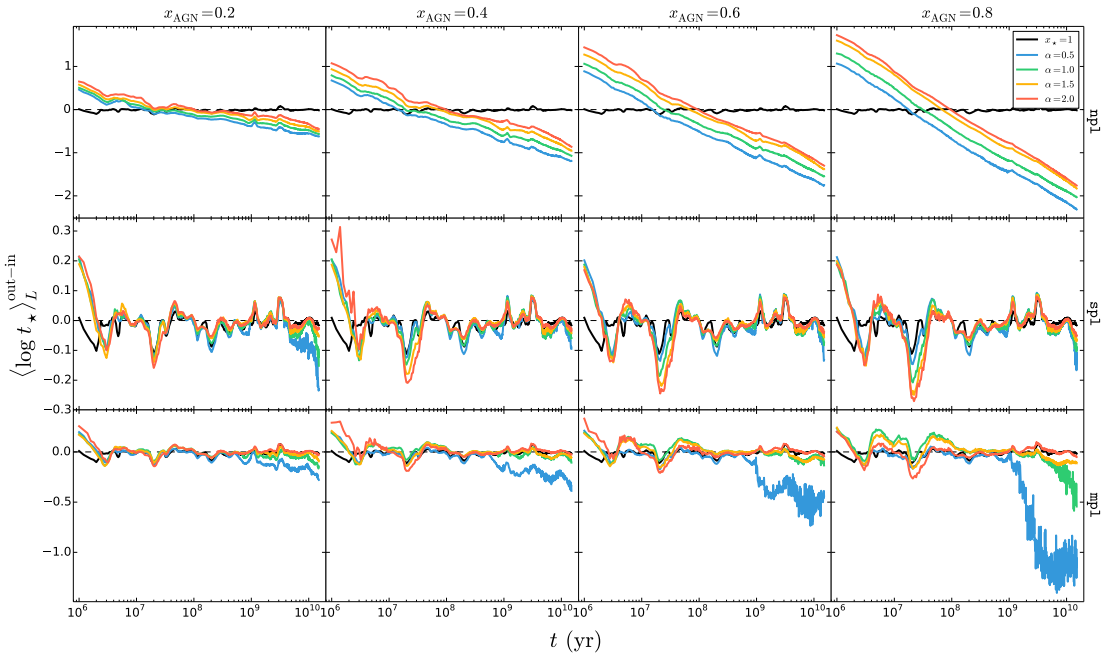

Fig. 7. Difference in the light-weighted mean stellar age $\langle \log t_\star \rangle_L$ between PSS and ESS values as a function of age t for an instantaneous burst SFH. Panel configuration and legend details are analogous to those of Fig. 6.

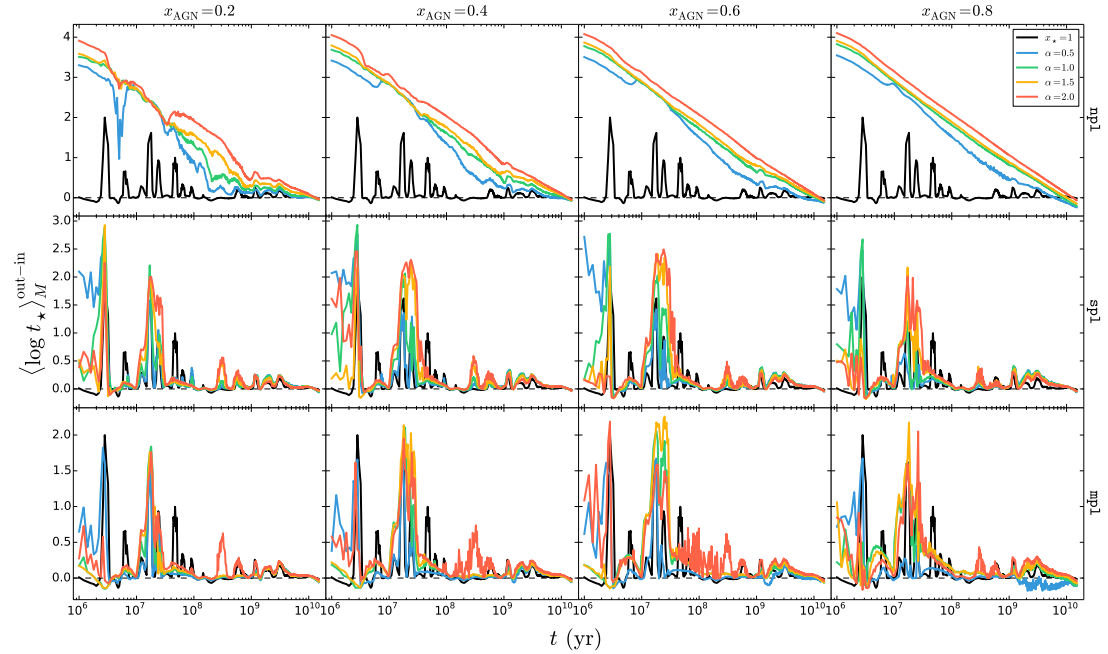

Fig. 8. Difference in the mass-weighted mean stellar age $\langle \log t_\star \rangle_M$ between PSS and ESS values as a function of age t for an instantaneous burst SFH. Panel configuration and legend details are analogous to those of Fig. 6.

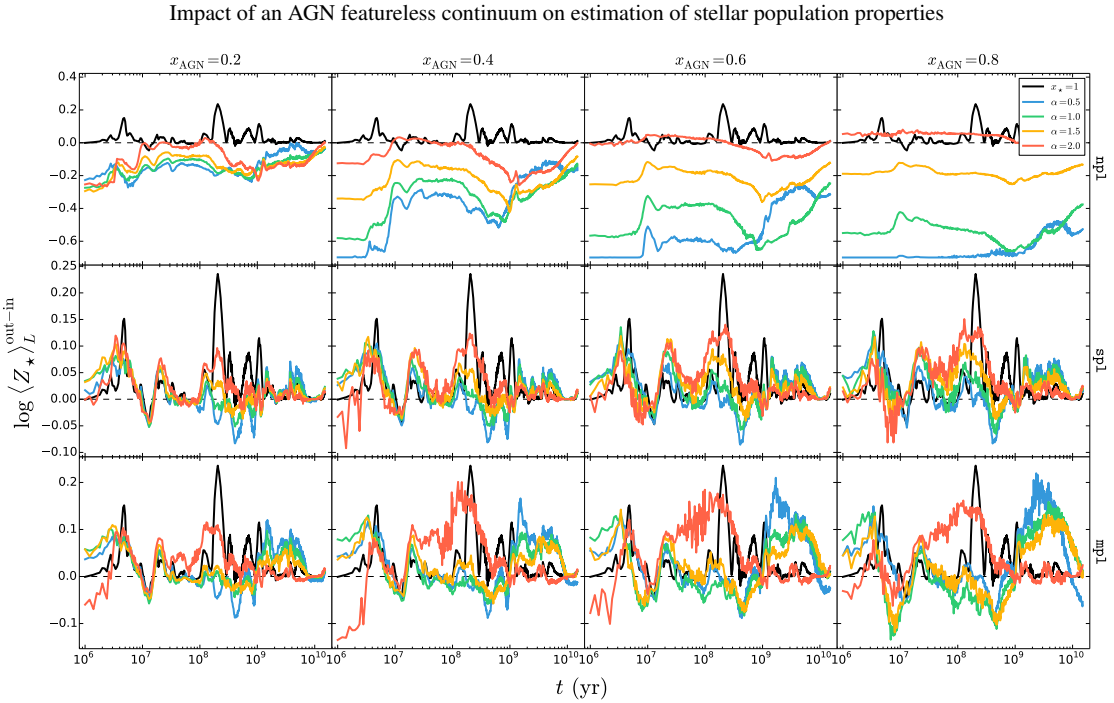

Fig. 9. Difference in the light-weighted mean stellar metallicity $\log\langle Z_\star\rangle_L$ between PSS and ESS values as a function of age t for an instantaneous burst SFH. Panel configuration and legend details are analogous to those of Fig. 6.

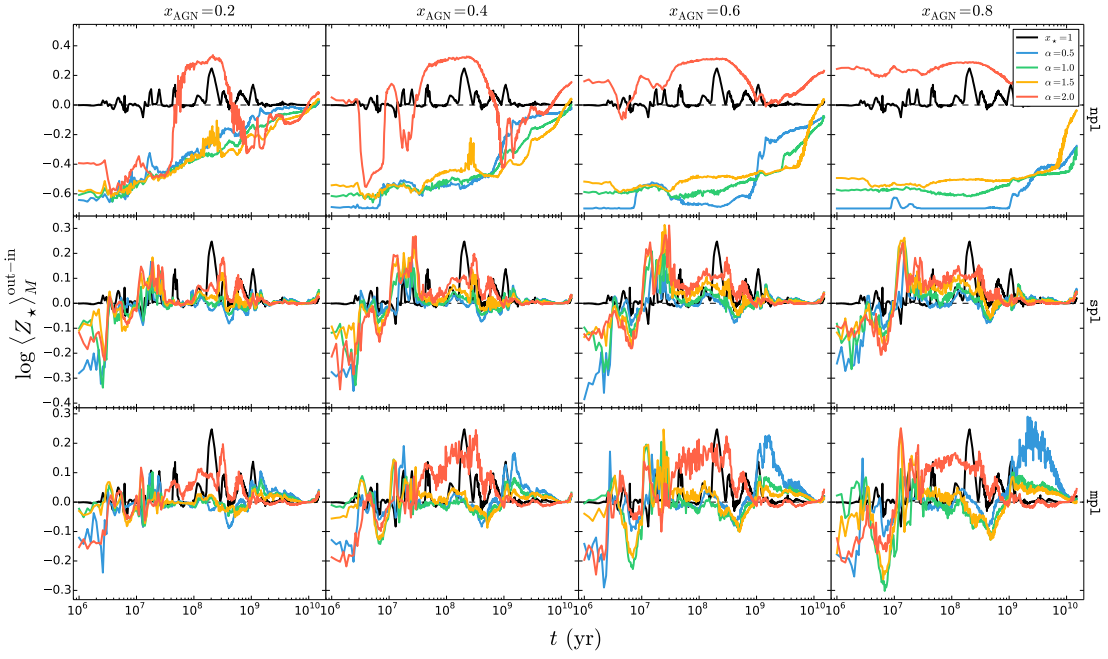

Fig. 10. Difference in the mass-weighted mean stellar metallicity $\log\langle Z_\star\rangle_M$ between PSS and ESS values as a function of age t for an instantaneous burst SFH. Panel configuration and legend details are analogous to those of Fig. 6.

PSS fits to compensate for the presence of a PL spectral component through a severely overestimated contribution from old, low-metallicity stars.

Regarding the impact of an AGN PL on the stellar continuum, stellar population biases correlate on first order with $x_{\rm AGN}$ and on second with α. These are mainly due to the combined effect of the dilution of stellar absorption features by the AGN continuum and a degeneracy between the AGN PL and young SSPs. The addition of a PL leads to a stellar age underestimation given the decrease of the D_n4000 Å break strength and simultaneously to a stellar metallicity overestimation due to the dilution of Balmer absorption features. Moreover, Balmer absorption features become weaker with age and their EWs are inversely correlated with D_n4000 for continuous SFHs (Kauffmann et al. 2003).

A question that naturally arises in view of these modelling biases pertains to the interpretation of the nature of evolved Lyman-photon-leaking galaxies hosting an AGN. Taken at face value, PSS fits might prompt the conclusion that these systems are extraordinarily massive and have assembled quasi-monolithically early on, which would be consistent with the much lower level of chemical enrichment as compared to local galaxies of equal $M_\star$. A possibly significant population of such old, ultra-massive galaxies erroneously included in galaxy statistics could then impact determinations of the cosmic SFH.

5. Conclusions

Synthetic spectra of active galaxies for solar metallicity and multiple SFHs were created with the ESS code Rebetiko and used to investigate how a simple AGN FC model impacts the estimation of stellar population properties with the state-of-the-art PSS code Starlight. The AGN continuum model is defined by its PL index α and AGN fractional contribution $x_{\rm AGN}$ to the λ_0 = 4020 Å monochromatic flux. The stellar spectral contribution is computed assuming solar metallicity SSPs from Bruzual & Charlot (2003) in both the creation of the synthetic spectra with ESS and the application of PSS. The accuracy of the estimated physical properties depends on the model age, α, $x_{\rm AGN}$ and, more importantly, the approach adopted for dealing with the AGN continuum:

1. Excluding any PL component in the fit can lead to uncertainties on stellar mass by up to ∼3.5 dex, light- and mass-weighted mean stellar age up to ∼2 and ∼4 dex, respectively, and on both light- and mass-weighted mean stellar metallicity up to ∼0.7 dex.
2. Including a single or multiple PL components in the fit leads to uncertainties on stellar mass overestimation up to ∼1 dex, light- and -mass-weighted mean stellar age up to ∼1.5 and ∼3 dex, respectively, and light- and mass-weighted mean stellar metallicity up to ∼0.2 and ∼0.4 dex, respectively.

The uncertainties on the stellar population properties estimated with PSS are weakly dependent on the SFH, in particular when no AGN model is included in the base of elements. These results might lead to the misinterpretation that evolved Lyman-photon-leaking galaxies hosting an AGN are particularly massive, metal poor, and formed monolithically when the universe was still very young. Hence, these results show the importance of accounting for AGN spectral contributions when applying state-of-the-art PSS to active galaxies for a viable estimation of their physical properties, such as star formation and chemical evolution histories.

Acknowledgements. This work was supported by Fundação para a Ciência e a Tecnologia (FCT) through national funds (UID/FIS/04434/2013) and by FEDER through COMPETE2020 (POCI-01-0145-FEDER-007672). We acknowledge support from the FCT through national funds (PTDC/FIS-AST/3214/2012) and by FEDER through COMPETE (FCOMP-01-0124-FEDER-029170). We thank the anonymous referee for valuable comments and suggestions. LSMC acknowledges funding by FCT through the grant CIAAUP-01/2016-BI in the context of the FCT project UID/FIS/04434/2013 & POCI-01-0145-FEDER-007672. JMG is supported by the fellowship SFRH/BPD/66958/2009 funded by FCT (Portugal) and POPH/FSE (EC) and by the fellowship CIAAUP-04/2016-BPD in the context of the FCT project UID/FIS/04434/2013 & POCI-01-0145-FEDER-007672. PP is supported by FCT through Investigador FCT contract IF/01220/2013/CP1191/CT0002 and by a Ciência 2008 contract, funded by FCT/MCTES (Portugal) and POPH/FSE (EC). We also acknowledge the exchange programme "Study of Emission-Line Galaxies with Integral-Field Spectroscopy" (SELGIFS, FP7-PEOPLE-2013-IRSES-612701), funded by the EU through the IRSES scheme.

References

Anders, P., Bissantz, N., Fritze-v. Alvensleben, U., de Grijs, R. 2004, MNRAS, 1, 196
Asari, N. V., Cid Fernandes, R., Stasińska, G., Torres-Papaqui, J. P., Mateus, A., Sodré, L., Schoenell, W., Gomes, J. M. 2007, MNRAS, 381, 263
Antonucci R., 1993, ARA&A, 31, 473
Baade, W. 1944 ApJ, 100 ,137
Baade, W. 1944 ApJ, 100 ,147
Benítez, E., Méndez-Abreu, J., Fuentes-Carrera, I., Cruz-González, I., Martínez, B., López-Martin, L., Jiménez-Bailón, E., León-Tavares, J., Chavushyan, V. H. 2013, ApJ, 763, 36
Bica E. 1988, A&A, 195, 76
Bon, N., Popović, L. C., Bon, E 2014, AdSpR, 54, 1389B
Boisson, C., Joly, M., Moultaka, J., Pelat, D., Serote Roos, M. 2000, A&A, 357, 850B
Bressan, A., Chiosi, C., Tantalo, R. 1996, ASPC, 98, 49
Bruzual, G., Charlot, S. 2003, MNRAS, 344, 1000
Calzetti, D., Armus, L., Bohlin, R. C., Kinney, A. L., Koornneef, K., Storchi-Bergmann, T. 2000, ApJ, 533, 682
Cardoso, L. S. M., Gomes, J.-M., Papaderos, P. 2016, A&A, 594, L2
Cerviño, M. 2013, NewAR, 57, 123
Chabrier, G. 2003, PASP, 115, 763
Ciesla, L., Charmandaris, V., Georgakakis, A., Bernhard, E., Mitchell, P. D., Buat, V., Elbaz, D., LeFloc'h, E., Lacey, C. G., Magdis, G. E., Xilouris, M. 2015, A&A, 576, 10
da Cunha E., Charlot S., Elbaz D. 2008, MNRAS, 388, 1595
Cid Fernandes R., Terlevich R. 1995, MNRAS 272, 423
Cid Fernandes, R. Jr., Storchi-Bergmann, T., Schmitt, H. R. 1998, MNRAS, 297, 579C
Cid Fernandes, R., Gu, Q., Melnick, J., Terlevich, E., Terlevich, R., Kunth, D., Rodrigues Lacerda, R., Joguet, B. 2004, MNRAS, 355, 273
Cid Fernandes, R., Mateus, A., Sodré, L., Stasińska, G., Gomes, J. M. 2005, MNRAS, 358, 363
Cid Fernandes, R., Stasińska, G., Schlickmann, M. S., Mateus, A., Vale Asari, N., Schoenell, W., Sodré, L. 2010, MNRAS, 403, 1036
Cid Fernandes, R., Stasińska, G., Mateus, A., Vale Asari, N. 2011, MNRAS, 413, 1687
Cid Fernandes, R., González Delgado, R. M., García Benito, R., Pérez, E., de Amorim, A. L., Sánchez, S. F., Husemann, B., Falcón Barroso, J., López-Fernández, R., Sánchez-Blázquez, P., Vale Asari, N., Vazdekis, A., Walcher, C. J., Mast, D. 2014, A&A, 561, 19
Coelho, P., Bruzual, G., Charlot, S., Weiss, A., Barbuy, B., Ferguson, J. W. 2007, MNRAS, 12, 498
Conroy, C. 2013, ARA&A, 51, 393
Dressler, A. 1984, ApJ, 286, 97D
Eracleous, M., Halpern, J. P. 2001, ApJ, 554, 240
Faber, S. M. 1972, A&A, 20, 361
Ferland, G. J., Netzer, H. 1983, ApJ, 264, 105
Fioc, M., Rocca-Volmerange, B. 1997, A&A, 10, 950

Gavazzi, G., Bonfanti, C., Sanvito, G., Boselli, A., Scodeggio, M. 2002 ApJ, 576, 135
Garcia-Rissmann, A., Vega, L. R., Asari, N. V., Cid Fernandes, R., Schmitt, H., González Delgado, R. M., Storchi-Bergmann, T. 2005, MNRAS, 359, 765
Goerdt, A., Kollatschny, W. 1998, A&A, 337, 699
Gomes, J. M., Papaderos, P., Kehrig, C., Vílchez, J. M., Lehnert, M. D., Sánchez, S. F., Ziegler, B., Breda, I., Dos Reis, S. N., Iglesias-Páramo, J., Bland-Hawthorn, J., Galbany, L., Bomans, D. J., Rosales-Ortega, F. F., Cid Fernandes, R., Walcher, C. J., Falcón-Barroso, J., García-Benito, R., Márquez, I., Del Olmo, A., Masegosa, J., Mollá, M., Marino, R. A., González Delgado, R. M., López-Sánchez, Á. R., CALIFA Collaboration 2016, A&A, 588, 68
Hayward, C. C.; Smith, D. J. B. 2015, MNRAS, 446, 1512
Heavens, A. F., Jimenez, R., Lahav, O. 2000, MNRAS, 317, 965
Heavens, A., Panter, B., Jimenez, R., Dunlop, J. 2004, Nat, 428, 625
Heckman, T. M. 1980, A&A, 88, 311
Heckman T.M., Krolik J., Meurer G., et al., 1995 ApJ 452, 549
Ho, L. C., Filippenko, A. V., Sargent, W. L. 1995, ApJS, 98, 477
Ho, L. C., Filippenko, A. V., Sargent, W. L. W. 1997, ApJS, 112, 315
Ho, L. C., Filippenko, A. V., Sargent, W. L. W. 2003, ApJ, 583, 159
Ho, L. 2008, ARA&A, 46, 475H
Ho, L. C., Kim, M. 2009, ApJS, 184, 398
Kauffmann, G., Heckman, T. M., Tremonti, C., Brinchmann, J., Charlot, S., White, S. D. M., Ridgway, S. E., Brinkmann, J., Fukugita, M., Hall, P. B., Ivezić, Ž., Richards, G. T., Schneider, D. P. 2003, MNRAS, 346, 1055
Kehrig, C., Monreal-Ibero, A., Papaderos, P., Vílchez, J. M., Gomes, J. M., Masegosa, J., Sánchez, S. F., Lehnert, M. D., Cid Fernandes, R., Bland-Hawthorn, J., Bomans, D. J., Marquez, I., Mast, D., Aguerri, J. A. L., López-Sánchez, ÃĄ. R., Marino, R. A., Pasquali, A., Perez, I., Roth, M. M., Sánchez-Blázquez, P., Ziegler, B. 2012, A&A, 540, 11
Koleva, M., Prugniel, Ph., Bouchard, A., Wu, Y. 2009, A&A, 7, 1269
Koski, A. T. 1978, ApJ, .223, 56
Kotulla, R., Fritze, U., Weilbacher, P., Anders, P. 2009, MNRAS, 6, 462
Krüger, H., Fritze-v. Alvensleben, U., Loose, H.-H. 1995, A&A, 11, 41
Leitherer, C., Schaerer, D., Goldader, J. D., González Delgado, R. M., Robert, C., Kune, D. F., de Mello, D. F., Devost, D., Heckman, T. M. 1999, ApJS, 7, 3
Le Borgne, J.-F., Bruzual, G., Pelló, R., Lançon, A., Rocca-Volmerange, B., Sanahuja, B., Schaerer, D., Soubiran, C., Vílchez-Gómez, R. 2003, A&A, 402, 433
Le Borgne, D., Rocca-Volmerange, B., Prugniel, P., Lançon, A., Fioc, M., Soubiran, C. 2004, A&A, 10, 881
MacArthur, L. A., González, J. J., Courteau, S. 2009, MNRAS, 5, 28
Maraston, C. 2005, MNRAS, 362, 799
Mateus, A., Sodré, L., Cid Fernandes, R., Stasińska, G., Schoenell, W., Gomes, J. M. 2006, MNRAS, 370, 721
Mathews, W. G., Ferland, G. J. 1987, ApJ, 323, 456
Mollá, M., García-Vargas, M. L., Bressan, A. 2009, MNRAS, 9, 451
Morgan W. W. 1956, PASP, 68, 509
Moultaka, J., Pelat, D. 2000, MNRAS, 314, 409
Moultaka, J., Boisson, C., Joly, M., Pelat, D. 2004, A&A, 420, 459
Moultaka, J. 2005, A&A, 430, 95
Netzer, H. 2015, ARA&A, 53, 365N
Nelson, C. H., N., Whittle, M. 1995, ApJS, 99, 67N
Noll, S., Burgarella, D., Giovannoli, E., Buat, V., Marcillac, D., Muñoz-Mateos, J. C. 2009, A&A, 507, 1793
O'Connell, R. W. 1976, ApJ, 206, 370
O'Connell, R. W. 1980, ApJ, 236, 430
Ocvirk, P., Pichon, C., Lançon, A., Thiébaut, E. 2006a, MNRAS, 365, 46
Ocvirk, P., Pichon, C., Lançon, A., Thiébaut, E. 2006b, MNRAS, 365, 74
Oke, J. B., Neugebauer, G., Becklin, E. E. 1970, ApJ, 159, 341
Papaderos, P., Gomes, J. M., Vílchez, J. M., Kehrig, C., Lehnert, M. D., Ziegler, B., Sánchez, S. F., Husemann, B., Monreal-Ibero, A., García-Benito, R., Bland-Hawthorn, J., Cortijo-Ferrero, C., de Lorenzo-Cáceres, A., del Olmo, A., Falcón-Barroso, J., Galbany, L., Iglesias-Páramo, J., López Sánchez, Á. R., Marquez, I., Mollá, M., Mast, D., van de Ven, G., Wisotzki, L. 2013, A&A, 555, L1
Pelat, D. 1997, MNRAS, 284, 365
Pelat, D. 1998, MNRAS, 299, 877
Renzini, A. 1981. Ann. Phys. 6, 87
Renzini, A., Buzzoni, A. 1986, ASSL, 122, 195
Ribeiro, B., Lobo, C., Antón, S., Gomes, J. M., & Papaderos, P. 2016, MNRAS, 456, 3899
Rocca-Volmerange, B., Guiderdoni, B. 1988, A&ASS, 75, 91
Roche, N., Humphrey, A., Lagos, P., Papaderos, P., Silva, M., Cardoso, L. S. M., Gomes, J. M. 2016, MNRAS, 459, 4259
Schmitt, H. R., Storchi-Bergmann, T., Cid Fernandes, R. 1999, MNRAS, 303, 173
Seyfert, C. K. 1943, ApJ, 97, 28
Serote Roos, M., Boisson, C., Joly, M., Ward, M. J. 1998, MNRAS, 301, 1
Stasińska, G. 1984a, A&AS, 55, 15
Stasińska, G. 1984b, A&A, 135, 341
Stasińska, G., Vale Asari, N., Cid Fernandes, R., Gomes, J. M., Schlickmann, M., Mateus, A., Schoenell, W., Sodré, L., Jr. 2008, MNRAS, 391, 29
Stasińska, G., Costa-Duarte, M. V., Vale Asari, N., Cid Fernandes, R., Sodré, L. 2015 MNRAS, 449, 559
Storchi-Bergmann, T., Baldwin, J. A., Wilson, A. S. 1993, ApJ, 410L, 11S
Storchi-Bergmann, T., Cid Fernandes, R., Schmitt, H. R. 1998, ApJ, 501, 94S
Spinrad, H., Taylor, B. J. 1972, ApJ, 171, 397
Tran, H. D. 1995, ApJ, 440, 597T
Terlevich, E., Díaz, A. I., Terlevich, R. 1990, MNRAS, 242, 271
Tinsley, B. M. 1968, ApJ, 151, 547
Tinsley, B. M. 1980, FCPh, 5, 287
Tojeiro, R., Heavens, A. F., Jimenez, R., Panter, B. 2007 MNRAS, 11, 1252
Vazdekis, A., Sánchez-Blázquez, P., Falcón-Barroso, J., Cenarro, A. J., Beasley, M. A., Cardiel, N., Gorgas, J., Peletier, R. F. 2010, MNRAS, 6, 1639
Vega, L. R., Asari, N. V., Cid Fernandes, R., Garcia-Rissmann, A., Storchi-Bergmann, T., GonzÃąlez Delgado, R. M., Schmitt, H. 2009, MNRAS, 393, 846
Veilleux, S., Osterbrock, D. E. 1987, ApJS, 63, 295
Walcher, J., Groves, B., Budavári, T; Dale, D. 2011, Ap&SS, 331, 1
Whipple, Fred L. 1935, Harvard College Observatory Circular, 404, 1
Wood D. B. 1966, ApJ, 145, 36
Worthey G. 1994, ApJS, 95, 107
York, D. G., Adelman, J., Anderson, Jr., J. E., SDSS Collaboration 2000 ApJ, 120, 1579
Zackrisson, E., Bergvall, N., Olofsson, K., Siebert, A. 2001, A&A, 9, 814

Appendix A: Additional resources

Figures A.1 and A.12 show the AGN fractional contribution $x_{\rm AGN}$ difference between PSS and ESS as a function of model age t for models with instantaneous burst and continuous SFHs, respectively, with increasing $x_{\rm AGN}$ from left- to -right-hand side panels. Top and bottom row panels show results for the `spl` and `mpl` fitting set-ups (Section 2.2). On the one hand, the results for `spl` show that the accuracy of the estimated $x_{\rm AGN}$ increases with α and $x_{\rm AGN}$. Moreover, there is a underestimation bump between 10^8 and 10^9 yr that is attenuated with increasing $x_{\rm AGN}$. On the other hand, the results for `mpl` show a systematic $x_{\rm AGN}$ under- and overestimation for $t \lesssim 10^8$ and $t \gtrsim 10^8$ yr with increasing $x_{\rm AGN}$, respectevely. This underestimation increases with decreasing α. Results for both `spl` and `mpl` show that the estimation of $x_{\rm AGN}$ is sensitive to the underlying stellar continuum shape.

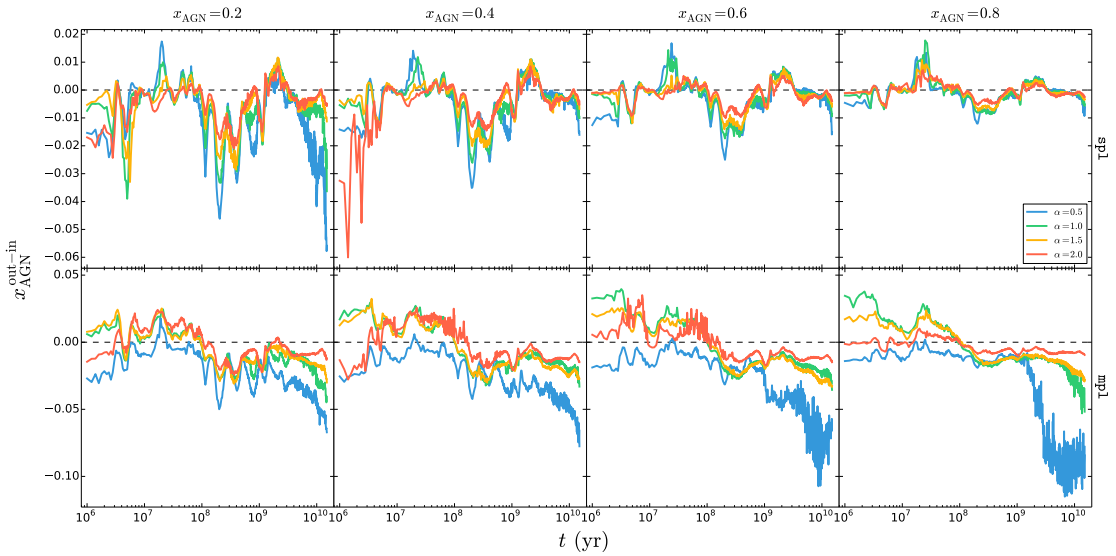

Fig. A.1. Difference in AGN fractional contribution $x_{\rm AGN}$ between PSS and ESS values as a function of model age t for an instantaneous burst SFH with increasing AGN fractional contribution $x_{\rm AGN}$ from left- to right-hand side panels. Top and bottom rows illustrate results for `spl` and `mpl`, respectively.

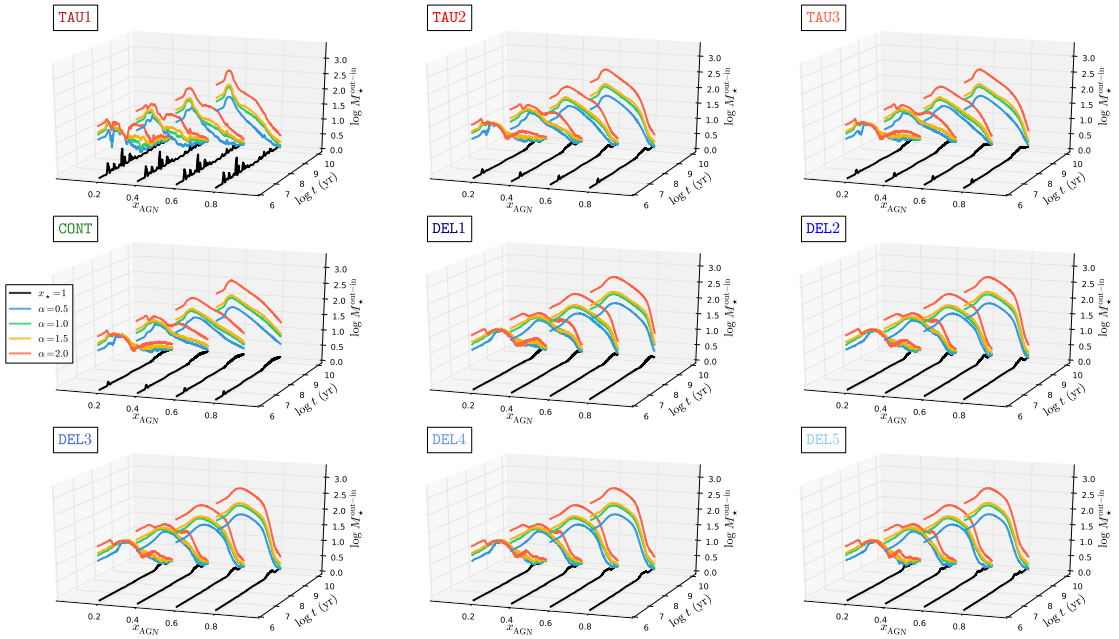

Fig. A.2. Difference in the stellar mass $M_\star$ (z-axis) between PSS and ESS values as a function of model age t (y-axis) and AGN fractional contribution $x_{\rm AGN}$ (x-axis). Black, blue, green, yellow, and red lines represent CSP models and active galaxy models with α = 0.5, 1.0, 1.5, and 2.0, respectively. Each panel corresponds to different SFHs (see Fig. 1 for label details).

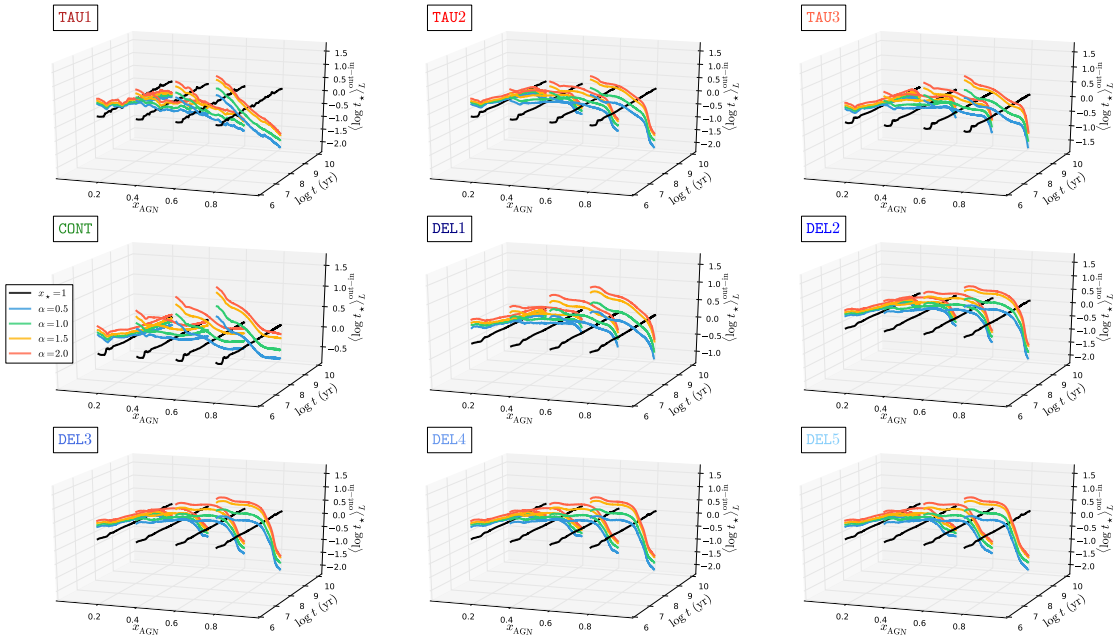

Fig. A.3. Difference in the light-weighted mean stellar age $\langle \log t_\star \rangle_L$ (z-axis) between PSS and ESS values as a function of model age t (y-axis) and AGN fractional contribution (x-axis). Panel configuration and legend details are analogous to those of Fig. A.2.

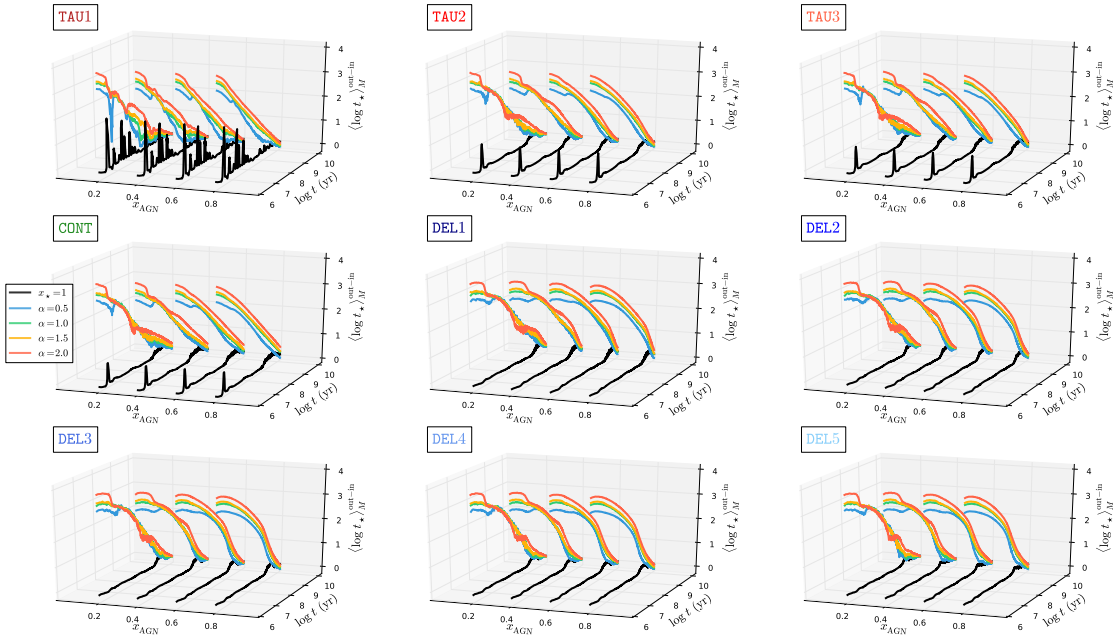

Fig. A.4. Difference in the mass-weighted mean stellar age $\langle \log t_\star \rangle_M$ (z-axis) between PSS and ESS values as a function of model age t (y-axis) and AGN fractional contribution (x-axis). Panel configuration and legend details are analogous to those of Fig. A.2.

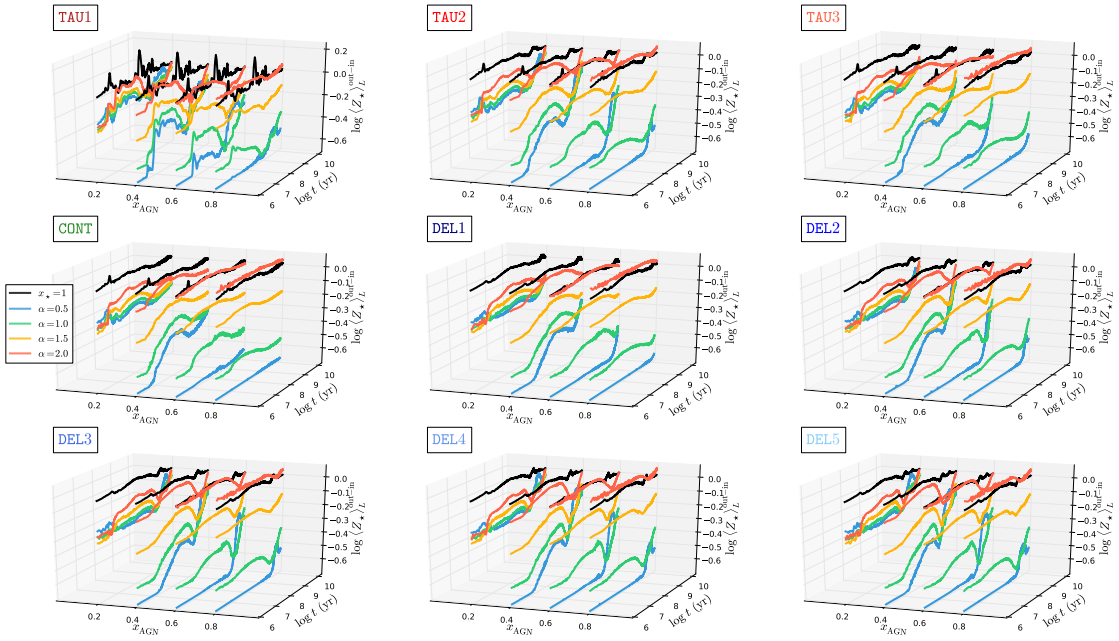

Fig. A.5. Difference in the light-weighted mean stellar metallicity $\log\langle Z_{\star}\rangle_L$ (z-axis) between PSS and ESS values as a function of model age t (y-axis) and AGN fractional contribution (x-axis). Panel configuration and legend details are analogous to those of Fig. A.2.

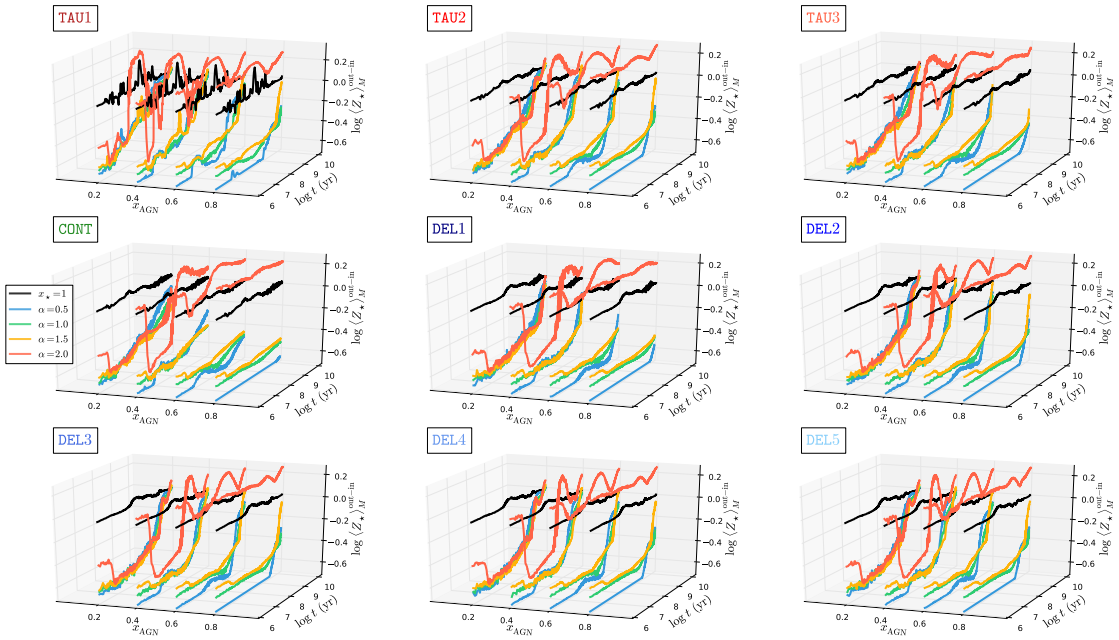

Fig. A.6. Difference in the mass-weighted mean stellar metallicity $\log\langle Z_{\star}\rangle_M$ (z-axis) between PSS and ESS values as a function of model age t (y-axis) and AGN fractional contribution (x-axis). Panel configuration and legend details are analogous to those of Fig. A.2.

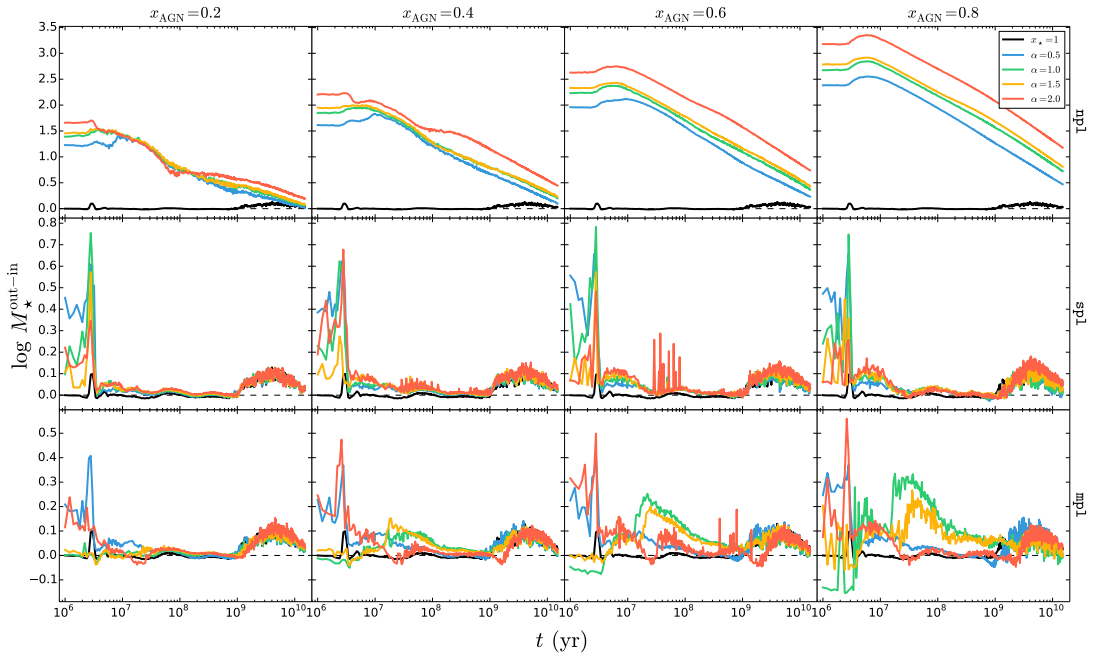

Fig. A.7. Difference in the total stellar mass $M_\star$ between PSS and ESS values as a function of model age t for a continuous SFH. Panel configuration and legend details are analogous to those of Fig. 6.

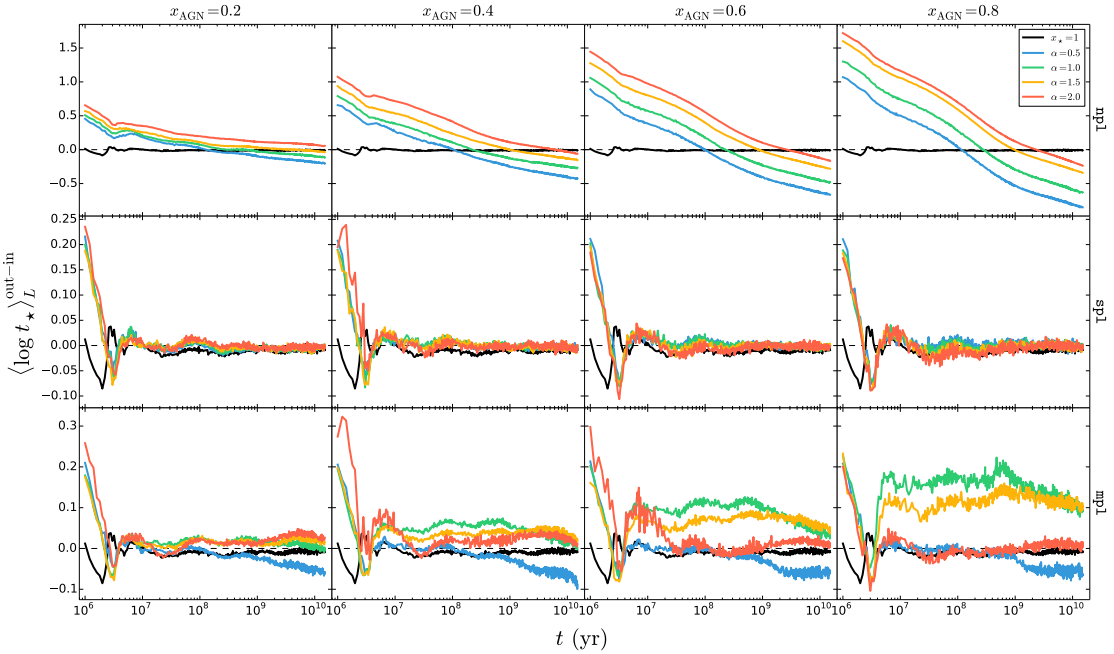

Fig. A.8. Difference in the light-weighted mean stellar age $\langle \log t_\star \rangle_L$ between PSS and ESS values as a function of model age t for a continuous SFH. Panel configuration and legend details are analogous to those of Fig. 6.

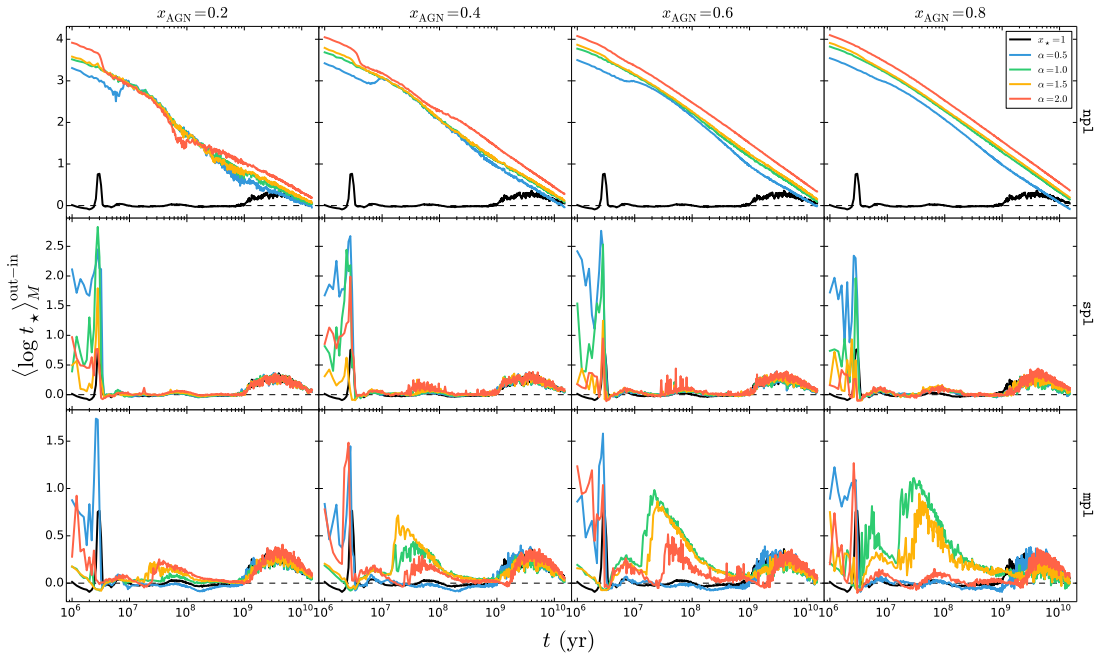

Fig. A.9. Difference in the mass-weighted mean stellar age $\langle \log t_\star \rangle_M$ between PSS and ESS values as a function of model age t for a continuous SFH. Panel configuration and legend details are analogous to those of Fig. 6.

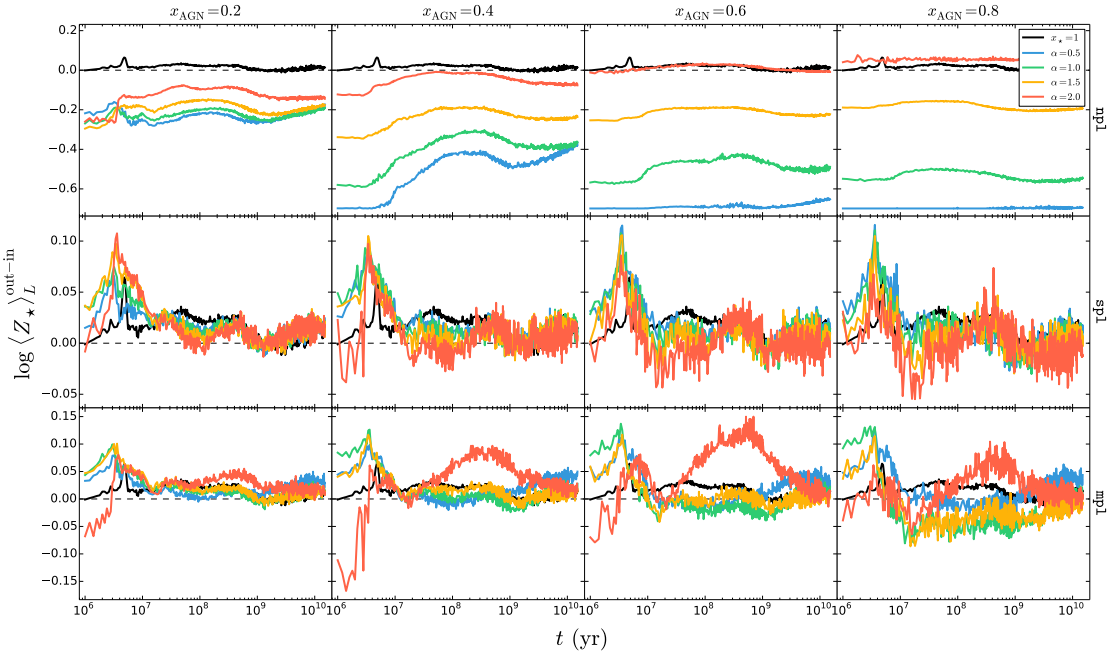

Fig. A.10. Difference in the light-weighted mean stellar metallicity $\log\langle Z_\star \rangle_L$ between PSS and ESS values as a function of model age t for a continuous SFH. Panel configuration and legend details are analogous to those of Fig. 6.

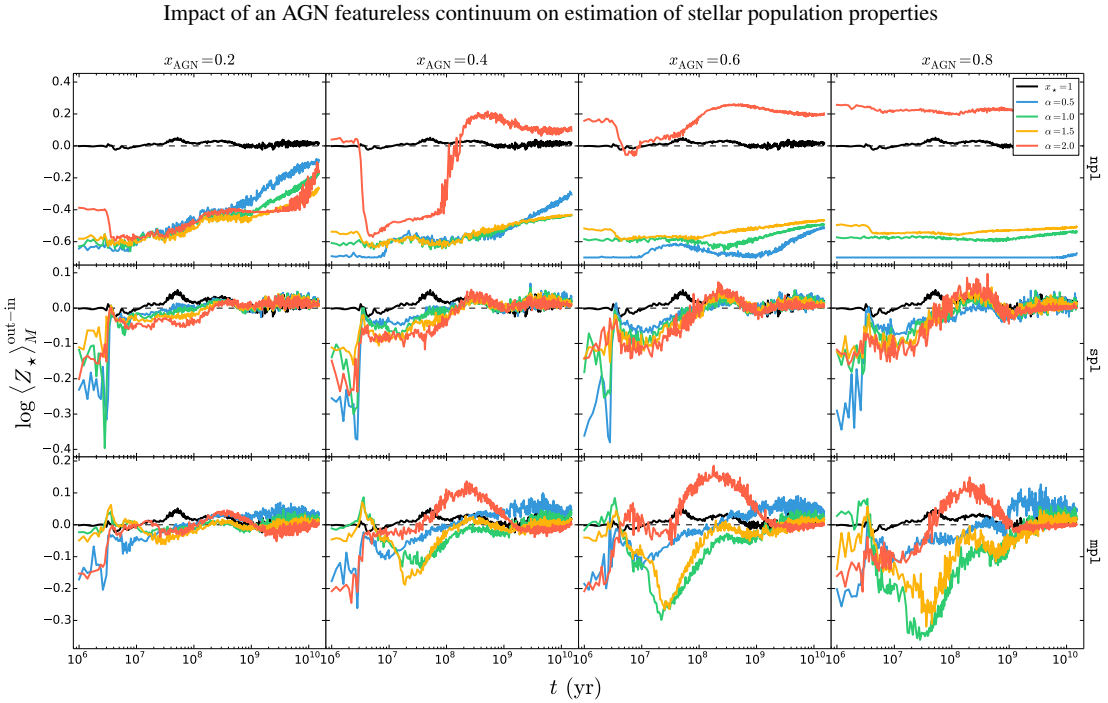

Fig. A.11. Difference in the mass-weighted mean stellar metallicity difference $\log\langle Z_\star\rangle_M$ PSS and ESS values as a function of model age t for a continuous SFH. Panel configuration and legend details are analogous to those of Fig. 6.

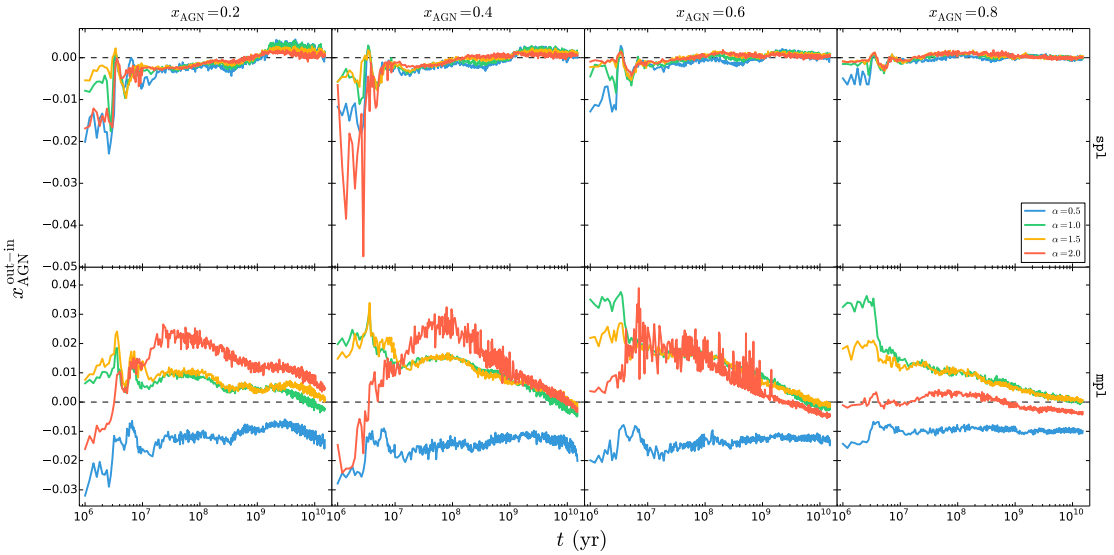

Fig. A.12. Difference in the AGN fractional contribution $x_{\rm AGN}$ between PSS and ESS values as a function of model age t for a continuous SFH. Panel configuration and legend details are analogous to those of Fig. A.1.

Abbreviations & Symbols

AG	**a**ctive **g**alaxy
AGB	**a**symptotic **g**iant **b**ranch
AGN	**a**ctive **g**alaxy **n**ucleus
BLR	**b**road-**l**ine **r**egion
CEH	**c**hemical **e**volution **h**istory
CMD	**c**olour **m**agnitude **d**iagram
CSP	**c**omposite **s**tellar **p**opulation
DR	**d**ata **r**elease
ESS	**e**volutionary **s**pectral **s**ynthesis
EW	**e**quivalent **w**idth
FADO	**F**itting **A**nalysis using **D**ifferential evolution **O**ptimisation
FC	**f**eatureless **c**ontinuum
FWHM	**f**ull **w**idth at **h**alf **m**aximum
HIIR	**HII r**egion
IFU	**i**ntegral **f**ield **u**nit
IMF	**i**nitial **m**ass **f**unction
ISM	**i**nter**s**tellar **m**edium
LINER	**l**ow **i**onization **n**uclear **e**mission-line **r**egion
M/L	**m**ass-**to**-**l**ight
NE	**n**ebular **e**mission
NIR	**n**ear-**i**nfra**r**ed
NLR	**n**arrow-**l**ine **r**egion
PL	**p**ower-**l**aw
PSS	**p**opulation **s**pectral **s**ynthesis
REBETIKO	**R**eckoning galaxy **E**mission **B**y means of **E**volutionary **T**asks with **I**nput **K**ey **O**bservables
SDSS	**S**loan **D**igital **S**ky **S**urvey
SED	**s**pectral **e**nergy **d**istribution
SFH	**s**tar **f**ormation **h**istory
SFR	**s**tar **f**ormation **r**ate
S/N	**s**ignal-**to**-**n**oise
SMBH	**s**uper **m**assive **b**lack **h**ole
SS	**s**pectral **s**ynthesis
SSP	**s**imple/**s**ingle **s**tellar **p**opulation
UV	**u**ltra**v**iolet

A_V	V-band extinction
χ^2	chi-squared
χ^2_λ	reduced chi-squared
Δ_λ	mean absolute percentage error
λ_0	normalisation wavelength
$\langle \log t_\star \rangle_L$	light-weighted mean logarithmic stellar age in units of year (yr)
$\langle \log t_\star \rangle_M$	mass-weighted mean logarithmic stellar age in units of year (yr)
$\log\langle Z_\star \rangle_L$	light-weighted logarithmic mean stellar metallicity
$\log\langle Z_\star \rangle_M$	mass-weighted logarithmic mean stellar metallicity
γ_i	light-fraction of the i$^{\text{th}}$ SSP in the base library
M_λ	best-fit spectrum
$M_\star$	total stellar mass in units of solar mass ($M_\odot$)
μ_i	mass-fraction of the i$^{\text{th}}$ SSP in the base library
$N_\star$	number of SSPs in the base library
O_λ	observed spectrum
$\sigma_\star$	stellar velocity dispersion
t_i	age of the i$^{\text{th}}$ SSP in the base library
$v_\star$	stellar velocity shift
$\vec{x}$	light- or mass-weighted population vector
Z_i	metallicity of the i$^{\text{th}}$ SSP in the base library

Bibliography

Abazajian, K., Adelman-McCarthy, J.K., Agüeros, M.A., Allam, S.S., Anderson, S.F., Annis, J., Bahcall, N.A., Baldry, I.K., Bastian, S., Berlind, A., Bernardi, M., Blanton, M.R., Blythe, N., Bochanski, J.J., Jr., Boroski, W.N., Brewington, H., Briggs, J.W., Brinkmann, J., Brunner, R.J., Budavári, T., Carey, L.N., Carr, M.A., Castander, F.J., Chiu, K., Collinge, M.J., Connolly, A.J., Covey, K.R., Csabai, I., Dalcanton, J.J., Dodelson, S., Doi, M., Dong, F., Eisenstein, D.J., Evans, M.L., Fan, X., Feldman, P.D., Finkbeiner, D.P., Friedman, S.D., Frieman, J.A., Fukugita, M., Gal, R.R., Gillespie, B., Glazebrook, K., Gonzalez, C.F., Gray, J., Grebel, E.K., Grodnicki, L., Gunn, J.E., Gurbani, V.K., Hall, P.B., Hao, L., Harbeck, D., Harris, F.H., Harris, H.C., Harvanek, M., Hawley, S.L., Heckman, T.M., Helmboldt, J.F., Hendry, J.S., Hennessy, G.S., Hindsley, R.B., Hogg, D.W., Holmgren, D.J., Holtzman, J.A., Homer, L., Hui, L., Ichikawa, S.i., Ichikawa, T., Inkmann, J.P., Ivezić, Ž., Jester, S., Johnston, D.E., Jordan, B., Jordan, W.P., Jorgensen, A.M., Jurić, M., Kauffmann, G., Kent, S.M., Kleinman, S.J., Knapp, G.R., Kniazev, A.Y., Kron, R.G., Krzesiński, J., Kunszt, P.Z., Kuropatkin, N., Lamb, D.Q., Lampeitl, H., Laubscher, B.E., Lee, B.C., Leger, R.F., Li, N., Lidz, A., Lin, H., Loh, Y.S., Long, D.C., Loveday, J., Lupton, R.H., Malik, T., Margon, B., McGehee, P.M., McKay, T.A., Meiksin, A., Miknaitis, G.A., Moorthy, B.K., Munn, J.A., Murphy, T., Nakajima, R., Narayanan, V.K., Nash, T., Neilsen, E.H., Jr., Newberg, H.J., Newman, P.R., Nichol, R.C., Nicinski, T., Nieto-Santisteban, M., Nitta, A., Odenkirchen, M., Okamura, S., Ostriker, J.P., Owen, R., Padmanabhan, N., Peoples, J., Pier, J.R., Pindor, B., Pope, A.C., Quinn, T.R., Rafikov, R.R., Raymond, S.N., Richards, G.T., Richmond, M.W., Rix, H.W., Rockosi, C.M., Schaye, J., Schlegel, D.J., Schneider, D.P., Schroeder, J., Scranton, R., Sekiguchi, M., Seljak, U., Sergey, G., Sesar, B., Sheldon, E., Shimasaku, K., Siegmund, W.A., Silvestri, N.M., Sinisgalli, A.J., Sirko, E., Smith, J.A., Smolčić, V., Snedden, S.A., Stebbins, A., Steinhardt, C., Stinson, G., Stoughton, C., Strateva, I.V., Strauss, M.A., SubbaRao, M., Szalay, A.S., Szapudi, I., Szkody, P., Tasca, L., Tegmark, M., Thakar, A.R., Tremonti, C., Tucker, D.L., Uomoto, A., Vanden Berk, D.E., Vandenberg, J., Vogeley, M.S., Voges, W., Vogt, N.P., Walkowicz, L.M., Weinberg, D.H., West, A.A., White, S.D.M., Wilhite, B.C., Willman, B., Xu, Y., Yanny, B., Yarger, J., Yasuda, N., Yip, C.W., Yocum, D.R., York, D.G., Zakamska, N.L., Zehavi, I., Zheng, W., Zibetti, S. & Zucker, D.B. (2003). The First Data Release of the Sloan Digital Sky Survey. *The Astrophysical Journal*, **126**, 2081–2086. (Cited on pages 6, 45 and 49.)

Abazajian, K.N., Adelman-McCarthy, J.K., Agüeros, M.A., Allam, S.S., Allende Prieto, C., An, D., Anderson, K.S.J., Anderson, S.F., Annis, J., Bahcall, N.A., Bailer-Jones, C.A.L., Barentine, J.C., Bassett, B.A., Becker, A.C., Beers, T.C., Bell, E.F., Belokurov, V., Berlind, A.A., Berman, E.F., Bernardi, M., Bickerton, S.J., Bizyaev, D., Blakeslee, J.P., Blanton, M.R., Bochanski, J.J., Boroski, W.N., Brewington, H.J., Brinchmann, J., Brinkmann, J., Brunner, R.J., Budavári, T., Carey, L.N., Carliles, S., Carr, M.A., Castander, F.J., Cinabro, D., Connolly, A.J., Csabai, I., Cunha, C.E., Czarapata, P.C., Davenport, J.R.A., de Haas, E., Dilday, B., Doi, M., Eisenstein, D.J., Evans, M.L., Evans, N.W., Fan, X., Friedman, S.D., Frieman, J.A., Fukugita, M., Gänsicke, B.T., Gates, E., Gillespie, B., Gilmore, G., Gonzalez, B., Gonzalez, C.F., Grebel, E.K., Gunn, J.E., Györy, Z., Hall, P.B., Harding, P., Harris, F.H., Harvanek, M., Hawley, S.L., Hayes, J.J.E., Heckman, T.M., Hendry, J.S., Hennessy, G.S., Hindsley, R.B., Hoblitt, J., Hogan, C.J., Hogg, D.W., Holtzman, J.A., Hyde, J.B., Ichikawa, S.i., Ichikawa, T., Im, M., Ivezić, Ž., Jester, S., Jiang, L., Johnson, J.A., Jorgensen, A.M., Jurić, M., Kent, S.M., Kessler, R., Kleinman, S.J., Knapp, G.R., Konishi, K., Kron, R.G., Krzesinski, J., Kuropatkin, N., Lampeitl, H., Lebedeva, S., Lee, M.G., Lee, Y.S., French Leger, R., Lépine, S., Li, N., Lima, M., Lin, H., Long, D.C., Loomis, C.P., Loveday, J., Lupton, R.H., Magnier, E., Malanushenko, O., Malanushenko, V., Mandelbaum, R., Margon, B., Marriner, J.P., Martínez-Delgado, D., Matsubara, T., McGehee, P.M., McKay, T.A., Meiksin, A., Morrison, H.L., Mullally, F., Munn, J.A., Murphy, T., Nash, T., Nebot, A., Neilsen, J., E. H., Newberg, H.J., Newman, P.R., Nichol, R.C., Nicinski, T., Nieto-Santisteban, M., Nitta, A., Okamura, S., Oravetz, D.J., Ostriker, J.P., Owen, R., Padmanabhan, N., Pan, K., Park, C., Pauls, G., Peoples, J., J., Percival, W.J., Pier, J.R., Pope, A.C., Pourbaix, D., Price, P.A., Purger, N., Quinn, T., Raddick, M.J., Re Fiorentin, P., Richards, G.T., Richmond, M.W., Riess, A.G., Rix, H.W., Rockosi, C.M., Sako, M., Schlegel, D.J., Schneider, D.P., Scholz, R.D., Schreiber, M.R., Schwope, A.D., Seljak, U., Sesar, B., Sheldon, E., Shimasaku, K., Sibley, V.C., Simmons, A.E., Sivarani, T., Allyn Smith, J., Smith, M.C., Smolčić, V., Snedden, S.A., Stebbins, A., Steinmetz, M., Stoughton, C., Strauss, M.A., SubbaRao, M., Suto, Y., Szalay, A.S., Szapudi, I., Szkody, P., Tanaka, M., Tegmark, M., Teodoro, L.F.A., Thakar, A.R., Tremonti, C.A., Tucker, D.L., Uomoto, A., Vanden Berk, D.E., Vandenberg, J., Vidrih, S., Vogeley, M.S., Voges, W., Vogt, N.P., Wadadekar, Y., Watters, S., Weinberg, D.H., West, A.A., White, S.D.M., Wilhite, B.C., Wonders, A.C., Yanny, B., Yocum, D.R., York, D.G., Zehavi, I., Zibetti, S. & Zucker, D.B. (2009). The Seventh Data Release of the Sloan Digital Sky Survey. *The Astrophysical Journal Supplement*, **182**, 543–558. (Cited on pages 45 and 46.)

Adelman-McCarthy, J.K., Agüeros, M.A., Allam, S.S., Anderson, K.S.J., Anderson, S.F., Annis, J., Bahcall, N.A., Baldry, I.K., Barentine, J.C., Berlind, A., Bernardi, M., Blanton, M.R., Boroski, W.N., Brewington, H.J., Brinchmann, J., Brinkmann, J., Brunner, R.J., Budavári, T., Carey, L.N., Carr, M.A., Castander, F.J., Connolly, A.J., Csabai, I., Czarapata, P.C., Dalcanton, J.J., Doi, M., Dong, F., Eisenstein, D.J., Evans, M.L.,

Fan, X., Finkbeiner, D.P., Friedman, S.D., Frieman, J.A., Fukugita, M., Gillespie, B., Glazebrook, K., Gray, J., Grebel, E.K., Gunn, J.E., Gurbani, V.K., de Haas, E., Hall, P.B., Harris, F.H., Harvanek, M., Hawley, S.L., Hayes, J., Hendry, J.S., Hennessy, G.S., Hindsley, R.B., Hirata, C.M., Hogan, C.J., Hogg, D.W., Holmgren, D.J., Holtzman, J.A., Ichikawa, S.i., Ivezić, Ž., Jester, S., Johnston, D.E., Jorgensen, A.M., Jurić, M., Kent, S.M., Kleinman, S.J., Knapp, G.R., Kniazev, A.Y., Kron, R.G., Krzesinski, J., Kuropatkin, N., Lamb, D.Q., Lampeitl, H., Lee, B.C., Leger, R.F., Lin, H., Long, D.C., Loveday, J., Lupton, R.H., Margon, B., Martínez-Delgado, D., Mandelbaum, R., Matsubara, T., McGehee, P.M., McKay, T.A., Meiksin, A., Munn, J.A., Nakajima, R., Nash, T., Neilsen, E.H., Jr., Newberg, H.J., Newman, P.R., Nichol, R.C., Nicinski, T., Nieto-Santisteban, M., Nitta, A., O'Mullane, W., Okamura, S., Owen, R., Padmanabhan, N., Pauls, G., Peoples, J., Jr., Pier, J.R., Pope, A.C., Pourbaix, D., Quinn, T.R., Richards, G.T., Richmond, M.W., Rockosi, C.M., Schlegel, D.J., Schneider, D.P., Schroeder, J., Scranton, R., Seljak, U., Sheldon, E., Shimasaku, K., Smith, J.A., Smolčić, V., Snedden, S.A., Stoughton, C., Strauss, M.A., SubbaRao, M., Szalay, A.S., Szapudi, I., Szkody, P., Tegmark, M., Thakar, A.R., Tucker, D.L., Uomoto, A., Vanden Berk, D.E., Vandenberg, J., Vogeley, M.S., Voges, W., Vogt, N.P., Walkowicz, L.M., Weinberg, D.H., West, A.A., White, S.D.M., Xu, Y., Yanny, B., Yocum, D.R., York, D.G., Zehavi, I., Zibetti, S. & Zucker, D.B. (2006). The Fourth Data Release of the Sloan Digital Sky Survey. *The Astrophysical Journal Supplement Series*, **162**, 38–48. (Cited on page 46.)

Allard, F. & Hauschildt, P.H. (1995). Model atmospheres for M (sub)dwarf stars. 1: The base model grid. *The Astrophysical Journal*, **445**, 433–450. (Cited on page 5.)

Alongi, M., Bertelli, G., Bressan, A., Chiosi, C., Fagotto, F., Greggio, L. & Nasi, E. (1993). Evolutionary sequences of stellar models with semiconvection and convective overshoot. I - Z = 0.008. *Astronomy and Astrophysics Supplement Series*, **97**, 851–871. (Cited on pages 5, 13, 14, 16 and 59.)

Alonso-Herrero, A., Pérez-González, P.G., Alexander, D.M., Rieke, G.H., Rigopoulou, D., Le Floc'h, E., Barmby, P., Papovich, C., Rigby, J.R., Bauer, F.E., Brandt, W.N., Egami, E., Willner, S.P., Dole, H. & Huang, J.S. (2006). Infrared Power-Law Galaxies in the Chandra Deep Field-South: Active Galactic Nuclei and Ultraluminous Infrared Galaxies. *The Astrophysical Journal*, **640**, 167–184. (Cited on page 48.)

Anders, P. & Fritze-v. Alvensleben, U. (2003). Spectral and photometric evolution of young stellar populations: The impact of gaseous emission at various metallicities. *Astronomy and Astrophysics*, **401**, 1063–1070. (Cited on pages 3, 9, 12 and 47.)

Anders, P., Bissantz, N., Fritze-v. Alvensleben, U. & de Grijs, R. (2004). Analysing observed star cluster SEDs with evolutionary synthesis models: systematic uncertainties. *Monthly Notices of the Royal Astronomical Society*, **347**, 196–212. (Cited on page 5.)

Antonucci, R. (1993). Unified models for active galactic nuclei and quasars. *Annual Review of Astronomy and Astrophysics*, **31**, 473–521. (Cited on page 7.)

Arimoto, N. & Yoshii, Y. (1986). Photometric and chemical evolution of galaxies based on an evolutionary method of population synthesis. *Astronomy and Astrophysics*, **164**, 260–273. (Cited on page 3.)

Arimoto, N. & Yoshii, Y. (1987). Chemical and photometric properties of a galactic wind model for elliptical galaxies. *Astronomy and Astrophysics*, **173**, 23–38. (Cited on page 3.)

Asari, N.V., Cid Fernandes, R., Stasińska, G., Torres-Papaqui, J.P., Mateus, A., Sodré, L., Schoenell, W. & Gomes, J.M. (2007). The history of star-forming galaxies in the Sloan Digital Sky Survey. *Monthly Notices of the Royal Astronomical Society*, **381**, 263–279. (Cited on pages 16, 47 and 49.)

Baade, W.. (1944a). The Resolution of Messier 32, NGC 205, and the Central Region of the Andromeda Nebula. *The Astrophysical Journal*, **100**, 137. (Cited on page 2.)

Baade, W.. (1944b). NGC 147 and NGC 185, Two New Members of the Local Group of Galaxies. *The Astrophysical Journal*, **100**, 147. (Cited on page 2.)

Bacon, R., Copin, Y., Monnet, G., Miller, B.W., Allington-Smith, J.R., Bureau, M., Carollo, C.M., Davies, R.L., Emsellem, E., Kuntschner, H., Peletier, R.F., Verolme, E.K. & de Zeeuw, P.T. (2001). The SAURON project - I. The panoramic integral-field spectrograph. *Monthly Notices of the Royal Astronomical Society*, **326**, 23–35. (Cited on page 3.)

Baldwin, J.A., Phillips, M.M. & Terlevich, R. (1981). Classification parameters for the emission-line spectra of extragalactic objects. *The Publications of the Astronomical Society of the Pacific*, **93**, 5–19. (Cited on pages 8, 45, 46, 48 and 49.)

Balogh, M.L., Morris, S.L., Yee, H.K.C., Carlberg, R.G. & Ellingson, E. (1999). Differential Galaxy Evolution in Cluster and Field Galaxies at $z \sim 0.3$. *The Astrophysical Journal*, **527**, 54–79. (Cited on pages 13 and 15.)

Belfiore, F., Maiolino, R., Maraston, C., Emsellem, E., Bershady, M.A., Masters, K.L., Yan, R., Bizyaev, D., Boquien, M., Brownstein, J.R., Bundy, K., Drory, N., Heckman, T.M., Law, D.R., Roman-Lopes, A., Pan, K., Stanghellini, L., Thomas, D., Weijmans, A.M. & Westfall, K.B. (2016). SDSS IV MaNGA - spatially resolved diagnostic diagrams: a proof that many galaxies are LIERs. *Monthly Notices of the Royal Astronomical Society*, **461**, 3111–3134. (Cited on page 3.)

Benítez, E., Méndez-Abreu, J., Fuentes-Carrera, I., Cruz-González, I., Martínez, B., López-Martin, L., Jiménez-Bailón, E., Chavushyan, V. & León-Tavares, J. (2013). Characterization of a Sample of Intermediate-type Active Galactic Nuclei. II. Host Bulge Properties and Black Hole Mass Estimates. *The Astrophysical Journal*, **763**, 136. (Cited on pages 16 and 27.)

Bennert, N., Jungwiert, B., Komossa, S., Haas, M. & Chini, R. (2006). Size and properties of the NLR in the Seyfert-2 galaxy NGC 1386. *Astronomy and Astrophysics*, **446**, 919–932. (Cited on page 48.)

Bergvall, N., Johansson, L. & Olofsson, K. (1986). ESO 428-G 14 - A new Seyfert 2 galaxy. *Astronomy and Astrophysics*, **166**, 92–96. (Cited on pages 27 and 44.)

Bessell, M.S., Brett, J.M., Wood, P.R. & Scholz, M. (1989). Colors of extended static model photospheres of M giants. *Astronomy and Astrophysics Supplement Series*, **77**, 1–30. (Cited on page 5.)

Bessell, M.S., Brett, J.M., Scholz, M. & Wood, P.R. (1991). Colors and stratifications of extended static model photospheres of M stars located on the FGB, AGB and supergiant branch. *Astronomy and Astrophysics Supplement Series*, **89**, 335–366. (Cited on page 5.)

Bica, E. (1988). Population synthesis in galactic nuclei using a library of star clusters. *Astronomy and Astrophysics*, **195**, 76–92. (Cited on pages 3, 5 and 6.)

Bohlin, R.C. & Gilliland, R.L. (2004). Hubble Space Telescope Absolute Spectrophotometry of Vega from the Far-Ultraviolet to the Infrared. *The Astrophysical Journal*, **127**, 3508–3515. (Cited on page 13.)

Bon, N., Popović, L.Č. & Bon, E. (2014). Efficiency tests for estimating the gas and stellar population parameters in Type 2 objects. *Advances in Space Research*, **54**, 1389–1400. (Cited on page 7.)

Boquien, M., Buat, V. & Perret, V. (2014). Impact of star formation history on the measurement of star formation rates. *Astronomy and Astrophysics*, **571**, A72. (Cited on page 12.)

Bregman, J.N. (1990). Continuum radiation from active galactic nuclei. *Astronomy and Astrophysics Review*, **2**, 125–166. (Cited on page 44.)

Bressan, A., Fagotto, F., Bertelli, G. & Chiosi, C. (1993). Evolutionary sequences of stellar models with new radiative opacities. II - Z = 0.02. *Astronomy and Astrophysics Supplement Series*, **100**, 647–664. (Cited on pages 5, 13, 14, 16 and 59.)

Brinchmann, J., Charlot, S., White, S.D.M., Tremonti, C., Kauffmann, G., Heckman, T. & Brinkmann, J. (2004). The physical properties of star-forming galaxies in the low-redshift Universe. *Monthly Notices of the Royal Astronomical Society*, **351**, 1151–1179. (Cited on page 5.)

Brown, R.L. & Mathews, W.G. (1970). Theoretical Continuous Spectra of Gaseous Nebulae. *The Astrophysical Journal*, **160**, 939. (Cited on page 11.)

Bruzual, A.G. (1983). Spectral evolution of galaxies. I - Early-type systems. *The Astrophysical Journal*, **273**, 105–127. (Cited on pages 3 and 4.)

Bruzual, G. & Charlot, S. (2003). Stellar population synthesis at the resolution of 2003. *Monthly Notices of the Royal Astronomical Society*, **344**, 1000–1028. (Cited on pages 1, 3, 4, 5, 6, 12, 13, 14, 16, 19, 47, 48 and 59.)

Bundy, K., Bershady, M.A., Law, D.R., Yan, R., Drory, N., MacDonald, N., Wake, D.A., Cherinka, B., Sánchez-Gallego, J.R., Weijmans, A.M., Thomas, D., Tremonti, C., Masters, K., Coccato, L., Diamond-Stanic, A.M., Aragón-Salamanca, A., Avila-Reese, V., Badenes, C., Falcón-Barroso, J., Belfiore, F., Bizyaev, D., Blanc, G.A., Bland-Hawthorn, J., Blanton, M.R., Brownstein, J.R., Byler, N., Cappellari, M., Conroy, C., Dutton, A.A., Emsellem, E., Etherington, J., Frinchaboy, P.M., Fu, H., Gunn, J.E., Harding, P., Johnston, E.J., Kauffmann, G., Kinemuchi, K., Klaene, M.A., Knapen, J.H., Leauthaud, A., Li, C., Lin, L., Maiolino, R., Malanushenko, V., Malanushenko, E., Mao, S., Maraston, C., McDermid, R.M., Merrifield, M.R., Nichol, R.C., Oravetz, D., Pan, K., Parejko, J.K., Sanchez, S.F., Schlegel, D., Simmons, A., Steele, O., Steinmetz, M., Thanjavur, K., Thompson, B.A., Tinker, J.L., van den Bosch, R.C.E., Westfall, K.B., Wilkinson, D., Wright, S., Xiao, T. & Zhang, K. (2015). Overview of the SDSS-IV MaNGA Survey: Mapping nearby Galaxies at Apache Point Observatory. *The Astrophysical Journal*, **798**, 7. (Cited on page 3.)

Buzzoni, A. (1989). Evolutionary population synthesis in stellar systems. I - A global approach. *The Astrophysical Journal Supplement Series*, **71**, 817–869. (Cited on page 4.)

Cardoso, L.S.M., Gomes, J.M. & Papaderos, P. (2016). Semi-empirical AGN detection threshold in spectral synthesis studies of Lyman-continuum-leaking early-type galaxies. *Astronomy and Astrophysics*, **594**, L2. (Cited on pages 27, 32 and 63.)

Cardoso, L.S.M., Gomes, J.M. & Papaderos, P. (2017). Impact of an AGN featureless continuum on the estimation of stellar population properties. *Astronomy and Astrophysics, arXiv:1705.04224*. (Cited on pages 27, 32 and 64.)

Castellanos, M., Díaz, A.I. & Terlevich, E. (2002). A comprehensive study of reported high-metallicity giant H II regions - I. Detailed abundance analysis. *Monthly Notices of the Royal Astronomical Society*, **329**, 315–335. (Cited on page 48.)

Cerviño, M. (2013). The stochastic nature of stellar population modelling. *New Astronomy Reviews*, **57**, 123–139. (Cited on page 3.)

Chabrier, G. (2003). Galactic Stellar and Substellar Initial Mass Function. *The Publications of the Astronomical Society of the Pacific*, **115**, 763–795. (Cited on pages 4, 5, 13, 14, 16, 19 and 59.)

Charbonnel, C., Meynet, G., Maeder, A. & Schaerer, D. (1996). Grids of stellar models. VI. Horizontal branch and early asymptotic giant branch for low mass stars (Z=0.020, 0.001). *Astronomy and Astrophysics Supplement*, **115**, 339. (Cited on pages 5 and 13.)

Charbonnel, C., Däppen, W., Schaerer, D., Bernasconi, P.A., Maeder, A., Meynet, G. & Mowlavi, N. (1999). Grids of stellar models. VIII. From 0.4 to 1.0 $M_{\odot}$ at Z=0.020 and Z=0.001, with the MHD equation of state. *Astronomy and Astrophysics Supplement*, **135**, 405–413. (Cited on pages 5 and 13.)

Charlot, S. & Bruzual, A.G. (1991). Stellar population synthesis revisited. *The Astrophysical Journal*, **367**, 126–140. (Cited on pages 3 and 4.)

Charlot, S. & Fall, S.M. (2000). A Simple Model for the Absorption of Starlight by Dust in Galaxies. *The Astrophysical Journal*, **539**, 718–731. (Cited on page 3.)

Chiosi, C., Bertelli, G. & Bressan, A. (1988). Integrated colours and ages of LMC clusters - The nature of the bimodal distribution of the (B-V) colours. *Astronomy and Astrophysics*, **196**, 84–108. (Cited on page 3.)

Cid Fernandes, R., Gu, Q., Melnick, J., Terlevich, E., Terlevich, R., Kunth, D., Rodrigues Lacerda, R. & Joguet, B. (2004). The star formation history of Seyfert 2 nuclei. *Monthly Notices of the Royal Astronomical*, **355**, 273–296. (Cited on pages 3, 7, 27 and 28.)

Cid Fernandes, R., Mateus, A., Sodré, L., Stasińska, G. & Gomes, J.M. (2005). Semi-empirical analysis of Sloan Digital Sky Survey galaxies - I. Spectral synthesis method. *Monthly Notices of the Royal Astronomical Society*, **358**, 363–378. (Cited on pages 3, 5, 6, 7, 9, 15, 16, 21, 25 and 31.)

Cid Fernandes, R., Stasińska, G., Mateus, A. & Vale Asari, N. (2011). A comprehensive classification of galaxies in the Sloan Digital Sky Survey: how to tell true from fake AGN? *Monthly Notices of the Royal Astronomical Society*, **413**, 1687–1699. (Cited on page 31.)

Cid Fernandes, R., González Delgado, R.M., García Benito, R., Pérez, E., de Amorim, A.L., Sánchez, S.F., Husemann, B., Falcón Barroso, J., López-Fernández, R., Sánchez-Blázquez, P., Vale Asari, N., Vazdekis, A., Walcher, C.J. & Mast, D. (2014). Resolving galaxies in time and space. II. Uncertainties in the spectral synthesis of datacubes. *Astronomy and Astrophysics*, **561**, A130. (Cited on page 16.)

Cid Fernandes, R., Jr., Storchi-Bergmann, T. & Schmitt, H.R. (1998). The Stellar Content of Active Galaxies. *Monthly Notices of the Royal Astronomical Society*, **297**, 579–616. (Cited on pages 7 and 27.)

Ciesla, L., Charmandaris, V., Georgakakis, A., Bernhard, E., Mitchell, P.D., Buat, V., Elbaz, D., LeFloc'h, E., Lacey, C.G., Magdis, G.E. & Xilouris, M. (2015). Constraining the properties of AGN host galaxies with spectral energy distribution modelling. *Astronomy and Astrophysics*, **576**, A10. (Cited on pages 7 and 8.)

Cimatti, A., Daddi, E. & Renzini, A. (2006). Mass downsizing and "top-down" assembly of early-type galaxies. *Astronomy and Astrophysics*, **453**, L29–L33. (Cited on pages 1 and 6.)

Coelho, P., Bruzual, G., Charlot, S., Weiss, A., Barbuy, B. & Ferguson, J.W. (2007). Spectral models for solar-scaled and α-enhanced stellar populations. *Monthly Notices of the Royal Astronomical Society*, **382**, 498–514. (Cited on pages 3 and 5.)

Coelho, P.R.T. (2014). A new library of theoretical stellar spectra with scaled-solar and α-enhanced mixtures. *Monthly Notices of the Royal Astronomical Society*, **440**, 1027–1043. (Cited on pages 3 and 5.)

Cole, S., Lacey, C.G., Baugh, C.M. & Frenk, C.S. (2000). Hierarchical galaxy formation. *Monthly Notices of the Royal Astronomical Society*, **319**, 168–204. (Cited on page 8.)

Colless, M., Dalton, G., Maddox, S., Sutherland, W., Norberg, P., Cole, S., Bland-Hawthorn, J., Bridges, T., Cannon, R., Collins, C., Couch, W., Cross, N., Deeley, K., De Propris, R., Driver, S.P., Efstathiou, G., Ellis, R.S., Frenk, C.S., Glazebrook, K., Jackson, C., Lahav, O., Lewis, I., Lumsden, S., Madgwick, D., Peacock, J.A., Peterson, B.A., Price, I., Seaborne, M. & Taylor, K. (2001). The 2dF Galaxy Redshift Survey: spectra and redshifts. *Monthly Notices of the Royal Astronomical Society*, **328**, 1039–1063. (Cited on pages 1 and 3.)

Conroy, C. (2013). Modeling the Panchromatic Spectral Energy Distributions of Galaxies. *Annual Review of Astronomy and Astrophysics*, **51**, 393–455. (Cited on page 3.)

Conroy, C., Gunn, J.E. & White, M. (2009). The Propagation of Uncertainties in Stellar Population Synthesis Modeling. I. The Relevance of Uncertain Aspects of Stellar Evolution and the Initial Mass Function to the Derived Physical Properties of Galaxies. *The Astrophysical Journal*, **699**, 486–506. (Cited on page 3.)

Corral, A., Della Ceca, R., Caccianiga, A., Severgnini, P., Brunner, H., Carrera, F.J., Page, M.J. & Schwope, A.D. (2011). The X-ray spectral properties of the AGN population in the XMM-Newton bright serendipitous survey. *Astronomy and Astrophysics*, **530**, A42. (Cited on page 48.)

Cousins, A.W.J. & Jones, D.H.P. (1976). Numerical simulation of natural photometric systems. *Memoirs of the Royal Astronomical Society*, **81**, 1–23. (Cited on page 13.)

Cowie, L.L., Songaila, A., Hu, E.M. & Cohen, J.G. (1996). New Insight on Galaxy Formation and Evolution From Keck Spectroscopy of the Hawaii Deep Fields. *The Astrophysical Journal*, **112**, 839. (Cited on pages 1 and 6.)

Coziol, R., Torres-Papaqui, J.P., Plauchu-Frayn, I., Islas-Islas, J.M., Ortega-Minakata, R.A., Neri-Larios, D.M. & Andernach, H. (2011). The nature and origin of Narrow Line AGN activity in a sample of isolated SDSS galaxies. *Revista Mexicana de Astronomía y Astrofísica*, **47**, 361–383. (Cited on pages 16 and 31.)

Croom, S.M., Lawrence, J.S., Bland-Hawthorn, J., Bryant, J.J., Fogarty, L., Richards, S., Goodwin, M., Farrell, T., Miziarski, S., Heald, R., Jones, D.H., Lee, S., Colless, M., Brough, S., Hopkins, A.M., Bauer, A.E., Birchall, M.N., Ellis, S., Horton, A., Leon-Saval, S., Lewis, G., López-Sánchez, Á.R., Min, S.S., Trinh, C. & Trowland, H. (2012). The Sydney-AAO Multi-object Integral field spectrograph. *Monthly Notices of the Royal Astronomical Society*, **421**, 872–893. (Cited on page 3.)

da Cunha, E., Charlot, S. & Elbaz, D. (2008). A simple model to interpret the ultraviolet, optical and infrared emission from galaxies. *Monthly Notices of the Royal Astronomical Society*, **388**, 1595–1617. (Cited on page 8.)

de Vaucouleurs, G. (1959). Classification and Morphology of External Galaxies. *Handbuch der Physik*, **53**, 275. (Cited on pages 4 and 12.)

Doi, M., Tanaka, M., Fukugita, M., Gunn, J.E., Yasuda, N., Ivezić, Ž., Brinkmann, J., de Haars, E., Kleinman, S.J., Krzesinski, J. & French Leger, R. (2010). Photometric Response Functions of the Sloan Digital Sky Survey Imager. *The Astrophysical Journal*, **139**, 1628–1648. (Cited on page 13.)

Dopita, M.A. & Sutherland, R.S. (1995). Spectral Signatures of Fast Shocks. II. Optical Diagnostic Diagrams. *The Astrophysical Journal*, **455**, 468. (Cited on page 8.)

Dopita, M.A. & Sutherland, R.S. (1996). Spectral Signatures of Fast Shocks. I. Low-Density Model Grid. *The Astrophysical Journal Supplement*, **102**, 161. (Cited on page 8.)

Draine, B.T. (2003). Interstellar Dust Grains. *Annual Review of Astronomy and Astrophysics*, **41**, 241–289. (Cited on page 7.)

Eracleous, M. & Halpern, J.P. (2001). NGC 3065: A Certified LINER with Broad, Variable Balmer Lines. *The Astrophysical Journal*, **554**, 240–244. (Cited on pages 7, 27 and 28.)

Faber, S.M. (1972). Quadratic programming applied to the problem of galaxy population synthesis. *Astronomy and Astrophysics*, **20**, 361–374. (Cited on pages 3, 5, 6, 7 and 21.)

Faber, S.M. & Jackson, R.E. (1976). Velocity dispersions and mass-to-light ratios for elliptical galaxies. *The Astrophysical Journal*, **204**, 668–683. (Cited on page 1.)

Fagotto, F., Bressan, A., Bertelli, G. & Chiosi, C. (1994a). Evolutionary sequences of stellar models with new radiative opacities. III. Z=0.0004 and Z=0.05. *Astronomy and Astrophysics Supplement*, **104**, 365–376. (Cited on pages 5, 13, 14, 16 and 59.)

Fagotto, F., Bressan, A., Bertelli, G. & Chiosi, C. (1994b). Evolutionary sequences of stellar models with new radiative opacities. IV. Z=0.004 and Z=0.008. *Astronomy and Astrophysics Supplement*, **105**, 29–38. (Cited on pages 5, 13, 14, 16 and 59.)

Fanelli, M.N., O'Connell, R.W., Burstein, D. & Wu, C.C. (1992). Spectral synthesis in the ultraviolet. IV - A library of mean stellar groups. *Astrophysical Journal Supplement Series*, **82**, 197–245. (Cited on page 5.)

Ferland, G.J. & Netzer, H. (1983). Are there any shock-heated galaxies. *The Astrophysical Journal*, **264**, 105–113. (Cited on pages 27, 44, 46 and 48.)

Ferland, G.J., Korista, K.T., Verner, D.A., Ferguson, J.W., Kingdon, J.B. & Verner, E.M. (1998). CLOUDY 90: Numerical Simulation of Plasmas and Their Spectra. *The Publications of the Astronomical Society of the Pacific*, **110**, 761–778. (Cited on pages 8, 15 and 43.)

Ferland, G.J., Porter, R.L., van Hoof, P.A.M., Williams, R.J.R., Abel, N.P., Lykins, M.L., Shaw, G., Henney, W.J. & Stancil, P.C. (2013). The 2013 Release of Cloudy. *Revista Mexicana de Astronomía y Astrofísica*, **49**, 137–163. (Cited on page 44.)

Fioc, M. & Rocca-Volmerange, B. (1997). PEGASE: a UV to NIR spectral evolution model of galaxies. Application to the calibration of bright galaxy counts. *Astronomy and Astrophysics*, **326**, 950–962. (Cited on pages 1, 3, 4, 5, 8 and 12.)

Fioc, M. & Rocca-Volmerange, B. (1999). PEGASE.2, a metallicity-consistent spectral evolution model of galaxies: the documentation and the code. *arXiv:astro-ph/9912179*. (Cited on page 8.)

Fluks, M.A., Plez, B., The, P.S., de Winter, D., Westerlund, B.E. & Steenman, H.C. (1994). On the spectra and photometry of M-giant stars. *Astronomy and Astrophysics Supplement*, **105**. (Cited on page 5.)

Garcia-Rissmann, A., Vega, L.R., Asari, N.V., Cid Fernandes, R., Schmitt, H., González Delgado, R.M. & Storchi-Bergmann, T. (2005). An atlas of calcium triplet spectra of active galaxies. *Monthly Notices of the Royal Astronomical Society*, **359**, 765–780. (Cited on pages 7, 27 and 32.)

Garcia-Vargas, M.L., Bressan, A. & Diaz, A.I. (1995). Predicted emission lines from giant HII regions ionized by aging star clusters. *Astronomy and Astrophysics Supplement*, **112**, 35. (Cited on page 48.)

García-Vargas, M.L., González-Delgado, R.M., Pérez, E., Alloin, D., Díaz, A. & Terlevich, E. (1997). The Stellar Content of Giant H II Regions in NGC 7714. *The Astrophysical Journal*, **478**, 112–123. (Cited on page 48.)

García-Vargas, M.L., Mollá, M. & Martín-Manjón, M.L. (2013). PopStar evolutionary synthesis models - III. Photometric properties of young star clusters and mixed populations. *Monthly Notices of the Royal Astronomical Society*, **432**, 2746–2772. (Cited on pages 3 and 7.)

Gavazzi, G., Bonfanti, C., Sanvito, G., Boselli, A. & Scodeggio, M. (2002). Spectrophotometry of Galaxies in the Virgo Cluster. I. The Star Formation History. *The Astrophysical Journal*, **576**, 135–151. (Cited on page 12.)

Gelman, A. & Rubin, D.B. (1992). Inference from iterative simulation using multiple sequences. *Statistical Science*, **7**, 457–472. (Cited on pages 33 and 34.)

Girardi, L., Bressan, A., Chiosi, C., Bertelli, G. & Nasi, E. (1996). Evolutionary sequences of stellar models with new radiative opacities. VI. Z=0.0001. *Astronomy and Astrophysics Supplement*, **117**, 113–125. (Cited on pages 5, 13, 14, 16 and 59.)

Girardi, L., Bressan, A., Bertelli, G. & Chiosi, C. (2000). Evolutionary tracks and isochrones for low- and intermediate-mass stars: From 0.15 to 7 $M_{\odot}$, and from Z=0.0004 to 0.03. *Astronomy and Astrophysics Supplement*, **141**, 371–383. (Cited on pages 5 and 13.)

Gladders, M.D. & Yee, H.K.C. (2000). A New Method For Galaxy Cluster Detection. I. The Algorithm. *The Astrophysical Journal*, **120**, 2148–2162. (Cited on page 1.)

Goerdt, A. & Kollatschny, W. (1998). Combined population and evolutionary synthesis of galaxy spectra. *Astronomy and Astrophysics*, **337**, 699–710. (Cited on pages 6 and 27.)

Gomes, J.M. & Papaderos, P. (2017). Fitting Analysis using Differential Evolution Optimization (FADO): Spectral population synthesis through genetic optimization under self-consistency boundary conditions. *ArXiv e-prints*. (Cited on pages 59 and 64.)

Gomes, J.M., Papaderos, P., Vílchez, J.M., Kehrig, C., Iglesias-Páramo, J., Breda, I., Lehnert, M.D., Sánchez, S.F., Ziegler, B., Dos Reis, S.N., Bland-Hawthorn, J., Galbany, L., Bomans, D.J., Rosales-Ortega, F.F., Walcher, C.J., García-Benito, R., Márquez, I., Del Olmo, A., Mollá, M., Marino, R.A., Catalán-Torrecilla, C., González Delgado, R.M., López-Sánchez, Á.R. & Califa Collaboration (2016a). Spiral-like star-forming patterns in CALIFA early-type galaxies. *Astronomy and Astrophysics*, **585**, A92. (Cited on page 3.)

Gomes, J.M., Papaderos, P., Vílchez, J.M., Kehrig, C., Iglesias-Páramo, J., Breda, I., Lehnert, M.D., Sánchez, S.F., Ziegler, B., Dos Reis, S.N., Bland-Hawthorn, J., Galbany, L., Bomans, D.J., Rosales-Ortega, F.F., Walcher, C.J., García-Benito, R., Márquez, I., Del Olmo, A., Mollá, M., Marino, R.A., Catalán-Torrecilla, C., González Delgado, R.M., López-Sánchez, Á.R. & Califa Collaboration (2016b). Spectroscopic aperture biases in inside-out evolving early-type galaxies from CALIFA. *Astronomy and Astrophysics*, **586**, A22. (Cited on page 3.)

Gomes, J.M., Papaderos, P., Kehrig, C., Vílchez, J.M., Lehnert, M.D., Sánchez, S.F., Ziegler, B., Breda, I., Dos Reis, S.N., Iglesias-Páramo, J., Bland-Hawthorn, J., Galbany, L., Bomans, D.J., Rosales-Ortega, F.F., Cid Fernandes, R., Walcher, C.J., Falcón-Barroso, J., García-Benito, R., Márquez, I., Del Olmo, A., Masegosa, J., Mollá, M., Marino, R.A., González Delgado, R.M., López-Sánchez, Á.R. & Califa Collaboration (2016c). Warm ionized gas in CALIFA early-type galaxies. 2D emission-line patterns and kinematics for 32 galaxies. *Astronomy and Astrophysics*, **588**, A68. (Cited on pages 3 and 29.)

Grevesse, N. & Sauval, A.J. (1998). Standard Solar Composition. *Space Science Reviews*, **85**, 161–174. (Cited on pages 45 and 48.)

Groves, B.A., Dopita, M.A. & Sutherland, R.S. (2004). Dusty, Radiation Pressure-Dominated Photoionization. I. Model Description, Structure, and Grids. *The Astrophysical Journal Supplement Series*, **153**, 9–73. (Cited on pages 44, 46 and 48.)

Gruenwald, R., Viegas, S.M. & Broguière, D. (1997). A New Generation of Photoionization Codes: Three-dimensional Models. The Bipolar Planetary Nebula IC 4406. *The Astrophysical Journal*, **480**, 283–289. (Cited on page 43.)

Hägele, G.F., Díaz, Á.I., Terlevich, E., Terlevich, R., Pérez-Montero, E. & Cardaci, M.V. (2008). Precision abundance analysis of bright HII galaxies. *Monthly Notices of the Royal Astronomical Society*, **383**, 209–229. (Cited on page 48.)

Hao, H., Elvis, M., Bongiorno, A., Zamorani, G., Merloni, A., Kelly, B.C., Civano, F., Celotti, A., Ho, L.C., Jahnke, K., Comastri, A., Trump, J.R., Mainieri, V., Salvato, M., Brusa, M., Impey, C.D., Koekemoer, A.M., Lanzuisi, G., Vignali, C., Silverman, J.D., Urry, C.M. & Schawinski, K. (2013). A quasar-galaxy mixing diagram: quasar spectral energy distribution shapes in the optical to near-infrared. *Monthly Notices of the Royal Astronomical Society*, **434**, 3104–3121. (Cited on pages 7 and 27.)

Hayward, C.C. & Smith, D.J.B. (2015). Should we believe the results of ultraviolet-millimetre galaxy spectral energy distribution modelling? *Monthly Notices of the Royal Astronomical Society*, **446**, 1512–1535. (Cited on pages 7 and 8.)

Heavens, A., Panter, B., Jimenez, R. & Dunlop, J. (2004). The star-formation history of the Universe from the stellar populations of nearby galaxies. *Nature*, **428**, 625–627. (Cited on pages 1, 5 and 6.)

Heavens, A.F., Jimenez, R. & Lahav, O. (2000). Massive lossless data compression and multiple parameter estimation from galaxy spectra. *Monthly Notices of the Royal Astronomical Society*, **317**, 965–972. (Cited on pages 5, 6, 9 and 15.)

Heckman, T.M. (1980). An optical and radio survey of the nuclei of bright galaxies - Activity in normal galactic nuclei. *Astronomy and Astrophysics*, **87**, 152–164. (Cited on pages 7, 27 and 28.)

Heckman, T.M. & Best, P.N. (2014). The Coevolution of Galaxies and Supermassive Black Holes: Insights from Surveys of the Contemporary Universe. *Annual Review of Astronomy and Astrophysics*, **52**, 589–660. (Cited on page 7.)

Ho, L.C. (2008). Nuclear Activity in Nearby Galaxies. *Annual Review of Astronomy and Astrophysics*, **46**, 475–539. (Cited on pages 7 and 27.)

Ho, L.C., Filippenko, A.V. & Sargent, W.L. (1995). A search for 'dwarf' Seyfert nuclei. 2: an optical spectral atlas of the nuclei of nearby galaxies. *The Astrophysical Journal Supplement Series*, **98**, 477–593. (Cited on pages 7 and 27.)

Ho, L.C., Filippenko, A.V. & Sargent, W.L.W. (1997). A Search for "Dwarf" Seyfert Nuclei. III. Spectroscopic Parameters and Properties of the Host Galaxies. *The Astrophysical Journal Supplement Series*, **112**, 315–390. (Cited on pages 7 and 27.)

Ho, L.C., Filippenko, A.V. & Sargent, W.L.W. (2003). A Search for "Dwarf" Seyfert Nuclei. VI. Properties of Emission-Line Nuclei in Nearby Galaxies. *The Astrophysical Journal*, **583**, 159–177. (Cited on pages 7 and 27.)

Hubble, E. (1929). A Relation between Distance and Radial Velocity among Extra-Galactic Nebulae. *Proceedings of the National Academy of Science*, **15**, 168–173. (Cited on page 1.)

Hubble, E.P. (1926). Extragalactic nebulae. *The Astrophysical Journal*, **64**. (Cited on pages 1, 4 and 12.)

Hummer, D.G. & Storey, P.J. (1987). Recombination-line intensities for hydrogenic ions. I - Case B calculations for H I and He II. *Monthly Notices of the Royal Astronomical Society*, **224**, 801–820. (Cited on page 12.)

Ibarra-Medel, H.J., Sánchez, S.F., Avila-Reese, V., Hernández-Toledo, H.M., González, J.J., Drory, N., Bundy, K., Bizyaev, D., Cano-Díaz, M., Malanushenko, E., Pan, K., Roman-Lopes, A. & Thomas, D. (2016). SDSS IV MaNGA: the global and local stellar mass assemby histories of galaxies. *Monthly Notices of the Royal Astronomical Society*, **463**, 2799–2818. (Cited on page 3.)

Johnson, H.L. & Morgan, W.W. (1953). Fundamental stellar photometry for standards of spectral type on the revised system of the Yerkes spectral atlas. *The Astrophysical Journal*, **117**, 313. (Cited on page 13.)

Joly, M. (1974). Study of the central region of M31. II. Synthetic models of stellar populations. *Astronomy and Astrophysics*, **33**, 177–186. (Cited on pages 3, 5 and 6.)

Jones, D.H., Saunders, W., Colless, M., Read, M.A., Parker, Q.A., Watson, F.G., Campbell, L.A., Burkey, D., Mauch, T., Moore, L., Hartley, M., Cass, P., James, D., Russell, K., Fiegert, K., Dawe, J., Huchra, J., Jarrett, T., Lahav, O., Lucey, J., Mamon, G.A., Proust, D., Sadler, E.M. & Wakamatsu, K.i. (2004). The 6dF Galaxy Survey: samples, observational techniques and the first data release. *Monthly Notices of the Royal Astronomical Society*, **355**, 747–763. (Cited on pages 1 and 3.)

Kauffmann, G., Heckman, T.M., White, S.D.M., Charlot, S., Tremonti, C., Brinchmann, J., Bruzual, G., Peng, E.W., Seibert, M., Bernardi, M., Blanton, M., Brinkmann, J., Castander, F., Csábai, I., Fukugita, M., Ivezic, Z., Munn, J.A., Nichol, R.C., Padmanabhan, N., Thakar, A.R., Weinberg, D.H. & York, D. (2003a). Stellar masses and star formation histories for 10^5 galaxies from the Sloan Digital Sky Survey. *Monthly Notices of the Royal Astronomical Society*, **341**, 33–53. (Cited on pages 5 and 6.)

Kauffmann, G., Heckman, T.M., White, S.D.M., Charlot, S., Tremonti, C., Peng, E.W., Seibert, M., Brinkmann, J., Nichol, R.C., SubbaRao, M. & York, D. (2003b). The dependence of star formation history and internal structure on stellar mass for 10^5 low-redshift galaxies. *Monthly Notices of the Royal Astronomical Society*, **341**, 54–69. (Cited on pages 5 and 6.)

Kauffmann, G., Heckman, T.M., Tremonti, C., Brinchmann, J., Charlot, S., White, S.D.M., Ridgway, S.E., Brinkmann, J., Fukugita, M., Hall, P.B., Ivezić, Ž., Richards, G.T. & Schneider, D.P. (2003c). The host galaxies of active galactic nuclei. *Monthly Notices of the Royal Astronomical Society*, **346**, 1055–1077. (Cited on pages 5, 6, 7, 8, 27, 31, 45, 46 and 49.)

Kehrig, C., Monreal-Ibero, A., Papaderos, P., Vílchez, J.M., Gomes, J.M., Masegosa, J., Sánchez, S.F., Lehnert, M.D., Cid Fernandes, R., Bland-Hawthorn, J., Bomans, D.J., Marquez, I., Mast, D., Aguerri, J.A.L., López-Sánchez, Á.R., Marino, R.A., Pasquali, A., Perez, I., Roth, M.M., Sánchez-Blázquez, P. & Ziegler, B. (2012). The ionized gas in the CALIFA early-type galaxies. I. Mapping two representative cases: NGC 6762 and NGC 5966. *Astronomy and Astrophysics*, **540**, A11. (Cited on pages 3 and 8.)

Kennicutt, R.C., Jr. (1989). The star formation law in galactic disks. *The Astrophysical Journal*, **344**, 685–703. (Cited on page 12.)

Kennicutt, R.C., Jr. (1998). The Global Schmidt Law in Star-forming Galaxies. *The Astrophysical Journal*, **498**, 541–552. (Cited on pages 1 and 13.)

Kewley, L.J., Dopita, M.A., Sutherland, R.S., Heisler, C.A. & Trevena, J. (2001). Theoretical Modeling of Starburst Galaxies. *The Astrophysical Journal*, **556**, 121–140. (Cited on pages 8, 45, 46 and 49.)

Kewley, L.J., Groves, B., Kauffmann, G. & Heckman, T. (2006). The host galaxies and classification of active galactic nuclei. *Monthly Notices of the Royal Astronomical Society*, **372**, 961–976. (Cited on pages 44, 45, 46 and 48.)

Koleva, M., Prugniel, P., Bouchard, A. & Wu, Y. (2009). ULySS: a full spectrum fitting package. *The Astrophysical Journal*, **501**, 1269–1279. (Cited on pages 3, 5, 6, 7, 9, 15 and 16.)

Kormendy, J. & Richstone, D. (1995). Inward Bound—The Search For Supermassive Black Holes In Galactic Nuclei. *Annual Review of Astronomy and Astrophysics*, **33**, 581. (Cited on page 7.)

Koski, A.T. (1978). Spectrophotometry of Seyfert 2 galaxies and narrow-line radio galaxies. *The Astrophysical Journal*, **223**, 56–73. (Cited on pages 7, 27, 28 and 31.)

Kotulla, R., Fritze, U., Weilbacher, P. & Anders, P. (2009). GALEV evolutionary synthesis models - I. Code, input physics and web interface. *Monthly Notices of the Royal Astronomical Society*, **396**, 462–484. (Cited on pages 3, 4, 5 and 12.)

Kraemer, S.B. & Crenshaw, D.M. (2000). Resolved Spectroscopy of the Narrow-Line Region in NGC 1068. III. Physical Conditions in the Emission-Line Gas. *The Astrophysical Journal*, **544**, 763–779. (Cited on pages 27, 46 and 48.)

Kroupa, P. (2001). On the variation of the initial mass function. *Monthly Notices of the Royal Astronomical Society*, **322**, 231–246. (Cited on pages 4 and 13.)

Krüger, H., Fritze-v. Alvensleben, U. & Loose, H.H. (1995). Optical and near infrared spectral energy distributions. of blue compact galaxies from evolutionary synthesis. *Astronomy and Astrophysics*, **303**, 41. (Cited on pages 1, 3, 4, 5, 8, 9 and 47.)

Kügler, S.D., Nilsson, K., Heidt, J., Esser, J. & Schultz, T. (2014). Properties of optically selected BL Lacertae candidates from the SDSS. *Astronomy and Astrophysics*, **569**, A95. (Cited on pages 27 and 29.)

Lacey, C. & Cole, S. (1993). Merger rates in hierarchical models of galaxy formation. *Monthly Notices of the Royal Astronomical Society*, **262**, 627–649. (Cited on page 59.)

Le Borgne, D., Rocca-Volmerange, B., Prugniel, P., Lançon, A., Fioc, M. & Soubiran, C. (2004). Evolutionary synthesis of galaxies at high spectral resolution with the code PEGASE-HR. Metallicity and age tracers. *Astronomy and Astrophysics*, **425**, 881–897. (Cited on pages 3 and 5.)

Le Borgne, J.F., Bruzual, G., Pelló, R., Lançon, A., Rocca-Volmerange, B., Sanahuja, B., Schaerer, D., Soubiran, C. & Vílchez-Gómez, R. (2003). STELIB: A library of stellar spectra at $R \sim 2000$. *Astronomy and Astrophysics*, **402**, 433–442. (Cited on pages 5 and 16.)

Leitherer, C., Schaerer, D., Goldader, J.D., Delgado, R.M.G., Robert, C., Kune, D.F., de Mello, D.F., Devost, D. & Heckman, T.M. (1999). Starburst99: Synthesis Models for Galaxies with Active Star Formation. *The Astrophysical Journal Supplement Series*, **123**, 3–40. (Cited on pages 3, 4, 5 and 8.)

Leitherer, C., Ortiz Otálvaro, P.A., Bresolin, F., Kudritzki, R.P., Lo Faro, B., Pauldrach, A.W.A., Pettini, M. & Rix, S.A. (2010). A Library of Theoretical Ultraviolet Spectra of Massive, Hot Stars for Evolutionary Synthesis. *The Astrophysical Journal Supplement*, **189**, 309–335. (Cited on page 5.)

Li, C., Wang, E., Lin, L., Bershady, M.A., Bundy, K., Tremonti, C.A., Xiao, T., Yan, R., Bizyaev, D., Blanton, M., Cales, S., Cherinka, B., Cheung, E., Drory, N., Emsellem, E., Fu, H., Gelfand, J., Law, D.R., Lin, L., MacDonald, N., Maraston, C., Masters, K.L., Merrifield, M.R., Pan, K., Sánchez, S.F., Schneider, D.P., Thomas, D., Wake, D., Wang, L., Weijmans, A.M., Wilkinson, D., Yoachim, P., Zhang, K. & Zheng, T. (2015). P-MaNGA: Gradients in Recent Star Formation Histories as Diagnostics for Galaxy Growth and Death. *The Astrophysical Journal*, **804**, 125. (Cited on page 3.)

Lilly, S.J., Le Fevre, O., Hammer, F. & Crampton, D. (1996). The Canada-France Redshift Survey: The Luminosity Density and Star Formation History of the Universe to $z \sim 1$. *The Astrophysical Journal Letters*, **460**, L1. (Cited on page 1.)

López Fernández, R., Cid Fernandes, R., González Delgado, R.M., Vale Asari, N., Pérez, E., García-Benito, R., de Amorim, A.L., Lacerda, E.A.D., Cortijo-Ferrero, C. & Sánchez, S.F. (2016). Simultaneous spectroscopic and photometric analysis of galaxies with STARLIGHT: CALIFA+GALEX. *Monthly Notices of the Royal Astronomical Society*, **458**, 184–199. (Cited on page 64.)

Lynden-Bell, D. (1969). Galactic Nuclei as Collapsed Old Quasars. *Nature*, **223**, 690–694. (Cited on page 7.)

MacArthur, L.A., González, J.J. & Courteau, S. (2009). Stellar population and kinematic profiles in spiral bulges and discs: population synthesis of integrated spectra. *Monthly Notices of the Royal Astronomical Society*, **395**, 28–63. (Cited on pages 5, 6, 9 and 15.)

Madau, P., Ferguson, H.C., Dickinson, M.E., Giavalisco, M., Steidel, C.C. & Fruchter, A. (1996). High-redshift galaxies in the Hubble Deep Field: colour selection and star formation history to $z \sim 4$. *Monthly Notices of the Royal Astronomical Society*, **283**, 1388–1404. (Cited on pages 1 and 6.)

Maeder, A. & Meynet, G. (1988). Tables of evolutionary star models from 0.85 to 120 solar masses with overshooting and mass loss. *Astronomy and Astrophysics Supplement Series*, **76**, 411–425. (Cited on page 4.)

Malkan, M.A. & Filippenko, A.V. (1983). The stellar and nonstellar continua of Seyfert galaxies Nonthermal emission in the near-infrared. *The Astrophysical Journal*, **275**, 477–492. (Cited on pages 27 and 28.)

Maraston, C. (1998). Evolutionary synthesis of stellar populations: a modular tool. *Monthly Notices of the Royal Astronomical Society*, **300**, 872–892. (Cited on page 4.)

Maraston, C. (2005). Evolutionary population synthesis: models, analysis of the ingredients and application to high-z galaxies. *Monthly Notices of the Royal Astronomical Society*, **362**, 799–825. (Cited on pages 4 and 5.)

Marcha, M.J.M. & Browne, I.W.A. (1996). The prediction of the spectral properties of BL Lac samples. *Monthly Notices of the Royal Astronomical Society*, **279**, 72–78. (Cited on page 27.)

Marcha, M.J.M., Browne, I.W.A., Impey, C.D. & Smith, P.S. (1996). Optical spectroscopy and polarization of a new sample of optically bright flat radio spectrum sources. *Monthly Notices of the Royal Astronomical Society*, **281**, 425–448. (Cited on pages 27 and 29.)

Martín-Manjón, M.L., García-Vargas, M.L., Mollá, M. & Díaz, A.I. (2010). PopStar evolutionary synthesis models II: optical emission-line spectra from giant HII regions. *Monthly Notices of the Royal Astronomical Society*, **403**, 2012–2032. (Cited on pages 7, 8, 9, 44 and 48.)

Mateus, A., Sodré, L., Cid Fernandes, R., Stasińska, G., Schoenell, W. & Gomes, J.M. (2006). Semi-empirical analysis of Sloan Digital Sky Survey galaxies - II. The bimodality of the galaxy population revisited. *Monthly Notices of the Royal Astronomical Society*, **370**, 721–737. (Cited on pages 21 and 31.)

Mathews, W.G. & Ferland, G.J. (1987). What heats the hot phase in active nuclei? *The Astrophysical Journal*, **323**, 456–467. (Cited on pages 7 and 44.)

McElroy, R., Croom, S.M., Pracy, M., Sharp, R., Ho, I.T. & Medling, A.M. (2015). IFU observations of luminous type II AGN - I. Evidence for ubiquitous winds. *Monthly Notices of the Royal Astronomical Society*, **446**, 2186–2204. (Cited on page 8.)

Meléndez, M., Kraemer, S.B., Weaver, K.A. & Mushotzky, R.F. (2011). Uncovering the Spectral Energy Distribution in Active Galaxies Using High-ionization Mid-infrared Emission Lines. *The Astrophysical Journal*, **738**, 6. (Cited on page 44.)

Meléndez, M., Heckman, T.M., Martínez-Paredes, M., Kraemer, S.B. & Mendoza, C. (2014). Theoretical modelling of emission-line galaxies: new classification parameters for mid-infrared and optical spectroscopy. *Monthly Notices of the Royal Astronomical Society*, **443**, 1358–1369. (Cited on pages 8 and 48.)

Mezcua, M., Lobanov, A.P., Chavushyan, V.H. & León-Tavares, J. (2011). Black hole masses and starbursts in X-shaped radio sources. *Astronomy and Astrophysics*, **527**, A38. (Cited on page 32.)

Mollá, M., García-Vargas, M.L. & Bressan, A. (2009). PopStar I: evolutionary synthesis model description. *Monthly Notices of the Royal Astronomical Society*, **398**, 451–470. (Cited on pages 3, 5, 8 and 16.)

Morgan, W.W. (1956). The Integrated Spectral Types of Globular Clusters. *Publications of the Astronomical Society of the Pacific*, **68**, 509. (Cited on page 2.)

Moultaka, J. (2005). A new inverse method for stellar population synthesis and error analysis. *Astronomy and Astrophysics*, **430**, 95–106. (Cited on pages 3 and 31.)

Moultaka, J. & Pelat, D. (2000). Error analysis for stellar population synthesis as an inverse problem. *Monthly Notices of the Royal Astronomical Society*, **314**, 409–419. (Cited on page 31.)

Noll, S., Burgarella, D., Giovannoli, E., Buat, V., Marcillac, D. & Muñoz-Mateos, J.C. (2009). Analysis of galaxy spectral energy distributions from far-UV to far-IR with CIGALE: studying a SINGS test sample. *Astronomy and Astrophysics*, **507**, 1793–1813. (Cited on page 8.)

Nussbaumer, H. & Schmutz, W. (1984). The hydrogenic 2s-1s two-photon emission. *Astronomy and Astrophysics*, **138**, 495. (Cited on page 11.)

O'Connell, R.W. (1976). Galaxy spectral synthesis. I - Stellar populations in the nuclei of giant ellipticals. *The Astrophysical Journal*, **206**, 370–390. (Cited on pages 3, 5 and 27.)

O'Connell, R.W. (1996). An Overview of Spectral Synthesis of Stellar Populations. In C. Leitherer, U. Fritze-von-Alvensleben & J. Huchra, eds., *From Stars to Galaxies: the Impact of Stellar Physics on Galaxy Evolution*, vol. 98 of *Astronomical Society of the Pacific Conference Series*, 3. (Cited on pages 5 and 6.)

Ocvirk, P., Pichon, C., Lançon, A. & Thiébaut, E. (2006a). STECMAP: STEllar Content from high-resolution galactic spectra via Maximum A Posteriori. *Monthly Notices of the Royal Astronomical Society*, **365**, 46–73. (Cited on pages 5, 6, 15 and 16.)

Ocvirk, P., Pichon, C., Lançon, A. & Thiébaut, E. (2006b). STECKMAP: STEllar Content and Kinematics from high resolution galactic spectra via Maximum A Posteriori. *Monthly Notices of the Royal Astronomical Society*, **365**, 74–84. (Cited on pages 5, 6, 15 and 16.)

O'Dell, S.L. (1986). The optical continuum emission of active galactic nuclei. *The Publications of the Astronomical Society of the Pacific*, **98**, 140–147. (Cited on page 7.)

Öhman, Y. (1934). Spectrographic Studies in the Red. *The Astrophysical Journal*, **80**, 171. (Cited on page 2.)

Oke, J.B. (1974). Absolute Spectral Energy Distributions for White Dwarfs. *The Astrophysical Journal Supplement*, **27**, 21. (Cited on page 13.)

Oke, J.B. & Gunn, J.E. (1974). The Distance of BL Lacertae. *The Astrophysical Journal*, **189**, L5. (Cited on pages 27 and 29.)

Oke, J.B., Neugebauer, G. & Becklin, E.E. (1970). Absolute Spectral Energy Distribution of Quasi-Stellar Objects from 0.3 to 2.2 Microns. *The Astrophysical Journal*, **159**, 341. (Cited on page 27.)

Osterbrock, D.E. (1989). *Astrophysics of gaseous nebulae and active galactic nuclei*. (Cited on pages 8 and 11.)

Osterbrock, D.E. & Ferland, G.J. (2006). *Astrophysics of gaseous nebulae and active galactic nuclei*. (Cited on pages 8, 11, 12, 44 and 48.)

Pacifici, C., da Cunha, E., Charlot, S., Rix, H.W., Fumagalli, M., Wel, A.v.d., Franx, M., Maseda, M.V., van Dokkum, P.G., Brammer, G.B., Momcheva, I., Skelton, R.E., Whitaker, K., Leja, J., Lundgren, B., Kassin, S.A. & Yi, S.K. (2015). On the importance of using appropriate spectral models to derive physical properties of galaxies at $0.7 < z < 2.8$. *Monthly Notices of the Royal Astronomical Society*, **447**, 786–805. (Cited on pages 9 and 47.)

Papaderos, P. & Gomes, J.M. (in prep.). (Cited on pages 11, 12 and 63.)

Papaderos, P. & Östlin, G. (2012). I Zw 18 as morphological paradigm for rapidly assembling high-z galaxies. *Astronomy and Astrophysics*, **537**, A126. (Cited on pages 9 and 47.)

Papaderos, P., Loose, H.H., Thuan, T.X. & Fricke, K.J. (1996). Optical structure and star formation in blue compact dwarf galaxies. I. Observations and profile decomposition. *Astronomy and Astrophysics Supplement*, **120**, 207–228. (Cited on page 12.)

Papaderos, P., Izotov, Y.I., Fricke, K.J., Thuan, T.X. & Guseva, N.G. (1998). On the age of the nearby blue compact dwarf galaxy SBS 0335-052. *Astronomy and Astrophysics*, **338**, 43–55. (Cited on pages 9 and 47.)

Papaderos, P., Gomes, J.M., Vílchez, J.M., Kehrig, C., Lehnert, M.D., Ziegler, B., Sánchez, S.F., Husemann, B., Monreal-Ibero, A., García-Benito, R., Bland-Hawthorn, J., Cortijo-Ferrero, C., de Lorenzo-Cáceres, A., del Olmo, A., Falcón-Barroso, J., Galbany, L., Iglesias-Páramo, J., López-Sánchez, Á.R., Marquez, I., Mollá, M., Mast, D., van de Ven, G. & Wisotzki, L. (2013). Nebular emission and the Lyman continuum photon escape fraction in CALIFA early-type galaxies. *Astronomy and Astrophysics*, **555**, L1. (Cited on pages 3, 16 and 29.)

Pelat, D. (1997). A new method to solve stellar population synthesis problems with the use of a data base. *Monthly Notices of the Royal Astronomical Society*, **284**, 365–375. (Cited on pages 5, 6 and 7.)

Pelat, D. (1998). Stellar population synthesis with more degrees of freedom than observables. *Monthly Notices of the Royal Astronomical Society*, **299**, 877–888. (Cited on pages 5, 6 and 7.)

Pickles, A.J. (1998). A Stellar Spectral Flux Library: 1150-25000 Å. *The Publications of the Astronomical Society of the Pacific*, **110**, 863–878. (Cited on page 5.)

Planck Collaboration, Ade, P.A.R., Aghanim, N., Arnaud, M., Ashdown, M., Aumont, J., Baccigalupi, C., Banday, A.J., Barreiro, R.B., Bartlett, J.G. & et al. (2016). Planck 2015 results. XIII. Cosmological parameters. *Astronomy and Astrophysics*, **594**, A13. (Cited on page 16.)

Price, K., Storn, R. & Lampinen, J. (2005). *Differential Evolution: A Practical Approach to Global Optimization*. Springer. (Cited on page 59.)

Quillen, A.C. & Bland-Hawthorn, J. (2008). When is star formation episodic? A delay differential equation 'negative feedback' model. *Monthly Notices of the Royal Astronomical Society*, **386**, 2227–2234. (Cited on page 12.)

Rauch, T. (2002). Synthetic Ionizing Spectra for Planetary Nebulae: A New Grid of Metal-Line Blanketed NLTE Model Atmospheres. In W.J. Henney, J. Franco & M. Martos, eds., *Revista Mexicana de Astronomia y Astrofisica Conference Series*, vol. 12 of *Revista Mexicana de Astronomia y Astrofisica*, 150–151. (Cited on page 5.)

Reichardt, C., Jimenez, R. & Heavens, A.F. (2001). Recovering physical parameters from galaxy spectra using MOPED. *Monthly Notices of the Royal Astronomical Society*, **327**, 849–867. (Cited on page 6.)

Renzini, A. (1981). Energetics of stellar populations. *Annales de Physique*, **6**, 87–102. (Cited on pages 3 and 4.)

Renzini, A. & Buzzoni, A. (1986). Global properties of stellar populations and the spectral evolution of galaxies. In C. Chiosi & A. Renzini, eds., *Spectral Evolution of Galaxies*, vol. 122 of *Astrophysics and Space Science Library*, 195–231. (Cited on page 4.)

Ribeiro, B., Lobo, C., Antón, S., Gomes, J.M. & Papaderos, P. (2016). Red galaxies with pseudo-bulges in the SDSS: closer to disc galaxies or to classical bulges? *Monthly Notices of the Royal Astronomical Society*, **456**, 3899–3914. (Cited on page 16.)

Richstone, D., Ajhar, E.A., Bender, R., Bower, G., Dressler, A., Faber, S.M., Filippenko, A.V., Gebhardt, K., Green, R., Ho, L.C., Kormendy, J., Lauer, T.R., Magorrian, J. & Tremaine, S. (1998). Supermassive black holes and the evolution of galaxies. *Nature*, **395**, A14. (Cited on page 7.)

Roche, N., Humphrey, A., Lagos, P., Papaderos, P., Silva, M., Cardoso, L.S.M. & Gomes, J.M. (2016). MUSE three-dimensional spectroscopy and kinematics of the gigahertz peaked spectrum radio galaxy PKS 1934-63: interaction, recently triggered active galactic nucleus and star formation. *Monthly Notices of the Royal Astronomical Society*, **459**, 4259–4280. (Cited on page 32.)

Röck, B., Vazdekis, A., Ricciardelli, E., Peletier, R.F., Knapen, J.H. & Falcón-Barroso, J. (2016). MILES extended: Stellar population synthesis models from the optical to the infrared. *Astronomy and Astrophysics*, **589**, A73. (Cited on pages 3, 5 and 64.)

Roos, O., Juneau, S., Bournaud, F. & Gabor, J.M. (2015). Thermal and Radiative Active Galactic Nucleus Feedback have a Limited Impact on Star Formation in High-redshift Galaxies. *The Astrophysical Journal*, **800**, 19. (Cited on page 44.)

Rosenberg, H. (1910). Über den Zusammenhang von Helligkeit und Spektraltypus in den Plejaden. *Astronomische Nachrichten*, **186**, 71. (Cited on page 2.)

Salpeter, E.E. (1955). The Luminosity Function and Stellar Evolution. *The Astrophysical Journal*, **121**, 161. (Cited on pages 4, 5 and 13.)

Sánchez, S.F., Kennicutt, R.C., Gil de Paz, A., van de Ven, G., Vílchez, J.M., Wisotzki, L., Walcher, C.J., Mast, D., Aguerri, J.A.L., Albiol-Pérez, S., Alonso-Herrero, A., Alves, J., Bakos, J., Bartáková, T., Bland-Hawthorn, J., Boselli, A., Bomans, D.J., Castillo-Morales, A., Cortijo-Ferrero, C., de Lorenzo-Cáceres, A., Del Olmo, A., Dettmar, R.J., Díaz, A., Ellis, S., Falcón-Barroso, J., Flores, H., Gallazzi, A., García-Lorenzo, B., González Delgado, R., Gruel, N., Haines, T., Hao, C., Husemann, B., Iglésias-Páramo, J., Jahnke, K., Johnson, B., Jungwiert, B., Kalinova, V., Kehrig, C., Kupko, D., López-Sánchez, Á.R., Lyubenova, M., Marino, R.A., Mármol-Queraltó, E., Márquez, I., Masegosa, J., Meidt, S., Mendez-Abreu, J., Monreal-Ibero, A., Montijo, C., Mourão, A.M., Palacios-Navarro, G., Papaderos, P., Pasquali, A., Peletier, R., Pérez, E., Pérez, I., Quirrenbach, A., Relaño, M., Rosales-Ortega, F.F., Roth, M.M., Ruiz-Lara, T., Sánchez-Blázquez, P., Sengupta, C., Singh, R., Stanishev, V., Trager, S.C., Vazdekis, A., Viironen, K., Wild, V., Zibetti, S. & Ziegler, B. (2012). CALIFA, the Calar Alto Legacy Integral Field Area survey. I. Survey presentation. *Astronomy and Astrophysics*, **538**, A8. (Cited on page 3.)

Sánchez-Blázquez, P., Peletier, R.F., Jiménez-Vicente, J., Cardiel, N., Cenarro, A.J., Falcón-Barroso, J., Gorgas, J., Selam, S. & Vazdekis, A. (2006). Medium-resolution Isaac Newton Telescope library of empirical spectra. *Monthly Notices of the Royal Astronomical Society*, **371**, 703–718. (Cited on pages 2, 13 and 16.)

Sandage, A. (1986). Star formation rates, galaxy morphology, and the Hubble sequence. *Astronomy and Astrophysics*, **161**, 89–101. (Cited on page 1.)

Sarzi, M., Falcón-Barroso, J., Davies, R.L., Bacon, R., Bureau, M., Cappellari, M., de Zeeuw, P.T., Emsellem, E., Fathi, K., Krajnović, D., Kuntschner, H., McDermid, R.M. & Peletier, R.F. (2006). The SAURON project - V. Integral-field emission-line kinematics of 48 elliptical and lenticular galaxies. *Monthly Notices of the Royal Astronomical Society*, **366**, 1151–1200. (Cited on page 3.)

Sarzi, M., Shields, J.C., Schawinski, K., Jeong, H., Shapiro, K., Bacon, R., Bureau, M., Cappellari, M., Davies, R.L., de Zeeuw, P.T., Emsellem, E., Falcón-Barroso, J., Krajnović, D., Kuntschner, H., McDermid, R.M., Peletier, R.F., van den Bosch, R.C.E., van de Ven, G. & Yi, S.K. (2010). The SAURON project - XVI. On the sources of ionization for the gas in elliptical and lenticular galaxies. *Monthly Notices of the Royal Astronomical Society*, **402**, 2187–2210. (Cited on page 3.)

Schaerer, D. & de Barros, S. (2009). The impact of nebular emission on the ages of $z \approx 6$ galaxies. *Astronomy and Astrophysics*, **502**, 423–426. (Cited on pages 5 and 7.)

Schaerer, D. & Pelló, R. (2005). Stellar populations and Lyα emission in two lensed $z \gtrsim 6$ galaxies. *Monthly Notices of the Royal Astronomical Society*, **362**, 1054–1064. (Cited on page 5.)

Schaller, G., Schaerer, D., Meynet, G. & Maeder, A. (1992). New grids of stellar models from 0.8 to 120 solar masses at Z = 0.020 and Z = 0.001. *Astronomy and Astrophysics Supplement Series*, **96**, 269–331. (Cited on pages 5 and 13.)

Schawinski, K., Thomas, D., Sarzi, M., Maraston, C., Kaviraj, S., Joo, S.J., Yi, S.K. & Silk, J. (2007). Observational evidence for AGN feedback in early-type galaxies. *Monthly Notices of the Royal Astronomical Society*, **382**, 1415–1431. (Cited on pages 45 and 46.)

Scheiner, J. (1899). On the spectrum of the great nebula in Andromeda. *The Astrophysical Journal*, **9**. (Cited on page 2.)

Schmidt, A.A., Bica, E. & Dottori, H.A. (1989). On the meaning of a minimization procedure applied to a degenerate astrophysical problem. *Monthly Notices of the Royal Astronomical Society*, **238**, 925–934. (Cited on pages 5 and 6.)

Schmidt, M. (1959). The Rate of Star Formation. *The Astrophysical Journal*, **129**, 243. (Cited on pages 1 and 12.)

Schmitt, H.R., Storchi-Bergmann, T. & Cid Fernandes, R. (1999). Spectral synthesis of the nuclear regions of Seyfert 2 and radio galaxies. *Monthly Notices of the Royal Astronomical Society*, **303**, 173–178. (Cited on pages 3, 7, 27 and 28.)

Serote Roos, M., Boisson, C., Joly, M. & Ward, M.J. (1998). Stellar populations in active galactic nuclei - I. The observations. *Monthly Notices of the Royal Astronomical Society*, **301**, 1–14. (Cited on page 31.)

Serra, P., Amblard, A., Temi, P., Burgarella, D., Giovannoli, E., Buat, V., Noll, S. & Im, S. (2011). CIGALEMC: Galaxy Parameter Estimation Using a Markov Chain Monte Carlo Approach with CIGALE. *The Astrophysical Journal*, **740**, 22. (Cited on page 12.)

Seyfert, C.K. (1943). Nuclear Emission in Spiral Nebulae. *The Astrophysical Journal*, **97**, 28. (Cited on page 7.)

Silva, L., Granato, G.L., Bressan, A. & Danese, L. (1998). Modeling the Effects of Dust on Galactic Spectral Energy Distributions from the Ultraviolet to the Millimeter Band. *The Astrophysical Journal*, **509**, 103–117. (Cited on page 7.)

Spinrad, H. & Taylor, B.J. (1971). The Stellar Content of the Nuclei of Nearby Galaxies. I. M31, M32, and M81. *The Astrophysical Journal Supplement*, **22**, 445. (Cited on page 5.)

Spinrad, H. & Taylor, B.J. (1972). The Stellar Content of the Nuclei of Nearby Galaxies. II. a Note on NGC 4594. *The Astrophysical Journal*, **171**, 397. (Cited on pages 3 and 4.)

Stasińska, G. (1984a). A grid of model nebulae photoionized by a power-law continuum. *Astronomy and Astrophysics Supplement Series*, **55**, 15–32. (Cited on pages 27, 44 and 46.)

Stasińska, G. (1984b). Confrontation of a sample of Seyfert 2 galaxies with photoionized models. *Astronomy and Astrophysics*, **135**, 341–355. (Cited on pages 27, 44, 46 and 48.)

Stasińska, G., Cid Fernandes, R., Mateus, A., Sodré, L. & Asari, N.V. (2006). Semi-empirical analysis of Sloan Digital Sky Survey galaxies - III. How to distinguish AGN hosts. *Monthly Notices of the Royal Astronomical Society*, **371**, 972–982. (Cited on pages 8, 16, 31, 44 and 48.)

Stasińska, G., Vale Asari, N., Cid Fernandes, R., Gomes, J.M., Schlickmann, M., Mateus, A., Schoenell, W., Sodré, L., Jr. & Seagal Collaboration (2008). Can retired galaxies mimic active galaxies? Clues from the Sloan Digital Sky Survey. *Monthly Notices of the Royal Astronomical Society: Letters*, **391**, L29–L33. (Cited on pages 8 and 16.)

Storchi-Bergmann, T., Fernandes, R.C. & Schmitt, H.R. (1998). The Nature of the Optical Light in Seyfert 2 Galaxies with Polarized Continua. *The Astrophysical Journal*, **501**, 94–102. (Cited on pages 7 and 27.)

Storn, R. & Price, K. (1996). Minimizing the real function of the icec'96 contest by differential evolution. In *IEEE conf. on Evolutionary Computation*, vol. 842, 844. (Cited on page 59.)

Storn, R. & Price, K. (1997). Differential evolution - a simple and efficient heuristic for global optimization over continuous spaces. *Journal of Global Optimization*, **11**, 341. (Cited on page 59.)

Stoughton, C., Lupton, R.H., Bernardi, M., Blanton, M.R., Burles, S., Castander, F.J., Connolly, A.J., Eisenstein, D.J., Frieman, J.A., Hennessy, G.S., Hindsley, R.B., Ivezić, Ž., Kent, S., Kunszt, P.Z., Lee, B.C., Meiksin, A., Munn, J.A., Newberg, H.J., Nichol, R.C., Nicinski, T., Pier, J.R., Richards, G.T., Richmond, M.W., Schlegel, D.J., Smith, J.A., Strauss, M.A., SubbaRao, M., Szalay, A.S., Thakar, A.R., Tucker, D.L., Vanden Berk, D.E., Yanny, B., Adelman, J.K., Anderson, J.E., Jr., Anderson, S.F., Annis, J., Bahcall, N.A., Bakken, J.A., Bartelmann, M., Bastian, S., Bauer, A., Berman, E., Böhringer, H., Boroski, W.N., Bracker, S., Briegel, C., Briggs, J.W., Brinkmann, J., Brunner, R., Carey, L., Carr, M.A., Chen, B., Christian, D., Colestock, P.L., Crocker, J.H., Csabai, I., Czarapata, P.C., Dalcanton, J., Davidsen, A.F., Davis, J.E., Dehnen, W., Dodelson, S., Doi, M., Dombeck, T., Donahue, M., Ellman, N., Elms, B.R., Evans, M.L., Eyer, L., Fan, X., Federwitz, G.R., Friedman, S., Fukugita, M., Gal, R., Gillespie, B., Glazebrook, K., Gray, J., Grebel, E.K., Greenawalt, B., Greene, G., Gunn, J.E., de Haas, E., Haiman, Z., Haldeman, M., Hall, P.B., Hamabe, M., Hansen, B., Harris, F.H., Harris, H., Harvanek, M., Hawley, S.L., Hayes, J.J.E., Heckman, T.M., Helmi, A., Henden, A., Hogan, C.J., Hogg, D.W., Holmgren, D.J., Holtzman, J., Huang, C.H., Hull, C., Ichikawa, S.I., Ichikawa, T., Johnston, D.E., Kauffmann, G., Kim, R.S.J., Kimball, T., Kinney, E., Klaene, M., Kleinman, S.J., Klypin, A., Knapp, G.R., Korienek, J., Krolik, J., Kron, R.G., Krzesiński, J., Lamb, D.Q., Leger, R.F., Limmongkol, S., Lindenmeyer, C., Long, D.C., Loomis, C., Loveday, J., MacKinnon, B., Mannery, E.J., Mantsch, P.M., Margon, B., McGehee, P., McKay, T.A., McLean, B., Menou, K., Merelli, A., Mo, H.J., Monet, D.G., Nakamura, O., Narayanan, V.K., Nash, T., Neilsen, E.H., Jr., Newman, P.R., Nitta, A., Odenkirchen, M., Okada, N., Okamura, S., Ostriker, J.P., Owen, R., Pauls, A.G., Peoples, J., Peterson, R.S., Petravick, D., Pope, A., Pordes, R., Postman, M., Prosapio, A., Quinn, T.R., Rechenmacher, R., Rivetta, C.H., Rix, H.W., Rockosi, C.M., Rosner, R., Ruthmansdorfer, K., Sandford, D., Schneider, D.P., Scranton, R., Sekiguchi, M., Sergey, G., Sheth, R., Shimasaku, K., Smee, S., Snedden, S.A., Stebbins, A., Stubbs, C., Szapudi, I., Szkody, P., Szokoly, G.P., Tabachnik, S., Tsvetanov, Z., Uomoto, A., Vogeley, M.S., Voges, W., Waddell, P., Walterbos, R., Wang, S.i., Watanabe, M., Weinberg, D.H., White, R.L., White, S.D.M., Wilhite, B., Wolfe, D., Yasuda, N., York, D.G., Zehavi, I. & Zheng, W. (2002). Sloan Digital Sky Survey: Early Data Release. *The Astrophysical Journal*, **123**, 485–548. (Cited on page 5.)

Strateva, I., Ivezić, Ž., Knapp, G.R., Narayanan, V.K., Strauss, M.A., Gunn, J.E., Lupton, R.H., Schlegel, D., Bahcall, N.A., Brinkmann, J., Brunner, R.J., Budavári, T., Csabai, I., Castander, F.J., Doi, M., Fukugita, M., Győry, Z., Hamabe, M., Hennessy, G., Ichikawa, T., Kunszt, P.Z., Lamb, D.Q., McKay, T.A., Okamura, S., Racusin, J., Sekiguchi, M., Schneider, D.P., Shimasaku, K. & York, D. (2001). Color Separation of Galaxy Types in the Sloan Digital Sky Survey Imaging Data. *The Astrophysical Journal*, **122**, 1861–1874. (Cited on page 1.)

Sutherland, R.S. & Dopita, M.A. (1993). Cooling functions for low-density astrophysical plasmas. *The Astrophysical Journal Supplement Series*, **88**, 253–327. (Cited on pages 8 and 43.)

Tinsley, B.M. (1968). Evolution of the Stars and Gas in Galaxies. *The Astrophysical Journal*, **151**, 547. (Cited on pages 3 and 4.)

Tinsley, B.M. (1972). Galactic Evolution. *Astronomy and Astrophysics*, **20**, 383. (Cited on pages 3 and 4.)

Tinsley, B.M. (1980). Evolution of the Stars and Gas in Galaxies. *Fundamentals of Cosmic Physics*, **5**, 287–388. (Cited on pages 1, 3 and 4.)

Tinsley, B.M. & Gunn, J.E. (1976). Evolutionary synthesis of the stellar population in elliptical galaxies. I - Ingredients, broad-band colors, and infrared features. *The Astrophysical Journal*, **203**, 52–62. (Cited on pages 3 and 4.)

Tojeiro, R., Heavens, A.F., Jimenez, R. & Panter, B. (2007). Recovering galaxy star formation and metallicity histories from spectra using VESPA. *Monthly Notices of the Royal Astronomical Society*, **381**, 1252–1266. (Cited on pages 3, 5, 6, 9, 15 and 16.)

Tojeiro, R., Wilkins, S., Heavens, A.F., Panter, B. & Jimenez, R. (2009). A Public Catalog of Stellar Masses, Star Formation and Metallicity Histories, and Dust Content from the Sloan Digital Sky Survey using VESPA. *The Astrophysical Journal Supplement*, **185**, 1–19. (Cited on pages 6, 15 and 16.)

Torres-Papaqui, J.P., Coziol, R., Plauchu-Frayn, I., Andernach, H. & Ortega-Minakata, R.A. (2013). What do the star formation histories of galaxies tell us about the Starburst-AGN connection? *Revista Mexicana de Astronomía y Astrofísica*, **49**, 311–332. (Cited on pages 16 and 38.)

Trager, S.C., Worthey, G., Faber, S.M., Burstein, D. & González, J.J. (1998). Old Stellar Populations. VI. Absorption-Line Spectra of Galaxy Nuclei and Globular Clusters. *The Astrophysical Journal Supplement Series*, **116**, 1–28. (Cited on pages 13 and 15.)

Tremonti, C.A., Heckman, T.M., Kauffmann, G., Brinchmann, J., Charlot, S., White, S.D.M., Seibert, M., Peng, E.W., Schlegel, D.J., Uomoto, A., Fukugita, M. & Brinkmann, J. (2004). The Origin of the Mass-Metallicity Relation: Insights from 53,000 Star-forming Galaxies in the Sloan Digital Sky Survey. *The Astrophysical Journal*, **613**, 898–913. (Cited on pages 2, 5 and 6.)

Tully, R.B. & Fisher, J.R. (1977). A new method of determining distances to galaxies. *Astronomy and Astrophysics*, **54**, 661–673. (Cited on page 1.)

Urry, C.M. & Padovani, P. (1995). Unified Schemes for Radio-Loud Active Galactic Nuclei. *Publications of the Astronomical Society of the Pacific*, **107**, 803. (Cited on page 7.)

Vaona, L., Ciroi, S., Di Mille, F., Cracco, V., La Mura, G. & Rafanelli, P. (2012). Spectral properties of the narrow-line region in Seyfert galaxies selected from the SDSS-DR7. *Monthly Notices of the Royal Astronomical Society*, **427**, 1266–1283. (Cited on page 16.)

Vazdekis, A. (1999). Evolutionary Stellar Population Synthesis at 2 Å Spectral Resolution. *The Astrophysical Journal*, **513**, 224–241. (Cited on page 3.)

Vazdekis, A., Sánchez-Blázquez, P., Falcón-Barroso, J., Cenarro, A.J., Beasley, M.A., Cardiel, N., Gorgas, J. & Peletier, R.F. (2010). Evolutionary stellar population synthesis with MILES - I. The base models and a new line index system. *Monthly Notices of the Royal Astronomical Society*, **404**, 1639–1671. (Cited on pages 1, 3, 4, 5, 6 and 16.)

Vázquez, G.A. & Leitherer, C. (2005). Optimization of Starburst99 for Intermediate-Age and Old Stellar Populations. *The Astrophysical Journal*, **621**, 695–717. (Cited on pages 3 and 5.)

Vega, L.R., Asari, N.V., Cid Fernandes, R., Garcia-Rissmann, A., Storchi-Bergmann, T., González Delgado, R.M. & Schmitt, H. (2009). The CaT strength in Seyfert nuclei revisited: analysing young stars and non-stellar light contributions to the spectra. *Monthly Notices of the Royal Astronomical Society*, **393**, 846–857. (Cited on pages 7, 27 and 28.)

Veilleux, S. & Osterbrock, D.E. (1987). Spectral classification of emission-line galaxies. *The Astrophysical Journal Supplement Series*, **63**, 295–310. (Cited on pages 7, 8, 27, 44, 45, 46, 48, 49 and 76.)

Walcher, J., Groves, B., Budavári, T. & Dale, D. (2011). Fitting the integrated spectral energy distributions of galaxies. *Astrophysics and Space Science*, **331**, 1–52. (Cited on page 3.)

Whipple, F.L. (1935). The Colors and Spectra of External Galaxies. *Harvard College Observatory Circular*, **404**, 1–21. (Cited on page 2.)

Wood, D.B. (1966). Multicolor Photoelectric Photometry of Galaxies. *The Astrophysical Journal*, **145**, 36. (Cited on pages 2 and 6.)

Worthey, G. (1994). Comprehensive stellar population models and the disentanglement of age and metallicity effects. *The Astrophysical Journal Supplement Series*, **95**, 107–149. (Cited on pages 6, 7 and 21.)

Worthey, G. & Ottaviani, D.L. (1997). Hγ and Hδ Absorption Features in Stars and Stellar Populations. *The Astrophysical Journal Supplement Series*, **111**, 377–386. (Cited on page 15.)

Worthey, G., Faber, S.M., Gonzalez, J.J. & Burstein, D. (1994). Old stellar populations. 5: Absorption feature indices for the complete LICK/IDS sample of stars. *The Astrophysical Journal Supplement Series*, **94**, 687–722. (Cited on page 15.)

York, D.G., Adelman, J., Anderson, J.E., Jr., Anderson, S.F., Annis, J., Bahcall, N.A., Bakken, J.A., Barkhouser, R., Bastian, S., Berman, E., Boroski, W.N., Bracker, S., Briegel, C., Briggs, J.W., Brinkmann, J., Brunner, R., Burles, S., Carey, L., Carr, M.A., Castander, F.J., Chen, B., Colestock, P.L., Connolly, A.J., Crocker, J.H., Csabai, I., Czarapata, P.C., Davis, J.E., Doi, M., Dombeck, T., Eisenstein, D., Ellman, N., Elms, B.R., Evans, M.L., Fan, X., Federwitz, G.R., Fiscelli, L., Friedman, S., Frieman, J.A., Fukugita, M., Gillespie, B., Gunn, J.E., Gurbani, V.K., de Haas, E., Haldeman, M., Harris, F.H., Hayes, J., Heckman, T.M., Hennessy, G.S., Hindsley, R.B., Holm, S., Holmgren, D.J., Huang, C.h., Hull, C., Husby, D., Ichikawa, S.I., Ichikawa, T., Ivezić, Ž., Kent, S., Kim, R.S.J., Kinney, E., Klaene, M., Kleinman, A.N., Kleinman, S., Knapp, G.R., Korienek, J., Kron, R.G., Kunszt, P.Z., Lamb, D.Q., Lee, B., Leger, R.F., Limmongkol, S., Lindenmeyer, C., Long, D.C., Loomis, C., Loveday, J., Lucinio, R., Lupton, R.H., MacKinnon, B., Mannery, E.J., Mantsch, P.M., Margon, B., McGehee, P., McKay, T.A., Meiksin, A., Merelli, A., Monet, D.G., Munn, J.A., Narayanan, V.K., Nash, T., Neilsen, E., Neswold, R., Newberg, H.J., Nichol, R.C., Nicinski, T., Nonino, M., Okada, N., Okamura, S., Ostriker, J.P., Owen, R., Pauls, A.G., Peoples, J., Peterson, R.L., Petravick, D., Pier, J.R., Pope, A., Pordes, R., Prosapio, A., Rechenmacher, R., Quinn, T.R., Richards, G.T., Richmond, M.W., Rivetta, C.H., Rockosi, C.M., Ruthmansdorfer, K., Sandford, D., Schlegel, D.J., Schneider, D.P., Sekiguchi, M., Sergey, G., Shimasaku, K., Siegmund, W.A., Smee, S., Smith, J.A., Snedden, S., Stone, R., Stoughton, C., Strauss, M.A., Stubbs, C., SubbaRao, M., Szalay, A.S., Szapudi, I., Szokoly, G.P., Thakar, A.R., Tremonti, C., Tucker, D.L., Uomoto, A., Vanden Berk, D., Vogeley, M.S., Waddell, P., Wang, S.i., Watanabe, M., Weinberg, D.H., Yanny, B., Yasuda, N. & SDSS Collaboration (2000). The Sloan Digital Sky Survey: Technical Summary. *The Astrophysical Journal*, **120**, 1579–1587. (Cited on pages 1 and 3.)

Zackrisson, E., Bergvall, N., Olofsson, K. & Siebert, A. (2001). A model of spectral galaxy evolution including the effects of nebular emission. *Astronomy and Astrophysics*, **375**, 814–826. (Cited on pages 3, 5 and 8.)

Zackrisson, E., Bergvall, N. & Leitet, E. (2008). The Impact of Nebular Emission on the Broadband Fluxes of High-Redshift Galaxies. *The Astrophysical Journal Letters*, **676**, L9. (Cited on pages 7, 8, 9 and 47.)

Zamorani, G., Henry, J.P., Maccacaro, T., Tananbaum, H., Soltan, A., Avni, Y., Liebert, J., Stocke, J., Strittmatter, P.A., Weymann, R.J., Smith, M.G. & Condon, J.J. (1981). X-ray studies of quasars with the Einstein Observatory. II. *The Astrophysical Journal*, **245**, 357–374. (Cited on page 44.)

Zanstra, H. (1961). The Gaseous Nebula as a Quantum Counter (George Darwin Lecture). *Quarterly Journal of the Royal Astronomical Society*, **2**, 137. (Cited on pages 12 and 45.)

para a minha Mãe